

---

Theses and Dissertations

---

Summer 2014

## Photopolymerized materials and patterning for improved performance of neural prosthetics

Bradley William Tuft  
*University of Iowa*

Follow this and additional works at: <https://ir.uiowa.edu/etd>



Part of the [Chemical Engineering Commons](#)

Copyright © 2014 Bradley William Tuft

This dissertation is available at Iowa Research Online: <https://ir.uiowa.edu/etd/1410>

---

### Recommended Citation

Tuft, Bradley William. "Photopolymerized materials and patterning for improved performance of neural prosthetics." PhD (Doctor of Philosophy) thesis, University of Iowa, 2014.  
<https://doi.org/10.17077/etd.lbif0oq0>

---

Follow this and additional works at: <https://ir.uiowa.edu/etd>



Part of the [Chemical Engineering Commons](#)

PHOTOPOLYMERIZED MATERIALS AND PATTERNING FOR  
IMPROVED PERFORMANCE OF NEURAL PROSTHETICS

by

Bradley William Tuft

A thesis submitted in partial fulfillment  
of the requirements for the Doctor of  
Philosophy degree in Chemical and Biochemical Engineering  
in the Graduate College of  
The University of Iowa

August 2014

Thesis Supervisor: Professor C. Allan Guymon

Graduate College  
The University of Iowa  
Iowa City, Iowa

CERTIFICATE OF APPROVAL

---

PH.D. THESIS

---

This is to certify that the Ph.D. thesis of

Bradley William Tuft

has been approved by the Examining Committee  
for the thesis requirement for the Doctor of Philosophy  
degree in Chemical and Biochemical Engineering at the August 2014 graduation.

Thesis Committee: \_\_\_\_\_  
C. Allan Guymon, Thesis Supervisor

\_\_\_\_\_  
Marlan Hansen

\_\_\_\_\_  
Jennifer Fiegel

\_\_\_\_\_  
Julie Jessop

\_\_\_\_\_  
Eric Nuxoll

To my dear Eve who fills my life with love, and to our wonderful children

Let us have integrity and not write checks with our tongues which our conduct cannot cash.

-Neal A. Maxwell, *Meeting the Challenges of Today*

## ACKNOWLEDGMENTS

First, I sincerely thank Dr. Allan Guymon for his guidance and instruction throughout my graduate career. I couldn't have asked for a better mentor and friend as a thesis advisor. Allan helped me to substantially improve my technical communication skills through his invaluable feedback on my writing and presentations. He has also provided a perfect balance between advising and encouraging project ownership throughout our time together which has strongly prepared me for success in future professional pursuits and research projects. His gentle, but persuasive, encouragement to apply for national fellowships and grants was instrumental in achieving some of the highlights of my graduate career. More could be, and indeed ought to be, said about his excellent mentoring but suffice it to say that I am profoundly grateful for his influence and I look forward to future correspondence with him through the years.

I also cannot give enough praise about Dr. Marlan Hansen, his research acumen, or his invaluable input and contributions during our research collaboration. There really must be two of him to get so much accomplished in so short a time. His optimism and graciousness are infectious and made our frequent meetings something truly to look forward to which is no small thing to say about meetings. It has also been my privilege to work with very talented lab technicians and researchers in Dr. Hansen's lab including Joseph Clarke, Linjing Xu, Jason Clark, Shufeng Li, Lichun Zhang, Kristy Truong, Andrew Erwood, and Alison Seline. I don't hesitate to attribute much of the success of this project to their irreplaceable efforts.

My thanks, too, for valuable contributions from fellow graduate colleagues including Soon Ki Kim, Brad Forney, Clint Cook, Brian Dillman, Kristan Worthington, Celine Baguenard, Todd Thorson, Jon Scholte, Jake McLaughlin, Braden Leigh, and Brian Green. Their input during research discussions has significantly benefited my project and their friendship and kindness have made the lab and the office enjoyable

places to be. I thank Scott White, Austin Hangartner, Krystian Perez, and Stephanie McCoy for their valuable work as talented undergraduate researchers. Interacting with and supervising them was an incredible learning experience. The assistance and support from the secretaries in the Department of Chemical and Biochemical Engineering was always timely, friendly, and exceptional for which I thank Linda Wheatley, Natalie Potter, Wendy Meyers, and Katie Shnedler.

I am grateful to Dr. David Britt for his willingness to take me into his lab as an undergraduate researcher with almost no research experience. His mentorship and recommendations, along with engineering training I received at Utah State University, were critical to my graduate career and in setting a course for my professional career.

I thank my parents, Will and Julene Tuft, for their encouragement and their love. Their time and sacrifices have blessed my life, and my educational pursuits, immeasurably. I also thank Jim and Elaine Brickey, my father and mother-in-law, for their crucial help along the way, including the extended summer stay at their place during our transition to graduate school.

Finally, I thank my dear wife, Eve, for her love and unwavering support as I have pursued my dreams. She continues to be a wonderful mother to our children as well as my best friend and confidant through whatever comes our way.

## ABSTRACT

Neural prosthetics are used to replace or substantially augment remaining motor and sensory functions of neural pathways that were lost or damaged due to physical trauma, disease, or genetics. However, due to poor spatial signal resolution, neural prostheses fail to recapitulate the intimate, precise interactions inherent to neural networks. Designing materials and interfaces that direct *de novo* nerve growth to spatially specific stimulating elements is, therefore, a promising method to enhance signal specificity and performance of prostheses such as the successful cochlear implant (CI) and the developing retinal implant.

In this work, the spatial and temporal reaction control inherent to photopolymerization was used to develop methods to generate micro and nanopatterned materials that direct neurite growth from prosthesis relevant neurons. In particular, neurite growth and directionality has been investigated in response to physical, mechanical, and chemical cues on photopolymerized surfaces. Spiral ganglion neurons (SGNs) serve as the primary neuronal model as they are the principal target for CI stimulation. The objective of the research is to rationally design materials that spatially direct neurite growth and to translate fundamental understanding of nerve cell-material interactions into methods of nerve regeneration that improve neural prosthetic performance.

A rapid, single-step photopolymerization method was developed to fabricate micro and nanopatterned physical cues on methacrylate surfaces by selectively blocking light with photomasks. Feature height is readily tuned from 100 nm – 10  $\mu$ m by modulating parameters of the photopolymerization including initiator concentration and species, light intensity, separation distance from the photomask, and radiation exposure time. Alignment of neural elements increases significantly with increasing feature amplitude and constant periodicity, as well as with decreasing periodicity and constant

amplitude. SGN neurite alignment strongly correlates ( $r = 0.93$ ) with the maximum feature slope. Neurite alignment is compared on unpatterned, unidirectional, and multidirectional photopolymerized micropatterns.

The effect of substrate rigidity on neurite alignment to physical cues was determined by maintaining equivalent pattern microfeatures, afforded by the reaction control of photopolymerization, while concomitantly altering the composition of several copolymer platforms to tune matrix stiffness. For each platform, neurite alignment to unidirectional patterns increases with increasing substrate rigidity. Interestingly, SGN neurites respond to material stiffness cues that are orders of magnitude higher (GPa) than what is typically ascribed to neural environments (kPa).

Finally, neurite behavior at bioactive borders of various adhesive molecules was evaluated on micropatterned materials to determine which cues took precedence in establishing neurite directionality. At low microfeatures aspect ratios, neurites align to the pattern direction but are then caused to turn and repel from or turn and align to bioactive borders. Conversely, physical cues dominate neurite path-finding as pattern feature slope increases, i.e. aspect ratio of sloping photopolymerized features increases, causing neurites to readily cross bioactive borders. The photopolymerization method developed in this work to generate micro and nanopatterned materials serves as an additional surface engineering tool that enables investigation of cell-material interactions including directed *de novo* neurite growth. The results of this interdisciplinary effort contribute substantially to polymer neural regeneration technology and will lead to development of advanced biomaterials that improve neural prosthetic tissue integration and performance by spatially directing nerve growth.

## TABLE OF CONTENTS

LIST OF TABLES .....	xi
LIST OF FIGURES .....	xii
CHAPTER	
1. INTRODUCTION .....	1
Biomaterials .....	4
Bioactive Materials .....	7
Neural Prosthetics .....	15
Retinal Prosthesis .....	16
Cochlear Prosthesis .....	21
Cochlear Implant Performance Limitation .....	30
Strategies to Improve Cochlear Implant Performance .....	31
Methods to Direct Cell and Neurite Growth .....	36
Chemical Cues .....	37
Physical Cues .....	45
Photopolymerization of Biomaterials .....	51
Research Summary .....	55
Notes .....	59
2. OBJECTIVES .....	82
3. MATERIALS AND EXPERIMENTAL METHODS .....	88
Materials and Sample Preparation .....	88
Polymer Characterization .....	93
Cell Culture and Characterization .....	96
Statistics .....	102
Notes .....	103
4. MICROPATTERNED METHACRYLATE POLYMERS DIRECT SPIRAL GANGLION NEURITE AND SCHWANN CELL GROWTH .....	105
Introduction .....	106
Experimental .....	108
Photopolymerization of Physical Guidance Cues .....	108
Spiral Ganglia Dissection and Culture .....	109
Spiral Ganglion Schwann Cell and Fibroblast Cultures .....	111
Determination of SGN Neurite Alignment to Patterns .....	111
Statistics .....	112
Results .....	112
MA Polymers Support SGN Survival and Neurite Growth .....	112

Photopatterning of Physical Guidance Cues.....	114
Micropatterned Polymers Direct SGN Neurite Growth.....	115
SGSC Alignment in the Absence of Neurites.....	117
SGSCs Remain Aligned to SGN Neurites .....	119
Turning of Neurites from SG Explants <i>in vitro</i> .....	120
Neurites Grow within Microchannel Grooves.....	122
Discussion.....	123
Conclusions.....	127
Notes .....	128
5. PHOTOPOLYMERIZED MICROFEATURES CONTROL THE EXTENT OF SPIRAL GANGLION NEURITE AND SCHWANN CELL ALIGNMENT .....	134
Introduction.....	135
Experimental.....	138
Photopolymerization of Micropatterned Substrates.....	138
Topographic Characterization.....	139
Cell Culture and Immunostaining.....	140
Characterization of Neurite and Glial Cell Alignment .....	141
Statistics .....	142
Results and Discussion .....	142
Photopolymerization of Surface Patterned Substrates.....	142
Alignment of Neuronal and Glial Cell Types.....	150
Controlling the Extent of Neurite and Glial Alignment.....	155
Neurite Alignment on Nano-scale Features.....	161
Correlation of Neurite Alignment to Microfeature Slope.....	164
Conclusions.....	166
Notes .....	167
6. NEURAL PATHFINDING ON UNI- AND MULTIDIRECTIONAL PHOTOPOLYMERIZED MICROPATTERNS.....	172
Introduction.....	173
Experimental.....	177
Uni- and Multidirectional Micropattern Fabrication .....	177
Uni- and Multidirectional Micropattern Characterization .....	178
Cell Culture and Immunostaining.....	179
Characterization of Neurite Alignment.....	180
Statistics .....	181
Results and Discussion .....	181
Photopolymerization of Uni/Multidirectional Patterns.....	181
Reaction Controlled Feature Modulation.....	184
Neurite Length and Branching.....	188
Neurite Behavior on Uni/Multidirectional Substrates .....	190
Conclusions.....	199
Notes .....	200

7. MATERIAL STIFFNESS EFFECTS ON NEURITE ALIGNMENT TO PHOTOPOLYMERIZED MICROPATTERNS.....	205
Introduction.....	206
Experimental.....	208
Fabrication of Patterned Films with Varied Matrix Rigidity.....	208
Topographic Characterization.....	209
SGN Culture, Survival, and Neurite Length.....	210
Material Surface Chemistry and Laminin Adsorption.....	211
Neurite Alignment on Patterns with Varied Matrix Rigidity.....	212
Statistics.....	212
Results and Discussion.....	213
Matching Feature Amplitude for Different Chemistries.....	213
Material Surface Chemistry and Protein Adsorption.....	219
SGN Survival and Neurite Length on MA Platforms.....	224
Neurite Alignment on Patterns with Varied Matrix Rigidity.....	228
Conclusions.....	233
Notes.....	234
8. BIOCHEMICAL BORDER CHALLENGES TO NEURITE ALIGNMENT ON PHOTOPOLYMERIZED PHYSICAL MICROPATTERNS.....	240
Introduction.....	241
Experimental.....	244
Physical Patterns for Biochemical Border Studies.....	244
Physical Micropattern Characterization.....	245
SGN and TGN Culture.....	246
Measurement of Neurite Behavior at Biochemical Borders.....	247
Statistics.....	247
Results and Discussion.....	248
Biochemical Borders on Micropatterned Polymers.....	248
SGN Neurite Behavior at Laminin-EphA4 Borders.....	252
SGN Neurite Behavior at Laminin-TnC Borders.....	259
TGN Neurite Behavior at Laminin-TnC Borders.....	266
Conclusions.....	271
Notes.....	273
9. CONCLUSIONS AND RECOMMENDATIONS.....	277
BIBLIOGRAPHY.....	293

## LIST OF TABLES

Table

5.1 Summary of micropattern dimensions, transitional slope, and neurite alignment.....164

## LIST OF FIGURES

### Figure

- 1.1. Neural tissue explant on a methacrylate polymer with micropatterned physical guidance cues. The explant body is found in the bottom right corner. NF200-labeled neurites (yellow) extend radially from the explant and are subsequently induced to align to the pattern which is oriented along the horizontal plane. Anti-S100 antibody (green) and Hoechst (blue) label glial cells and their nuclei. See Chapter 4. ....13
- 1.2. Representation of an epi-retinal sensory prosthesis. An optical signal is sent from a camera to a microelectrode array attached to the surface of the retina. Electrodes directly stimulate remaining functional retinal neurons to simulate visual perception. Image courtesy of the Department of Energy 2008 .....17
- 1.3. Representation of the elements of an epiretinal prosthesis within the intra-ocular space. Image used with permission from Elsevier. ....19
- 1.4. Schematic of the human ear. The outer ear and ear canal collect and channel sound waves to the middle ear. The instrumentation of the middle ear amplifies and transmits transmits and amplifies sound waves to the inner ear. The inner ear, which includes the sea-shell shaped cochlea, transduces the mechanical vibration of sound into a neurological signal to be processed by the brain. Image courtesy of NASA, 2010. ....24
- 1.5. Cross-sectional representation of the three spiral chambers that extend the length of the cochlea. Shown are the 1) scala media, 2) scala vestibule, 3) scala tympani, 4) Reissner's membrane, 5) basilar membrane, 6) tectorial membrane, 7) stria vascularis, 8) spiral ganglion neurons (SGNs), and 9) osseous spiral lamina. The organ of Corti is housed within the scala media and is positioned directly on top of the basilar membrane. ....25
- 1.6. Depiction of the organ of Corti within the cochlea where mechanical vibrations of sound are transduced into neurological signals. Pictured are the 1) inner hair cells, 2) outer hair cells, 3) tunnel of Corti, 4) basilar membrane, 5) reticular lamina, 6) tectorial membrane, 7) Dieters' cells, 8) space of Nuel, 9) Hensen's cells, and 10) inner spiral sulcus. ....26
- 1.7. Representation of the cochlear implant (CI). The CI provides auditory perception to individuals with severe hearing loss and is currently the most successful neural prosthetic. ....28
- 1.8. Cross-sectional representation of the cochlea. The CI electrode array is inserted up the scala tympani to maintain proximity to SGNs. ....29

- 1.9. Schematic of the spatially organized neural regeneration strategy. Directed SGN *de novo* neurite growth to specific electrodes will improve CI stimulatory specificity, lower current requirements, decrease problematic channel interactions, and enhance tonal perception. The cochlea is represented as if laid out from the base to the apex from left to right. SGNs and their neurites are represented by blue dots and blue lines, respectively. Neurite outgrowth is precisely directed by physical guidance cues. ....36
- 1.10. Schematic of the photolithography process. 1) A silicon wafer is first prepared by removing organic residues with an oxidizing agents such as reactive O<sub>2</sub> plasma and then chemically treated to promote photoresist adhesion. 2) Photoresist is spin-coated on the wafer surface and baked to drive off organic solvent. 3) The photoresist layer is selectively exposed to UV radiation through a glass-chrome photomask. 4) Positive photoresists become soluble upon UV exposure while negative photoresists crosslink and become insoluble when exposed to UV. Soluble regions are removed during a wash step leaving a pattern of photoresist whose thickness is based on parameters of the spin-coating step and the viscosity of the photoresist. 5) Reactive ion etching, or other dry etch methods, are employed to etch away the silicon substrate. Regions beneath photoresist remain protected. Photoresist is also etched away during this step but is designed to have a much slower etch rate than the silicon substrate. 6) Remaining photoresist is removed during a stripping or lift off step and the sample is further cleaned and prepared for future applications. ....38
- 1.11. Depiction of the microcontact printing process. 1) A liquid prepolymer is cast over a master template which is usually a micropatterned silicon wafer fabricated by photolithography. 2) The liquid prepolymer conformally coats master template features and is cured in place to form a negative image elastomeric stamp. 3) Patterned stamps are inked via simple adsorption from solution. 4) The stamp is brought into contact with the substrate to be inked. 5) A spatial replica of the stamps raised features is inked on the substrate surface following removal of the stamp. ....40
- 1.12. Representation of the microfluidic patterning process. 1) An micropatterned stamp formed by photo and soft lithography is placed in contact with the substrate to be patterned. 2) An inking solution with the dissolved active agent is drawn through the microchannels formed between the stamp and the substrate. 3) The substrate is inked in the spatial pattern of the flow channels. ....42

1.13.	Diagram of the photo-functionalization process. 1) An inking solution with the active agent is spread by capillary forces between a substrate and a photomask. The substrate is modified such that upon UV irradiation the active agent covalently binds to the surface. 2) The substrate is covalently modified with the active agent in the spatial pattern of the transparent regions of the photomask. ....	44
1.14.	Examples of physical cues used to influence cellular outcomes. Courtesy of NIH Public Access, 2010. ....	46
1.15.	Classes of common photoinitiators. Shown are generic structures for 1) benzoin derivatives, 2) benzyl ketals, 3) $\alpha$ -hydroxyalkylphenones, 4) acylphosphine oxides, and 5) $\alpha$ -aminoalkylphenones. ....	52
3.1.	Chemical structures of monomers, silane coupling agent, and photoinitiators used in this work. Shown are (a) hexyl methacrylate, (b) 1,6-hexanediol dimethacrylate, (c) hexyl acrylate, (d) 1,6-hexanediol diacrylate, (e) 2-hydroxyethyl methacrylate, (f) 3-tri(methoxysilyl)propyl methacrylate, and (g) 2,2-dimethoxy-2-phenylacetophenone. ....	90
3.2.	Schematic of glass substrate methacrylate procedure. Microscope slides were cleaned and oxidized with reactive O <sub>2</sub> plasma and then treated with a methacrylated silane coupling agent. Glass slide methacrylation enabled covalent bonding of the photopolymerized thin-film to the supporting substrate and prevented polymer delamination during cell-material interaction studies. ....	91
3.3.	Schematic of white light interferometer used to analyze photopatterned micro- and nano-scale physical guidance cues. A coherent beam is split with part of the beam going to the detector and another portion being reflected off the sample. Using the destructive interference of wave superposition the detector takes a stack of images and puts them together to generate a depth profile. Image courtesy of Veeco Metrology. ....	93
3.4.	Schematic of scanning electron microscope used to further characterize microfeature surface morphology and polymer cross sections. An electron beam is accelerated, focused, and then rastered across a substrate surface. Secondary electrons emitted by the sample are detected by the microscope detectors and used to generate a three-dimensional image. ....	94
3.5.	Representation of neurite alignment measurement. Neural processes are stained with fluorescent NF200 antibodies and captured by fluorescence microscopy. Image J is used to measure the total length of the neurite and the aligned length in the pattern direction which is always set horizontally. Neurite alignment is calculated as a ratio as described in equation 3.2. ....	99

3.6.	Representation of glial cell alignment measurement. Schwann cells are stained with fluorescent S100 antibodies and captured by fluorescence microscopy. Image J is used to measure the angle made between the major axis of an ellipse fitted around the cell relative to the pattern direction set horizontally. ....	101
4.1.	Schematic of a photopatterning process. A) Monomer solution is spread over a glass substrate. UV light passes through the mask photoinitiating the system. B) Monomer that is exposed to UV polymerizes quickly and forms ridges while monomer in shadowed regions polymerizes slowly to form grooves between ridges. ....	109
4.2.	SGN survival and neurite growth on HMA/HDDMA unpatterned polymer with and without laminin. A) Dissociated SG cultures grown on 20%HMA/80%HDDMA (left) and 80%HDDMA/20%HMA (right) and immunostained with anti-NF200 (red) and anti-S100 (green) antibodies. Scale bar = 250 $\mu$ m. The top row represents cultures on laminin-coated polymer and the bottom row represents cultures on polymers without laminin coating. B) SGN survival on indicated MA polymer composition with or without laminin coating. Legend indicates percent of HMA in HMA/HDDMA mixture. Neurons were cultured in three cloning cylinders for each condition with laminin coated glass used as control. Experiments were repeated in triplicate and survival was determined relative to control for each set of cultures. The average number of viable neurons counted across all controls was 521 $\pm$ 258 (mean $\pm$ SD) per well. There was no statistically significance difference in neurite survival among the different conditions ( $p = 0.306$ , one way ANOVA). C) SGN neurite length on indicated MA polymer composition with or without laminin coating. Legend indicates percent of HMA in HMA/HDDMA mixture and “n” represents the number of neurites measured in each condition. There was no statistically significance difference in neurite length among the different conditions ( $p = 0.608$ , one way ANOVA). ....	113
4.3.	Examples of a multicolor 3D (left) and graphical (right) schematic derived by interferometry characterizing photopolymerized microridges in methacrylate polymers with channel depth of $\sim 1.8 \mu$ m. ....	115
4.4.	Dissociated SGN neurite growth on unpatterned or patterned HMA/HDDMA. A,B) Dissociated SG cultures grown on unpatterned or patterned HMA/HDDMA and immunostained with anti-NF200 antibody. Neurite growth on unpatterned polymer is random whereas neurites on micropatterned polymers parallel the pattern. C) Drawing represents measurement of neurite length as well as the measurement of cell body to nerve terminus parallel to the pattern used to assess the extent of neurite alignment to pattern. D) Mean ( $\pm$ SD) ratios of neurite length to end-to-end distance for neurites on unpatterned or patterned HMA/HDDMA are significantly different by Student’s two-tailed t-test ( $p < 0.001$ ). ....	116

- 4.5. Spiral ganglion Schwann cells, but not fibroblasts, align with micropatterns in the absence of neurites. A) Cell alignment was determined by measuring the angle ( $\theta$ ) of an ellipse fitted to the major axis of the cell relative to the pattern. B) Histogram of orientation angle for SCs and fibroblasts on patterned or unpatterned polymers (n = 354, 300 and 76 for SC on patterned polymer, SC on unpatterned polymer and fibroblasts on patterned polymer respectively). Over 75% of SCs on patterned polymer were oriented within 30 degrees to the pattern. The difference in alignment of SCs on patterned polymers vs SC's on unpatterned polymers and fibroblasts on patterned polymers was significant ( $p < 0.001$ , ANOVA with post-hoc Dunn's Method). .....118
- 4.6. Spiral ganglion Schwann cells remain closely associated with neurites even when they are not in line with the pattern. Dissociated SG culture on patterned HMA/HDDMA and immunostained with anti-NF200 (red) and anti-S100 (green) antibodies. Arrows denote SCs aligned with neurites that fail to follow the pattern, which is parallel to the horizontal plane. ....119
- 4.7. Spiral ganglion explant on patterned HMA/HDDMA polymer. A) The explant body is outlined with a dashed red line on the bottom right corner. NF200-labeled neurites (yellow) extend initially from the explant in a radial fashion and are subsequently induced to turn parallel to the pattern which is oriented along the horizontal plane. Anti-S100 antibody (green) and Hoechst (blue) were used to label SCs and nuclei respectively. Notably, there are several S100-negative cell nuclei clustered close to the explant, as exemplified in the higher magnification images below. B) White arrowheads indicate S100-negative cell nuclei. C) Image taken further away from the explant ( $\sim 200 \mu\text{m}$ ) demonstrating that all nuclei are associated with S100-positive cells. The micropatterned MAs support SC outgrowth more favorably than S100-negative cells such as fibroblasts.....121
- 4.8. Micropatterned HDDMA induced turning of SGN neurites from SG explants. A) The initial neurite angle relative to the pattern was compared to the angle change from initial to terminal segment ( $\Delta\theta$ ) to determine the extent of turning by neurites in patterned and unpatterned polymer environments. B-D) Scatterplots of SGN neurite growth on glass (B), unpatterned HDDMA (C) and HDDMA with micropatterning (D) demonstrate that neurite growth on micropatterned HDDMA has a direct correlation between the initial angle to the pattern and the angle change between the initial and terminal neurite segment. ....124

- 4.9. SGN neurite grow within the microgrooves of patterned HMA/HDDMA. A) Section of confocal z-stack from SG culture immunostained with anti-S100 (green) and anti-NF200 (red) antibodies. The neurite grows within the groove, demonstrated as a cellular stripe between acellular ridges. Scale bar = 50  $\mu\text{m}$ . B) Ninety degree rotation of the stack to allow viewing down the x-axis. The grooves are evident as the regions with thicker S100 labeling compared with the ridges. The neurite (red) remains confined to the groove region. Scale bar = 3  $\mu\text{m}$ . .....126
- 5.1. Schematic of photopatterning process. A) Photopolymerizable monomer is selectively exposed to UV light through a photomask resulting in raised microfeatures across the surface. B) A 2D profile is shown of a micropatterned HMA-co-HDDMA substrate with a 50  $\mu\text{m}$  periodicity and a channel amplitude of 1  $\mu\text{m}$ . Inset: 3D representation of a 100  $\mu\text{m}^2$  area derived by white light interferometry. ....143
- 5.2. Representative SEM images of micropatterned HMA-co-HDDMA polymers. A-C) SEM images are shown of a pattern with a 50  $\mu\text{m}$  periodicity and a channel amplitude of 8  $\mu\text{m}$ . D-F) SEM images are shown of a pattern with a 10  $\mu\text{m}$  periodicity and a channel amplitude of 1  $\mu\text{m}$ . Top down view (A),(D); Cross-sectional view (B),(E); Angled cross-sectional view (C),(F). Note the gradual transitions between ridges and grooves. ....145
- 5.3. Tuning of micropattern features by variations in photomask band sizing, light intensity, photoinitiator concentration, and UV exposure time. A) Feature frequency is controlled by photomask design. Amplitude profiles represent photomasks with periodicities of 100, 50, 33, and 10  $\mu\text{m}$ . Maximum attainable amplitude is limited as periodicity (mask band size) decreases. B) Channel amplitude is controlled by varying initiating light intensity and UV exposure time. C) Channel amplitude is also tuned by varying photoinitiator concentration as well as UV exposure time. Periodicity for all trials in (B) and (C) is 50  $\mu\text{m}$ . Each point indicates mean $\pm$ SD.....147
- 5.4. Neurite growth from dissociated SGNs (A),(B), DRGNs (C),(D), and TGNs (E),(F) on unpatterned (left column) and patterned (right column) HMA-co-HDDMA polymers. Neurite growth extends randomly on unpatterned substrates but aligns to topographic features on patterned substrates. Cultures were stained with anti-NF200 antibodies. Micropatterned substrates have periodicities of 50  $\mu\text{m}$  and channel amplitudes of 3  $\mu\text{m}$ . The pattern is oriented horizontally. ....151

- 5.5. Unaligned length per neurite length ratios (mean±SE) for multiple neuronal types cultured on unpatterned and patterned substrates. A) Neurite alignment from dissociated SGNs, DRGNs, and TGNs is statistically different on patterned substrates compared to unpatterned controls (\*p < 0.005, Mann-Whitney Rank Sum test). SGN neurites align more strongly to the pattern than DRGN and TGN neurites (\*\*p < 0.001, one way ANOVA). B) Dendritic neurite (MAP 2-positive) alignment from dissociated CGNs is statistically different on patterned substrates compared to an unpatterned control (\*p < 0.005, Mann-Whitney Rank Sum test). However, axonal neurite (Tau-positive) alignment from dissociated CGNs is not statistically different (p = 0.135) from an unpatterned control. Micropatterns used for each neuronal culture have periodicities of 50 μm and channel amplitudes of 3 μm. The number in each bar represents the number of neurites measured. Error bars represent standard error of the mean (SE).....153
- 5.6. AC alignment on unpatterned and patterned substrates. A-B) ACs demonstrate typical morphology on unpatterned polymers. However, ACs elongate and align on patterned (B) polymers. C) The alignment angle (mean ± SE) of ACs on unpatterned substrates is statistically different from the alignment angle on patterned substrates (\*p < 0.005, Mann-Whitney Rank Sum test). The number in each bar represents the number of ACs measured. D) Representation of the cumulative percent of ACs at or below the angle relative to the pattern direction indicated in the x-axis. 55% of ACs align to the pattern (angle of 10° or less) and greater than 90% of ACs are within 30° or less of the pattern direction. Micropatterns used for AC alignment have periodicities of 50 μm and channel amplitude of 3 μm.....154

- 5.7. SGN neurite and SGSC alignment on patterns with constant periodicity (50  $\mu\text{m}$ ) but varying amplitude. A) SGN neurite length is not statistically different when cultured on patterns that have channel amplitudes of 1, 3, and 8  $\mu\text{m}$ . B) Representation of the cumulative percent of neurites at or below the length indicated in the x-axis. The spread of neurite lengths for the population of SGN neurites is also not affected by the given channel amplitudes. C) SGN neurite alignment (mean  $\pm$  SE) increases significantly with increasing channel amplitude (\* $p < 0.001$ , one way ANOVA). SGN neurite alignment was measured as a ratio of unaligned length per neurite length,  $[(T_L - A_L)/T_L]$ . Ratios that approach zero indicate the highest degree of alignment. D) Representation of the cumulative percent of neurites at or below the unaligned length per neurite length ratio indicated in the x-axis. 93% of the SGN neurite population cultured on 8  $\mu\text{m}$  deep channels falls within a low unaligned length per neurite length ratio of 0.10 compared to 39% and 50% on 1 and 3  $\mu\text{m}$  channels, respectively. E) SGSC alignment (mean  $\pm$  SE) increases significantly with increasing channel depth (\* $p < 0.005$ , one way ANOVA). SGSC orientation was measured as the angle made between the pattern and the major axis of an ellipse fitted around the cell. F) Representation of the cumulative percent of SGSCs at or below the angle relative to the pattern direction indicated in the x-axis. 70% of SGSCs align (i.e. angle of  $10^\circ$  or less) to patterns with channels that are 8  $\mu\text{m}$  in amplitude compared to 30% and 40% that align to 1  $\mu\text{m}$  and 3  $\mu\text{m}$  deep channels, respectively. ....157
- 5.8. DRGN neurite alignment on patterns with constant periodicity (50  $\mu\text{m}$ ) but varying amplitude. A) DRGN neurite alignment (mean  $\pm$  SE) increases significantly with increasing channel amplitude (\* $p < 0.005$ , one way ANOVA). DRGN neurite alignment was measured as a ratio of unaligned length per neurite length,  $[(T_L - A_L)/T_L]$ . Ratios that approach zero indicate the highest degree of alignment. B) Dissociated neurite growth from DRGNs on a pattern with 8  $\mu\text{m}$  deep channels and a 50  $\mu\text{m}$  periodicity. DRGN primary neurites and their branches strongly align to the pattern direction on 8  $\mu\text{m}$  deep channels compared to the spread of neurite growth near the cell body on 3  $\mu\text{m}$  deep channels (Fig 5.4C). ....159
- 5.9. SGN neurite alignment on patterns with constant amplitude (1  $\mu\text{m}$ ) but varying periodicity. A) SGN neurite alignment (mean  $\pm$  SE) increases significantly with decreasing periodicity (\* $p < 0.005$ , one way ANOVA). SGN neurite alignment was measured as a ratio of unaligned length per neurite length,  $[(T_L - A_L)/T_L]$ . Ratios that approach zero indicate the highest degree of alignment. B) Representation of the cumulative percent of neurites at or below the unaligned length per neurite length ratio indicated in the x-axis. 97% of the SGN neurite population cultured on patterns with a 10  $\mu\text{m}$  periodicity falls within a low unaligned length per neurite length ratio of 0.10 compared to 63% and 49% on patterns with 33 and 50  $\mu\text{m}$  periodicities, respectively .....160

- 5.10. SGN neurite alignment to nano-scale (<1  $\mu\text{m}$ ) features. A-B) Cross-sectional SEM images demonstrate the depth of the pattern features compared to the thickness of the polymer film. C) SGN neurites strongly align to patterns with 10  $\mu\text{m}$  periodicities and 250 nm and 500 nm amplitudes (\* $p < 0.005$ , one way ANOVA). D) SGN neurite growth extends randomly on unpatterned HMA-co-HDDMA polymers. E-F) SGN neurite growth strongly aligns to patterns with 10  $\mu\text{m}$  periodicity and 250 nm amplitudes (E) as well as to patterns with 50  $\mu\text{m}$  periodicities and 8  $\mu\text{m}$  amplitudes (F). Interestingly, there is no statistical difference ( $p = 0.369$ ) between SGN neurite alignment on the patterns described in E and F. Cultures were stained with anti-NF200 antibodies (D-F). The pattern is oriented horizontally. ....163
- 5.11. Linear regression correlation of SGN neurite alignment with average (A) and maximum slope (B) of groove-ridge transitions. SGN neurite alignment strongly correlates with maximum feature slope. ....165
- 6.1. Schematic of micropattern fabrication process for neural pathfinding studies. A) Photopolymerizable monomer is selectively exposed to UV light through a photomask resulting in micropatterns across the substrate surface. B,C) Representation of transparent (white) and reflective (black) band size of the photomasks. D,E) White light optical profiling 3D images of parallel and 90° angled micropatterned HMA-co-HDDMA substrates representing 100  $\mu\text{m}^2$  areas and channel amplitudes of 7  $\mu\text{m}$ . ....183
- 6.2. Representative SEM micrographs of micropatterned HMA-co-HDDMA thin films. A) A top-down view of a parallel or unidirectional micropattern with a 50  $\mu\text{m}$  feature spacing and 7  $\mu\text{m}$  amplitude . B) A tilted-cross sectional view of a parallel pattern demonstrating film thickness and gradual transitions between raised and depressed features. C,D) Top-down and tilted-cross sectional views of repeating 90° angle or multidirectional micropattern with a 7  $\mu\text{m}$  amplitude. ....185
- 6.3. Channel amplitude is modulated by shuttering the UV light source at specific time increments. Feature depth for parallel and 90° angle patterns is similar at each exposure. Each point indicates mean  $\pm$  SD. ....187

- 6.4. SGN survival, total and primary neurite length (NL), and branching on unpatterned controls and on parallel and 90° angle micropatterns of HMA-co-HDDMA polymer substrates. A) SGN survival on unpatterned and micropatterned substrates normalized to a tissue culture plastic (TCP) control. B) Total and primary SGN neurite lengths are significantly shorter than corresponding lengths on parallel patterns and unpatterned controls (\*p < 0.05, ANOVA). C,D) Significantly more branches per neurite length and per neurite on 90° angle patterns are observed compared to neurites on parallel patterns and unpatterned controls (\*p < 0.05, ANOVA). Error bars represent standard error of the mean (SE). .....188
- 6.5. SGN neurite alignment on variations in topographic cues. A-C) Immunofluorescent images of neurite growth from dissociated SGNs on unpatterned (A), parallel (B), and 90° angle (C) substrates. D-F) Distribution of SGN neurite segment angles relative to the horizontal plane on unpatterned (D), parallel (E), and 90° angle (F) substrates. Regenerative neurite growth orients randomly on unpatterned substrates as evidenced by a nearly equal distribution of neurite segment angles relative to the horizontal plane. Neurites strongly align to unidirectional topographic cues with 70% of the neurite segment angles at or below 20° from the pattern direction. Neurites on repeating 90° angle patterns do not closely track multidirectional cues as demonstrated by the low incidence of 45° angle neurite segments. They do align somewhat to the horizontal plane, although with a broader distribution of angles than on parallel patterns. Dissociated cultures were stained with anti-NF200 antibodies. Micropatterned substrates have a channel amplitude of 7 μm.....191
- 6.6. SGSC alignment on variations in topographic cues. A-C) Immunofluorescent images of SGSCs on unpatterned (A), parallel (B), and 90° angle (C) substrates. D-F) Distribution of SGSC angles relative to the horizontal plane on unpatterned (D), parallel (E), and 90° angle (F) substrates. SGSCs orient randomly on unpatterned substrates and align strongly to unidirectional topographic cues with 80% of the cell angles at or below 20° from the pattern direction. SGSCs on repeating 90° angle patterns do not closely track multidirectional cues as demonstrated by the low incidence of 45° cellular angles. Dissociated cultures were stained with anti-S100 antibodies. Micropatterned substrates have a channel amplitude of 7 μm.....194

- 6.7. SGN percent neurite length in depressed microfeatures and feature crossing per neurite length on uni- and multidirectional topographic cues. A) The majority of SGN neurite length on both parallel and 90° angle patterns is located in the grooves (\*p < 0.05, Mann-Whitney Rank Sum test). B,C) Immunofluorescent images of SGN neurite growth in groove microfeatures. D) SGN neurites crossed ridge-groove transitions significantly more on multidirectional patterns compared to unidirectional substrates (\*p < 0.05, Mann-Whitney Rank Sum test). E,F) Immunofluorescent images of SGN neurites crossing ridge-groove transitions on various micropatterns. Dissociated cultures were stained with anti-NF200 antibodies. Micropatterned substrates have a channel amplitude of 7 μm.....196
- 6.8. Number of turns per SGN neurite on substrates with varied topography. SGN neurites turned significantly more on unpatterned surfaces compared to patterned substrates and on patterns that change direction compared to unidirectional morphologies (\*p < 0.05, ANOVA).....198
- 7.1. Photopolymerization of micropatterns on methacrylate thin film surfaces. A) UV exposure of the pre-polymer formulation is selectively blocked with a photomask to alter local reaction kinetics on the surface that result in raised or depressed microfeatures. B) 2D profile of a 50/50 PEGDMA-co-EGDMA ridge-groove-ridge transition generated by white light interferometry. C) 3D representation of a micropatterned methacrylate surface formed during a masked photopolymerization. All patterns used for this study have a 50 μm periodicity and a channel amplitude of 2 μm.....213
- 7.2. Chemical structures of the monomers used for micropattern fabrication. Shown are (a) hexyl methacrylate (HMA), (b) 1,6-hexanediol dimethacrylate (HDDMA), (c) polyethylene glycol dimethacrylate (PEGDMA,  $M_n = 600$ ), and (d) ethylene glycol dimethacrylate (EGDMA).....216
- 7.3. Micropattern feature height is tuned by modulating UV exposure time. A) HMA-co-HDDMA amplitude profiles for various compositions and exposure times. Maximum channel amplitudes are similar but occur at earlier polymerization times with increased diene concentration. B) PEGDMA-co-EGDMA amplitude profiles for various compositions and exposure times. Maximum amplitudes occur early in the reaction due to rapid vitrification caused by polymerization of high molecular weight PEGDMA monomers. Final amplitudes level off at a similar height of approximately 1.5 μm for both series. Each composition was masked with a 50 μm periodicity glass-chrome photomask and was mixed with 1 wt% DMPA as the photoinitiator. Error bars represent standard deviation (SD).....217

- 7.4. Representative top down (TD) and cross-section (CS) scanning electron micrographs of micropatterned polymer surfaces of each methacrylate composition.....219
- 7.5. Static water contact angle on unpatterned methacrylate substrates. Surface polarity increases slightly with increasing HMA concentration for the HMA-co-HDDMA series with a 5° difference between the 20 and 40 wt % compositions. No statistical difference in contact angle is observed across the PEGDMA-co-EGDMA series. The PEGDMA-co-EGDMA series is substantially more polar and wettable with an average contact angle 30° lower than the other methacrylate series (\*p<0.05 one way ANOVA, Dunn's). Error bars represent SD. ....221
- 7.6. Laminin adsorption on methacrylate thin films. Laminin adsorption is no different on non-polar HMA-co-HDDMA substrates compared to polar PEGDMA-co-EGDMA substrates. The glass control adsorbed less laminin from solution than did methacrylate films. (\*p < 0.05 one way ANOVA, Tukey Test). Error bars represent standard error of the mean (SE).....222
- 7.7. SGN survival on unpatterned TCP and methacrylate thin films. A-C) Immunofluorescent images of *de novo* neurite growth from dissociated SGNs illustrate random neurite outgrowth on unpatterned TCP (A) and on unpatterned HMA-co-HDDMA (B), and PEGDMA-co-EGDMA (C) films. No significant difference in SGN survival is observed when cultured on HMA-co-HDDMA substrates compared to PEGDMA-co-EGDMA substrates. SGN survival on polymer substrates is also similar to survival on a tissue culture plastic (TCP) control (p = 0.125, one way ANOVA). Error bars represent SE. ....225
- 7.8. SGN neurite length on micropatterned methacrylate thin films. Neurite length is significantly shorter on PEGDMA-co-EGDMA substrates compared to HMA-co-HDDMA substrates. The average difference in length between the two series is 40 μm. No significant difference in neurite length is observed between the TCP control and polymer substrates (\*p < 0.05, one way ANOVA, Dunn's Method). Error bars represent SE .....226

- 7.9. Modulus and SGN neurite alignment on the HMA-co-HDDMA series. A) Material modulus significantly increases with increasing crosslinker concentration (\* $p < 0.05$  one way ANOVA, Tukey Test). Error bars represent SD. B) SGN neurite alignment on micropatterned HMA-co-HDDMA substrates. Neurite alignment significantly increases (i.e. alignment ratio  $T_L/A_L$  decreases) with increasing substrate stiffness (\* $p < 0.05$  one way ANOVA, Dunn's Method). C) Representative immunofluorescent image of SGN neurite growth on micropatterned HMA-co-HDDMA polymers. Neurite outgrowth orients to the pattern direction which is set horizontally during alignment measurement. Error bars represent SE. The micropattern for each composition has a 50  $\mu\text{m}$  periodicity and a 2  $\mu\text{m}$  amplitude. ....229
- 7.10. Modulus and SGN neurite alignment on PEGDMA-co-EGDMA series. A) Material modulus significantly decreases with increasing large PEGDMA monomer content (\* $p < 0.05$  one way ANOVA, Tukey Test). Error bars represent SD. B) SGN neurite alignment on micropatterned PEGDMA-co-EGDMA substrates. Neurite alignment significantly increases (i.e. alignment ratio  $T_L/A_L$  decreases) with increasing substrate stiffness (\* $p < 0.05$  one way ANOVA, Dunn's Method). C) Representative immunofluorescent image of SGN neurite growth on micropatterned PEGDMA-co-EGDMA polymers. Neurite outgrowth orients to the pattern direction which is set horizontally during alignment measurement. Error bars represent SE. The micropattern for each composition has a 50  $\mu\text{m}$  periodicity and a 2  $\mu\text{m}$  amplitude. ....232
- 8.1. Fluorescence images of biochemical borders on unpatterned and micropatterned HMA-co-HDDMA polymers. Shown are chemical borders of laminin (red) and ephrin A4 (green) on unpatterned (A) and micropatterned (B) substrates, and of laminin (red) and tenascin C (no stain) on unpatterned (C) and micropatterned (D) substrates. The represented micropatterns have dimensions of 50  $\mu\text{m}$  periodicity and 1.5  $\mu\text{m}$  amplitude (B) and 20  $\mu\text{m}$  periodicity and 1.5  $\mu\text{m}$  amplitude (D). Borders were established by placing coverslips adjacently over respective protein solutions on polymer substrates. The yellow line in (A) and (B) is an artefact from mixed fluorescence at the border. ....245

- 8.2. Immunofluorescence images of TGNs on photopolymerized methacrylate polymers. The images represent neurite behaviors quantified at biochemical borders on micropatterned substrates. A-C) Neurite cross, turn/parallel (A), repel (B), and stop (C) behaviors are shown. The biochemical border between laminin and tenascin C is represented as a yellow dashed line. Regions coated with laminin and tenascin C are demarcated with a yellow L and T, respectively. Dissociated TGNs are stained with fluorescent anti-NF200 antibody (red). Immunofluorescence of adsorbed biochemical is not shown to facilitate identification of neurite behavior. The pattern for each image is set horizontally and has a periodicity of 20  $\mu\text{m}$  and a channel amplitude of 1.5  $\mu\text{m}$ .....248
- 8.3. SGN neurite crossing behavior at the biochemical border between laminin (Lam) and EphA4 on micropatterned polymer substrates. A-C) Immunofluorescence images of dissociated SGNs cultured on unpatterned (A), 50  $\mu\text{m}$  periodicity (P50) (B), and 20  $\mu\text{m}$  periodicity (P20) (C) parallel micropattern substrates. SGNs are stained with fluorescent NF200 antibody. The biochemical border is marked with a dashed yellow line and the laminin and EphA4 sides are marked with a yellow L or E, respectively. D-F) Proportion of scored neurites that cross the biochemical border from laminin to EphA4 (D), from EphA4 to laminin (E), from laminin to laminin (F), and from ephrin A4 to ephrin A4. SGN neurites cross the biochemical border significantly more when cultured on patterns with narrow features (i.e. low periodicities) compared to unpatterned substrates and wide features. Neurites are much more likely to cross from an EphA4 substrate to a laminin coating than from laminin to ephrin A4 even on unpatterned surfaces. All patterned substrates have a microfeature amplitude of 1.5  $\mu\text{m}$ .....250
- 8.4. Non-crossing SGN neurite behavior at the biochemical border between laminin (Lam) and ephrin A4 (EphA4) on micropatterned polymers. A,B) Proportion of scored neurites that exhibit turn/parallel, repel, and stop behaviors when approaching the biochemical border starting from the laminin (A) and ephrin A4 (B) sides, respectively. All patterned substrates have a microfeature amplitude of 1.5  $\mu\text{m}$ . .....254

- 8.5. SGN neurite crossing behavior at the biochemical border between laminin (Lam) and tenascin C (TnC) on micropatterned polymer substrates. A-C) Immuno-fluorescence images of dissociated SGNs cultured on unpatterned (A), 50  $\mu\text{m}$  periodicity (P50) (B), and 20  $\mu\text{m}$  periodicity (P20) (C) parallel micropattern substrates. SGNs are stained with fluorescent NF200 antibody. The biochemical border is marked with a dashed yellow line and the laminin and tenascin C sides are marked with a yellow L or T, respectively. D-F) Proportion of scored neurites that cross the biochemical border from laminin to tenascin C (D), from ephrin A4 to laminin (E), from laminin to laminin (F), and from ephrin A4 to ephrin A4. SGN neurites cross the biochemical border significantly more when cultured on patterns with narrow features (i.e. low periodicities) compared to unpatterned substrates and wide features. Neurites are much more likely to cross from ephrin A4 coated substrate to a laminin coating than from laminin to ephrin A4 even on unpatterned surfaces. All patterned substrates have a microfeature amplitude of 1.5  $\mu\text{m}$ . .....258
- 8.6. Non-crossing SGN neurite behavior at the biochemical border between laminin (Lam) and tenascin C (TnC) on micropatterned polymers. A,B) Proportion of scored neurites that exhibit turn/parallel, repel, and stop behaviors when approaching the biochemical border starting from the laminin (A) and tenascin C (B) sides, respectively. All patterned substrates have a microfeature amplitude of 1.5  $\mu\text{m}$ . .....261
- 8.7. TGN neurite crossing behavior at the biochemical border between laminin (Lam) and tenascin C (TnC) on micropatterned polymer substrates. A-C) Immuno-fluorescence images of dissociated SGNs cultured on unpatterned (A), 50  $\mu\text{m}$  periodicity (P50) (B), and 20  $\mu\text{m}$  periodicity (P20) (C) parallel micropattern substrates. TGNs are stained with fluorescent NF200 antibody. The biochemical border is marked with a dashed yellow line and the laminin and tenascin C sides are marked with a yellow L or T, respectively. D-F) Proportion of scored neurites that cross the biochemical border from laminin to tenascin C (D) and from tenascin C to laminin (E). TGN neurites cross the biochemical border significantly more when cultured on patterns with narrow features (i.e. low periodicities) compared to unpatterned substrates and wide features. All patterned substrates have a microfeature amplitude of 1.5  $\mu\text{m}$ . .....263
- 8.8. Non-crossing TGN neurite behavior at the biochemical border between laminin (Lam) and tenascin C (TnC) on micropatterned polymers. A,B) Proportion of scored neurites that exhibit turn/parallel, repel, and stop behaviors when approaching the biochemical border starting from the laminin (A) and tenascin C (B) sides, respectively. All patterned substrates have a microfeature amplitude of 1.5  $\mu\text{m}$ . .....266

## CHAPTER 1

### INTRODUCTION

Advances in biomaterials, micro- and nanofabrication, tissue engineering, cell and molecular biology, and biotechnology in the last six decades have enabled the development and rapid growth of a now burgeoning world medical device market with an estimated value of \$286 billion in 2013.<sup>1</sup> For most of the first implantable medical device applications, a primary concern centered on using materials that could replace or augment lost or impaired physiological function while remaining bioinert, i.e. mitigating deleterious host response such as chronic inflammation.<sup>2</sup> For example, poly(methyl methacrylate) intraocular lenses were developed to treat patients with cataracts after Sir Harold Ridley observed that shards of the material were well tolerated in the eyes of aviators who were hit by debris from shattered plastic canopies of Spitfire fighter planes during World War II.<sup>3,4</sup> As biomaterial scientists and tissue engineers have come to better understand key factors that dictate medical device performance, particularly regarding the crucial interface between the biological system and synthetic materials, the focus has shifted increasingly to bioactive surfaces and constructs that elicit favorable biological responses such as wound healing, osseointegration, directed cell growth, and controlled cellular differentiation.<sup>5-8</sup> Because favorable physical and chemical interactions at the biointerface of the medical device often require location specific signaling, photo-dependent processes such as photolithography and photopolymerization are increasingly exploited in biomaterial and tissue engineering studies and device fabrication due to their inherent spatial control.<sup>9-12</sup> Accordingly, within the overlap between biomaterials science and photopolymerization technology lies substantial potential to develop advanced bioactive materials and constructs that meet challenging and complex treatment requirements which will save lives as well as improve the quality of life for millions.

This work develops and explores the use of photopolymerized materials and patterning methods to spatially direct as well as to test the pathfinding ability of *de novo* neurite outgrowth from neurons that are relevant to neural prostheses. Precisely directing neurites to specific electrodes would substantially increase the number of prosthesis signal channels which would greatly enhance device performance and improve the experience for the user.<sup>13-15</sup> Photopolymerization is an ideal production platform for this work, and for biomaterial and tissue engineering applications generally, due to several unique advantages that differentiate it from traditional thermal and redox initiated polymerizations. These advantages include: 1) ultra-rapid hardening with some polymerizations reaching high conversion within fractions of a second; 2) no volatile organic solvents are required as viscosity of the system can be adjusted by varying monomer to oligomer ratios of the pre-polymer formulation; 3) excellent spatial control of the reaction as polymerization only occurs in areas irradiated with light; 4) temporal control afforded by controlled shuttering of the irradiation source; 5) many photo-initiated polymerizations are carried out under mild (i.e. biocompatible) ambient conditions; and 6) low energy consumption during polymerization and stable pre-polymer formulations.<sup>16,17</sup>

Furthermore, photopolymerization represents one of the most rapidly expanding platforms for materials production. Photo-curing methodology has gained prominence in recent years for curing of polymer films in emerging applications in electronic and optical materials, adhesives, conformal coatings, and high-resolution rapid prototyping of 3D objects.<sup>16,18-21</sup> In addition to a wide variety of industrial applications, photopolymerization is emerging as a production platform of choice in biomaterials science with a well-established subfield in dental materials and restorations.<sup>22</sup> A diverse array of photopolymers, including many methacrylates (MAs), exhibit excellent biocompatibility and serve as relatively bio-inert surfaces for *in vitro* and *in vivo* studies and clinical applications including tissue engineering and drug delivery.<sup>23-25</sup> Final

material properties are readily tunable by modulating pre-polymer formulation and by altering photopolymerization parameters. For example, mechanical and surface properties and topographical textures can be tuned to mimic biological tissue.<sup>26-29</sup> Physical characteristics of photopolymers are controlled by altering the material chemistry and the crosslinking density. Changing these factors alters material swelling capabilities, surface chemistry, wettability, mechanical strength, network architecture, and degradation time in accordance with the desired material properties.<sup>26,30,31</sup> Crosslinking density and mechanical strength have shown particular importance in cell and neurite growth.<sup>32-34</sup>

The unique advantages of photopolymerization outlined above are crucial to the studies presented in this work. The spatial and temporal control of photopolymerization was used to generate micro-and nano-patterned photopolymer surfaces that enabled contact guidance studies of *de novo* neurite pathfinding from spiral ganglion neurons (SGNs). SGNs are the primary target for cochlear implant (CI) stimulation and are located in the inner ear. Patterned substrates were fabricated by masking light exposure to alter local reaction kinetics across a substrate surface resulting in globally ordered topographic feature development. Chapter 4 represents a proof of concept study for the micropatterned photopolymerization strategy and illustrates general biocompatibility with inner ear neural tissue as well as significant contact guidance of neurite outgrowth from dissociated neurons as well as directed growth from intact neural tissue, i.e. inner ear explants cultured on micropatterned polymers.

Chapter 5 explores the extent of SGN neurite alignment to uni-directional cues by altering microfeature spacing, amplitude, and feature slope transitions. SGN neurite alignment is compared to alignment from other neurons with supporting or glial cell alignment also being explored. Chapter 6 probes the neural pathfinding of SGN neurites on complex, multi-directional micropatterns with comparisons to uni-directional and unpatterned controls. In Chapter 7, micropatterned amplitudes and spacings are manipulated to be constant across a variety of compositional changes with varying cross-

linking density in two co-methacrylate series to explore neurite pathfinding response to materials with varied stiffness. Finally, Chapter 8 explores the synergistic and antagonistic effects of physisorbed bioactive molecules on top of micropatterned photopolymerized polymers and their effects on neurite alignment.

As an introduction to the work, this chapter reviews the necessary background information and technical literature pertinent to the presented topic of directing and characterizing neural pathfinding from prosthesis-relevant neurons in response to photopolymerized materials and bioactive patterning. The chapter is divided into six main sections. The first two sections provide conceptual background and history in biomaterials science and neural prosthetics with particular focus on cochlear implant history, function, and performance limitations. The next two sections overview strategies to enhance the signal resolution and performance of cochlear prostheses with emphasis on methods used to spatially control cellular outgrowth by both chemical and physical bioactive patterning. A fifth section expounds on photopolymerization methodology and illustrates research avenues for its use in biomaterials science and applications. Finally, a research overview and summary is provided in the last section regarding photopolymerized patterning and inner ear neural pathfinding in relation to micropatterns developed in this study.

## **Biomaterials**

Biomaterials science is a relatively new discipline with the majority of its history and significant advances occurring primarily within the last six decades.<sup>35</sup> While the primary focus of the field is materials science, including the development, control, and characterization of bulk and surface properties favorable to biological applications, the complexity of the challenges associated with the field require a high degree of interdisciplinary work involving mechanical engineering, computer aided design and

finite element analysis, cellular and molecular biology, surface science, composites technology, physiology, optics, and tissue engineering. Examples of the range of medical devices that fall within biomaterials science include cardiovascular stents and pumps, orthopedic applications including artificial joints and bone cement, dental materials, intraocular lens implants, artificial skin and wound dressings, sutures, neural prosthetics, and drug delivery systems.<sup>2,36</sup> With such a broad array of devices and technologies that comprise a major part of the field, how might the term *biomaterial* be defined? One prominent and general definition provided during expansion of the field in the 1980's is:

“A biomaterial is a nonviable material used in a medical device, intended to interact with biological systems.”<sup>37</sup>

All of the medical device examples given above fit within this concise and general biomaterial definition. However, it should be noted that ongoing advances in biomaterials science have made even this general definition too constricting. Many current biomaterial applications do not serve a direct medical function but are part of *in vitro* studies and quantitative analyses such as blood protein assays, diagnostic gene arrays, constructs for *in vitro* cell culture, and other biosensor and diagnostic studies.<sup>38,39</sup> Furthermore, substantial advances in tissue engineering and stem cell research in the last decade have made the “nonviable material” descriptor a moot point in this general but aging biomaterials definition. For example, many tissue engineering studies are increasingly moving towards technology that incorporates living cells and tissue into tailor-made constructs for eventual clinical applications.<sup>40,41</sup> In light of these and other technological advances in the field, an even less restrictive definition would be:

A biomaterial is *any* material that is intended to interact with a biological system.

Thus defined, the field almost becomes a tautology of its title word – *biomaterials*. Regardless of precise semantics, it is clear that biomaterials has a profound impact on human health, the global economy, and on a broad spectrum of technical fields that are part of interdisciplinary efforts and applications to address complex biological and medical challenges.

While materials foreign to the human body have been used for thousands of years to address lost or impaired anatomical function (e.g. dental implants),<sup>42,43</sup> the history of biomaterials science is generally understood to refer to modern synthetic materials that were developed with the advent and use of plastics in the mid-twentieth century. Many of the materials and technologies that began to see use in medical applications were originally developed for military efforts in World War II.<sup>3</sup> Examples of early materials tested for medical use include nylon, urethanes, methacrylates, silicones, and metals such as titanium and stainless steel. Initial attempts with these materials during surgical operations were, essentially, high risk trials and were used as a last resort by physicians and surgeons when other options were exhausted.

For example, Willem Kolff developed a creative, albeit rudimentary, artificial kidney consisting of wood slats, a 100 liter tub, and over 100 ft of cellulose sausage casing as a membrane for blood dialysis for patients who faced no other alternative than an unpleasant death that could take a month or more following kidney failure.<sup>44</sup> Some of the first attempts at creating an artificial heart or a ventricular assist device used poly(vinyl chloride) and polyurethane.<sup>45,46</sup> In addition to artificial organs, vascular grafts were developed using silk and nylon in the 1950's and the first stents to prevent blood vessel occlusion following coronary angioplasty were made of stainless steel and developed in the 1980's.<sup>47,48</sup>

For most biomaterial applications in the mid-twentieth century, the primary goal for a material or device was simply to perform a function, such as enable dialysis of blood like a kidney or serve as a mechanical pump like a heart, while at the same time

remaining sufficiently inert, or bioinert, to prevent device failure. Because of the novelty of the materials and of the field, there was little if any information or prior consideration regarding the biocompatibility of the material. Effects of the body's foreign material response on a device were often observed or documented *after* catastrophic failure.<sup>2</sup> Initial understanding of the key factors involved in the body's response to foreign materials was extremely limited in the early history of modern biomaterials. Though, it should be noted that many of the early attempts with synthetic materials and devices under a medical and scientific environment that was not as heavily regulated as it is today were crucial to build the foundational concepts of biocompatibility and acceptable host response that so strongly inform current biomaterials research.

### Bioactive Materials

The work of physicians and surgeons to save patient's lives or their quality of life with new synthetic materials is the recognizable origin of modern biomaterials science. As the field developed and as factors dictating the response of biological systems to synthetic materials began to be elucidated, polymer chemists, materials scientists, and engineers and biologists of diverse technical backgrounds became increasingly involved in biomedical material development. This period of biomaterials history is often referred to as the 2<sup>nd</sup> or bioactive generation of biomaterials.<sup>35</sup> Whereas the primary goal for initial biomedical materials was to achieve appropriate functional properties while at the same time preventing harmful interactions with the host, the focus of this new generation of biomaterials was to develop devices and constructs with engineered properties and cues that elicited specific, favorable biological interactions. A material is considered bioactive if it promotes desirable biological or cellular outcomes.

One of the most successful avenues of research for the bioactive materials approach is the use of glasses, ceramics, and composites for orthopedic applications. Specific compositions of these materials were tailor-made to bond to bone by developing

an adherent interface with the biological system.<sup>49,50</sup> The process is referred to as osseointegration and can result in an interface that in many cases has physical properties that are equal to or even greater than either the material itself or the bone tissue it is bound to. Osseointegration was first illustrated using compositions of CaO, Na<sub>2</sub>O, SiO<sub>2</sub>, and P<sub>2</sub>O<sub>5</sub> in carefully tuned proportions.<sup>51</sup> For these bioactive glass compositions three important relationships were discovered to create a surface that actively bonds with bone in an aqueous media: 1) there should be less than 60 mol% of SiO<sub>2</sub>; 2) high CaO and Na<sub>2</sub>O content increases activity; and 3) the ratio of CaO to P<sub>2</sub>O<sub>5</sub> should be high. Interestingly, glasses that have very similar compositions but do not fall within a tight set of proportions do not actively bond to bone. Adding as little as 3 wt% AL<sub>2</sub>O<sub>3</sub> to a common bioactive silica glass composition completely prevents bonding to bone.<sup>49</sup> The sensitive interplay between dynamic biological systems and materials for medical applications illustrates the complexity of biomaterials challenges but also highlights the broad impact the field has had on interdisciplinary work. This specific application of osseointegration required engineers and materials scientists with experience in glass and ceramic chemistry as well as biologists and pathologists to evaluate biological response.

In addition to bone-binding glasses and ceramics, a wide variety of materials have been designed and modified for favorable bioactive outcomes in biomaterials science applications. The evolution of cardiovascular stents used to prevent blood vessel restenosis following balloon angioplasty illustrates the importance of the bioactive rather than simply bioinert materials approach. As previously described, the first stents used to treat atherosclerosis, a condition in which the internal lumen of arteries are obstructed by buildup of plaques, were made of stainless steel and silver solder points.<sup>47,48</sup> The stent performed a crucial structural support function after widening of an arterial lumen with balloon angioplasty and the first stenting materials were considered bioinert in that they did not incite significant negative host response. However, with bare metal stents, up to 50% of patients had treated vasculature undergo restenosis within six months of

percutaneous cardiovascular intervention procedures.<sup>52</sup> Restenosis is complex, but it is believed that stent-tissue interactions interfere with vasculature healing and re-endothelialization which leads to proliferation of smooth muscle cells, greater production of extra cellular matrix (ECM), and narrowing of the inner lumen leading to eventual occlusion.<sup>53</sup>

To address the serious and potentially fatal complication of restenosis following balloon angioplasty and a stenting procedure, biomaterials scientist modified the 'bioinert' bare wire stents with bioactive coatings consisting of degradable polymers impregnated with drugs that inhibit smooth muscle cell proliferation and ECM synthesis. Using drug-eluting stents (DES) has shown to be the most effective method to prevent restenosis events.<sup>54-56</sup> For many DES, a polymer coating, which commonly consists of a mixture of polyethylene-vinyl acetate and poly-n-butyl methacrylate, is imbued with drugs and coated on the stent's metallic mesh. Effective and common drugs used in DES that inhibit proliferation of smooth muscle cells are rapamycin and paclitaxel.<sup>57-59</sup> The drugs are released to the surrounding cellular environment either by diffusion through the polymer matrix coating, or by degradation of the film. Both diffusion and degradation for either delivery method are readily controllable by tuning cross-link density, proportion of hydrolytically degradable groups in a network, and other material properties of the polymeric coating.

For both the bioactive glass-ceramic and DES applications, multi-disciplinary and innovative solutions using existing technologies were developed to transition from a bioinert to a bioactive paradigm. Similar bioactivation technologies have been developed for many other avenues of biomaterials research which will be briefly mentioned here. Surface-bound protein passivation is one such bioactive material modification approach. It is well understood that materials implanted in the body are nearly instantaneously coated with proteins in the blood and interstitial fluids.<sup>60</sup> Therefore, the biological system in contact with a synthetic material often interacts with and reacts to the adsorbed protein

layer rather than the surface of the material itself. These interactions dictate important cellular events such as cell survival, growth, and differentiation.<sup>61</sup> Accordingly, one method of bioactivation intended to reduce negative aspects of foreign body response to implantable materials that has had mixed success is to passivate the surface of a device with proteins such as albumin.<sup>61,62</sup> Albumin is the most prevalent protein in the blood and has been shown to significantly decrease the recruitment of phagocytes to a material surface compared to untreated controls which further mitigates foreign body response.<sup>63</sup> However, the coatings lack stability as pre-adsorbed albumin has been shown to be readily replaced by fibrinogen protein in the blood, and covalently bound albumin has also been shown to be degraded by leukocytes resulting in an increase of pro-inflammatory components at the implant site.

Hydrogels have also undergone a rapid evolution from a simple but thoroughly explored bioinert platform of poly(ethylene glycol) matrices to carefully tuned three-dimensional extracellular microenvironments incorporated with enzymes, hydrolytic groups, attachment peptides, chemo-attractive signaling, and proteolytic ligands that enable cell-determined network remodeling.<sup>64-67</sup> Current synthetic hydrogel matrices continue as idealized biomaterial constructs which lack the chemical and spatial complexity of native ECM, but rapid advances in bioactive materials engineering and cellular microbiology may eventually strongly mimic the necessary microenvironment required for advanced tissue regeneration and even organ-specific morphogenesis.<sup>68</sup> Indeed, the rapid expansion of tissue engineering and its tremendous potential in medical applications is largely attributable to significant advances in the field of hydrogel research. Tissue engineering is an expansive topic and belongs to a third class of biomaterials referred to as bioregenerative rather than the bioinert or bioactive classes of materials already discussed. The reader is directed to several excellent review articles for an introduction.<sup>65,68-72</sup>

Related to hydrogel research, another significant development during the second generation of biomaterials science is the development of resorbable or biodegradable materials. Resorbable materials fulfill a functional, structural, or regenerative need for a given medical application and are removed either by hydrolytic degradation or by active cellular processes over time. Accordingly, the once distinct biology-material boundary is gradually eliminated which can prevent deleterious foreign body responses such as chronic inflammation or fibrosis. Material degradation is also advantageous in that no further surgeries are required to remove the device. Degradation rates are readily tuned by altering network chemistry, equilibrium swelling ratios, and cross-linking density. It should be noted that toxicity of the degradation products must be well established and that pre-mature failure of a device due to degradation must also be taken into account for these types of applications. Examples of widely used hydrolytic polymers include polyglycolic acid (PGA) and polylactic acid (PLA) with a range of properties available by varying the copolymer ratio of the two polymers. Biodegradable sutures are one example of a successful resorbable material and have been in clinical use since the 1960s.

Controlled drug delivery is another important application of bioactive materials with demonstrated success and substantial potential for future medical treatments. It is also very strongly related to both hydrogel and resorbable materials research.<sup>73</sup> Controlled drug delivery systems (CDDSs) initially gained prominence due to their capacity to address two important pharmacological problems, namely: 1) location specific delivery of a drug, and 2) sustained therapeutic dose treatment.<sup>74</sup> Drugs administered orally or injected intravenously circulate through the body's vasculature requiring a higher drug dose than necessary to produce a therapeutic effect for some conditions and can lead to complications. Similarly, sustained therapeutic dose treatment is ideal for many conditions rather than the cyclical dose levels that rise above a maximum desired concentration where side-effects are more likely to occur and then subsequently falling below a sufficient blood-plasma concentration of the drug to

produce any therapeutic effect. First generation CCDSs were designed with silicone drug reservoirs encased in membranes that controlled drug release kinetics.<sup>75</sup> The membranes consisted of either silicone rubber or poly(ethylene-co-vinyl acetate) with the ‘zero-order’ rate of release being tuned by controlling the thickness of the membrane. Since the first devices developed in the 1960’s, CDDSs have been customized for a variety of applications including intrauterine devices (IUDs), vascular stent coatings, dermal patches, and ocular inserts. CDDSs have also miniaturized from macro-devices down to nano-scale particle or micelle carriers with an increasingly broad range of bioactive deliverables including traditional pharmacological agents, proteins and enzymatic treatments, gene therapy vectors, and nucleic acid-based drugs.<sup>2</sup> Furthermore, CDDSs are now targeted to specific anatomical sites such as damaged vasculature, alveoli in the lungs, tumors, and subcutaneous injection sites.<sup>76</sup>

As a final category of bioactive materials discussed in this section, and of particular relevance to the studies presented in this thesis, cellular outcomes including adhesion, spreading, alignment, and gene expression have been influenced and controlled using physical and mechanical material cues.<sup>28,77-82</sup> Specifically, a variety of fabrication methods have been employed to create ordered micro- and nano-scale topographical cues to influence cell fate and material mechanical properties have been tuned to modulate microenvironmental properties to alter cell response. During development and regeneration, cells encounter a complex milieu of signals, including bioactive molecules and physical topographic cues of their surrounding environment to which they must respond to perform vital interactions and functions. Accordingly, biomaterials scientists have designed materials that exhibit physical or mechanical cues that effect meaningful biological outcomes for a given cellular niche. Previously, efforts to direct cellular outcomes typically relied on the use of chemically bioactive molecules. A major limitation of such strategies is that the bioactive molecules are inherently unstable complicating the production and practical use of biomaterials coated with micropatterned

bioactive molecules.<sup>2,35,60</sup> To overcome these and other hurdles, materials scientists have begun to exploit the ability of imposed topography or mechanical property differences to influence cellular responses (Fig 1.1).

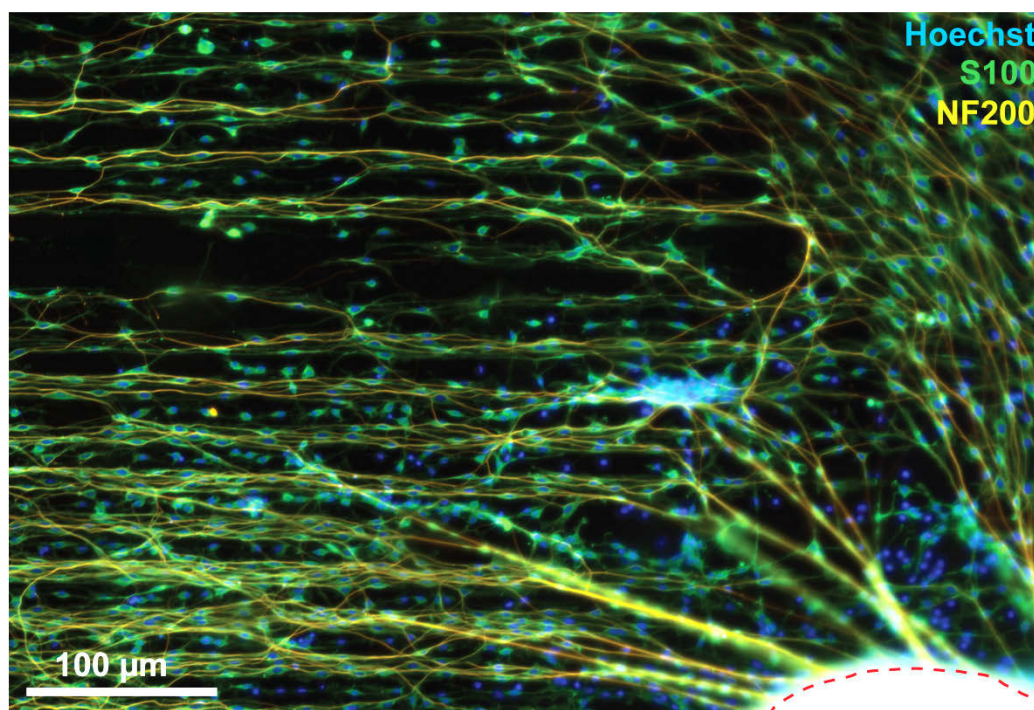


**Figure 1.1.** Neural tissue explant on a methacrylate polymer with micropatterned physical guidance cues. The explant body is found in the bottom right corner. NF200-labeled neurites (yellow) extend radially from the explant and are subsequently induced to align to the pattern which is oriented along the horizontal plane. Anti-S100 antibody (green) and Hoechst (blue) label glial cells and their nuclei. See Chapter 4.

For example, increased neurotrophin expression was observed by Schwann cells that were cultured on microgrooved chitosan and poly(D,L-lactide) compared to those grown on smooth substrates.<sup>83</sup> Epithelial cells elongated and aligned on silicon oxide substrates that had ridge and groove depths as small as 70nm.<sup>84</sup> Also, human gingival fibroblast cells showed modified gene expression and increased elongation and size on

microgrooved, titanium-coated substrates.<sup>77</sup> Depending on the microfabrication method employed, pattern dimensions such as ridge width, groove depth, and pattern shape can be tuned to induce or strengthen desired cellular outcomes.<sup>85-87</sup>

Beyond alteration of topographic features, mechanical properties of biomaterial substrates have recently been demonstrated to play a crucial role in final cellular outcomes.<sup>88,89</sup> Similar to the movement induced by chemically repulsive or attractive cues referred to as chemotaxis, cellular movements based on interactions with mechanical cues were coined as 'durotaxis'.<sup>90</sup> Numerous tissue engineering studies show that cell fate is significantly influenced by the mechanical stiffness of its micro-environment. Migration and adhesion of endothelial cells, myoblasts, and osteoblasts were regulated by tuning substrate stiffness.<sup>91-93</sup> Significantly, neurites from chick dorsal root ganglia grew longer down a stiffness gradient than up and were also longer than the control samples with no mechanical gradient.<sup>33</sup> Dorsal root ganglion neurite extension rate has also been shown to inversely correlate to mechanical stiffness in agarose gels.<sup>94</sup> Further, PC 12 neurons displayed robust growth on harder substrates and were observed to have a softness threshold at which relatively little neurite growth was observed.<sup>95</sup>

Additionally, cross-link density and mechanical strength directly influence differentiation pathways of stem cells,<sup>91</sup> as well as growth, adhesion, and morphology of several cell-types, including neurons.<sup>91,96,97</sup> Polymer platforms offer chemical diversity and allow for modulation of material stiffness based on concentration of multi-functional monomers ( $f \geq 3$ ), flexibility of monomers used (e.g. flexible long chain poly(ethylene glycol) versus rigid p-divinyl benzene), and on bulk material properties such as glass transition temperature ( $T_g$ ) and crystallinity, which arise from intermolecular interactions.

With significant and ongoing therapeutic developments in medical areas as diverse as joint replacements, artificial ligaments, cardiovascular stents, dialysis membranes, contact lenses, bioresorbable constructs, drug delivery systems, and neural prosthetics, it is clear that biomaterials science has a tremendous impact on human health,

a broad array of technical fields, and on the economy. The complexity of the challenges the science aims to address require considerable multidisciplinary effort in many sub-disciplines of engineering, materials science, technology, and medicine. This section has provided a brief history of biomaterials dealing primarily with the advent and development of synthetic polymers in the mid-twentieth century. Biomaterials encompass such a wide array of devices and applications that the term can now be broadly defined as *any* material intended to interact with a biological system. The three main periods or biomaterial classifications were briefly described, namely: 1) bioinert materials which are intended to perform a specific function while also preventing or mitigating deleterious host responses; 2) bioactive materials which are targeted to elicit specific, favorable interactions with the biological system; and 3) bioregenerative materials which are aimed to regenerate completely functional replacement tissue. Particular emphasis was given on bioactive materials as they are most relevant to the work of directing and determining the pathfinding ability of *de novo* neurite growth from prosthesis-relevant neurons in response to bioactive material cues presented in this thesis.

### **Neural Prosthetics**

Neural prostheses are devices that are engineered to meaningfully interact with the nervous system to replace or substantially augment motor and sensory functions of neural pathways that have been lost or damaged due to physical trauma, disease, or genetics.<sup>98-100</sup> For sensory prostheses, such as the successful cochlear implant and the developing retinal implant, lost sensory function is compensated through use of an artificial sensor, i.e. microphone for auditory loss and cameras for visual impairment.<sup>14,15</sup> The artificial sensor then transmits the received signal to a computer chip that uses carefully developed algorithms to send a meaningful frequency signal to the prosthesis electrodes. Electrodes fire an electrical pulse to directly stimulate remaining healthy

nerve cells which causes a neural action potential that is transmitted to the brain and perceived as rudimentary sight or sound. For motor prostheses, the process is reversed.<sup>98,101</sup> Sensory elements of the prosthesis are used to detect action potentials from proximal segments of the nervous system. The signal is processed through computing equipment and then meaningfully transmitted to distal portions of the peripheral nervous systems to effect muscle movement and control. Ongoing work in biomaterial science, neuroscience, and biomedical and tissue engineering aims to improve the performance of successful devices as well as to develop new devices that will treat an array of neurological trauma and disorders.

For currently available or developing neural prostheses, a primary challenge that limits their performance is poor integration with the target tissue.<sup>15,102</sup> In particular, neural prostheses are limited to providing few effective signal channels due to spatial signal resolution limitations which prevent precise stimulation of specific neural populations. If the interface between the patient and the device were improved to enable greater specificity in spatial stimulation, then significantly more effective signal channels would be available. Increasing the number of effective channels would simulate increasingly natural sensory and motor information which would significantly improve the quality of life for patients with neural prostheses. This section will focus primarily on the retinal and cochlear implants as sensory prostheses. However, because the nervous system is generally dependent upon signaling that is location specific, analogous signal resolution challenges are expected for all devices that interact with the nervous system. Precise spatial signal control will, therefore, be critical to achieve significant performance improvements in next-generation neural-prosthetics.

### Retinal Prosthesis

Restoring a sense of sight to individuals with significant vision loss would have a remarkable impact on their quality of life and is of major interest to scientists in diverse

technical fields associated with neural prosthetics. Photoreceptor loss is a major contributor to severe vision impairment and is often attributable to retinitis pigmentosa (RP) and age-related macular degeneration (AMD) which are hereditary retinal degenerative diseases.<sup>103,104</sup> Interestingly, similar to the cochlear implant which will be discussed in the next section, functional neural tissue that remains following the loss of photoreceptor cells can be triggered to fire action potentials via direct electrical stimulation from developing retinal neural prostheses (Fig 1.2).

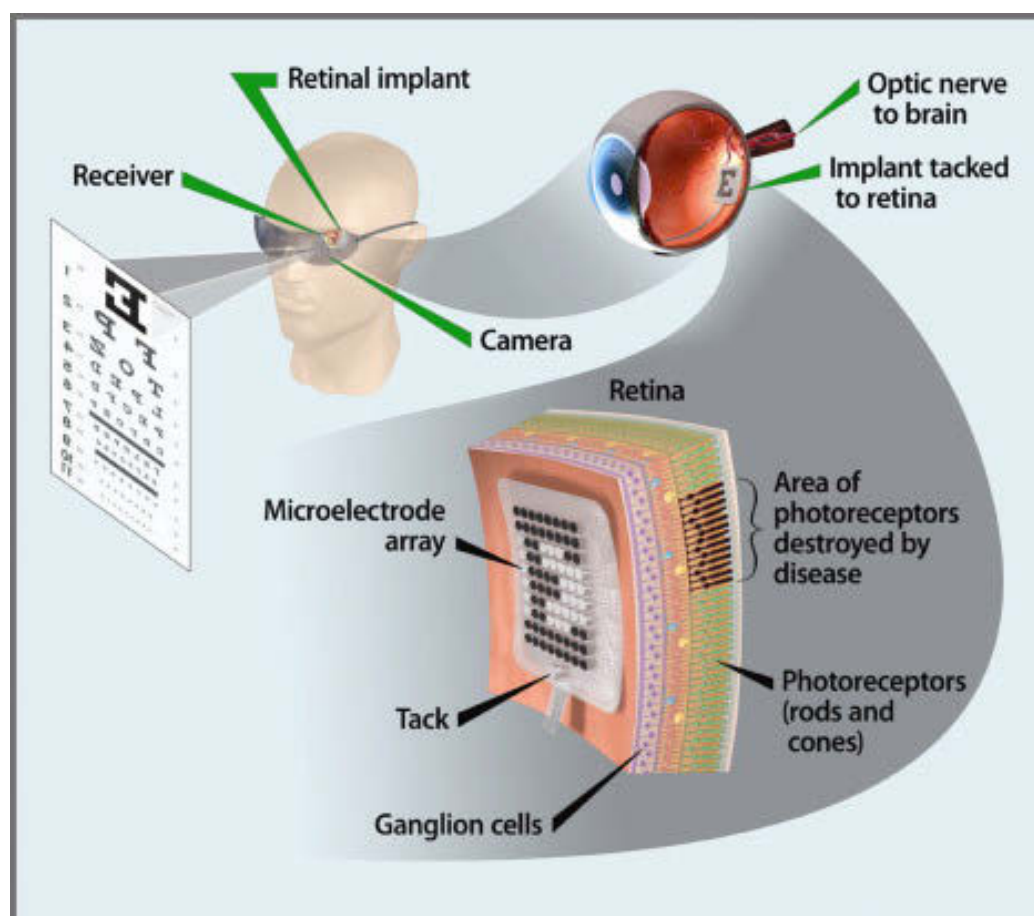


**Figure 1.2.** Representation of an epi-retinal sensory prosthesis. An optical signal is sent from a camera to a microelectrode array attached to the surface of the retina. Electrodes directly stimulate remaining functional retinal neurons to simulate visual perception. Image courtesy of the Department of Energy, 2008.

Progress in retinal implants has mainly occurred in the past two decades with multiple types of devices that stimulate different regions of the visual pathway being considered.<sup>105-107</sup> Various research groups outside the U.S. have even began initial human trials with implantable retinal prostheses. While important advances have been achieved within a relatively short time, considerable challenges remain regarding electrode design and stimulus parameters, retinal attachment methods, polymer coatings and packaging for biocompatibility, and mechanical property constraints.<sup>108</sup> At present, retinal prostheses are not commercially available, as are cochlear implants, but a broadly successful device is expected to be developed within the near future.

In a healthy eye, visible light is perceived via phototransduction through photoreceptor cells, or rods and cones, in the retina. The retina contains the primary sensory equipment of the eye and consists of multiple layers of cells including retinal ganglion cells, i.e. eye nerve cells, which ultimately carry a visual stimulus to the brain. A variety of anatomical structures in the visual pathway provide other critical functions.<sup>109</sup> The cornea allows light to enter the eye and also enables focusing of an image onto the retina in conjunction with the eye's lens. The sclera is the mechanically durable, white outer layer of the eye that protects internal structures. Most of the ocular volume between the cornea and the retina is filled with a clear gel called vitreous humor.

RP and AMD cause death of photoreceptor cells as well as loss of other neuronal cells in the retina. However, up to 30% of retinal ganglion neurons and 80% of bipolar cells are viable that could be polarized via direct electrical stimulation.<sup>110</sup> Retinal prostheses, therefore, serve as a type of bionic eye which enable visual simulation in the retina by bypassing the damaged photoreceptor cell layer which normally provides the phototransduction function necessary to transmute light stimulus into a neural action potential. The epiretinal and subretinal prostheses are two different approaches to accomplish retinal stimulation via electrical stimulus. Epiretinal prostheses, as shown in

Figure 1.3, are contained within the intraocular space and are in direct contact with the retina's surface which places them adjacent to remaining retinal ganglion cells.<sup>111,112</sup> For

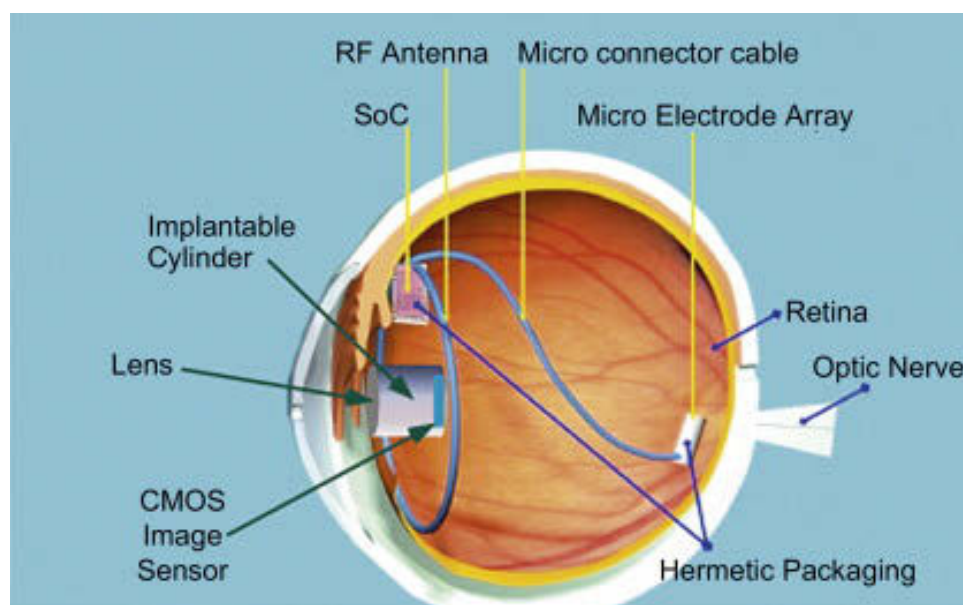


**Figure 1.3.** Representation of the elements of an epiretinal prosthesis within the intraocular space.<sup>2</sup>

the subretinal approach, a gap between the photoreceptor layer and the retinal pigment epithelium is created and microelectrode arrays are placed in the new space to stimulate neuronal cells in the inner layers of the retina.<sup>113,114</sup> Multiple types of subretinal approaches are being developed including optical-to-electrical signal amplification, photosensitive diode arrays, and neurotransmitter stimulation methods.<sup>115-117</sup> Direct stimulation of the optic nerve is another approach that has been explored by various research groups to restore a sense of sight.<sup>118-120</sup> However, because the optic nerve is a dense bundle of millions of neural processes extending from the retina it may be prohibitively difficult to realize any meaningful stimulation pattern.

It is interesting to note the role of central nervous system image processing as a signal travels to the brain in the visual pathway. One recent study demonstrated that restoring limited vision capability did not occur immediately following implantation of a retinal prosthesis but gradually improved during months of experience with the device.<sup>107</sup> Similarly, the same central nervous system phenomenon occurs for cochlear implant patients which is a principal reason why early implantation in infants leads to significantly improved outcomes compared to later implantations. Crucial elements of the central nervous system and visual input pathway are still developing in relation to external signal input at a very young age and are more readily able to adapt and respond to the artificial signals from neural prostheses.

In addition to electrical stimulation considerations, a prominent practical and safety concern is the mechanical design and properties of the portion of the implant that contacts the delicate retinal tissue. As previously mentioned, the retina is the sensory machinery of the eye and is a delicate multilayer tissue only 200  $\mu\text{m}$  thick with a Young's modulus down in the low kPa range.<sup>121,122</sup> Due to the sensitivity of the tissue there is potential to easily damage the delicate layer by mechanical or chemical means. Accordingly, synthetic polymers have been used as a crucial biomaterial in micro-electrode array design as their properties are readily tuned to meet challenging microcellular environmental needs. To prevent retinal tearing or damage, the polymer should exhibit an extremely low Young's modulus to mimic that of the native retinal environment. By carefully tuning material properties, relatively safe implantation has been achieved with a variety of polymers used in other biomaterial applications.<sup>123</sup> Polyimide, parylene, and poly(dimethyl siloxane) (PDMS) have each been used to varying degree of success in the design and implantation of epiretinal prostheses.<sup>124</sup> While the material properties and biocompatibility of parylene and polyimide are suitable for the application, their mechanical strength can lead to cutting of the surface retinal tissue if produced as very thin sheets. Due to their excellent flexibility and viscoelastic

behavior that can mimic retinal tissue at appropriate compositions, PDMS and PEG are often used to completely coat parts of the intraocular implantation including other polymeric pieces.<sup>125</sup>

Though the epiretinal prosthesis has advanced significantly since its initial development, challenges remain which limit its effectiveness.<sup>105</sup> Of particular relevance to this thesis work, is the unintended electrical excitation of neural tissue at the electrode-tissue interface caused by spatial separation of the electrode array from the target retinal ganglion neurons. The resulting non-specific neuronal excitation precludes high resolution stimulation which ultimately limits the visual acuity that can be obtained with the prosthesis. The distance between the electrode array and the target neurons has been measured to be approximately 250  $\mu\text{m}$  in thickness.<sup>126</sup> Various research groups are developing the subretinal prosthesis approach, in part, to avoid or mitigate the effects of this limitation, as previously mentioned. An alternative strategy to improve spatial signal resolution would use a biomaterial and neural tissue engineering approach to precisely direct *de novo* neurite growth from the target neurons toward prosthesis electrodes. This type of gapless-interface stands to substantially increase the number of effective stimulatory channels which would greatly enhance device performance. The bioactive material gapless-interface approach will be covered in greater detail in the following sections.

### Cochlear Prosthesis

The cochlear implant (CI) is the most successful neural prosthetic since the advent of modern biomaterials in the mid-twentieth century. Whereas the retinal implant's main development and advancements have occurred within the last two decades without a main prosthetic being commercially available, the development of the CI began in the 1960's, and was first commercially available in the early 70s. The CI is a sensory prosthesis that serves as a bionic ear to reconnect deaf patients with the auditory environment and

restore basic sound perception including voice comprehension. As of December 2012, 324,000 patients have had their hearing partially restored with this successful neural prosthetic according to the Food and Drug Administration.

The history of the CI's development is a model of productive collaboration between academia, entrepreneurs, and industry to bring a promising concept from an idea to a fully realized product that improves quality of life and adds economic value. Initial development of what is now CI technology occurred in the 1960s and 70s, but the initial concept to electrically stimulate the nervous system was proposed in the early 1800s.<sup>127</sup> Electrical stimulation specifically of the auditory nerve was also investigated in the 1930s and 40s.<sup>128-131</sup> The first rudimentary CI was a single electrode system that was implanted in two deaf individuals by Dr. William House.<sup>132</sup> This system exhibited poor biocompatibility and led to medical complications but both patients indicated a sense of sound when electrical stimulation was applied. House later went on to collaborate with Jack Urban, an engineer, to develop what would ultimately become the first commercialized sensory prosthesis. The device was commercialized by 3M and approved by the US Food and Drug Administration in 1984.

Other than the efforts by Dr. House and his first collaborators, efforts at universities in the US and Australia, along with industrial collaborations, further informed cochlear prosthesis technology leading to the successful CIs available today. For example, at Stanford University two research groups explored the use of multi-site or multi-channel stimulation to improve the current one electrode approach. Dr. Simmons developed a prosthesis with a group of six stainless-steel electrodes to be implanted in the modiolus of a deaf patient to stimulate the auditory nerve.<sup>133</sup> Another Stanford group developed a very large scale integration (VLSI) processor as part of a multi-channel CI device.<sup>134</sup> The university began a collaboration with Biostem as an industrial partner in the early 1980s but the venture did not lead to commercially available prostheses. At the University of California, San Francisco, Michelson and coworkers developed a form-

fitting device with both single and four-channel designs.<sup>135</sup> The initial commercialization of the system through Storz was not successful but the design was later obtained by Advanced Bionics Corp. which is one of only two major CI manufacturers in the US. At the University of Melbourne in Australia, Clark and coworkers developed a 22-electrode CI system. The device was manufactured through a collaboration with Nucleus Limited which later led to the business spin-off named Cochlear. Cochlear is the current CI market leader commanding approximately 75% of the market. These and other efforts by multiple university research groups and businesses have enabled the growth and success of the world-wide CI market. Importantly, the success of the CI has laid a crucial foundation for the future growth and advancement of the field of neural prosthetics and of devices that interact with the nervous system generally.

Prior to exploring how a CI works, as well as discussing its current limitations, it is first important to understand how sound is perceived in a healthy auditory pathway. Sound is a frequency of pressure waves moving through a medium such as air. The pressure waves are collected by the outer ear – the *pinna* – and transferred through the ear canal to the *tympanic membrane* or eardrum (Fig 1.4).<sup>136</sup> The eardrum vibrates in sync with the frequency of the pressure waves. Three small connected bones, a hammer (*malleus*), an anvil (*incus*), and a stirrup (*stapes*), in the middle ear oscillate with the frequency of the sound to transfer the auditory signal to the inner ear. The bones and their flexible connections are important as they produce a mechanical advantage that allows the tympanic membrane to vibrate in air but also enables vibration of the comparatively dense fluid in the cochlea. This mechanical advantage is further reinforced by the large ratio of the area of the tympanic membrane in relation to the area of the foot plate of the stapes. Accordingly, the force of an auditory signal is amplified when transferred to fluid in the cochlea via the cochlear oval window. After a sound is collected by the outer ear and transferred and amplified through the instrumentation of the middle ear, it is passed to the inner ear where the frequency of the pressure waves will be transduced to



**Figure 1.4.** Schematic of the human ear. The outer ear and ear canal collect and channel sound waves to the middle ear. The instrumentation of the middle ear amplifies and transmits transmits and amplifies sound waves to the inner ear. The inner ear, which includes the sea-shell shaped cochlea, transduces the mechanical vibration of sound into a neurological signal to be processed by the brain. Image courtesy of NASA, 2010.

electrochemical neural signals that the brain will interpret as a sound. Semicircular canals which are crucial to a sense of balance and the *cochlea*, which transduces mechanical vibrations into neural signals, make up the inner ear.

The cochlea is a sea-shell shaped osseous structure in the inner ear. Three spiraling chambers extend the length of the cochlea from the base to the apex, the *scala vestibule*, *scala media*, and *scala tympani* (Fig 1.5). The fluid and the electrolytic concentration of the fluid in each spiral chamber are crucial to the electrochemical process that leads to firing of neural action potentials.<sup>136</sup> The central chamber – *scala media* – houses the *organ of Corti* which contains the *hair cells* that enable machanotransduction of auditory signals.<sup>137</sup> Spiral ganglion neurons (SGNs) connect or

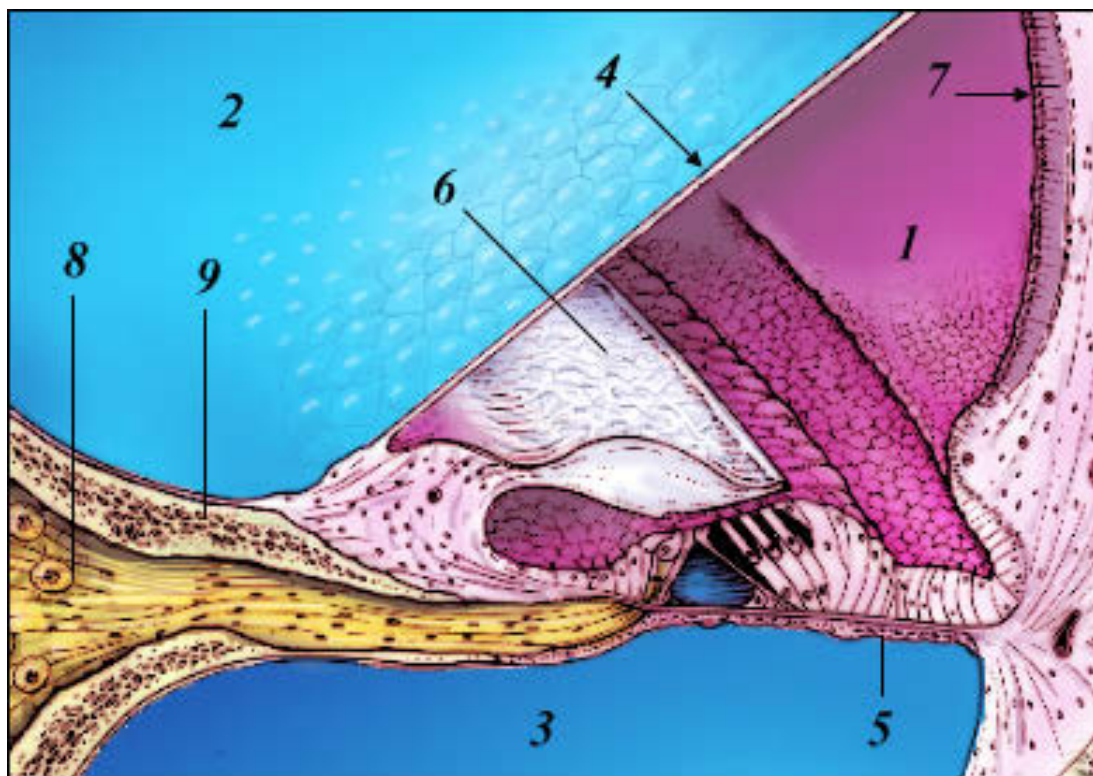


**Figure 1.5.** Cross-sectional representation of the three spiral chambers that extend the length of the cochlea. Shown are the 1) scala media, 2) scala vestibule, 3) scala tympani, 4) Reissner's membrane, 5) basilar membrane, 6) tectorial membrane, 7) stria vascularis, 8) spiral ganglion neurons (SGNs), and 9) osseous spiral lamina. The organ of Corti is housed in the scala media and is positioned directly on top of the basilar membrane.<sup>138</sup>

synapse with the hair cells and are the primary neurons responsible for transmitting auditory information to the brain. The organ of Corti rests on the *basilar membrane*. Mechanical properties of the basilar membrane are ideally suited to enable perception of specific tones as different portions of the membrane oscillate or resonate maximally at different sound frequencies. This type of spatial organization is referred to as *tonotopic* or tone dependent organization and is crucial to the ear's perception of a broad range of frequencies.<sup>136,139</sup> An average human ear can detect sounds in the 50 Hz – 20 kHz range. Higher frequencies, or higher pitches, are detected at the base of the cochlea and the lowest frequencies are detected at the apex. As the basilar membrane oscillates it forces

the small extensions from the hair cells called *cilia* to contact and bend against the *tectorial membrane* (Fig 1.6). Bending of the cilia opens transmembrane ion channels allowing for depolarization of the cell leading to the firing of an action potential in the SGNs that synapse with the stimulated hair cells. This signal is then finally sent to the brain. The process of perceiving sound can be summarized as three main steps: 1) collection of sound (i.e. pressure waves) by the outer ear; 2) transmission and amplification of sound vibration by the equipment of the middle ear; and 3) transduction of the mechanical stimulus of sound into a neural signal via the instrumentation in the cochlea which is part of the inner ear.

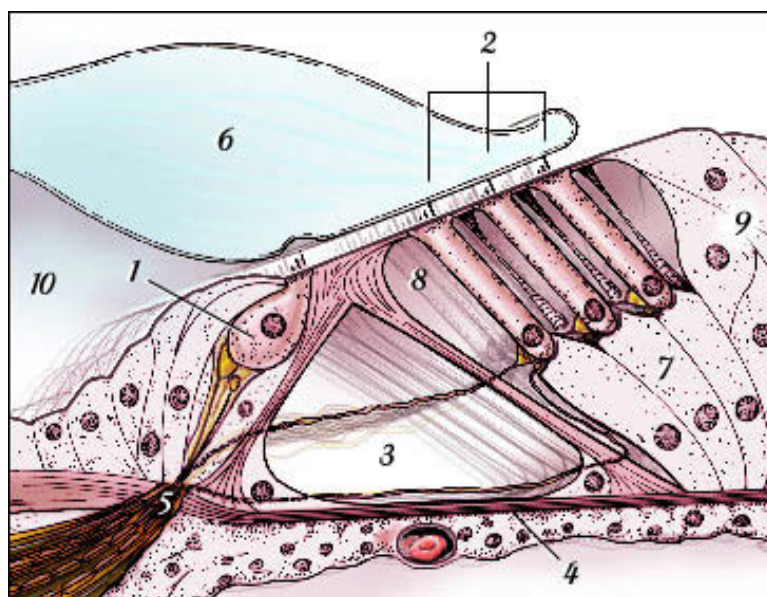


**Figure 1.6.** Depiction of the organ of Corti within the cochlea where mechanical vibrations of sound are transduced into neurological signals. Pictured are the 1) inner hair cells, 2) outer hair cells, 3) tunnel of Corti, 4) basilar membrane, 5) Habenula perforata, 6) tectorial membrane, 7) Dieters' cells, 8) space of Nuel, 9) Hensen's cells, and 10) inner spiral sulcus.<sup>138</sup>

Having established the basics of the auditory pathway, we are now able to consider the function of CI prostheses as well as to discuss a current significant limitation to their performance. The CI has been commercially available for over 40 years and is by far the most successful neural prosthetic to date. CIs enable basic sound and speech comprehension for patients with severe or even complete sensorineural hearing loss.<sup>140</sup> Sensorineural hearing loss is usually caused by abnormality or death of the hair cells in the cochlea. Loss of the hair cells or of their function precludes the critical mechanotransduction step in the auditory pathway severely limiting or completely preventing auditory information from being sent to the brain via SGNs. If sensorineural hearing loss is not yet “severe to profound” it is treated with hearing aids which amplify the auditory signal sent to the inner ear to maximize the stimulation of remaining functional hair cells and SGN synapses.<sup>14</sup>

Other types of hearing loss can be treated with alternative therapeutic solutions. For example, conductive hearing loss, which is a functional deficiency of the outer or middle ear to transmit sound to the inner ear, can be treated using a bone anchored hearing aid (BAHA).<sup>141,142</sup> The BAHA functions by conducting sound frequencies through the bones in the skull to the healthy inner ear, thus effectively bypassing functional deficiencies in the outer or middle ear. For mild to moderate sensorineural hearing loss and for conductive hearing loss, function of the inner ear is satisfactory but a portion of the auditory pathway must either be amplified or bypassed to enable contact with the auditory environment. However, for severe to profound sensorineural hearing loss, there are no devices other than the CI which will improve auditory perception since the critical mechanotransduction step from an environmental vibration to a neural signal is missing due to nearly complete loss of hair cells or hair cell function.

Accordingly, to enable basic sound perception for patients with severe to profound sensorineural hearing loss, the CI implant is designed to directly and meaningfully stimulate the inner ear nerve cells that remain following the loss of hair cell

function. As seen in Figure 1.7, the CI implant consists of several main parts including an microphone, external and internal signal processors, an internal cable, and the electrode array which is inserted into the cochlea via the round window. The microphone detects sound waves from the environment and transduces them into an electrical signal. The external and internal signal processors manipulate the electronic signal from the microphone to produce frequency and amplitude information to be sent to the stimulating electrodes. The processed signal travels through the internal cable to the electrode array, inserted into the cochlea during the implantation surgery.

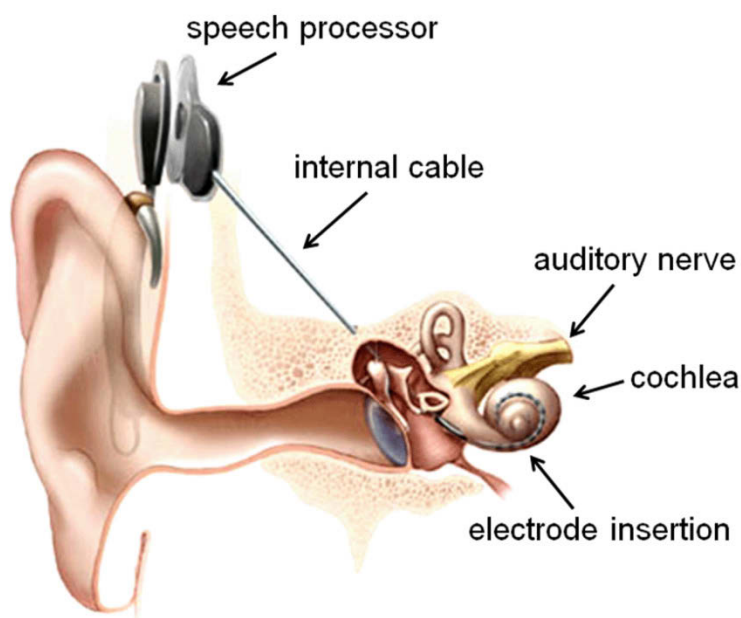


**Figure 1.7.** Representation of the cochlear implant (CI). The CI provides auditory perception to individuals with severe hearing loss and is currently the most successful neural prosthetic. Adapted from web reference.<sup>143</sup>

Current electrode arrays are inserted up the scala tympani for proximity to SGNs.

SGNs are the primary neurons responsible for auditory perception and are, accordingly,

the target neurons for stimulation by a CI prosthesis (Fig 1.8). To prevent central nervous system infection, which could lead to potentially fatal or debilitating meningitis, the electrode array should not disrupt the osseous wall of the *modiolus* where the SGNs are housed.<sup>144,145</sup> The processed signal is then transmitted by an electric pulse from the electrode array to directly stimulate remaining healthy SGNs. Finally, SGNs transmit the auditory information to the brain. The CI is a remarkable success story in biomedical engineering and serves as a bionic ear for patients with severe to profound sensorineural hearing loss that could not otherwise contact their auditory environment.

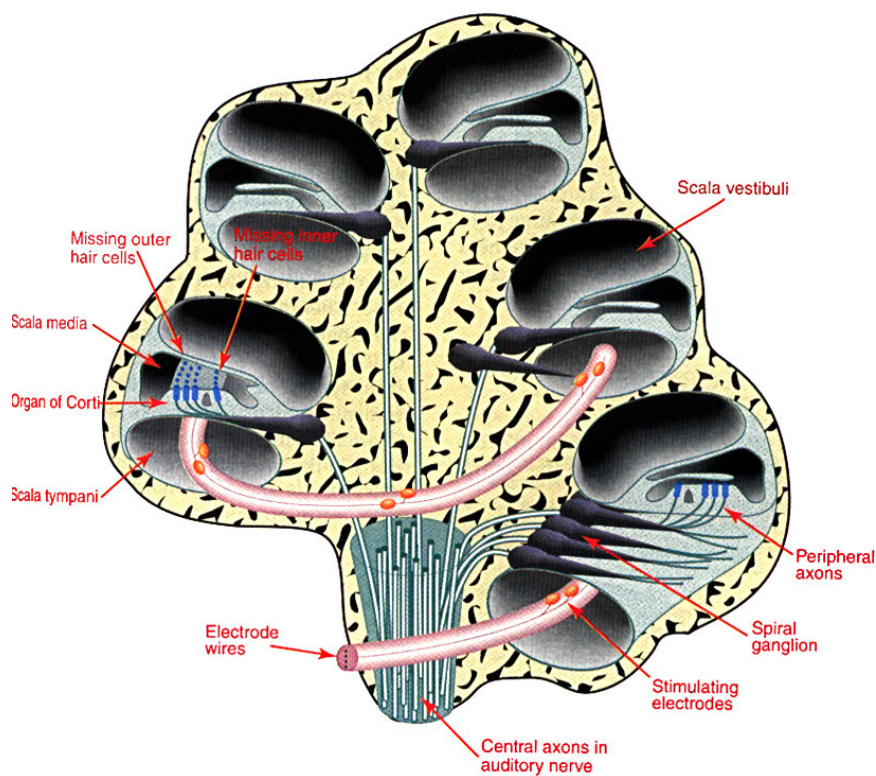


**Figure 1.8.** Cross-sectional representation of the cochlea. The CI electrode array is inserted up the scala tympani to maintain proximity to SGNs.<sup>146</sup>

### Cochlear Implant Performance Limitation

CIs restore or improve auditory perception for nearly all users. However, clinical performance of CIs has plateaued in recent years because the total number of usable or effective frequency channels is limited due to poor integration with the patient's precise, spatially dependent tonal perception in the inner ear.<sup>14,15</sup> Most recipients perform poorly with complex auditory tasks such as hearing in noise or music appreciation.<sup>147</sup> As previously mentioned, the first CIs had a single electrode which enabled basic sound perception but poor voice comprehension since a large number of SGNs was stimulated simultaneously. Current prostheses are multi-channel systems which allow for stimulation of specific regions of SGNs within the cochlea which provides more effective stimulation channels. Increasing the number of effective channels has substantially improved sound perception and voice comprehension compared to the first rudimentary CI prostheses.<sup>148,149</sup>

While the design and function of the prosthesis are crucial, a variety of patient factors also significantly impact the therapeutic effects on an individual's auditory performance with the device including: duration of deafness, age of onset of deafness, age at implantation, duration of CI use, electrode placement during surgery, and the number of remaining healthy SGNs in the inner ear.<sup>148</sup> However, following the development of multi-channel prostheses, the primary CI performance improvements in the last three decades that are not due to patient differences have come from progress in auditory signal processing algorithms and technology.<sup>14</sup> It should be noted, however, that these advances are substantial, with CI patients scoring 20% on speech recognition tests in the 1980s up to 80% by the turn of the 21<sup>st</sup> century.<sup>150</sup> However, performance plateaus in the last decade indicate that auditory performance is increasingly limited by the interface with the current CI design.

Degeneration of SGN neurites following deafness likely contributes to the limited ability of CI recipients to understand complex auditory signals.<sup>151-153</sup> Current electrode

arrays lie in the scala tympani and stimulate the SGN cell bodies or central fibers within the modiolus. One of the principal challenges to prosthesis integration and function that prevents further performance advances is non-specific excitation of SGNs due to electrical current spread in the cochlea. The distance between the stimulating electrodes and the neurons that they activate results in spread of the current, stimulation of SGNs over a broad frequency range, and significant interaction of adjacent channels.<sup>151,154,155</sup> Though current CIs have up to 24 distinct electrodes, a maximum of only 8 effective or perceptual channels are achieved with current CI technology.<sup>156</sup> Thus, the tonotopic precision inherent to the auditory system is poorly exploited by the implant and limits patient auditory performance.<sup>147,157</sup> Accordingly, increasing the number of effective signal channels provided by the prosthesis would substantially improve auditory performance outcomes for CI users as the device would make better use of the tonotopic spatial organization within the cochlea and the CNS auditory pathway.

### **Strategies to Improve Cochlear Implant Performance**

To address current CI limitations that have led to a plateau in auditory performance in recent years, researchers are focusing on several strategies to improve the selectivity of SGN stimulation within the cochlea.<sup>14</sup> Enhancing selectivity is anticipated to support a greater number of effective or perceptual signaling channels which in turn will improve auditory performance. One such strategy is to reduce the distance between the stimulating elements of the prosthesis and the sensory elements of the nervous system by positioning the electrode array as close as possible to the SGNs in the modiolus. Electrical signals have been shown to decay exponentially over short distances in the cochlea.<sup>158,159</sup> Accordingly, a much lower current is required to cause an action potential in a neuron the closer its position to a stimulating electrode. By reducing the current required for neural excitation, a more refined pattern of stimulation could be achieved as

there would be less spread of current to cause non-specific excitation within the cochlea. Furthermore, while the selectivity of each electrode would be enhanced, electrode density could also be increased since the electrodes could be smaller and, therefore, stimulate smaller groups of neurons independently.

The two largest CI manufacturers, Cochlear and Advanced Bionics, have developed prostheses with perimodiolar – i.e. modiolus enclosing or surrounding – electrode arrays to enhance signaling specificity and prosthesis performance.<sup>160,161</sup> An electrode array is considered perimodiolar if it is situated very closely to the modiolus throughout the curvature of the cochlea and if the electrode contacts are directly faced towards the modiolus.<sup>162,163</sup> As anticipated, evoked-potential recording illustrated that lower current thresholds were effective when the electrodes were placed in closer proximity to the SGNs.<sup>164</sup> Unfortunately, there was no substantial improvement in speech perception for patients with perimodiolar implants despite the use of lower current thresholds.<sup>165</sup> Two potential reasons that may prevent greater progress with perimodiolar implants are that the electrodes are still too far from the SGNs which prevents greater signal specificity and that longitudinal current spread in the scala tympani via the perilymph still causes non-specific signaling and channel interactions.<sup>14,166</sup>

Another strategy to improve CI performance is to optimize the number and firing pattern of electrodes that are triggered at a given time. Two sub-fields within this strategy are to create favorable current super-positions that generate ‘virtual channels’ between electrodes and another is to attempt to avoid any channel cross-over by preventing electrodes that are near each other from firing at or near the same time.<sup>167,168</sup> Both of these plans focus on electronic and computational methods to increase stimulatory specificity. For the virtual channel or current steering approach, channel interactions are deliberately produced by firing electrodes that are in close proximity to one another causing an overlap of stimulating current. Interactions depend on the direction and magnitude of stimulation from a given electrode in relation to other localized currents. It

has been illustrated that maximum excitation sites can be manipulated to occur between electrodes using the current steering technique.<sup>167</sup>

However, determining which interactions are beneficial and which are problematic has proven difficult. Furthermore, while the site of maximal excitation can be shifted, the degree of non-specific neural excitation remains the same. That is, an effective channel at a different tonal location within the cochlea can be developed but proximate channels could not be simultaneously stimulated due to signal spread. The effective channels are essentially shifted but not improved. Furthermore, difficult electrical problems challenge this strategy as well since neural excitation does not necessarily occur in a smooth continuum between electrodes but has been shown to jump.<sup>169</sup> Recent research efforts are underway to further focus the stimulating current during multi-electrode stimulation events. The phased array in this approach would, through substantial electrical interaction, produce carefully focused current profiles throughout the scala tympani. However, this method is also dogged by electrical and electrode design problems as the device would require more current during stimulation events and the number of electrodes would need to increase significantly to achieve sufficient current focusing channels.

The reduced signal interaction method uses the opposite strategy of the current steering or focusing approach. In this method, speech processor algorithms are programmed to prevent electrodes in close proximity from firing at or near the same time to prevent current overlap at any given location along the length of the electrode array. Sufficient time is allowed between proximate firings to allow neural membrane charge up to dissipate.<sup>168</sup> This method has been applied commercially as speech processor technology in Cochlear Corporation's CIs. The speech processor programming reduces the likelihood of simultaneous firing of adjacent electrodes that have been plotted to specific frequency bands within a given region of the cochlea. Though the approach has seen some success in improving auditory performance by reducing channel interactions, ultimately, the

number of effective channels remains constant which, again, rapidly leads to a plateau in possible prosthesis performance.

Another strategy used to increase CI stimulatory specificity is to reduce longitudinal current spread during an electrode trigger event by reducing the volume of the conductive perilymph that surrounds the electrode array in the scala tympani. Perilymph is the electrolytic fluid which normally fills the scala tympani. Longitudinal current spread is viewed as the prime means by which non-specific SGN excitation occurs and, if prevented, could increase the number of effective or perceptual channels for a CI user. If electrical current could be directed radially towards the modiolus rather than spreading longitudinally along the scala tympani then it may increase specificity and substantially improve auditory performance.

To displace perilymph and to position the electrode array in close proximity to the modiolus, a “positioner” is inserted into the scala media along with the internal cable during implantation. At least one report has shown that speech perception improved with the positioner than without it.<sup>170</sup> Furthermore, recent evidence illustrates that space-filling electrode arrays which occupy most of the volume in the scala tympani in which they are inserted may increase signal specificity.<sup>171</sup> However, due to differences in electrode design in this study, it is difficult to ascribe any improvements in auditory perception to a reduction in the volume of perilymph. Improvements could be due to the electrode design itself or to the positioning of the electrode array relative to the modiolus. In both perilymph displacing approaches, either incorporating an additional positioner piece or using a space-filling electrode array, the risk of intracochlear damage and post-surgical complications increases.<sup>172</sup>

Finally, as a variation to the above mentioned strategy to reduce the distance between the electrode array and neural elements in the cochlea, there is lively interest in developing methods to promote the regrowth of the peripheral SGN neurites into close proximity, or even into contact, with the stimulating electrodes.<sup>13,153,173-176</sup> SGN neurite

regeneration is promoted via a neurotrophin stimulus. This approach would more closely mimic the auditory pathway of a healthy ear in which SGN neurites synapse with hair cells some distance away from the modiolus. Significantly reducing the distance between the electrode array and neural processes stands to greatly increase the number of effective frequency channels and, hence, the quality of sound perception and voice comprehension for CI users. *However, to be useful, neurite outgrowth must preserve the precise tonotopic spatial organization of the cochlea.* Accordingly, a final application using this approach will likely require significant advances in tissue and neural engineering, sustained application of neurotrophic factors and other pharmacological actives, and development of bioactive polymers that enable and direct neurite outgrowth.

In a healthy cochlea, SGNs receive trophic support from hair cells.<sup>177</sup> The loss of hair cells in various types of sensorineural hearing loss generally leads to degeneration of SGNs due to lack of trophic support. Longer periods of deafness diminish positive outcomes with a CI prosthesis largely due to the described SGN degeneration.<sup>178</sup> Treatment with neurotrophic factors is known to prevent SGN degeneration and stimulate neurite outgrowth.<sup>179-181</sup> However, outgrowth occurs as disorganized projections failing to recapitulate the spatial organization inherent to a healthy cochlea.<sup>182-184</sup> Disorganized regeneration may actually reduce, rather than improve, the spatial fidelity and resolution of the electrical stimulation. Accordingly, the work presented in this thesis explores the possibility of using surface topographic features to precisely guide *de novo* SGN neurite growth (Fig 1.9). Micro- and nano-scale physical guidance cues are fabricated and tuned using the inherent spatial and temporal control of photopolymerization. As poor tissue integration represents a major limitation of nearly all neural prostheses (e.g. retinal implants), the results of these studies will not only inform efforts to improve CI performance but also carry broad implications for regenerative neuroscience and bioengineering.

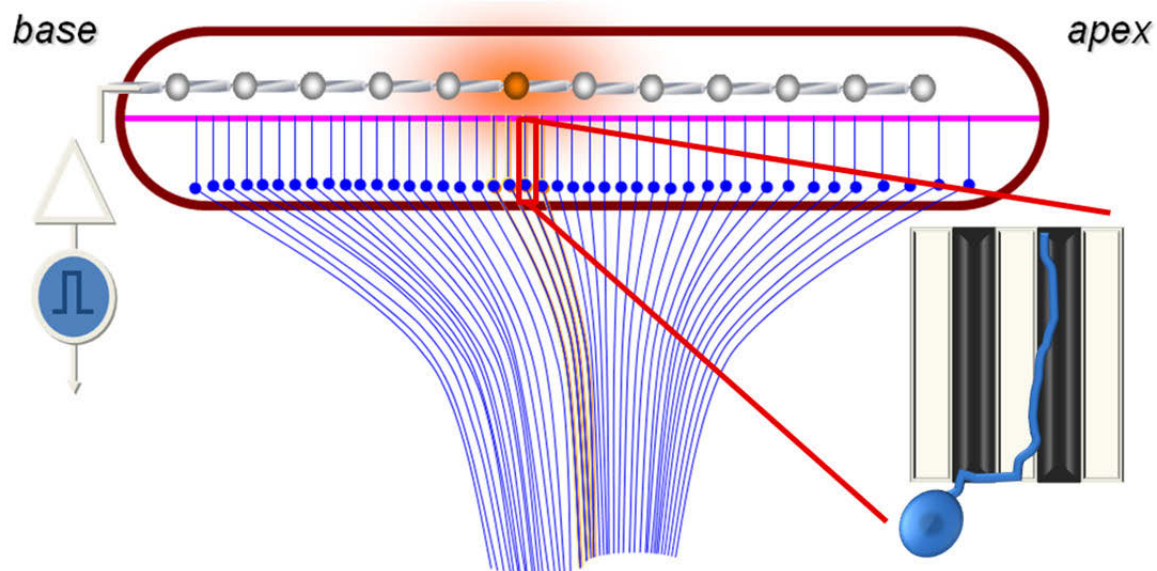


**Figure 1.9.** Schematic of the spatially organized neural regeneration strategy. Directed SGN *de novo* neurite growth to specific electrodes will improve CI stimulatory specificity, lower current requirements, decrease problematic channel interactions, and enhance tonal perception. The cochlea is represented as if laid out from the base to the apex from left to right. SGNs and their neurites are represented by blue dots and blue lines, respectively. Neurite outgrowth is precisely directed by physical guidance cues.

### Methods to Direct Cell and Neurite Growth

During tissue formation, development, and regeneration, cells encounter and must respond to a complex milieu of signals, including bioactive molecules and physical topographic cues of their surrounding microenvironment. Biomaterials scientists and biomedical engineers have designed or modified materials accordingly to mimic or synthesize micro- and nano-scale cues to elicit favorable cellular responses such as oriented cell outgrowth or directed stem cell lineage. This section provides a brief overview of research efforts aimed at directing cell and neurite growth through a variety of bioactive chemical or physical guidance cues. Particular emphasis is given to research that includes physical contact guidance cues, directed neurite outgrowth work, and

patterns developed via photomasked lithography, polymerization, or chemical functionalization.

### Chemical Cues

The most crucial interactions between a biomedical device and its host, or between any biomaterial and a biological system, generally occur at the material-biology interface. Bulk properties of a biomaterial or tissue engineering construct also play important roles, particularly in load-bearing applications such as bone or joint replacement or cartilage repair.<sup>185,186</sup> However, the ultimate performance of a device or material, and whether it is rejected by the body's immune system, are largely determined by what the local cells 'see' or 'feel' in the forms of chemical or physical stimulus at the material surface. Due to significant advances in micro- and nano-fabrication technology and in surface characterization techniques, the capacity to specifically tailor and pattern environments for particular cellular niches and outcomes is expanding at a rapid pace. The variety of approaches being utilized to predictably alter material surface chemical properties is continually expanding and enables control of cellular behaviors such as migration, proliferation, stem cell differentiation, adhesion, pre-determined apoptosis, and intercellular communication.<sup>187</sup> While it is beyond the scope of this introduction to detail each permutation of these methods, several broad categories for surface chemical modification are of particular importance and generally enable the other types of functionalization schemes.

Microcontact printing ( $\mu$ CP) is likely the most well-known and widely explored method utilized to spatially control the chemical modification of a material surface.<sup>188,189</sup> A micropatterned stamp is inked with a bioactive molecule and then pressed against the substrate that is to be chemically patterned.  $\mu$ CP technology is enabled by photolithography methods developed by the electronics industry and is performed in conjunction with soft-lithography casting of an elastomer on an etched master template.

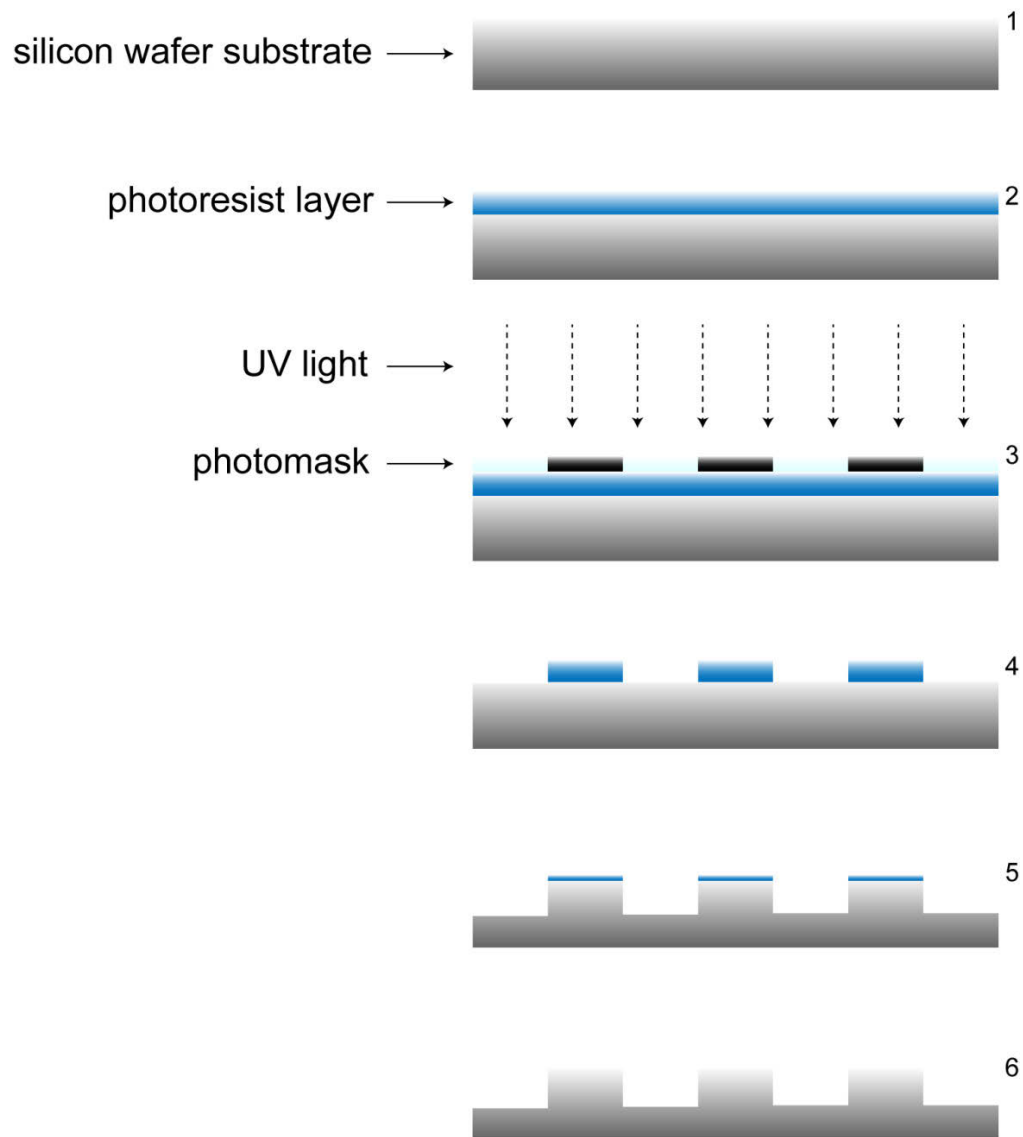


**Figure 1.10.** Schematic of the photolithography process. 1) A silicon wafer is first prepared by removing organic residues with an oxidizing agents such as reactive  $O_2$  plasma and then chemically treated to promote photoresist adhesion. 2) Photoresist is spin-coated on the wafer surface and baked to drive off organic solvent. 3) The photoresist layer is selectively exposed to UV radiation through a glass-chrome photomask. 4) Positive photoresists become soluble upon UV exposure while negative photoresists crosslink and become insoluble when exposed to UV. Soluble regions are removed during a wash step leaving a pattern of photoresist whose thickness is based on parameters of the spin-coating step and the viscosity of the photoresist. 5) Reactive ion etching, or other dry etch methods, are employed to etch away the silicon substrate. Regions beneath photoresist remain protected. Photoresist is also etched away during this step but is designed to have a much slower etch rate than the silicon substrate. 6) Remaining photoresist is removed during a stripping or lift off step and the sample is further cleaned and prepared for future applications.

Traditional photolithography techniques are used to develop the master template (Fig 1.10). First, a silicon wafer is spin-coated with a photoresist and baked to harden the resist by solvent degassing. The photoresist-coated wafer is then brought into contact or close proximity with a quartz photomask. Quartz is used in place of soda lime glass since it has better ultra-violet (UV) transmission properties. A thin, reflective chromium pattern coats the photomask and can be configured in carefully planned geometric configurations using computer-aided design. The photoresist layer is then selectively exposed to UV light through the photomask. Depending on the type of photoresist, regions exposed to light will either become soluble (positive resist) or insoluble (negative resist). Following UV exposure, a subsequent lift-off process removes any soluble photoresist regions. The lift-off step is followed by an etching step, e.g. reactive ion etching, to control the depth of the features. Generally, the photoresist etches at a much slower rate than the underlying wafer which enables tuning of substrate topography based on the specific microfabrication recipe. Finally, a photoresist stripping step is used to remove any residual surface photoresist and the wafer is then thoroughly cleaned prior to use. It should be noted that the complexity of the surface can increase substantially if the process has multiple photoresist and etching steps.

Following the fabrication of a micropatterned silicon master, an elastomeric material, typically poly(dimethyl siloxane) (PDMS) is cast and cured on top of the master template (Fig 1.11). The viscosity and surface tension of the pre-stamp formulation should be appropriate to enable conformal spread across micropatterned features. PDMS is popular since it is inexpensive, cures readily with heat after mixing, and remains flexible post-cure to enable conformal contact of the stamp on a target substrate. However, other agarose gels, alternative siloxanes, and poly-olefin plastomers have also been used as stamping materials.<sup>190-192</sup> PDMS stamps can be further treated to add functionality. For instance, the stamps are commonly treated with reactive oxygen plasma to oxidize the surface, increasing the surface energy and facilitating adsorption of various

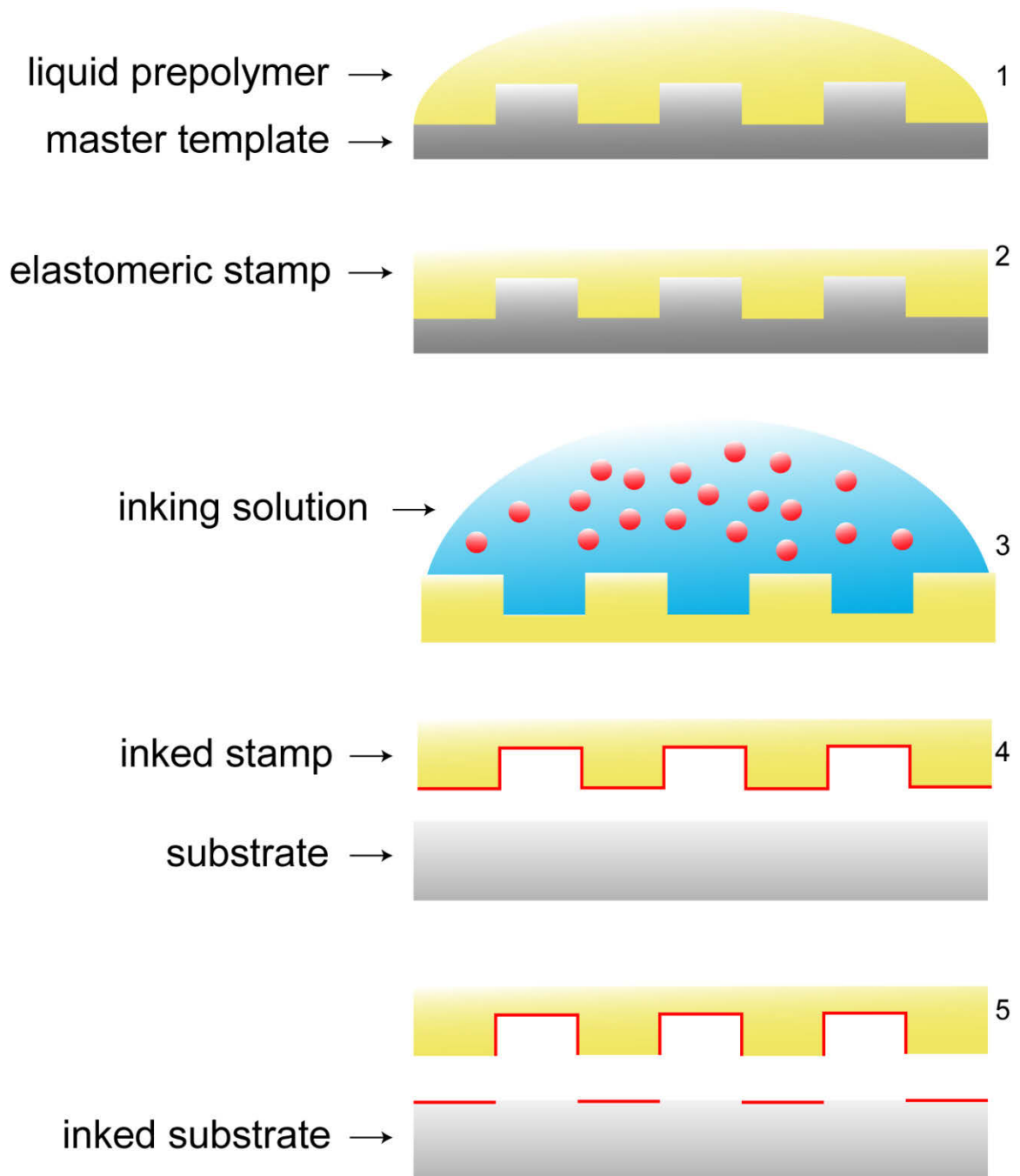


**Figure 1.11.** Depiction of the microcontact printing process. 1) A liquid prepolymer is cast over a master template which is usually a micropatterned silicon wafer fabricated by photolithography. 2) The liquid prepolymer conformally coats master template features and is cured in place to form a negative image elastomeric stamp. 3) Patterned stamps are inked via simple adsorption from solution. 4) The stamp is brought into contact with the substrate to be inked. 5) A spatial replica of the stamps raised features is inked on the substrate surface following removal of the stamp.

bioactive molecules. Furthermore, they can be treated with an immense variety of silane coupling agents with distinctive chemical moieties for applications as specific as immobilization of antibodies for high affinity protein binding methods.<sup>193</sup>

While the micropatterned ‘soft’ stamp can be coated with an array of bioactive inks, the most common inks used to spatially direct cell and neurite growth by chemical cues use adhesion promoting proteins or smaller peptide sequences.<sup>188</sup> Integrins are a crucial class of adhesive proteins expressed in the extra cellular matrix (ECM) around cells which facilitate cell-ECM interactions.<sup>194</sup> Collagen, laminin, fibronectin, and vitronectin are common integrins found in the ECM as well as used in inks for microcontact printing. The bioactive ink, such as the choice of integrin, should match the targeted cellular niche – further highlighting the importance of multi-disciplinary work in biomaterials applications as materials scientists may need to work with biochemists and microbiologists to optimize the final ink composition.

$\mu$ CP, and its permutations, have enabled directed cellular patterning for a variety of cell types and have also enabled guided neural process growth. For example, endothelial cells are known to selectively adhere to squares and grid lines of fibronectin printed by  $\mu$ CP methods.<sup>195</sup> Fibroblasts, which are common cells forming connective tissue in the body, only attach to and proliferate on adhesive peptide regions patterned with an RGD functionalized poly-L-lysine-g-poly(ethylene glycol) copolymer ink.<sup>196</sup> Interestingly,  $\mu$ CP has even been used to pattern (capture) *Escherichia coli* as part of a diffraction based optical bacteria detector.<sup>197</sup> For neuronal cultures, laminin, another integrin protein, is used for  $\mu$ CP experiments to direct neural process growth and form controlled neural networks. For example, laminin was patterned via  $\mu$ CP at various node sizes and line widths to precisely position cells from a PCC7-MzN neural blastoma cell system and to induce directed cell differentiation.<sup>198</sup> Micropatterned PDMS stamps with features 3 – 5  $\mu$ m in width were also used to biofunctionalize polystyrene, glass, and silicon-oxide surfaces with the oligopeptide binding sequence of laminin to enable

formation of neural networks with hippocampal neurons.<sup>199</sup> Hippocampal neural networks were also directed by  $\mu$ CP of polylysine-laminin conjugates.<sup>200</sup>

Another prominent chemical patterning method for directed cell-material interactions, and one that is closely related to  $\mu$ CP, is microfluidic patterning. Microfluidic patterning follows the same steps as  $\mu$ CP but in place of using an elastomeric stamp to ink a surface with bioactive molecules, the micropatterned elastomer instead acts as a barrier to create channels through which a solution containing bioactive ligands can pass. The underlying substrate is subsequently coated with the bioactive solution only in regions where the fluid was allowed to flow (Fig 1.12). Complex patterns with multiple types of bioactives are

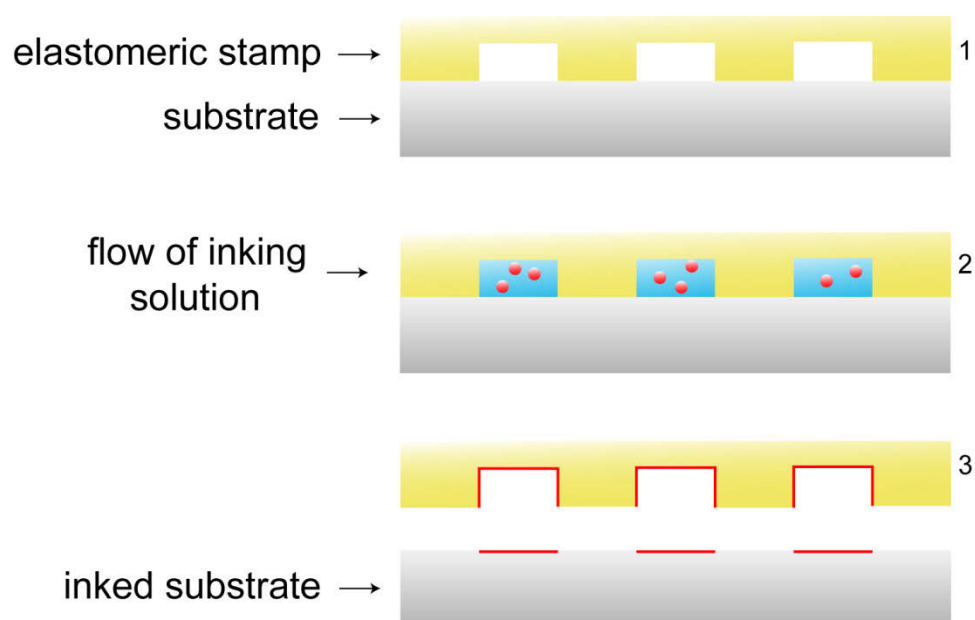


**Figure 1.12.** Representation of the microfluidic patterning process. 1) An micropatterned stamp formed by photo and soft lithography is placed in contact with the substrate to be patterned. 2) An inking solution with the dissolved active agent is drawn through the microchannels formed between the stamp and the substrate. 3) The substrate is inked in the spatial pattern of the flow channels.

significantly easier to generate than when using  $\mu$ CP.<sup>201,202</sup> Tuning of bioactive density is also more readily controlled, however patterns are limited to open flow channels. Microfluidic patterning can even be employed in tandem with  $\mu$ CP by first inking the elastomeric stamp before pressing the stamp to a substrate to create microchannels through which a solution with a different bioactive can flow.<sup>203</sup> Microfluidics have been used to generate ligand gradients of permissive and inhibitory cues to direct neurite outgrowth from dorsal root ganglion neurons.<sup>204</sup> Neurite extension is directed by both inhibitory chondroitin sulfate proteoglycan and permissive laminin gradient patterns. When the cues are presented simultaneously, neurite extension is controlled by the direction of the ligand gradients. Microfluidics have also been used to direct neurite growth from cortical neurons by supplying a constant netrin growth factor gradient in solution rather than by functionalizing a planar surface by adsorption.<sup>205</sup> The physical microchannels normally used to direct bioactive solutions across a substrate in microfluidics are also known to direct neural process growth.<sup>206</sup> More information on the state-of-the-art in microfluidic technology is available in an excellent review.<sup>207</sup>

A significant drawback for both the  $\mu$ CP and microfluidic patterning methods is that adsorbed coatings exhibit poor stability due to weak physicochemical interactions. Accordingly, covalent functionalization of bioactives on 2D surfaces and within 3D matrices has been developed to improve effectiveness and longevity of a chemically modified biomaterial. Microfluidics and  $\mu$ CP rely on the spatial control of photomasked exposure during a photolithography process to develop intricate patterns for substrate functionalization. Similarly, photo-functionalization methods are employed to covalently bind bioactive moieties to a synthetic material for improved stability (Fig 1.13.)

For example, the peptide binding sequence in laminin was conjugated to benzophenone, which cleaves to form free radicals upon exposure to UV light, and was spatially patterned as a covalently bound gradient across a polymer surface by altering the scan speed of a Cd/HE UV laser.<sup>208</sup> Similarly, diode lasers were used to covalently

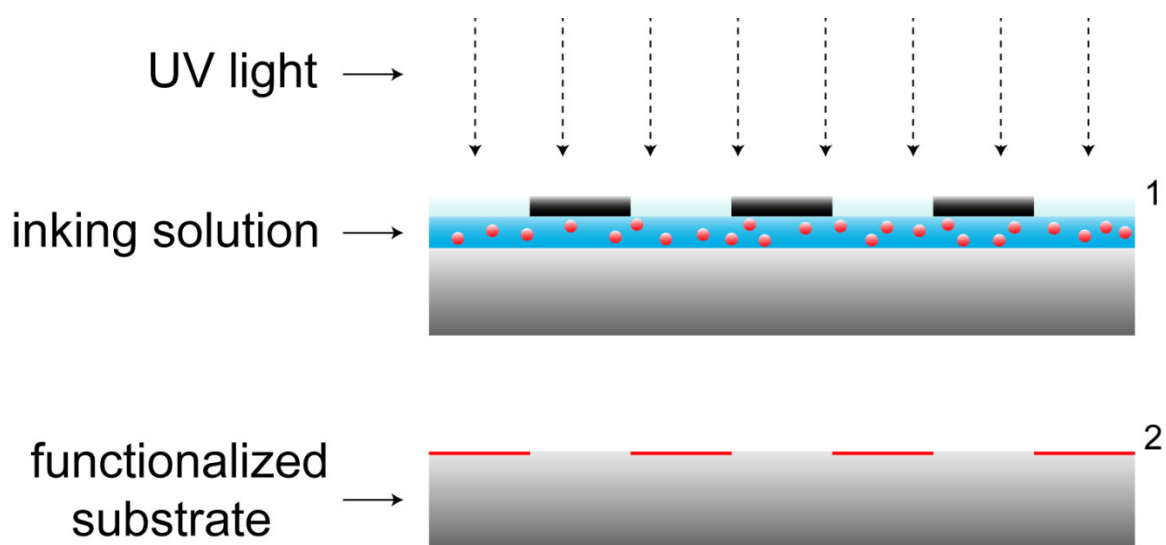


**Figure 1.13.** Diagram of the photo-functionalization process. 1) An inking solution with the active agent is spread by capillary forces between a substrate and a photomask. The substrate is modified such that upon UV irradiation the active agent covalently binds to the surface. 2) The substrate is covalently modified with the active agent in the spatial pattern of the transparent regions of the photomask.

bind a fluorophore conjugated-biotin and laminin binding sequence to a planar surface with high resolution spatial control to direct DRG neurite outgrowth.<sup>209,210</sup> Furthermore, a photoactively derivatized chitosan surface was covalently modified with nerve growth factor using UV light and photomasking to spatially guide neural process growth from superior cervical ganglion neurons.<sup>211</sup> An elegant two-photon photochemical functionalization scheme has also been employed to spatially pattern a variety of growth factors throughout the volume of a 3D hydrogel construct.<sup>212,213</sup>

In addition to patterned chemical cues developed with  $\mu$ CP, microfluidic, and photo-functionalization methods, cells are also known to respond to the chemical properties of the synthetic material substrate. For example, recent work illustrates that surface wettability of low density polyethylene can be tuned via oxygen plasma exposure to improve 3T3 fibroblast proliferation.<sup>214</sup> Additionally, murine chondrocytic and

sarcoma osteogenic cells were not able to proliferate on superhydrophobic surfaces while fibroblast cells thrived on the same surfaces.<sup>215</sup> Furthermore, human umbilical endothelial cells show more robust adhesion, growth, and coverage on materials that were modified by plasma exposure to have an optimum water contact angle for endothelial cell proliferation.<sup>216</sup> The bulk and surface biochemical properties of a material can also be modulated by conjugating polymer precursors with bioactive moieties, such as the small peptide chain integrin binding sequence RGD. Cell adhesion and proliferation are known to be enhanced by improving cell anchorage properties of a material with this method.<sup>25,217</sup> Acrylate monomers, commonly used for photopolymerized materials, are readily conjugated to the amine terminus of an RGD sequence to enable this approach.<sup>218</sup>

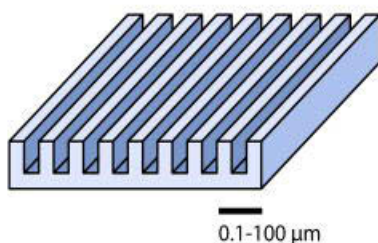
### Physical Cues

A major limitation to the chemical patterning methods for directed cell and neurite growth just discussed, and others which were not included,<sup>219</sup> is that bioactive molecules are inherently unstable which significantly complicates the production and practical use of biomaterials patterned with bioactive molecules.<sup>35</sup> The stability hurdle is particularly challenging for long-term implant applications.<sup>2</sup> For example, because albumin is the most prevalent protein found in blood it has been frequently used in attempts to passivate a material surface towards the host immune system.<sup>62,220</sup> However, other blood proteins such as fibrinogen and immunoglobulin can readily displace adsorbed albumin on a biomaterial surface. Indeed, even covalently bound albumin is unstable upon implantation as leukocytes degrade the attached protein into pro-inflammatory components at the implant site.<sup>60</sup>

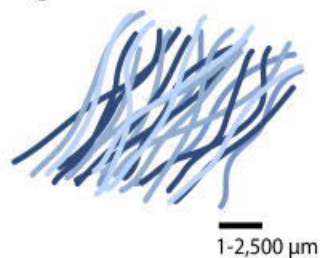
To overcome these and other hurdles, biomaterials scientists and tissue engineers have begun to exploit the ability of material physical cues including surface topography and mechanical stiffness to influence a wide variety of cellular responses (Fig 1.14.).<sup>80,81,221,222</sup> For example, the cell shape of human gingival fibroblasts was

## Anisotropic Topography

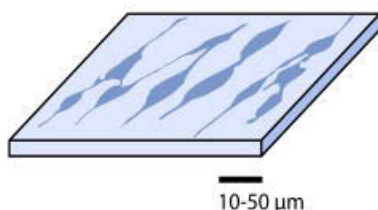
### Grooved Surfaces



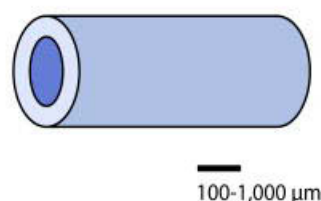
### Aligned Fibers



### Cell-inspired Topographies

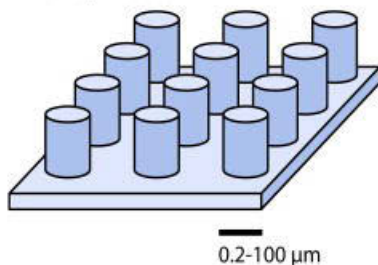


### Guidance Conduits



## Isotropic Topography

### Pillars/Posts



### Nanorough Surfaces

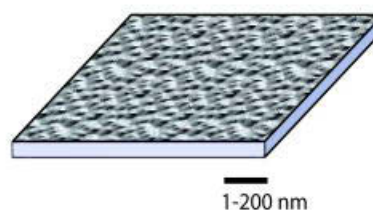


**Figure 1.14.** Examples of physical cues used to influence cellular outcomes. Courtesy of NIH Public Access, 2010.

significantly modulated by micromachined grooves 3  $\mu\text{m}$  in depth on titanium coated surfaces. Furthermore, the fibronectin transcriptional, post-transcriptional, and ECM secreted levels were over 2-fold higher on physical micropatterns compared to smooth substrata.<sup>223</sup> Physical micropatterns were also shown to induce increased neurotrophin expression from Schwann cells (SCs) that were cultured on microgrooved chitosan and

poly(D,L-lactide) (PLA) compared to those grown on unpatterned controls.<sup>83</sup> Nano-pit topographies are known to reduce adhesion and spreading of human fibroblasts and to cause interaction and response from cell filopodia when fabricated as small as 35 nm in diameter.<sup>224,225</sup> Human epithelial cells elongated on silicon oxide substrates that had ridge and groove depths as small as 70 nm.<sup>84</sup> These contact guidance studies, along with many others, illustrate the significant potential to promote favorable neural outcomes such as directed process growth.

The vast majority of research exploring cell-material interactions to physical guidance cues is centered on traditional photolithography technology.<sup>35,226,227</sup> See the previous “Chemical Cues” section in this introduction as well as an informative review for detailed steps in the photolithography process to generate micro- and sub-micron features.<sup>219</sup> Photolithography was explored and extensively developed with the advent and expansion of semiconductor manufacture within the electronics industry. It has also been increasingly employed for cellular and medicinal applications during the last two decades.<sup>187,228</sup> One reason for the dominance of this particular production method for cell-material interaction studies is the superb spatial control enabled by the photomasking and etching steps during substrate production. Also, the technology is very well established and diversified due to its immense importance in fabricating semiconductor devices for the electronics industry. Many universities and research institutions have core micro- and nanofabrication facilities based on traditional photolithography and its derivatives and have fostered interdisciplinary research efforts to maximize the effectiveness of these centers. Other prominent methods that employ physical cues to direct cell behavior, particularly neurite outgrowth, but do not require the spatial control of photolithography include hollow nerve guidance conduits, intraluminal guidance structures, and electrospun micro- and nano-fibers.<sup>229-232</sup>

Using hollow tubing for neural regeneration and repair was first proposed and demonstrated in the late 19th century using a hollow bone tube as the guidance

conduit.<sup>233</sup> Since then, hollow nerve conduits have now become sufficiently established to serve as alternatives to nerve auto-grafts for repair of peripheral nervous system (PNS) defects less than 4 cm. However, auto-grafts remain the gold standard for repair since they provide the greatest functional recovery.<sup>234</sup> Nerve conduits reduce scar tissue formation, limit myofibroblast ingrowth, direct regenerating peripheral processes towards distal targets, and enable accumulation of nerve growth factors in a tight volume which increases neuronal survival and neurite extension rate.<sup>235</sup>

To improve neural regeneration and functional outcomes of nerve guidance conduits, researchers have modified the constructs with intraluminal guidance structures. The principal aim for including these features is to induce maximal uni-directional neurite outgrowth to span great distances representative of large nerve gaps. For example, a poly(glycolic acid)-collagen nerve guidance tube was modified with laminin-coated collagen fibers which enabled regeneration across an 8 cm nerve gap.<sup>236</sup> Collagen fibers have also been used to repair 2 – 3 cm nerve gaps without the presence of an outer conduit.<sup>237,238</sup> Unfortunately, functional recovery was either not characterized or poor for these collagen fiber applications. A variety of fiber materials such as poly(L-lactide), poly(glycolic acid) and poly(acrylonitrile-co-methacrylate), as well as fiber diameters and packing densities have been explored in attempts to improve functional recovery outcomes.<sup>239-242</sup>

In addition to the changes in cellular responses such as adhesion, gene expression, spreading, and proliferation induced by micro- and nano-scale topography, a major cellular outcome observed on physically patterned substrates is the alignment to anisotropic features. Polarization of a cell or alignment of a neurite is particularly prevalent in response to parallel ridge-groove morphologies. Micropattern dimensions such as ridge width, groove depth, and feature spacing can be altered during the fabrication process to tune the degree of the pattern's influence.<sup>85-87</sup> The mechanisms by which cells sense and transduce changes in the physical environment into specific cellular

responses remain largely unknown. Topography is believed to induce tension in the cytoskeleton and the cell membrane that is subsequently transduced by second messenger molecules to modulate cellular responses.<sup>243,244</sup> Neurite alignment behavior to substrate topography is of particular significance to this work as it may enable spatial organization of neurites in a manner that dramatically improves prosthesis signal resolution and performance.

Like a variety of other cell types, neurites are also strongly influenced by cell-scale polymer surface morphology and often align to repeating micro- or nano-scale topographical stimuli. For example, axonal growth from sensory ganglia taken from adult mice showed significant directional growth on nano-patterned grooves of polymethylmethacrylate (PMMA).<sup>245</sup> Neurites from PC 12 cells aligned to features ranging from 70 to 1900 nm in width and their neuritogenesis behavior changed markedly on features of various sizes.<sup>246</sup> While process alignment generally occurs in the direction of anisotropic features, neurites are known to grow perpendicularly to microfeatures used for contact guidance studies.<sup>247</sup> The terminus of a neurite extension from a neural soma or nerve body is referred to as the growth cone. The growth cone is a sensitive apparatus that interacts with environmental chemical and physical cues to inform and direct the *de novo* growth path of a developing neural process.<sup>248</sup> Growth cones are known to integrate multiple cues that can be separated by time or space and can also respond to additive or competing cues.<sup>249</sup> Understanding and precisely directing the pathfinding behavior of neural growth cones is crucial to the development of therapeutic solutions to nerve injuries and to overcoming neural prosthesis performance limitations.

Neural process response to cell-scale topographies has been quantified on the basis of average neurite length, maximum neurite length, branch formation, and number of neurites formed per cell.<sup>250-252</sup> Even greater emphasis has been placed on quantifying neurite alignment to anisotropic features, e.g. parallel ridge-groove morphologies.<sup>253,254</sup> For instance, neurite outgrowth has been characterized by grouping alignment data into

angular bins and demonstrating that the frequency of neurites which align to given topographical cues rises or falls based on feature dimensions.<sup>255,256</sup> A Fourier-transform method has been devised to quantify alignment from an entire field of view of a neural network rather than from individual neuronal bodies.<sup>245</sup> Neurite alignment has also been quantified in response to imposed glial cell-mimicking topography.<sup>257</sup> A wide variety of groove widths and depths fabricated via photolithography are known to alter the degree of neural process alignment – often in a manner that depends on the neuronal type.<sup>81,253,255,258,259</sup>

Beyond alteration of topographic features, mechanical properties of the polymer substrates may also affect neuronal behavior and neurite orientation.<sup>32,33,221,260</sup> Similar to the movement induced by chemically repulsive or attractive cues referred to as chemotaxis, cellular movements based on interactions with mechanical cues were coined as ‘durotaxis’ by Lo et al.<sup>90</sup> Numerous tissue engineering studies show that cell fate is significantly influenced by the mechanical stiffness of its micro-environment. Migration and adhesion of endothelial cells, myoblasts, and osteoblasts were regulated by tuning substrate stiffness.<sup>91-93</sup> Significantly, neurites from chick dorsal root ganglia grew longer down a stiffness gradient than up, and were also longer than the control samples with no mechanical gradient.<sup>33</sup> Balgude et al. demonstrated that neurite extension rate was inversely correlated to mechanical stiffness in agarose gels.<sup>94</sup> Further, PC 12 neurons displayed robust growth on harder substrates and were observed to have a softness threshold at which relatively little neurite growth was observed.<sup>95</sup>

Taken together, the alignment of neurites from a variety of neuronal types to designed topography and material mechanical cues inspire confidence that similar material strategies could be employed to improve the performance of neural prosthetics. Research in the last two decades illustrates a variety of methods to direct *de novo* neurite outgrowth including aligned microfibers, parallel micro- and nano-channel morphology, axonal conduits<sup>261</sup>, cyto-mimetic patterning, bioactive molecule patterning<sup>262-265</sup>,

diffusion gradients of chemo-attractants, and electrical fields<sup>266</sup>. However, the principle focus of many of these studies is to induce neurites, particularly those of the sciatic nerve, to optimally extend in one direction to bridge large gaps typical of nerve injuries. Using similar guidance techniques may also be advantageous to address spatial resolution challenges at the neural-prosthetic interface by enabling spatial control of regenerative sensory neurites specific to the prosthesis.

### **Photopolymerization of Biomaterials**

Photo-initiated polymerization and functionalization techniques represent attractive alternatives to traditional photolithography for the generation of chemically or physically patterned biomaterials for contact guidance. In general, direct photopolymerization or photo-functionalization of a bioactive material is fast, low cost, and readily tunable between each sample run whereas lithographically etched features require many more process steps, hazardous reagents, expensive microfabrication equipment, and different master templates for each desired feature height. Furthermore, photopolymerization is rapidly expanding as an effective, versatile, and environmentally friendly materials production platform. During the last two decades its use has expanded tremendously in a range of applications as diverse as thin film coatings,<sup>267,268</sup> 3D prototyping,<sup>269,270</sup> optical lenses,<sup>271,272</sup> photolithography,<sup>273,274</sup> and microfluidics.<sup>275,276</sup> Recent studies also demonstrate the versatility of photopolymerization for a variety of biological applications. For example, photopolymerization can be performed under reaction conditions mild enough to co-encapsulate plasmid DNA and cells in a degradable, methacrylate hydrogel without compromising function of the plasmid DNA or viability of the encapsulated cells upon release.<sup>277</sup> 3D tissue-engineering scaffolds with a range of pore sizes and architectures are generated through a single, spatially controlled photopolymerization step in order to determine the effect of substrate geometry and

porosity on cell behavior and *in vivo* reaction.<sup>278</sup> Moreover, a variety of high performance dental materials are cured by photo-crosslinking reactions.<sup>279,280</sup>

In addition to the advantages just outlined, photopolymerization is ideal for bioactive material patterning due to its inherent spatial and temporal reaction control. Spatial control is achieved by selectively masking the pre-polymer formulation from initiating light and temporal control is afforded through shuttering of the light source at specific time increments. For a typical photo-initiated radical chain growth polymerization, a small concentration of photo-initiator in the pre-polymer formulation absorbs photons and undergoes bond cleavage that results in the generation of reactive free radicals.<sup>281</sup> As an initiation step, the free radical species then react with electron rich double bonds on polymerizable moieties, e.g. (meth)acrylates, of the surrounding monomer which begins the polymerization. Figure 1.15 provides the basic structure of several classes of photoinitiators used in industry and academia. Propagation continues

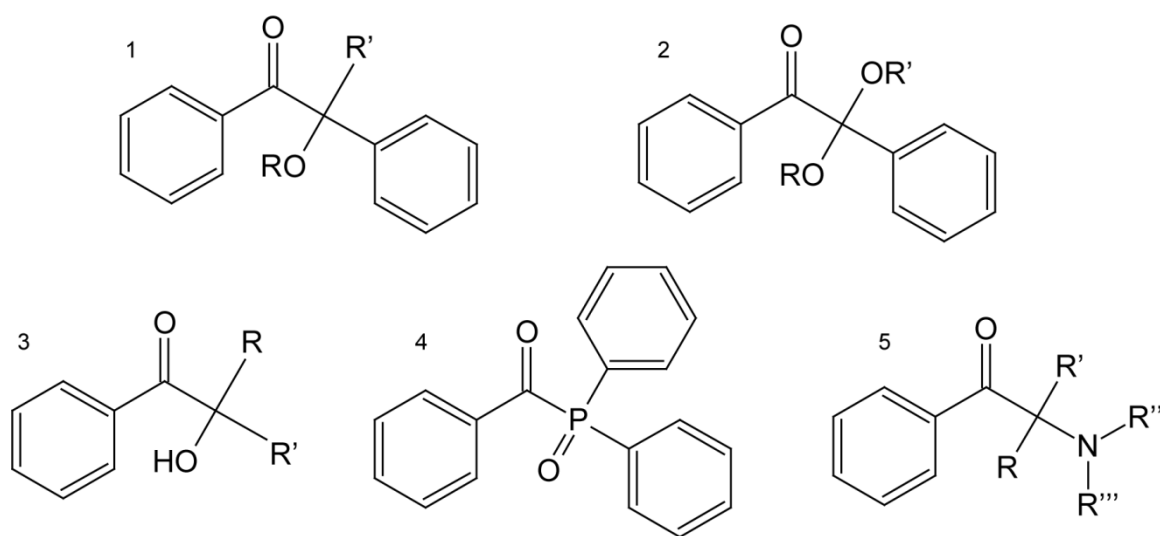


**Figure 1.15.** Classes of common photoinitiators. Shown are generic structures for 1) benzoin derivatives, 2) benzyl ketals, 3)  $\alpha$ -hydroxyalkylphenones, 4) acylphosphine oxides, and 5)  $\alpha$ -aminoalkylphenones.

through polymerizable groups until the growing kinetic chain is terminated via recombination with another radical or through hydrogen abstraction and disproportionation. The rate of propagation for a typical radical chain polymerization is given in equation 1.1

$$R_p = k_p [M] \left( \frac{R_i}{2k_t} \right)^{\frac{1}{2}} \quad (1.1)$$

where  $R_p$  is propagation rate,  $k_p$  is the propagation rate constant,  $[M]$  is the monomer concentration,  $R_i$  is the polymerization initiation rate, and  $k_t$  is the termination rate constant. For photoinitiated polymerization,  $R_i$  is described by equation 1.2

$$R_i = 2\phi I_0 (1 - e^{-\varepsilon b [I]}) \quad (1.2)$$

where  $\phi$  is the efficiency of initiation,  $I_0$  is the incident light intensity,  $\varepsilon$  is the molar absorptivity of the photoinitiator at a given wavelength of light,  $b$  is the thickness of the system, and  $[I]$  is the photoinitiator concentration. Substituting equation 1.2 into 1.1 yields the propagation rate for photopolymerization as shown in equation 1.3.

$$R_p = k_p [M] \left( \frac{\phi I_0 (1 - e^{-\varepsilon b [I]})}{k_t} \right)^{\frac{1}{2}} \quad (1.3)$$

Because the rate of propagation for a photo-initiated polymerization depends on absorbance of light, local reaction speeds can be modulated across a substrate surface by selectively masking incident irradiation. Other advantages inherent to photopolymerization include: rapid reaction rate at room temperature, low energy input, mild reaction conditions, and chemical versatility of monomer systems.

Accordingly, 2D and 3D biomaterials are readily patterned by controlling sample light exposure in both space and time. For example, a polyfluorene derivative was directly photopatterned on a poly(ethyleneimine) substrate by spatially controlling

crosslinking reactions prior to washing steps to generate cyto-adhesive and non-adhesive stripes.<sup>282</sup> Sequential photopolymerization steps were employed to create trapping and sorting wells to isolate single cells based on imaged phenotype.<sup>283</sup> Direct photopatterning methods have also been utilized to generate cytocompatible hydrogels with tunable degradation profiles<sup>284</sup> and with controlled microarchitecture<sup>285</sup> for tissue regeneration and cell encapsulation applications. Additionally, photopolymerization was used to surface functionalize polymeric substrates with immunosuppressive proteins to provide bioactive protection against activated T cells.<sup>286</sup> Each of these studies illustrates and utilizes specific advantages inherent to UV curing for cellular applications including excellent temporal and spatial control, mild reaction conditions, and few process steps.

Additionally, a wide array of photopolymers exhibit excellent biocompatibility and serve as relatively bio-inert surfaces for *in vitro* and *in vivo* applications. Methacrylates (MAs) are commonly used in many photopolymerization studies and were among the first successful polymer systems to serve as functional biomaterials. Their biocompatibility was first demonstrated during the development of the intraocular lens<sup>4</sup> and has since been confirmed in contact lens applications,<sup>287</sup> dental resins,<sup>288</sup> cellular encapsulation,<sup>289</sup> and bone cements.<sup>186</sup> As such, MAs have become a materials platform of choice for many tissue engineering and drug delivery applications.<sup>23,25</sup>

Beyond biocompatibility, photopolymer characteristics are readily manipulated to exhibit a range of mechanical, chemical, and surface properties that allow for design of materials tailored to suit intended biological interfaces.<sup>28,86,290,291</sup> Physical characteristics of photopolymers can be controlled by altering the material chemistry and the crosslinking density. Changing these factors alters material swelling capabilities, surface chemistry, wettability, mechanical strength, network architecture, and degradation time in accordance with the desired material properties.<sup>30,31,291</sup> Crosslinking density and mechanical strength have shown particular importance in cell and neurite growth.<sup>32-34</sup>

## Research Summary

The cochlear implant (CI) enables basic speech perception for individuals with profound hearing loss. Its success is one of the greatest accomplishments of the modern biomedical device and biomaterials era. However, the CI also illustrates difficult technical challenges associated with functional limitations of neural prosthetics. CIs enable basic speech perception by directly stimulating inner ear nerve cells with an electrical pulse that bypasses the damaged or non-functional mechanotransduction machinery of the inner ear. The most significant advances in CI technology since its initial development have been the shift to multi-channel devices followed by dramatic improvement in speech processor algorithms and electrode firing patterns. Unfortunately, clinical performance of the prosthesis has rapidly plateaued in recent years as current spread within the cochlea causes non-specific neuronal excitation and results in few perceptual channels for the user. As a result, CI patients struggle with complex auditory stimuli such as music appreciation, voice comprehension in environments with noise, and voice intonations. Reducing the distance between sensory elements of the nervous system and the electrode array of the prosthesis stands to greatly improve spatial signaling resolution of the device. Increasing spatial resolution would enable more perceptual channels and substantially improve the auditory performance of CI patients.

For the proximate growth strategy to be effective, tone dependent spatial arrangement of auditory sensory elements must be preserved and will require directional control of regenerating neurites. Recent studies demonstrate that many cell types, including neural glia and neurons and their processes, can be spatially directed by topographical, stiffness, and chemical cues of a biomaterial surface. Accordingly, this work develops and explores the use of photopolymerized materials and patterning to spatially direct as well as to test the pathfinding ability of *de novo* neurite outgrowth from neurons that are relevant to the CI prosthesis. Ultimately, the understanding gained from

these studies regarding SGN cellular and neural process interactions with engineered guidance cues will be used for the larger goal of overcoming signaling limitations of the patient-implant interface of the CI neural prosthetic. As the nervous system is generally dependent on location specific signaling, analogous signal resolution limitations are anticipated for all devices that interact with the nervous system. Precise spatial signal control will, therefore, be critical to achieve significant performance improvements in next generation neural-prosthetics.

The work is presented as five interrelated chapters. Significant advances in functional outcomes achieved with CIs will likely require neural engineering approaches to improve the prosthesis interface. Accordingly, as an initial proof of concept, survival and alignment of inner ear neural elements including spiral ganglion neurons (SGNs) and spiral ganglion Schwann cells (SGSCs) are evaluated on common methacrylate photopolymers in chapter 4. Direct photo-patterning of the methacrylate surface is also developed in this chapter. Alignment of SGN neurites is evaluated with both dissociated cultures and as neural tissue from inner ear explants. Chapter 5 significantly expands on this work by thoroughly exploring the extent of SGN neurite alignment to parallel line-space gratings based on feature dimensions. The spatial and temporal control of photopolymerization are shown to enable significant surface feature modulation based on polymerization reaction parameters. Feature depth is readily controlled from the micro to nano-scale by tuning photoinitiator concentration, UV exposure time, and initiating light intensity. Microchannel width is controlled by photomask band spacing. Developing precise control of surface microfeatures enables careful probing of neurite response based on feature dimensions. Neurites alignment is evaluated on patterns with constant periodicity and increasing height as well as on micropatterns with constant amplitude but increasing periodicity. SGSC spatial orientation is also measured in tandem with SGN neurite outgrowth. Interestingly, neurite alignment is found to strongly correlate to feature slope that occurs between ridge-groove transitions. The alignment and cellular

behavior of a variety of neuronal and glial cell types are also evaluated as comparisons to inner ear neural elements. The research presented in these two chapters firmly establish that *de novo* neurite growth from inner ear SGNs can be directed by bioactive material physical cues and that photopolymerization enables facile control of a variety of surface patterns for contact guidance studies and for future clinical application.

In chapter 6, the turning and pathfinding ability of neurites presented with multidirectional surface cues is explored as successful improvement of the neural prosthesis interface will likely require complex turning events. Understanding neurite pathfinding behavior in response to turning cues will enable development of bioactive materials that predictably orient nerve growth to spatially distinct electrodes. A repeating 90° pattern is used to represent a topographic challenge on which to evaluate the turning capability and neural pathfinding of *de novo* neurite growth from SGNs. Uni-directional, i.e. parallel, micropatterns and unpatterned photopolymers serve as comparisons.

Chapters 7 and 8 enlarge the scope of the work by investigating SGN neurite response to material mechanical and surface chemical properties, respectively. In chapter 7, the reaction modulated microfeature control developed in previous chapters is employed to create micropatterns with identical amplitude and spacing across two methacrylate copolymer series. For each methacrylate series, crosslinking density is controlled by varying crosslinker content in the pre-polymer formulation. Neurite alignment is then evaluated on each polymer series to determine the effect of material stiffness on neurite alignment to topographical surface cues. Understanding neurite response to mechanical cues will inform material choice and design considerations, including material mechanical properties, when designing eventual clinical applications. In chapter 8, bioactive chemical borders are established on physical microfeatures to determine the strength of physical cues when neural growth cones are presented with conflicting cues. Neurite behavior is measured at biochemical borders as a cross, turn, stop, or repel event. Both the chemical borders and the physical patterns are shown to

significantly affect neurite outgrowth. Importantly, physical cues are illustrated to dominate neurite trajectory at sufficiently high micropattern feature frequencies.

## Notes

1. Espicom Business Intelligence Ltd *The World Medical Markets Fact Book*; **2008**.
2. Buddy, R.; Hoffman, A.; Schoen, F.; Lemons, J. *Biomaterials Science An Introduction to Materials in Medicine*; Academic Press: Waltham, MA, **2012**; , pp 1573.
3. Ridley, N. Intraocular acrylic lenses. *Trans Ophthalmol. Soc. U. K.* **1951**, 617-621.
4. Apple, D. J.; Sims, J. Harold Ridley and the invention of the intraocular lens. *Surv. Ophthalmol.* **1996**, *40*, 279-292.
5. Metcalfe, A. D.; Ferguson, M. W. Tissue engineering of replacement skin: the crossroads of biomaterials, wound healing, embryonic development, stem cells and regeneration. *J. R. Soc. Interface* **2007**, *4*, 413-437.
6. Petrie, T. A.; Raynor, J. E.; Reyes, C. D.; Burns, K. L.; Collard, D. M.; Garcia, A. J. The effect of integrin-specific bioactive coatings on tissue healing and implant osseointegration. *Biomaterials* **2008**, *29*, 2849-2857.
7. Sarig-Nadir, O.; Livnat, N.; Zajdman, R.; Shoham, S.; Seliktar, D. Laser photoablation of guidance microchannels into hydrogels directs cell growth in three dimensions. *Biophys. J.* **2009**, *96*, 4743-4752.
8. Li, W.; Tuli, R.; Huang, X.; Laquerriere, P.; Tuan, R. Multilineage differentiation of human mesenchymal stem cells in a three-dimensional nanofibrous scaffold. *Biomaterials* **2005**, *26*, 5158-5166.
9. Eisenbarth, E. Biomaterials for tissue engineering. *Adv. Eng. Mater.* **2007**, *9*, 1051-1060.
10. Fisher, J. P.; Dean, D.; Engel, P. S.; Mikos, A. G. Photoinitiated polymerization of biomaterials. *Annu. Rev. Mater. Res.* **2001**, *31*, 171-181.
11. Lin, C.; Anseth, K. S. PEG hydrogels for the controlled release of biomolecules in regenerative medicine. *Pharm. Res.* **2009**, *26*, 631-643.
12. Ainslie, K. M.; Desai, T. A. Microfabricated implants for applications in therapeutic delivery, tissue engineering, and biosensing. *Lab Chip* **2008**, *8*, 1864-1878.
13. Pettingill, L. N.; Richardson, R. T.; Wise, A. K.; O'Leary, S. J.; Shepherd, R. K. Neurotrophic factors and neural prostheses: Potential clinical applications based upon findings in the auditory system. *IEEE Trans. Biomed. Eng.* **2007**, *54*, 1138-1148.
14. O'Leary, S. J.; Richardson, R. R.; McDermott, H. J. Principles of design and biological approaches for improving the selectivity of cochlear implant electrodes. *J. Neural Eng.* **2009**, *6*, 055002.

15. Leach, J. B.; Achyuta, A. K.; Murthy, S. K. Bridging the divide between neuroprosthetic design, tissue engineering and neurobiology. *Front. Neuroeng* **2010**, *2*, 18.
16. Glockner, P.; Jung, T.; Struck, S.; Studer, K. *Radiation Curing for Coatings and Printing Inks: Technical Basics and Applications*; Vincentz Network GmbH & Co KG: Hannover, Germany, **2008**, pp 172.
17. Lu, H.; Stansbury, J. W.; Bowman, C. N. Towards the elucidation of shrinkage stress development and relaxation in dental composites. *Dent. Mater.* **2004**, *20*, 979-986.
18. Kaur, M.; Srivastava, A. K. Photopolymerization: A review. *J. Macromol. Sci. Polym. Rev.* **2002**, *C42*, 481-512.
19. Decker, C. Kinetic study and new applications of UV radiation curing. *Macromol. Rapid Commun.* **2002**, *23*, 1067-1093.
20. Yagci, Y.; Jockusch, S.; Turro, N. J. Photoinitiated polymerization: Advances, challenges, and opportunities. *Macromolecules* **2010**, *43*, 6245-6260.
21. Decker, C. The use of UV irradiation in polymerization. *Polym. Int.* **1998**, *45*, 133-141.
22. Stansbury, J. W. Curing dental resins and composites by photopolymerization. *J. Esthet. Dent.* **2000**, *12*, 300-8.
23. Bryant, S. J.; Nuttelman, C. R.; Anseth, K. S. Cytocompatibility of UV and visible light photoinitiating systems on cultured NIH/3T3 fibroblasts in vitro. *J. Biomater. Sci. Polym. Ed.* **2000**, *11*, 439-457.
24. Masters, K. S.; Shah, D. N.; Leinwand, L. A.; Anseth, K. S. Crosslinked hyaluronan scaffolds as a biologically active carrier for valvular interstitial cells. *Biomaterials* **2005**, *26*, 2517-2525.
25. Clapper, J. D.; Pearce, M. E.; Guymon, C. A.; Salem, A. K. Biotinylated biodegradable nanotemplated hydrogel networks for cell interactive applications. *Biomacromolecules* **2008**, *9*, 1188-1194.
26. Kloxin, A. M.; Kasko, A. M.; Salinas, C. N.; Anseth, K. S. Photodegradable hydrogels for dynamic tuning of physical and chemical properties. *Science* **2009**, *324*, 59-63.
27. Kloxin, A. M.; Benton, J. A.; Anseth, K. S. In situ elasticity modulation with dynamic substrates to direct cell phenotype. *Biomaterials* **2010**, *31*, 1-8.
28. Karuri, N. W.; Porri, T. J.; Albrecht, R. M.; Murphy, C. J.; Nealey, P. F. Nano- and microscale holes modulate cell-substrate adhesion, cytoskeletal organization, and

- integrin localization in Sv40 human corneal epithelial cells. *IEEE Trans. Nanobioscience* **2006**, *5*, 273-280.
29. Teixeira, A.; McKie, G.; Foley, J.; Berticse, P.; Nealey, P.; Murphy, C. The effect of environmental factors on the response of human corneal epithelial cells to nanoscale substrate topography. *Biomaterials* **2006**, *27*, 3945-3954.
  30. Rydholm, A. E.; Held, N. L.; Benoit, D. S.; Bowman, C. N.; Anseth, K. S. Modifying network chemistry in thiol-acrylate photopolymers through postpolymerization functionalization to control cell-material interactions. *J. Biomed. Mater. Res. Part A* **2008**, *86A*, 23-30.
  31. Fisher, J. P.; Dean, D.; Engel, P. S.; Mikos, A. G. Photoinitiated polymerization of biomaterials. *Annu. Rev. Mater. Res.* **2001**, *31*, 171-181.
  32. Mahoney, M. J.; Anseth, K. S. Three-dimensional growth and function of neural tissue in degradable polyethylene glycol hydrogels. *Biomaterials* **2006**, *27*, 2265-2274.
  33. Sundararaghavan, H. G.; Monteiro, G. A.; Firestein, B. L.; Shreiber, D. I. Neurite growth in 3D collagen gels with gradients of mechanical properties. *Biotechnol. Bioeng.* **2009**, *102*, 632-643.
  34. Hale, N. A.; Yang, Y.; Rajagopalan, P. Cell migration at the interface of a dual chemical-mechanical gradient. *ACS App. Mater. Interfaces* **2010**, *8*, 2317-2324
  35. Ratner, B. D.; Bryant, S. J. Biomaterials: Where we have been and where we are going. *Annu. Rev. Biomed. Eng.* **2004**, *6*, 41-75.
  36. Lutolf, M. P.; Hubbell, J. A. Synthetic biomaterials as instructive extracellular microenvironments for morphogenesis in tissue engineering. *Nat. Biotechnol.* **2005**, *23*, 47-55.
  37. Williams, D. Definitions in Biomaterials. *Proceedings of a Consensus Conference of the European Society for Biomaterials* **1987**, *4*.
  38. Lawrence, B. D.; Cronin-Golomb, M.; Georgakoudi, I.; Kaplan, D. L.; Omenetto, F. G. Bioactive silk protein biomaterial systems for optical devices. *Biomacromolecules* **2008**, *9*, 1214-1220.
  39. Yan, H.; Xiaoying, L.; Jingwu, M.; Nan, H. In vitro investigation of protein adsorption and platelet adhesion on inorganic biomaterial surfaces. *Appl. Surf. Sci.* **2008**, *255*, 257-259.
  40. Fu, R.; Wang, Y.; Liu, S.; Shih, T.; Lin, H.; Chen, Y.; Sung, J.; Lu, C.; Wei, J.; Wang, Z.; Huang, S.; Tsai, C.; Shyu, W.; Lin, S. Decellularization and recellularization technologies in tissue engineering. *Cell Transplant.* **2014**, *23*, 621-630.

41. Totonelli, G.; Maghsoudlou, P.; Fishman, J. M.; Orlando, G.; Ansari, T.; Sibbons, P.; Birchall, M. A.; Pierro, A.; Eaton, S.; De Coppi, P. Esophageal tissue engineering: A new approach for esophageal replacement. *World J. Gastroenterol.* **2012**, *18*, 6900-6907.
42. Bobbio, A. The first endosseous alloplastic implant in the history of man. *Bull. Hist. Dent.* **1972**, *20*, 1-6.
43. Crubezy, E.; Murail, P.; Girard, L.; Bernadou, J. P. False teeth of the Roman world. *Nature* **1998**, *391*, 29-29.
44. Kolff, W. J. The artificial kidney and its effect on the development of other artificial organs. *Nat. Med.* **2002**, *8*, 1063-1065.
45. Akutsu, T.; Dreyer, B.; Kolff, W. J. Polyurethane artificial heart valves in animals. *J. Appl. Physiol.* **1959**, *14*, 1045-1048.
46. Kolff, W. J. Early years of artificial organs at the Cleveland Clinic - Part II: Open heart surgery and artificial hearts. *Asaio J.* **1998**, *44*, 123-128.
47. Edgahl, R. H.; Hume, D. M.; Schlang, H. A. Plastic venous prostheses. *Surg. Forum* **1955**, *5*, 235-41.
48. Palmaz, J. C.; Sibbitt, R. R.; Reuter, S. R.; Garcia, F.; Tio, F. O. Expandable intrahepatic portacaval-shunt stents - early experience in the dog. *Am. J. Roentgenol.* **1985**, *145*, 821-825.
49. Gross, U.; Kinne, R.; Schmitz, H. J.; Strunz, V. The response of bone to surface-active glasses. *Crc Critical Rev. Biocompat.* **1988**, *4*, 155-179.
50. Hench, L. L. Bioceramics - from Concept to Clinic. *J. Am. Ceram. Soc.* **1991**, *74*, 1487-1510.
51. Hench, L. L.; Splinter, R. J.; Allen, W. C.; Greenlee, T. K. Bonding mechanisms at the interface of ceramic prosthetic materials. *J. Biomed. Mater. Res.* **1971**, *5*, 117-141.
52. Virmani, R.; Farb, A. Pathology of in-stent restenosis. *Curr. Opin. Lipidol.* **1999**, *10*, 499-506.
53. Nakazawa, G.; Vorpahl, M.; Finn, A. V.; Narula, J.; Virmani, R. One step forward and two steps back with drug-eluting-stents from preventing restenosis to causing late thrombosis and nouveau atherosclerosis. *JACC Cardiovasc. Imaging* **2009**, *2*, 625-628.
54. Daemen, J.; Serruys, P. W. Drug-eluting stent update 2007 part I: A survey of current and future generation drug-eluting stents: Meaningful advances or more of the same? *Circulation* **2007**, *116*, 316-328.

55. Daemen, J.; Serruys, P. W. Drug-eluting stent update 2007 - Part II: Unsettled issues. *Circulation* **2007**, *116*, 961-968.
56. Moses, J. W.; Leon, M. B.; Popma, J. J.; Fitzgerald, P. J.; Holmes, D. R.; O'Shaughnessy, C.; Caputo, R. P.; Kereiakes, D. J.; Williams, D. O.; Teirstein, P. S.; Jaeger, J. L. SIRIUS Investigators Sirolimus-eluting stents versus standard stents in patients with stenosis in a native coronary artery. *N. Engl. J. Med.* **2003**, *349*, 1315-1323.
57. Sousa, J. E.; Serruys, P. W.; Costa, M. A. New frontiers in cardiology - Drug-eluting stents: Part I. *Circulation* **2003**, *107*, 2274-2279.
58. Sousa, J. E.; Serruys, P. W.; Costa, M. A. New frontiers in cardiology - Drug-eluting stents: Part II. *Circulation* **2003**, *107*, 2383-2389.
59. Ong, A. T.; Serruys, P. W. Technology insight: an overview of research in drug-eluting stents. *Nat. Clin. Pract. Cardiovasc. Med.* **2005**, *2*, 647-658.
60. Bryers, J. D.; Giachelli, C. M.; Ratner, B. D. Engineering biomaterials to integrate and heal: The biocompatibility paradigm shifts. *Biotechnol. Bioeng.* **2012**, *109*, 1898-1911.
61. Wilson, C. J.; Clegg, R. E.; Leavesley, D. I.; Pearcy, M. J. Mediation of biomaterial-cell interactions by adsorbed proteins: A review. *Tissue Eng.* **2005**, *11*, 1-18.
62. Hu, W. J.; Eaton, J. W.; Tang, L. P. Molecular basis of biomaterial-mediated foreign body reactions. *Blood* **2001**, *98*, 1231-1238.
63. Tang, L. P.; Eaton, J. W. Fibrin(ogen) mediates acute inflammatory responses to biomaterials. *J. Exp. Med.* **1993**, *178*, 2147-2156.
64. Knop, K.; Hoogenboom, R.; Fischer, D.; Schubert, U. S. Poly(ethylene glycol) in drug delivery: Pros and cons as well as potential alternatives. *Angew. Chem. Int. Ed. Engl.* **2010**, *49*, 6288-6308.
65. Drury, J. L.; Mooney, D. J. Hydrogels for tissue engineering: Scaffold design variables and applications. *Biomaterials* **2003**, *24*, 4337-4351.
66. Zhu, J. Bioactive modification of poly(ethylene glycol) hydrogels for tissue engineering. *Biomaterials* **2010**, *31*, 4639-4656.
67. Lewis, K. J.; Anseth, K. S. Hydrogel scaffolds to study cell biology in four dimensions. *MRS Bull* **2013**, *38*, 260-268.
68. Lutolf, M. P.; Hubbell, J. A. Synthetic biomaterials as instructive extracellular microenvironments for morphogenesis in tissue engineering. *Nat. Biotechnol.* **2005**, *23*, 47-55.

69. Langer, R.; Vacanti, J. P. Tissue engineering. *Science* **1993**, *260*, 920-926.
70. Griffith, L. G.; Naughton, G. Tissue engineering - Current challenges and expanding opportunities. *Science* **2002**, *295*, 1009-+.
71. Lee, K. Y.; Mooney, D. J. Hydrogels for tissue engineering. *Chem. Rev.* **2001**, *101*, 1869-1879.
72. Hench, L. L.; Polak, J. M. Third-generation biomedical materials. *Science* **2002**, *295*, 1014.
73. Vallet-Regi, M.; Balas, F.; Arcos, D. Mesoporous materials for drug delivery. *Angew. Chem. Int. Ed.* **2007**, *46*, 7548-7558.
74. Hoffman, A. S. The origins and evolution of "controlled" drug delivery systems. *J. Controlled Release* **2008**, *132*, 153-163.
75. Folkman, J.; Long, D. M. The use of silicone rubber as a carrier for prolonged drug therapy. *J. Surg. Res.* **1964**, *4*, 139-42.
76. Lawson, H. C.; Sampath, P.; Bohan, E.; Park, M. C.; Hussain, N.; Olivi, A.; Weingart, J.; Kleinberg, L.; Brem, H. Interstitial chemotherapy for malignant gliomas: the Johns Hopkins experience. *J. Neurooncol.* **2007**, *83*, 61-70.
77. Chou, L.; Firth, J.; Uitto, V.; Brunette, D. Substratum surface topography alters cell shape and regulates fibronectin mRNA level, mRNA stability, secretion and assembly in human fibroblasts. *J. Cell. Sci.* **1995**, *108*, 1563-1573.
78. Dalby, M. J.; Biggs, M. J.; Gadegaard, N.; Kalna, G.; Wilkinson, C. D.; Curtis, A. S. G. Nanotopographical stimulation of mechanotransduction and changes in interphase centromere positioning. *J. Cell. Biochem.* **2007**, *100*, 326-338.
79. Dalby, M. J.; Gadegaard, N.; Riehle, M. O.; Wilkinson, C. D.; Curtis, A. S. Investigating filopodia sensing using arrays of defined nano-pits down to 35 nm diameter in size. *Int. J. Biochem. Cell Biol.* **2004**, *36*, 2005-2015.
80. Clark, P.; Connolly, P.; Curtis, A. S.; Dow, J. A.; Wilkinson, C. D. Topographical control of cell behavior 1. Simple step cues. *Development* **1987**, *99*, 439-448.
81. Clark, P.; Connolly, P.; Curtis, A. S.; Dow, J. A.; Wilkinson, C. D. Topographical control of cell behavior 2. Multiple grooved substrata. *Development* **1990**, *108*, 635-644.
82. Karuri, N. W.; Liliensiek, S.; Teixeira, A. I.; Abrams, G.; Campbell, S.; Nealey, P. F.; Murphy, C. J. Biological length scale topography enhances cell-substratum adhesion of human corneal epithelial cells. *J. Cell. Sci.* **2004**, *117*, 3153-3164.

83. Hsu, S.; Lu, P. S.; Ni, H.; Su, C. Fabrication and evaluation of microgrooved polymers as peripheral nerve conduits. *Biomed. Microdevices* **2007**, *9*, 665-674.
84. Teixeira, A. I.; Abrams, G. A.; Bertics, P. J.; Murphy, C. J.; Nealey, P. F. Epithelial contact guidance on well-defined micro- and nanostructured substrates. *J. Cell. Sci.* **2003**, *116*, 1881-1892.
85. Miller, C.; Jeftinija, S.; Mallapragada, S. Synergistic effects of physical and chemical guidance cues on neurite alignment and outgrowth on biodegradable polymer substrates. *Tissue Eng.* **2002**, *8*, 367-378.
86. Song, M.; Uhrich, K. E. Optimal micropattern dimensions enhance neurite outgrowth rates, lengths, and orientations. *Ann. Biomed. Eng.* **2007**, *35*, 1812-1820.
87. Rajnicek, A. M.; Britland, S.; McCaig, C. D. Contact guidance of CNS neurites on grooved quartz: influence of groove dimensions, neuronal age and cell type. *J. Cell. Sci.* **1997**, *110*, 2905-2913.
88. Discher, D. E.; Janmey, P.; Wang, Y. Tissue cells feel and respond to the stiffness of their substrate. *Science* **2005**, *310*, 1139-1143.
89. Wang, Y.; Chen, C. S. Cell adhesion and mechanical stimulation in the regulation of mesenchymal stem cell differentiation. *J. Cell. Mol. Med.* **2013**, *17*, 823-832.
90. Lo, C. M.; Wang, H. B.; Dembo, M.; Wang, Y. L. Cell movement is guided by the rigidity of the substrate. *Biophys. J.* **2000**, *79*, 144-152.
91. Engler, A. J.; Griffin, M. A.; Sen, S.; Bonnetmann, C. G.; Sweeney, H. L.; Discher, D. E. Myotubes differentiate optimally on substrates with tissue-like stiffness: pathological implications for soft or stiff microenvironments. *J. Cell Biol.* **2004**, *166*, 877-887.
92. Brown, X. Q.; Ookawa, K.; Wong, J. Y. Evaluation of polydimethylsiloxane scaffolds with physiologically-relevant elastic moduli: Interplay of substrate mechanics and surface chemistry effects on vascular smooth muscle cell response. *Biomaterials* **2005**, *26*, 3123-3129.
93. Kong, H. J.; Polte, T. R.; Alsberg, E.; Mooney, D. J. FRET measurements of cell-contraction forces and nano-scale clustering of adhesion ligands varied by substrate stiffness. *Proc. Natl. Acad. Sci. U. S. A.* **2005**, *102*, 4300-4305.
94. Balgude, A. P.; Yu, X.; Szymanski, A.; Bellamkonda, R. V. Agarose gel stiffness determines rate of DRG neurite extension in 3D cultures. *Biomaterials* **2001**, *22*, 1077-1084.
95. Leach, J. B.; Brown, X. Q.; Jacot, J. G.; DiMilla, P. A.; Wong, J. Y. Neurite outgrowth and branching of PC12 cells on very soft substrates sharply decreases below a threshold of substrate rigidity. *J. Neural Eng.* **2007**, *4*, 26-34.

96. Flanagan, L.; Ju, Y.; Marg, B.; Osterfield, M.; Janmey, P. Neurite branching on deformable substrates. *Neuroreport* **2002**, *13*, 2411-2415.
97. Bryant, S. J.; Chowdhury, T. T.; Lee, D. A.; Bader, D. L.; Anseth, K. S. Crosslinking density influences chondrocyte metabolism in dynamically loaded photocrosslinked poly(ethylene glycol) hydrogels. *Ann. Biomed. Eng.* **2004**, *32*, 407-417.
98. Peckham, P. H.; Knutson, J. S. Functional electrical stimulation for neuromuscular applications. *Annu. Rev. Biomed. Eng.* **2005**, *7*, 327-360.
99. Chow, A. Y.; Chow, V. Y.; Packo, K. H.; Pollack, J. S.; Peyman, G. A.; Schuchard, R. The artificial silicon retina microchip for the treatment of vision loss from retinitis pigmentosa. *Arch. Ophthalmol.* **2004**, *122*, 460-469.
100. Brazzelli, M.; Murray, A.; Fraser, C. Efficacy and safety of sacral nerve stimulation for urinary urge incontinence: A systematic review. *J. Urol.* **2006**, *175*, 835-841.
101. Peckham, P. H.; Keith, M. W.; Kilgore, K. L.; Grill, J. H.; Wuolle, K. S.; Thrope, G. B.; Gorman, P.; Hobby, J.; Mulcahey, M. J.; Carroll, S.; Hentz, V. R.; Wiegner, A.; Implantable neuroprosthesis Res Grp efficacy of an implanted neuroprosthesis for restoring hand grasp in tetraplegia: A multicenter study. *Arch. Phys. Med. Rehabil.* **2001**, *82*, 1380-1388.
102. Winter, J. O.; Cogan, S. F.; Rizzo, J. F. Retinal prostheses: current challenges and future outlook. *J. Biomater. Sci. Polym. Ed.* **2007**, *18*, 1031-1055.
103. Shintani, K.; Shechtman, D. L.; Gurwood, A. S. Review and update: Current treatment trends for patients with retinitis pigmentosa. *J. Am. Optom. Assoc.* **2009**, *80*, 384-401.
104. Augustin, A. J.; Kirchhof, J. Inflammation and the pathogenesis of age-related macular degeneration. *Expert Opin. Ther. Targets* **2009**, *13*, 641-651.
105. Rizzo, J. F.; Wyatt, J.; Humayun, M.; de Juan, E.; Liu, W. T.; Chow, A.; Eckmiller, R.; Zrenner, E.; Yagi, T.; Abrams, G. Retinal prosthesis - An encouraging first decade with major challenges ahead. *Ophthalmol.* **2001**, *108*, 13-14.
106. Asher, A.; Segal, W. A.; Baccus, S. A.; Yaroslavsky, L. P.; Palanker, D. V. Image processing for a high-resolution optoelectronic retinal prosthesis. *IEEE Trans. Biomed. Eng.* **2007**, *54*, 993-1004.
107. Chader, G. J.; Weiland, J.; Humayun, M. S. Artificial vision: needs, functioning, and testing of a retinal electronic prosthesis. *Neurother.: Prog. Restor. Neurosci. Neurol.* **2009**, *175*, 317-332.
108. Bertschinger, D. R.; Beknazar, E.; Simonutti, M.; Safran, A. B.; Sahel, J. A.; Rosolen, S. G.; Picaud, S.; Salzmann, J. A review of in vivo animal studies in retinal prosthesis research. *Graefes Arch. Clin. Exp. Ophthalmol.* **2008**, *246*, 1505-1517.

109. Bron, A.; Tripathi, R.; Tripathi, B. *Wolff's Anatomy of the Eye and Orbit*; London, UK, **2001**, 225-455.
110. Humayun, M. S.; Prince, M.; de Juan, E.; Barron, Y.; Moskowitz, M.; Klock, I. B.; Milam, A. H. Morphometric analysis of the extramacular retina from postmortem eyes with retinitis pigmentosa. *Invest. Ophthalmol. Vis. Sci.* **1999**, *40*, 143-148.
111. Caspi, A.; Dorn, J. D.; McClure, K. H.; Humayun, M. S.; Greenberg, R. J.; McMahon, M. J. Feasibility Study of a Retinal Prosthesis. *Arch. Ophthalmol.* **2009**, *127*, 398-401.
112. Roessler, G.; Laube, T.; Brockmann, C.; Kirschkamp, T.; Mazinani, B.; Goertz, M.; Koch, C.; Krisch, I.; Sellhaus, B.; Trieu, H. K.; Weis, J.; Bornfeld, N.; Roethgen, H.; Messner, A.; Mokwa, W.; Walter, P. Implantation and Explantation of a Wireless Epiretinal Retina Implant Device: Observations during the EPIRET3 Prospective Clinical Trial. *Invest. Ophthalmol. Vis. Sci.* **2009**, *50*, 3003-3008.
113. Stett, A.; Mai, A.; Herrmann, T. Retinal charge sensitivity and spatial discrimination obtainable by subretinal implants: key lessons learned from isolated chicken retina. *J. Neural Eng.* **2007**, *4*, S7-S16.
114. Besch, D.; Sachs, H.; Szurman, P.; Guelicher, D.; Wilke, R.; Reinert, S.; Zrenner, E.; Bartz-Schmidt, K. U.; Gekeler, F. Extraocular surgery for implantation of an active subretinal visual prosthesis with external connections: feasibility and outcome in seven patients. *Br. J. Ophthalmol.* **2008**, *92*, 1361-1368.
115. Palanker, D.; Vankov, A.; Huie, P.; Baccus, S. Design of a high-resolution optoelectronic retinal prosthesis. *J. Neural Eng.* **2005**, *2*, S105-20.
116. Peyman, G.; Chow, A. Y.; Liang, C. P.; Chow, V. Y.; Perlman, J. I.; Peachey, N. S. Subretinal semiconductor microphotodiode array. *Ophthalmic Surg. Lasers* **1998**, *29*, 234-241.
117. Peterman, M.; Mehenti, N.; Bilbao, K.; Lee, C.; Leng, T.; Noolandi, J.; Bent, S.; Blumenkranz, M.; Fishman, H. The artificial synapse chip: A flexible retinal interface based on directed retinal cell growth and neurotransmitter stimulation. *Artif. Organs* **2003**, *27*, 975-985.
118. Chowdhury, V.; Morley, J. W.; Coroneo, M. T. Evaluation of extralocular electrodes for a retinal prosthesis using evoked potentials in cat visual cortex. *J. Clin. Neurosci.* **2005**, *12*, 574-579.
119. Sakaguchi, H.; Fujikado, T.; Fang, X. Y.; Kanda, H.; Osanai, M.; Nakauchi, K.; Ikuno, Y.; Kamei, M.; Yagi, T.; Nishimura, S.; Ohji, M.; Yagi, T.; Tano, Y. Transretinal electrical stimulation with a suprachoroidal multichannel electrode in rabbit eyes. *Jpn. J. Ophthalmol.* **2004**, *48*, 256-261.

120. Shandurina, A. N.; Panin, A. V.; Sologubova, E. K.; Kolotov, A. V.; Goncharenko, O. I.; Nikol'skii, A. V.; Logunov V. Results of the use of therapeutic periorbital electrostimulation in neurological patients with partial atrophy of the optic nerves. *Neurosci. Behav. Physiol.* **1996**, *26*, 137-42.
121. Worthington, K. S.; Wiley, L. A.; Bartlett, A. M.; Stone, E. M.; Mullins, R. F.; Salem, A. K.; Guymon, C. A.; Tucker, B. A. Mechanical properties of murine and porcine ocular tissues in compression. *Exp. Eye Res.* **2014**, *121*, 194-199.
122. Chen, K.; Rowley, A. P.; Weiland, J. D. Elastic properties of porcine ocular posterior soft tissues. *J. Biomed. Mater. Res. Part A* **2010**, *93A*, 634-645.
123. Ameri, H.; Ratanapakorn, T.; Ufer, S.; Eekhardt, H.; Humayun, M. S.; Weiland, J. D. Toward a wide-field retinal prosthesis. *J. Neural Eng.* **2009**, *6*, 035002.
124. Kazemi, M.; Basham, E.; Sivaprakasam, M.; Wang, G.; Rodger, D.; Weiland, J.; Tai, Y. C.; Liu, W.; Humayun, M. A test microchip for evaluation of hermetic packaging technology for biomedical prosthetic implants. *IEEE Eng. Med. Biol. Soc. Conf.* **2004**, *6*, 4093-5.
125. Montezuma, S. R.; Loewenstein, J.; Scholz, C.; Rizzo, J. F.,III Biocompatibility of materials implanted into the subretinal space of Yucatan pigs. *Invest. Ophthalmol. Vis. Sci.* **2006**, *47*, 3514-3522.
126. Greenberg, R. Analysis of electrical stimulation of the vertebrate retina - work towards a retinal prosthesis, The Johns Hopkins University, Baltimore, MD, **1998**.
127. Simmons, F. B. Electrical Stimulation of Auditory Nerve in Man. *Arch. Otolaryngol.* **1966**, *84*, 2-&.
128. Stevens, S. S.; Jones, R. C. The mechanism of hearing by electrical stimulation. *J. Acoust. Soc. Am.* **1939**, *10*, 261-269.
129. Stevens, S. S. On hearing by electrical stimulation. *J. Acoust. Soc. Am.* **1937**, *8*, 191-195.
130. Jones, R. C.; Stevens, S. S.; Lurie, M. H. Three mechanisms of hearing by electrical stimulation. *J. Acoust. Soc. Am.* **1940**, *12*, 281-290.
131. Gersuni, G. V.; Volokhov, A. A. On the electrical excitability of the auditory organ on the effect of alternating currents on the normal auditory apparatus. *J. Exp. Psychol.* **1936**, *19*, 370-382.
132. House, W. F.; Urban, J. Long-Term Results of Electrode Implantation and Electronic Stimulation of Cochlea in Man. *Ann. Otol. Rhinol. Laryngol.* **1973**, *82*, 504-517.

133. Simmons, F. B.; Epley, J. M.; Lummis, R. C.; Guttman, N.; Frishkop.Ls; Harmon, L. D.; Zwicker, E. Auditory Nerve - Electrical Stimulation in Man. *Science* **1965**, *148*, 104-&.
134. White, R. L. Review of Current Status of Cochlear Prostheses. *IEEE Trans. Biomed. Eng.* **1982**, *29*, 233-238.
135. Michelso.Rp Electrical Stimulation of Human Cochlea - Preliminary Report. *Arch. Otolaryngol.* **1971**, *93*, 317-&.
136. Geisler, C. *From Sound to Synapse: Physiology of the Mammalian Ear*; Oxford University Press: New York, NY, **1998**.
137. Dallos, P.; Popper, A.; Fay, R. *The Cochlea*; Springer Handbook of Auditory Research; Springer: New York, NY, **1996**, *8*, 551.
138. Promenade 'Round the Cochlea - Cross Section of Single Turn of the Cochlea. <http://www.neuroreille.com/promenade/english/cochlea/fcochlea.htm> (accessed July 3, 2014).
139. Popper, A.; Fay, R. *The Mammalian Auditory Pathway: Neurophysiology*; Springer-Verlag: New York, NY, **1991**.
140. Pettingill, L. N.; Richardson, R. T.; Wise, A. K.; O'Leary, S. J.; Shepherd, R. K. Neurotrophic factors and neural prostheses: Potential clinical applications based upon findings in the auditory system. *IEEE Trans. Biomed. Eng.* **2007**, *54*, 1138-1148.
141. Snik, A. F. M.; Mylanus, E. A. M.; Cremers, C. W. R. J. The bone-anchored hearing aid - A solution for previously unresolved otologic problems. *Otolaryngol. Clin. North Am.* **2001**, *34*, 365-+.
142. Tjellstrom, A.; Hakansson, B.; Granstrom, G. Bone-anchored hearing aids - Current status in adults and children. *Otolaryngol. Clin. North Am.* **2001**, *34*, 337-+.
143. Wikipedia - Cochlear Implant. [http://en.wikipedia.org/wiki/Cochlear\\_implant](http://en.wikipedia.org/wiki/Cochlear_implant) (accessed July 3, 2014).
144. Bhatia, K.; Gibbin, K. P.; Nikolopoulos, T. P.; O'Donoghue, G. M. Surgical complications and their management in a series of 300 consecutive pediatric cochlear implantations. *Otol. Neurotol.* **2004**, *25*, 730-739.
145. Cunningham, C. D.; Slattery, W. H.; Luxford, W. M. Postoperative infection in cochlear implant patients. *Otolaryngol. Head Neck Surg.* **2004**, *131*, 109-114.
146. Loeb, G. The Functional Replacement of the Ear. *Sci. Am.* **1985**, *252*, 104.

147. McDermott, H. J. Music perception with cochlear implants: a review. *Trends Amplif.* **2004**, *8*, 49-82.
148. Loizou, P. C. Introduction to cochlear implants. *IEEE Eng. Med. Biol. Mag.* **1999**, *18*, 32-42.
149. Zeng, F.; Rebscher, S.; Harrison, W.; Sun, X.; Feng, H. Cochlear implants: system design, integration, and evaluation. *IEEE Rev. Biomed. Eng.* **2008**, *1*, 115-42.
150. Patrick, J. F.; Busby, P. A.; Gibson, P. J. The development of the Nucleus Freedom Cochlear implant system. *Trends Amplif.* **2006**, *10*, 175-200.
151. Rubinstein, J. T. How cochlear implants encode speech. *Curr. Opin. Otolaryngol. Head Neck Surg.* **2004**, *12*, 444-8.
152. Alam, S. A.; Robinson, B. K.; Huang, J.; Green, S. H. Prosurvival and proapoptotic intracellular signaling in rat spiral ganglion neurons in vivo after the loss of hair cells. *J. Comp. Neurol.* **2007**, *503*, 832-852.
153. Pfungst, B. E.; Bowling, S. A.; Colesa, D. J.; Garadat, S. N.; Raphael, Y.; Shibata, S. B.; Strahl, S. B.; Su, G. L.; Zhou, N. Cochlear infrastructure for electrical hearing. *Hear. Res.* **2011**, *281*, 65-73.
154. Sly, D. J.; Heffer, L. F.; White, M. W.; Shepherd, R. K.; Birch, M. G.; Minter, R. L.; Nelson, N. E.; Wise, A. K.; O'Leary, S. J. Deafness alters auditory nerve fibre responses to cochlear implant stimulation. *Eur. J. Neurosci.* **2007**, *26*, 510-522.
155. Shepherd, R. K.; Roberts, L. A.; Paolini, A. G. Long-term sensorineural hearing loss induces functional changes in the rat auditory nerve. *Eur. J. Neurosci.* **2004**, *20*, 3131-3140.
156. Dorman, M. F.; Loizou, P. C.; Fitzke, J.; Tu, Z. M. The recognition of sentences in noise by normal-hearing listeners using simulations of cochlear-implant signal processors with 6-20 channels. *J. Acoust. Soc. Am.* **1998**, *104*, 3583-3585.
157. Wilson, B. S.; Dorman, M. F. Cochlear implants: A remarkable past and a brilliant future. *Hear. Res.* **2008**, *242*, 3-21.
158. Black, R. C.; Clark, G. M.; Patrick, J. F. Current distribution measurements within the human cochlea. *IEEE Trans. Biomed. Eng.* **1981**, *28*, 721-725.
159. Black, R. C.; Clark, G. M.; Tong, Y. C.; Patrick, J. F. Current distributions in cochlear stimulation. *Ann. N. Y. Acad. Sci.* **1983**, *405*, 137-145.
160. Richter, B.; Aschendorff, A.; Lohnstein, P.; Husstedt, H.; Nagursky, H.; Laszig, R. The Nucleus Contour electrode array: A radiological and histological study. *Laryngoscope* **2001**, *111*, 508-514.

161. Zwolan, T.; Kileny, P.; Smith, S.; Mills, D.; Koch, D.; Osberger, M. Adult cochlear implant patient performance with evolving electrode technology. *Otol. Neurotol.* **2001**, *22*, 844-849.
162. Tykocinski, M.; Cohen, L. T.; Pyman, B. C.; Roland, T.; Treaba, C.; Palamara, J.; Dahm, M. C.; Shepherd, R. K.; Xu, J.; Cowan, R. S.; Cohen, N. L.; Clark, G. M. Comparison of electrode position in the human cochlea using various perimodiolar electrode arrays. *Am. J. Otol.* **2000**, *21*, 205-211.
163. Frijns, J.; Briaire, J.; Grote, J. The importance of human cochlear anatomy for the results of modiolus-hugging multichannel cochlear implants. *Otol. Neurotol.* **2001**, *22*, 340-349.
164. Cohen, L.; Saunders, E.; Knight, M.; Cowan, R. Psychophysical measures in patients fitted with Contour (TM) and straight Nucleus electrode arrays. *Hear. Res.* **2006**, *212*, 160-175.
165. Fitzgerald, M. B.; Shapiro, W. H.; McDonald, P. D.; Neuburger, H. S.; Ashburn-Reed, S.; Immerman, S.; Jethanamest, D.; Roland, J. T.; Svirsky, M. A. The effect of perimodiolar placement on speech perception and frequency discrimination by cochlear implant users. *Acta Otolaryngol.* **2007**, *127*, 378-383.
166. Snyder, R. L.; Middlebrooks, J. C.; Bonham, B. H. Cochlear implant electrode configuration effects on activation threshold and tonotopic selectivity. *Hear. Res.* **2008**, *235*, 23-38.
167. Firszt, J. B.; Koch, D. B.; Downing, M.; Litvak, L. Current steering creates additional pitch percepts in adult cochlear implant recipients. *Otol. Neurotol.* **2007**, *28*, 629-636.
168. McDermott, H.; McKay, C.; Vandali, A. A new portable sound processor for the University-of-Melbourne Nucleus limited multielectrode cochlear implant. *J. Acoust. Soc. Am.* **1992**, *91*, 3367-3371.
169. Frijns, J. H.; Kalkman, R. K.; Vanpoucke, F. J.; Bongers, J. S.; Briaire, J. J. Simultaneous and non-simultaneous dual electrode stimulation in cochlear implants: evidence for two neural response modalities. *Acta Otolaryngol.* **2009**, *129*, 433-439.
170. van der Beek, F. B.; Boermans, P. P.; Verbist, B. M.; Briaire, J. J.; Frijns, J. H. Clinical evaluation of the clarion CII HiFocus 1 with and without positioner. *Ear Hear.* **2005**, *26*, 577-592.
171. Snyder, R. L.; Middlebrooks, J. C.; Bonham, B. H. Cochlear implant electrode configuration effects on activation threshold and tonotopic selectivity. *Hear. Res.* **2008**, *235*, 23-38.
172. Tykocinski, M.; Cohen, L.; Pyman, B.; Roland, T.; Treaba, C.; Palamara, J.; Dahm, M.; Shepherd, R.; Xu, J.; Cowan, R.; Cohen, N.; Clark, G. Comparison of electrode

- position in the human cochlea using various perimodiolar electrode arrays. *Am. J. Otol.* **2000**, *21*, 205-211.
173. Shibata, S. B.; Budenz, C. L.; Bowling, S. A.; Pflugst, B. E.; Raphael, Y. Nerve maintenance and regeneration in the damaged cochlea. *Hear. Res.* **2011**, *281*, 56-64.
174. Roehm, P. C.; Hansen, M. R. Strategies to preserve or regenerate spiral ganglion neurons. *Curr. Opin. Otolaryngol. Head Neck Surg.* **2005**, *13*, 294-300.
175. Richardson, R. T.; Noushi, F.; O'Leary, S. Inner ear therapy for neural preservation. *Audiol. Neurootol.* **2006**, *11*, 343-356.
176. Whilton, D. S.; Tieu, D.; Grover, M.; Reilly, B.; Coulson, M. T. Spontaneous association of glial cells with regrowing neurites in mixed cultures of dissociated spiral ganglia. *Neurosci* **2009**, *161*, 227-235.
177. Ylikoski, J.; Pirvola, U.; Moshnyakov, M.; Palgi, J.; Arumäe, U.; Saarna, M. Expression patterns of neurotrophin and their receptor mRNAs in the rat inner ear. *Hear. Res.* **1993**, *65*, 69-78.
178. Nadol, J.; Young, Y.; Glynn, R. Survival of spiral ganglion-cells in profound sensorineural hearing-loss - Implications for cochlear implantation. *Ann. Otol. Rhinol. Laryngol.* **1989**, *98*, 411-416.
179. Miller, J.; Chi, D.; O'Keefe, L.; Kruszka, P.; Raphael, Y.; Altschuler, R. Neurotrophins can enhance spiral ganglion cell survival after inner hair cell loss. *Int. J. Dev. Neurosci.* **1997**, *15*, 631-643.
180. Staecker, H.; Kopke, R.; Malgrange, B.; Lefebvre, P.; VandeWater, T. NT-3 and/or BDNF therapy prevents loss of auditory neurons following loss of hair cells. *Neuroreport* **1996**, *7*, 889-894.
181. Wise, A. K.; Richardson, R.; Hardman, J.; Clark, G.; O'Leary, S. Resprouting and survival of guinea pig cochlear neurons in response to the administration of the neurotrophins brain-derived neurotrophic factor and neurotrophin-3. *J. Comp. Neurol.* **2005**, *487*, 147-165.
182. Glueckert, R.; Bitsche, M.; Miller, J. M.; Zhu, Y.; Prieskorn, D. M.; Altschuler, R. A.; Schrott-Fischer, A. Deafferentation-associated changes in afferent and efferent processes in the guinea pig cochlea and afferent regeneration with chronic intrascalar brain-derived neurotrophic factor and acidic fibroblast growth factor. *J. Comp. Neurol.* **2008**, *507*, 1602-1621.
183. Altschuler, R. A.; Cho, Y.; Ylikoski, J.; Pirvola, U.; Magal, E.; Miller, J. M. Rescue and regrowth of sensory nerves following deafferentation by neurotrophic factors. *Ann. NY. Acad. Sci.* **1999**, *884*, 305-311.

184. Wise, A.; Hume, C.; Flynn, B.; Jeelall, Y.; Suhr, C.; Sgro, B.; O'Leary, S.; Shepherd, R.; Richardson, R. Effects of Localized Neurotrophin Gene Expression on Spiral Ganglion Neuron Resprouting in the Deafened Cochlea. *Mol. Ther.* **2010**.
185. Xiao, Y.; Friis, E. A.; Gehrke, S. H.; Detamore, M. S. Mechanical Testing of Hydrogels in Cartilage Tissue Engineering: Beyond the Compressive Modulus. *Tissue Eng. Part B Rev.* **2013**, *19*, 403-412.
186. Kenny, S. M.; Buggy, M. Bone cements and fillers: A review. *J. Mater. Sci. Mater. Med.* **2003**, *14*, 923-938.
187. Lim, J. Y.; Donahue, H. J. Cell sensing and response to micro- and nanostructured surfaces produced by chemical and topographic patterning. *Tissue Eng.* **2007**, *13*, 1879-1891.
188. Falconnet, D.; Csucs, G.; Michelle Grandin, H.; Textor, M. Surface engineering approaches to micropattern surfaces for cell-based assays. *Biomaterials* **2006**, *27*, 3044-3063.
189. Singhvi, R.; Kumar, A.; Lopez, G. P.; Stephanopoulos, G. N.; Wang, D. I.; Whitesides, G. M.; Ingber, D. E. Engineering cell-shape and function. *Science* **1994**, *264*, 696-698.
190. Mayer, M.; Yang, J.; Gitlin, I.; Gracias, D. H.; Whitesides, G. M. Micropatterned agarose gels for stamping arrays of proteins and gradients of proteins. *Proteomics* **2004**, *4*, 2366-2376.
191. Schmid, H.; Michel, B. Siloxane polymers for high-resolution, high-accuracy soft lithography. *Macromolecules* **2000**, *33*, 3042-3049.
192. Csucs, G.; Kunzler, T.; Feldman, K.; Robin, F.; Spencer, N. D. Microcontact printing of macromolecules with submicrometer resolution by means of polyolefin stamps. *Langmuir* **2003**, *19*, 6104-6109.
193. Bernard, A.; Fitzli, D.; Sonderegger, P.; Delamarche, E.; Michel, B.; Bosshard, H. R.; Biebuyck, H. Affinity capture of proteins from solution and their dissociation by contact printing. *Nat. Biotechnol.* **2001**, *19*, 866-869.
194. Humphries, J. D.; Byron, A.; Humphries, M. J. Integrin ligands at a glance. *J. Cell. Sci.* **2006**, *119*, 3901-3903.
195. Kam, L.; Boxer, S. G. Cell adhesion to protein-micropatterned-supported lipid bilayer membranes. *J. Biomed. Mater. Res.* **2001**, *55*, 487-495.
196. Csucs, G.; Michel, R.; Lussi, J. W.; Textor, M.; Danuser, G. Microcontact printing of novel co-polymers in combination with proteins for cell-biological applications. *Biomaterials* **2003**, *24*, 1713-1720.

197. St John, P.; Davis, R.; Cady, N.; Czajka, J.; Batt, C.; Craighead, H. Diffraction-based cell detection using a microcontact printed antibody grating. *Anal. Chem.* **1998**, *70*, 1108-1111.
198. Lauer, L.; Klein, C.; Offenhausser, A. Spot compliant neuronal networks by structure optimized micro-contact printing. *Biomaterials* **2001**, *22*, 1925-1932.
199. Klein, C. L.; Scholl, M.; Maelicke, A. Neuronal networks in vitro: formation and organization on biofunctionalized surfaces. *J. Mater. Sci. Mater. Med.* **1999**, *10*, 721-727.
200. Kam, L.; Shain, W.; Turner, J.; Bizios, R. Axonal outgrowth of hippocampal neurons on micro-scale networks of polylysine-conjugated laminin. *Biomaterials* **2001**, *22*, 1049-1054.
201. Delamarche, E.; Bernard, A.; Schmid, H.; Bietsch, A.; Michel, B.; Biebuyck, H. Microfluidic networks for chemical patterning of substrate: Design and application to bioassays. *J. Am. Chem. Soc.* **1998**, *120*, 500-508.
202. Delamarche, E.; Bernard, A.; Schmid, H.; Michel, B.; Biebuyck, H. Patterned delivery of immunoglobulins to surfaces using microfluidic networks. *Science* **1997**, *276*, 779-781.
203. Cuvelier, D.; Rossier, O.; Bassereau, P.; Nassoy, P. Micropatterned "adherent/repellent" glass surfaces for studying the spreading kinetics of individual red blood cells onto protein-decorated substrates. *Eur. Biophys. J.* **2003**, *32*, 342-354.
204. Li, G. N.; Liu, J.; Hoffman-Kim, D. Multi-molecular gradients of permissive and inhibitory cues direct neurite outgrowth. *Ann. Biomed. Eng.* **2008**, *36*, 889-904.
205. Bhattacharjee, N.; Li, N.; Keenan, T. M.; Folch, A. A neuron-benign microfluidic gradient generator for studying the response of mammalian neurons towards axon guidance factors. *Integr. Biol.* **2010**, *2*, 669-679.
206. Shin, H. S.; Kim, H. J.; Min, S. K.; Kim, S. H.; Lee, B. M.; Jeon, N. L. Compartmental culture of embryonic stem cell-derived neurons in microfluidic devices for use in axonal biology. *Biotechnol. Lett.* **2010**, *32*, 1063-1070.
207. Tehranirokh, M.; Kouzani, A. Z.; Francis, P. S.; Kanwar, J. R. Microfluidic devices for cell cultivation and proliferation. *Biomicrofluidics* **2013**, *7*, 051502.
208. Adams, D. N.; Kao, E. Y.; Hypolite, C. L.; Distefano, M. D.; Hu, W.; Letourneau, P. C. Growth cones turn and migrate up an immobilized gradient of the laminin IKVAV peptide. *J. Neurobiol.* **2005**, *62*, 134-147.

209. Belisle, J. M.; Correia, J. P.; Wiseman, P. W.; Kennedy, T. E.; Costantino, S. Patterning protein concentration using laser-assisted adsorption by photobleaching, *LAPAP. Lab Chip* **2008**, *8*, 2164-2167.
210. Belisle, J. M.; Levin, L. A.; Costantino, S. High-content neurite development study using optically patterned substrates. *PLoS One* **2012**, *7*, e35911.
211. Yu, L. M. Y.; Miller, F. D.; Shoichet, M. S. The use of immobilized neurotrophins to support neuron survival and guide nerve fiber growth in compartmentalized chambers. *Biomaterials* **2010**, *31*, 6987-6999.
212. Wylie, R. G.; Ahsan, S.; Aizawa, Y.; Maxwell, K. L.; Morshead, C. M.; Shoichet, M. S. Spatially controlled simultaneous patterning of multiple growth factors in three-dimensional hydrogels. *Nat. Mater.* **2011**, *10*, 799-806.
213. Wylie, R. G.; Shoichet, M. S. Three-dimensional spatial patterning of proteins in hydrogels. *Biomacromolecules* **2011**, *12*, 3789-3796.
214. Kim, S. H.; Ha, H. J.; Ko, Y. K.; Yoon, S. J.; Rhee, J. M.; Kim, M. S.; Lee, H. B.; Khang, G. Correlation of proliferation, morphology and biological responses of fibroblasts on LDPE with different surface wettability. *J. Biomater. Sci. Polym. Ed.* **2007**, *18*, 609-622.
215. Oliveira, S. M.; Song, W.; Alves, N. M.; Mano, J. F. Chemical modification of bioinspired superhydrophobic polystyrene surfaces to control cell attachment/proliferation RID A-4418-2009. *Soft Matter* **2011**, *7*, 8932-8941.
216. Solouk, A.; Cousins, B. G.; Mirzadeh, H.; Solati-Hashtjin, M.; Najarian, S.; Seifalian, A. M. Surface modification of POSS-nanocomposite biomaterials using reactive oxygen plasma treatment for cardiovascular surgical implant applications. *Biotechnol. Appl. Biochem.* **2011**, *58*, 147-161.
217. Peppas, N. A.; Hilt, J. Z.; Khademhosseini, A.; Langer, R. Hydrogels in biology and medicine: From molecular principles to bionanotechnology. *Adv Mater* **2006**, *18*, 1345-1360.
218. Hern, D. L.; Hubbell, J. A. Incorporation of adhesion peptides into nonadhesive hydrogels useful for tissue resurfacing. *J. Biomed. Mater. Res.* **1998**, *39*, 266-276.
219. Falconnet, D.; Csucs, G.; Grandin, H. M.; Textor, M. Surface engineering approaches to micropattern surfaces for cell-based assays. *Biomaterials* **2006**, *27*, 3044-3063.
220. Kao, W. Y. Evaluation of protein-modulated macrophage behavior on biomaterials: designing biomimetic materials for cellular engineering. *Biomaterials* **1999**, *20*, 2213-2221.

221. Discher, D. E.; Janmey, P.; Wang, Y. L. Tissue cells feel and respond to the stiffness of their substrate. *Science* **2005**, *310*, 1139-1143.
222. Bettinger, C. J.; Langer, R.; Borenstein, J. T. Engineering substrate topography at the micro- and nanoscale to control cell function. *Angew. Chem. Int. Ed.* **2009**, *48*, 5406-5415.
223. Chou, L. S.; Firth, J. D.; Uitto, V. J.; Brunette, D. M. Substratum surface-topography alters cell-shape and regulates fibronectin messenger-RNA level, messenger-RNA stability, secretion and assembly in human fibroblasts. *J. Cell. Sci.* **1995**, *108*, 1563-1573.
224. Dalby, M. J.; Biggs, M. J.; Gadegaard, N.; Kalna, G.; Wilkinson, C. D.; Curtis, A. S. G. Nanotopographical stimulation of mechanotransduction and changes in interphase centromere positioning. *J. Cell. Biochem.* **2007**, *100*, 326-338.
225. Dalby, M. J.; Gadegaard, N.; Riehle, M. O.; Wilkinson, C. D.; Curtis, A. S. Investigating filopodia sensing using arrays of defined nano-pits down to 35 nm diameter in size. *Int. J. Biochem. Cell Biol.* **2004**, *36*, 2005-2015.
226. Borenstein, J. T.; Weinberg, E. J.; Orrick, B. K.; Sundback, C.; Kaazempur-Mofrad, M. R.; Vacanti, J. P. Microfabrication of three-dimensional engineered scaffolds. *Tissue Eng.* **2007**, *13*, 1837-1844.
227. Singhvi, R.; Stephanopoulos, G.; Wang, D. I. Effects of substratum morphology on cell physiology - Review. *Biotechnol. Bioeng.* **1994**, *43*, 764-771.
228. Curtis, A.; Wilkinson, C. Topographical control of cells. *Biomaterials* **1997**, *18*, 1573-1583.
229. Daly, W.; Yao, L.; Zeugolis, D.; Windebank, A.; Pandit, A. A biomaterials approach to peripheral nerve regeneration: bridging the peripheral nerve gap and enhancing functional recovery. *J. R. Soc. Interface* **2012**, *9*, 202-221.
230. Konofaos, P.; Halen, J. P. Nerve repair by means of tubulization: Past, present, future. *J. Reconstr. Microsurg.* **2013**, *29*, 149-163.
231. Mey, J.; Brook, G.; Hodde, D.; Kriebel, A. Electrospun fibers as substrates for peripheral nerve regeneration. *Biomed. App. Polym. Nanofib.* **2012**, *246*, 131-170.
232. Daly, W. T.; Yao, L.; Abu-rub, M. T.; O'Connell, C.; Zeugolis, D. I.; Windebank, A. J.; Pandit, A. S. The effect of intraluminal contact mediated guidance signals on axonal mismatch during peripheral nerve repair. *Biomaterials* **2012**, *33*, 6660-6671.
233. Ijpma, F. F.; De Graaf, R. C.; Meek, M. F. The early history of tubulation in nerve repair. *J. Hand Surg. Eur. Vol.* **2008**, *33E*, 581-586.

234. Pabari, A.; Yang, S. Y.; Seifalian, A. M.; Mosahebi, A. Modern surgical management of peripheral nerve gap. *J. Plast. Reconstr. Aesthet. Surg.* **2010**, *63*, 1941-1948.
235. Lundborg, G. A 25-year perspective of peripheral nerve surgery: Evolving neuroscientific concepts and clinical significance. *J. Hand Surg. Amer. Vol.* **2000**, *25A*, 391-414.
236. Matsumoto, K.; Ohnishi, K.; Kiyotani, T.; Sekine, T.; Ueda, H.; Nakamura, T.; Endo, K.; Shimizu, Y. Peripheral nerve regeneration across an 80-mm gap bridged by a polyglycolic acid (PGA)-collagen tube filled with laminin-coated collagen fibers: a histological and electrophysiological evaluation of regenerated nerves. *Brain Res.* **2000**, *868*, 315-328.
237. Yoshii, S.; Oka, M. Collagen filaments as a scaffold for nerve regeneration. *J. Biomed. Mater. Res.* **2001**, *56*, 400-405.
238. Yoshii, S.; Oka, M.; Shima, M.; Taniguchi, A.; Akagi, M. Bridging a 30-mm nerve defect using collagen filaments. *J. Biomed. Res. Part A* **2003**, *67A*, 467-474.
239. Clements, I. P.; Kim, Y.; English, A. W.; Lu, X.; Chung, A.; Bellamkonda, R. V. Thin-film enhanced nerve guidance channels for peripheral nerve repair. *Biomaterials* **2009**, *30*, 3834-3846.
240. Toba, T.; Nakamura, T.; Shimizu, Y.; Matsumoto, K.; Ohnishi, K.; Fukuda, S.; Yoshitani, M.; Ueda, H.; Hori, Y.; Endo, K. Regeneration of canine peroneal nerve with the use of a polyglycolic acid-collagen tube filled with laminin-soaked collagen sponge: A comparative study of collagen sponge and collagen fibers as filling materials for nerve conduits. *J. Biomed. Mater. Res.* **2001**, *58*, 622-630.
241. Wang, X.; Hu, W.; Cao, Y.; Yao, J.; Wu, J.; Gu, X. Dog sciatic nerve regeneration across a 30-mm defect bridged by a chitosan/PGA artificial nerve graft. *Brain* **2005**, *128*, 1897-1910.
242. Lee, D.; Choi, B.; Park, J.; Zhu, S.; Kim, B.; Huh, J.; Lee, S.; Jung, J.; Kim, S. Nerve regeneration with the use of a poly(L-lactide-co-glycolic acid)-coated collagen tube filled with collagen gel. *J. Craniomaxillofac. Surg.* **2006**, *34*, 50-56.
243. Dalby, M. Topographically induced direct cell mechanotransduction. *Med. Eng. Phys.* **2005**, *27*, 730-742.
244. Dalby, M.; Childs, S.; Riehle, M.; Johnstone, H.; Affrossman, S.; Curtis, A. Fibroblast reaction to island topography: changes in cytoskeleton and morphology with time. *Biomaterials* **2003**, *24*, 927-935.
245. Johansson, F.; Carlberg, P.; Danielsen, N.; Montelius, L.; Kanje, M. Axonal outgrowth on nano-imprinted patterns. *Biomaterials* **2006**, *27*, 1251-1258.

246. Foley, J. D.; Grunwald, E. W.; Nealey, P. F.; Murphy, C. J. Cooperative modulation of neuritogenesis by PC12 cells by topography and nerve growth factor. *Biomaterials* **2005**, *26*, 3639-3644.
247. Nagata, I.; Nakatsuji, N. Rodent CNS neuroblasts exhibit both perpendicular and parallel contact guidance on the aligned parallel neurite bundle. *Development* **1991**, *112*, 581-590.
248. O'Donnell, M.; Chance, R. K.; Bashaw, G. J. Axon growth and guidance: Receptor regulation and signal transduction. *Annu. Rev. Neurosci.* **2009**, *32*, 383-412.
249. Kalil, K.; Dent, E. Touch and go: Guidance cues signal to the growth cone cytoskeleton. *Curr. Opin. Neurobiol.* **2005**, *15*, 521-526.
250. Haq, F.; Anandan, V.; Keith, C.; Zhang, G. Neurite development in PC12 cells cultured on nanopillars and nanopores with sizes comparable with filopodia. *Int. J. Nanomedicine* **2007**, *2*, 107-115.
251. Gomez, N.; Lu, Y.; Chen, S.; Schmidt, C. E. Immobilized nerve growth factor and microtopography have distinct effects on polarization versus axon elongation in hippocampal cells in culture. *Biomaterials* **2007**, *28*, 271-284.
252. Mahoney, M.; Chen, R.; Tan, J.; Saltzman, W. The influence of microchannels on neurite growth and architecture. *Biomaterials* **2005**, *26*, 771-778.
253. Miller, C.; Jefinija, S.; Mallapragada, S. Synergistic effects of physical and chemical guidance cues on neurite alignment and outgrowth on biodegradable polymer substrates. *Tissue Eng.* **2002**, *8*, 367-378.
254. Miller, C.; Jefinija, S.; Mallapragada, S. Micropatterned Schwann cell-seeded biodegradable polymer substrates significantly enhance neurite alignment and outgrowth. *Tissue Eng.* **2001**, *7*, 705-715.
255. Walsh, J.; Manwaring, M.; Tresco, P. Directional neurite outgrowth is enhanced by engineered meningeal cell-coated substrates. *Tissue Eng.* **2005**, *11*, 1085-1094.
256. Hanson, J. N.; Motala, M. J.; Heien, M. L.; Gillette, M.; Sweedler, J.; Nuzzo, R. G. Textural guidance cues for controlling process outgrowth of mammalian neurons. *Lab Chip* **2009**, *9*, 122-131.
257. Richardson, J. A.; Rementer, C. W.; Bruder, J. M.; Hoffman-Kim, D. Guidance of dorsal root ganglion neurites and Schwann cells by isolated Schwann cell topography on poly(dimethyl siloxane) conduits and films. *J. Neural Eng.* **2011**, *8*, 046015.
258. Hirono, T.; Torimitsu, K.; Kawana, A.; Fukuda, J. Recognition of artificial microstructures by sensory nerve-fibers in culture. *Brain Res.* **1988**, *446*, 189-194.

259. Li, N.; Folch, A. Integration of topographical and biochemical cues by axons during growth on microfabricated 3-D substrates. *Exp. Cell Res.* **2005**, *311*, 307-316.
260. Lu, M.; Hsiang, S.; Lai, T.; Yao, C.; Lin, L.; Chen, Y. Influence of cross-linking degree of a biodegradable genipin-cross-linked gelatin guide on peripheral nerve regeneration. *J. Biomater. Sci. Polym. Ed.* **2007**, *18*, 843-863.
261. Wangenstein, K. J.; Kalliainen, L. K. Collagen tube conduits in peripheral nerve repair: A retrospective analysis. *Hand* **2009**.
262. Schmalenberg, K. E.; Uhrich, K. E. Micropatterned polymer substrates control alignment of proliferating Schwann cells to direct neuronal regeneration. *Biomaterials* **2005**, *26*, 1423-1430.
263. Branch, D. W.; Wheeler, B. C.; Brewer, G. J.; Leckband, D. E. Long-term stability of grafted polyethylene glycol surfaces for use with microstamped substrates in neuronal cell culture. *Biomaterials* **2001**, *22*, 1035-1047.
264. Gustavsson, P.; Johansson, F.; Kanje, M.; Wallman, L.; Linsmeier, C. E. Neurite guidance on protein micropatterns generated by a piezoelectric microdispenser. *Biomaterials* **2007**, *28*, 1141-1151.
265. Oliva, A. A.; James, C. D.; Kingman, C. E.; Craighead, H. G.; Banker, G. A. Patterning axonal guidance molecules using a novel strategy for microcontact printing. *Neurochem. Res.* **2003**, *28*, 1639-1648.
266. Yao, L.; Pandit, A.; Yao, S.; McCaig, C. D. Electric field-guided neuron migration: A novel approach in neurogenesis. *Tissue Eng. Part B Rev.* **2011**, *17*, 143-153.
267. Khire, V. S.; Harant, A. W.; Watkins, A. W.; Anseth, K. S.; Bowman, C. N. Ultrathin patterned polymer films on surfaces using thiol-ene polymerizations. *Macromolecules* **2006**, *39*, 5081-5086.
268. Khire, V. S.; Lee, T. Y.; Bowman, C. N. Surface modification using thiol-acrylate conjugate addition reactions. *Macromolecules* **2007**, *40*, 5669-5677.
269. Young, J.; Fox, S.; Anseth, K. A novel device for producing three-dimensional objects. *J. Manuf. Sci. E-T ASME* **1999**, *121*, 474-477.
270. Neckers, D. Architecture with photopolymerization. *Polym. Eng. Sci.* **1992**, *32*, 1481-1489.
271. Zwiers, R.; Dortant, G. Aspherical lenses produced by a fast high-precision replication process using UV-curable coatings. *Appl. Opt.* **1985**, *24*, 4483-4488.
272. McMahan, T.; Zadnik, K. Twenty-five years of contact lenses - The impact on the cornea and ophthalmic practice. *Cornea* **2000**, *19*, 730-740.

273. Willson, C.; Trinqué, B. The evolution of materials for the photolithographic process. *J. Photopolym. Sci. TEC.* **2003**, *16*, 621-627.
274. Gates, B.; Xu, Q.; Stewart, M.; Ryan, D.; Willson, C.; Whitesides, G. New approaches to nanofabrication: Molding, printing, and other techniques. *Chem. Rev.* **2005**, *105*, 1171-1196.
275. Beebe, D.; Moore, J.; Bauer, J.; Yu, Q.; Liu, R.; Devadoss, C.; Jo, B. Functional hydrogel structures for autonomous flow control inside microfluidic channels. *Nature* **2000**, *404*, 588.
276. Luo, N.; Metters, A.; Hutchison, J.; Bowman, C.; Anseth, K. A methacrylated photoiniferter as a chemical basis for microlithography: Micropatterning based on photografting polymerization. *Macromolecules* **2003**, *36*, 6739-6745.
277. Quick, D. J.; Anseth, K. S. Gene delivery in tissue engineering: A photopolymer platform to coencapsulate cells and plasmid DNA. *Pharmaceut. Res.* **2003**, *20*, 1730-1737.
278. Bryant, S. J.; Cuy, J. L.; Hauch, K. D.; Ratner, B. D. Photo-patterning of porous hydrogels for tissue engineering. *Biomaterials* **2007**, *28*, 2978-2986.
279. Stansbury, J. W.; Bowman, C. N.; Newman, S. M. Shining a light on dental composite restoratives. *Phys. Today* **2008**, *61*, 82-83.
280. Lovell, L.; Berchtold, K.; Elliott, J.; Lu, H.; Bowman, C. Understanding the kinetics and network formation of dimethacrylate dental resins. *Polym. Adv. Technol.* **2001**, *12*, 335-345.
281. Jaegermann, P.; Lenzian, F.; Rist, G.; Mobius, K. Time-resolved ESR and EPR during the photolysis of  $\omega,\omega$ -dimethoxy- $\omega$ -phenyl-acetophenone. *Chem. Phys. Lett.* **1987**, *140*, 615-619.
282. Baek, N. S.; Kim, Y. H.; Han, Y. H.; Lee, B. J.; Kim, T.; Kim, S.; Choi, Y.; Kim, G. H.; Chung, M.; Jung, S. Facile photopatterning of polyfluorene for patterned neuronal networks. *Soft Matter* **2011**, *7*, 10025-10031.
283. Sun, T.; Kovac, J.; Voldman, J. Image-based single-cell sorting via dual-photopolymerized microwell arrays. *Anal. Chem.* **2014**, *86*, 977-981.
284. Hao, Y.; Shih, H.; Muñoz, Z.; Kemp, A.; Lin, C. Visible light cured thiol-vinyl hydrogels with tunable degradation for 3D cell culture. *Acta Biomater.* **2014**, *10*, 104-114.
285. Nichol, J. W.; Koshy, S. T.; Bae, H.; Hwang, C. M.; Yamanlar, S.; Khademhosseini, A. Cell-laden microengineered gelatin methacrylate hydrogels. *Biomaterials* **2010**, *31*, 5536-5544.

286. Hume, P. S.; Anseth, K. S. Inducing local T cell apoptosis with anti-Fas-functionalized polymeric coatings fabricated via surface-initiated photopolymerizations. *Biomaterials* **2010**, *31*, 3166-3174.
287. Kapoor, Y.; Thomas, J. C.; Tan, G.; John, V. T.; Chauhan, A. Surfactant-laden soft contact lenses for extended delivery of ophthalmic drugs. *Biomaterials* **2009**, *30*, 867-878.
288. Pameijer, C. H.; Zmener, O. Resin materials for root canal obturation. *Dent. Clin. North Am.* **2010**, *54*, 325-344.
289. Uludag, H.; De Vos, P.; Tresco, P. A. Technology of mammalian cell encapsulation. *Adv. Drug Deliv. Rev.* **2000**, *42*, 29-64.
290. Teixeira, A. I.; McKie, G. A.; Foley, J. D.; Berticsc, P. J.; Nealey, P. F.; Murphy, C. J. The effect of environmental factors on the response of human corneal epithelial cells to nanoscale substrate topography. *Biomaterials* **2006**, *27*, 3945-3954.
291. Kloxin, A. M.; Kasko, A. M.; Salinas, C. N.; Anseth, K. S. Photodegradable hydrogels for dynamic tuning of physical and chemical properties. *Science* **2009**, *324*, 59-63.

## CHAPTER 2

### OBJECTIVES

As methods to fabricate and characterize biomaterials and tissue engineering constructs with greater complexity and detail have advanced in the past three decades, research in these fields increasingly focuses on developing bioactive materials that drive favorable biological outcomes. For instance, the strategy to spatially control neurite outgrowth towards specific prosthesis electrodes has tremendous potential to drastically enhance the performance of neural prosthetics. Improving sensory prosthesis tissue integration in this manner will decrease problematic current spread that causes non-specific neuronal excitation and will subsequently increase the number of perceptual channels available to a user. Added perceptual channels will, in turn, enable biological functional output that more closely imitates the precise spatial signaling of the native nervous system. Accordingly, this research explores photopolymer materials and patterning methods to develop systems with micro- and nano-scale cues that direct nerve growth and aid in elucidating neural pathfinding behavior. Predictably orienting *de novo* neurite growth from spiral ganglion neurons (SGNs), which are the target neurons for CI stimulation, has not been previously demonstrated. Developing photopolymerization methods to rapidly and directly generate cell-scale physical features will substantially expand systems and tools available for cell-material contact guidance research and for biomedical device modification and enhancement.

Furthermore, understanding how photopolymerization parameters such as photoinitiator choice and concentration, crosslinker content, light intensity, and radiation exposure time influence feature formation will enable fabrication of tailor-made cues for specific cellular niches. As demonstrated in other cell-material action studies, biological systems are also known to respond to mechanical cues of synthetic biomaterial constructs. It will, therefore, be crucial to understand SGN neurite response to material

stiffness cues in relation to their alignment to physical features since final material properties of a future medical device could significantly affect neural pathfinding. The ultimate goal of the collaborative research presented in this thesis is to develop materials that predictably direct nerve growth to improve prosthetic performance and, thus, improve quality of life for patients with neural prostheses. Specific research objectives include to:

1. Verify that topographic microfeatures can be directly fabricated via photopolymerization and that inner ear neural tissue, including SGN neurites and SGSCs, thrive on typical photopolymer materials and align to photopatterned physical cues.
2. Control development and final morphology of micropattern features by modulating photopolymerization parameters to determine the extent of SGN alignment in relation to changes in feature spacing, height, and transitional slope.
3. Explore and measure SGN neurite pathfinding and turning capability by challenging advancing neural growth cones with photopolymerized multidirectional cues and compare outgrowth behavior to unpatterned and unidirectional controls.
4. Characterize the effects of material stiffness and surface polarity on SGN neurite alignment and behavior when neurons are cultured on photopolymers with identical physical cues but vary in composition and cross-link density.
5. Examine the capability of micropatterned physical cues to direct SGN neurite outgrowth in the presence of biochemical border challenges.

Completion of the first research objective (Chapter 4) will demonstrate the feasibility of the directed neural growth strategy on photopolymerized micropatterns.

Specifically, the survival and cellular behavior of SGSCs, dissociated SGNs, and inner ear tissue explants on various photopolymer compositions will be investigated to demonstrate biocompatibility of the photopolymer materials. Cellular behavior will also be quantified on materials with and without an adsorbed layer of laminin, an integrin binding peptide that facilitates neuronal surface attachment. Next, micropattern surface cues will be developed on photopolymer surfaces by selectively masking light to alter local reaction kinetics throughout the polymerization. Directly photopatterning surface microfeatures through radiation curing stands in contrast to the multi-step and often expensive and time consuming process of etching silicon masters in traditional photolithographic applications. Micropatterns will be characterized by white light interferometry. Inner ear neural tissue will be tested on unpatterned and micropatterned substrates to determine alignment capability to photopatterned physical guidance cues. Neurite alignment to micropatterns will be explored and demonstrated for both dissociated neurons and for intact neural tissue. This objective serves as a proof-of-concept study and establishes a research foundation upon which the remaining objectives are pursued.

The second research objective (Chapter 5) will illustrate the sensitivity of SGN neurite pathfinding in response to physical features with varying widths, depths, and transitional slopes. After establishing that micropatterns can be directly generated by photopolymerization and photomasking in objective 1, the second research objective will substantially expand on this theme by illustrating the high degree of control over feature formation available by simple modulation of photopolymerization reaction parameters such as photoinitiator concentration, UV light intensity, radiation exposure time, and photomask band spacing. A range of channel amplitudes across several orders of magnitude will be generated for neurite contact guidance studies based on the inherent spatial and temporal control of UV curing and micropattern morphology will be characterized by scanning electron microscopy and white light interferometry. The

alignment behavior of multiple neuronal and glial cell types will be evaluated on various physical micropatterns as a comparison to SGN neurite and SG glial alignment. Correlation of neurite alignment to microfeature transitional slope will be established by measuring neurite alignment following image capture by immunofluorescence microscopy and characterizing feature transitions with atomic force microscopy. Realization of this research objective will inform the design of biomedical devices that have photopatterned physical features with appropriate dimensions for directed neurite growth. Precisely directing SGN growth in this manner will advance efforts to improve neural prosthetic tissue integration by enhancing the prosthesis interface.

To rationally design a cochlear biomedical device with an interface which directs nerve growth to spatially specific electrodes, it will likely be necessary to determine pathfinding and turning behavior of *de novo* neurite growth from SGNs. Accordingly, accomplishing the third research objective (Chapter 6) will improve understanding of SGN neurite pathfinding and SGSC response in relation to multidirectional physical micropatterns to aid prosthesis interface design. As little is known about SGN neurite pathfinding in response to physical cues, a simple pattern of repeating 90° angles or directional cues will be utilized to explore SGN process response. Multidirectional patterns will be developed and controlled based on the photopolymerization methods set forth in the first and second research objectives. Moreover, SGN neurites on multidirectional micropatterns will be challenged with physical features shown to induce high degrees of alignment on unidirectional patterns as demonstrated in objective 2. A variety of neuronal and neurite behaviors will be characterized and compared on unpatterned, unidirectional, and multidirectional substrates including neuronal survival, neurite length, neurite branching, proportion of neurite outgrowth on raised or in depressed surface features, neurite turning, degree of microfeature crossing, and neurite segment alignment to the pattern direction. Developing methods to understand neural pathfinding and to guide *de novo* neurite growth to specific stimulatory elements will

enable design of innovative biomaterials that improve functional outcomes of devices that interface with the nervous system.

Realization of the fourth and fifth research objectives (Chapters 7 and 8) will elucidate the effects of material mechanical properties on physical feature contact guidance and determine topographic feature dimensions that overcome conflicting biochemical border signals. Methacrylate thin-film stiffness will be modified by varying the cross-link density of the final material by either increasing the amount of cross-linker in the prepolymer formulation or by increasing the size of the spacer unit between cross-links. Controlling photopolymerization parameters, as established in previous research objectives, will enable production of micropatterns with identical physical features on a variety of polymer compositions despite differences in reaction kinetics. Neurite response to material stiffness will be evaluated by characterizing and comparing SGN neurite alignment to unidirectional micropatterns on each polymer composition. Material stiffness will be measured by dynamic mechanical analysis. Because cells must respond to a variety of mechanical and chemical cues in their micro-environment or niche, it may be necessary to design physical guidance cues that overcome conflicting chemical cues. Accordingly, SGN neural process alignment will be evaluated on photopatterned materials that are coated with two distinct biochemical cues. Neurite alignment and behavior will be evaluated at the dynamic biochemical border to determine physical features that dominate neural process directional growth outcomes.

Completion of these research objectives will identify the topographic features and material properties necessary for fabrication of scaffolds that can be used for future *in vivo* neural regeneration models including the design of enhanced neuron-prostheses interfaces. Furthermore, these studies will develop and substantially improve fundamental understanding of photopatterning technologies designed to guide regeneration of auditory nerve fibers to directly interface with CI electrodes. Thus, while each objective addresses fundamental questions on how cellular processes interact with

physical features in their microenvironment, they also provide a necessary foundation for translational clinical application. Precisely directed SGN process growth will greatly improve the ability of CIs to represent complex auditory signals and improve auditory performance for its user. The results will also inform efforts to improve the interface of other neural prostheses and nerve repair conduits with target tissue.

## CHAPTER 3

### MATERIALS AND EXPERIMENTAL METHODS

The general materials and experimental procedures used to investigate neural pathfinding on photopolymerized physical guidance cues are outlined in this chapter. The first section introduces the photopolymerizable monomers, which consist mainly of methacrylates, and the photoinitiators employed for generation of micropatterned polymer films. The next section describes the characterization of polymer samples with white light interferometry, scanning electron microscopy, atomic force microscopy, water contact angle goniometry, and dynamic mechanical analysis. The third section describes experimental procedures to culture target neural populations and the measurements used to evaluate their behavior on unpatterned controls and on photopatterned physical guidance cues. Neural behaviors examined include neuronal survival, neurite alignment and length, neurite branching, proportion of neurite outgrowth on raised or in depressed surface features, neurite turning, degree of microfeature crossing, and change in terminal angle relative to initial angle from the neuronal soma. Most neural behaviors were measured after fixing the cell culture with paraformaldehyde, staining neural tissue with cell-specific antibodies, and then visualizing the cells using immunofluorescence microscopy. Captured fluorescence images were then evaluated using Image J software. Statistical analyses are briefly described in the final section.

#### **Materials and Sample Preparation**

Experiments to photopattern micro- and nano-scale physical guidance cues on polymer surfaces were performed with commercially available monomers and photoinitiators. Materials were used as received without further purification. Based on initial photopolymerization and cell-material interaction experiments, a system of hexyl

methacrylate (HMA, Aldrich) with 1,6-hexanediol dimethacrylate (HDDMA, Aldrich) as the crosslinker was used as the primary polymer platform for the majority of neurite alignment studies. The HMA-co-HDDMA system was used in each research objective for primarily two reasons: 1) it has been shown to support the attachment, survival, and growth of SGNs and spiral ganglion Schwann cells (SGSCs) under *in vitro* conditions based on experimental data and observations collected in our labs<sup>1,2</sup> and 2) its micropattern development, including channel amplitude profile versus exposure time at given conditions, has been well developed in our lab enabling facile fabrication of similar uni- and multidirectional features for neural pathfinding comparisons. Weight ratio of the mono- to di- methacrylate monomers was varied depending on the research objective.

When testing neurite response to material stiffness and surface polarity cues, poly(ethylene glycol) (PEGDMA, Aldrich,  $M_n = 600$ ) with ethylene glycol (EGDMA, Aldrich) was used as a relatively flexible and polar alternative platform. PEGDMA produces an elastic and soft polymer structure due to the flexible ether linkage and long linear chains (repeating ethylene glycol units) between crosslinks.<sup>3,4</sup> Furthermore, the glass transition temperature ( $T_g$ ) of PEGDMA is well below room temperature allowing for long range segmental motion of polymer chains which maintains the substrate in the rubbery region of the visco-elastic regime. Addition of EGDMA, which is a short chained version of PEGDMA with only one ethylene glycol repeat unit, results in higher crosslinking density per unit volume in the polymer and will increase the material modulus. Conversely, HMA-co-HDDMA is a very stiff cross-linked polymer system that has a  $T_g$  well above room temperature. Increasing the concentration of HMA, which has a functionality of two ( $f = 2$ ) for linear chains, will decrease crosslinking density and yield less rigid materials. Using these two systems provided a wide range of mechanical stiffness characteristics, ranging from a very flexible and rubbery polymer to a very stiff and glassy polymer. Additionally, hexyl acrylate (HA, Aldrich), 1,6-hexanediol diacrylate (HDDA, Sartomer), and 2-hydroxyethyl methacrylate (HEMA, Aldrich) were

used for feature formation kinetics studies. 2,2-dimethoxy-2-phenylacetophenone (DMPA, BASF) and *bis*(acyl)phosphine oxide (BAPO) were used as photoinitiators. Monomer and photoinitiator chemical structures are shown in Figure 3.1.

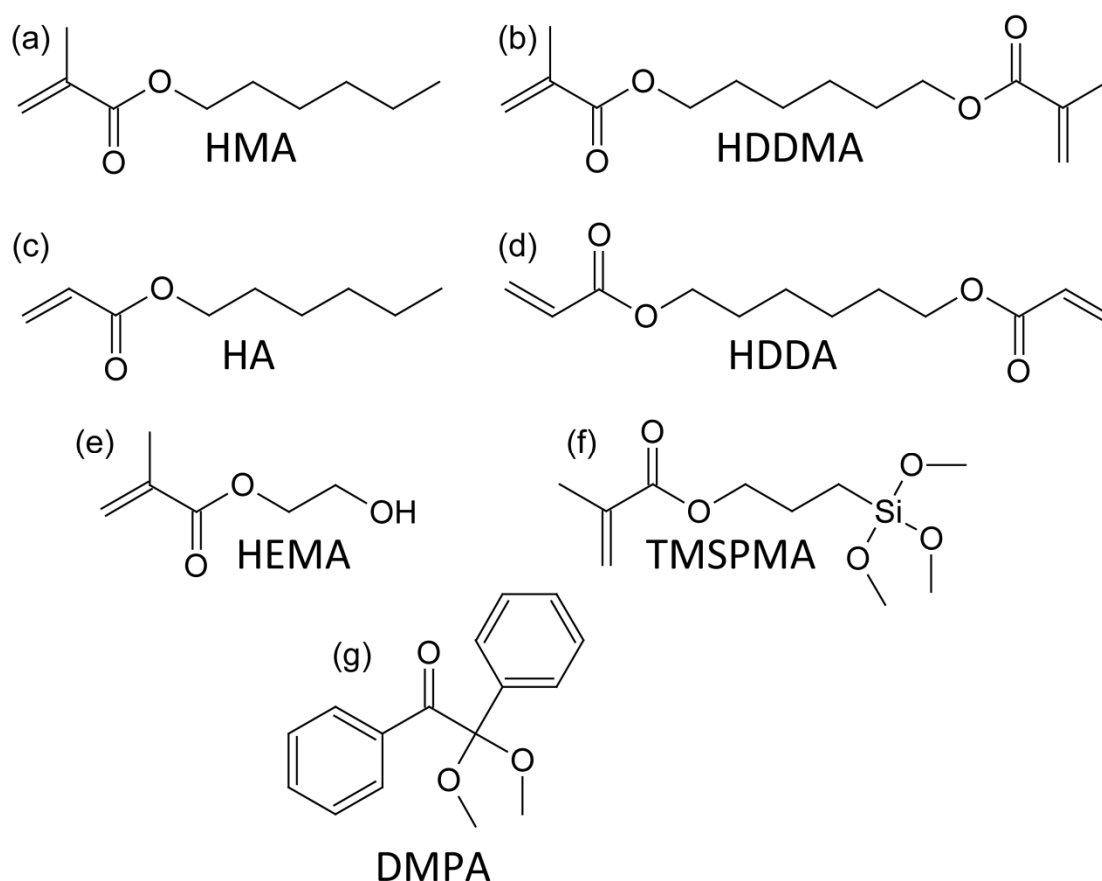


**Figure 3.1** Chemical structures of monomers, silane coupling agent, and photoinitiators used in this work. Shown are (a) hexyl methacrylate, (b) 1,6-hexanediol dimethacrylate, (c) hexyl acrylate, (d) 1,6-hexanediol diacrylate, (e) 2-hydroxyethyl methacrylate, (f) 3-tri(methoxysilyl)propyl methacrylate, and (g) 2,2-dimethoxy-2-phenylacetophenone.

To prevent polymer delamination and facilitate cellular microscopy studies, polymer films were generated on methacrylated or functionalized glass slides (Fig 3.2). Standard microscope glass slides (2.54 cm x 7.62 cm x 0.1 cm) were functionalized with

the silane coupling agent 3-(trimethoxysilyl)propyl methacrylate (Aldrich). Prior to treatment with the coupling agent, slides were first cleaned and oxidized with O<sub>2</sub> plasma for 3 min at 30 W RF power (PDC-001 Harrick Plasma Expanded Cleaner, Ithaca, NY) while under 300 mTorr vacuum. Following removal from the plasma chamber, slides were immersed in a 1/100 v/v solution of the silane coupling agent and n-hexane (Aldrich) overnight in a covered container at room temperature (~21°C). Each slide was then rinsed with fresh hexanes and dried in the fume hood before being placed in a sealed container. Functionalized slides were used immediately as a substrate for polymerization.

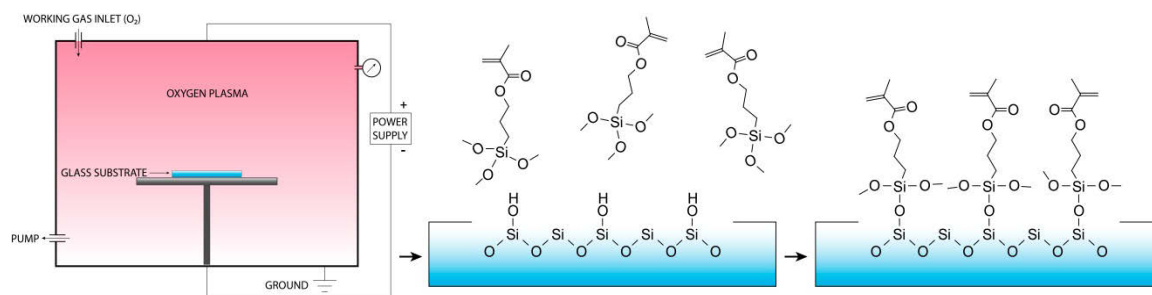


**Figure 3.2** Schematic of glass substrate methacrylate procedure. Microscope slides were cleaned and oxidized with reactive O<sub>2</sub> plasma and then treated with a methacrylated silane coupling agent. Glass slide methacrylation enabled covalent bonding of the photopolymerized thin-film to the supporting substrate and prevented polymer delamination during cell-material interaction studies.

Photopolymerization of micropatterned polymer thin-films was performed with standard UV curing equipment in conjunction with photomasking techniques. Specifically, all methacrylate monomer mixtures were prepared with 1 wt% of DMPA as the photoinitiator unless otherwise specified. Copolymer compositions are represented as whole numbers (e.g. 40/60, 50/50) but each polymer fraction is 0.5 wt% less to account for the photoinitiator. A volume of 20  $\mu$ L from pre-polymer formulations was pipetted

onto the center of a functionalized slide then covered with a 2.54 cm x 2.54 cm x 0.1 cm glass-chrome Ronchi rule photomask (Applied Image Inc., Rochester, NY) for parallel patterns or with a cut untreated glass slide of the same dimensions for unpatterned samples. Capillary forces caused the formulations to spread evenly under the photomasks. Photopolymerization was performed with a high-pressure mercury vapor arc lamp (Omnicure S1500, Lumen Dynamics, Ontario, Canada) at a 365 nm light intensity of 16 mW/cm<sup>2</sup>. Light intensity was measured with a Cole-Parmer Series 9811 radiometer. The curing module was equipped with an 8 mm aperture x 50 mm length beam homogenizing fused silica light pipe (Edmund Optics) and a collimating lens (RLQ-1, Asahi Spectra). Microfeature amplitude was tuned by shuttering UV radiation at specific times to prevent further initiation events resulting in rapid termination of the polymerization. Following the set exposure time, the photomask was removed from the polymer and the sample was washed with 95% ethanol (Aldrich) to remove residual surface monomer. Rinsed samples were then post cured for 10 min under the same light source and intensity to maximize monomer conversion without reducing surface channel amplitude due to trough back-filling.

For bioactive border challenge experiments, photopatterned polymer substrates were sequentially coated with poly-L-ornithine (100 µg/ml) at room temperature and 10 µg laminin (20 µg/ml, 0.5 ml in Hank's Balanced Salt Solution, Life Technologies) at 4 °C overnight. The laminin solution was removed by pipette and surfaces were washed three times. An equal volume of RIPA buffer containing 50 mM Tris-HCl, 1% NP-40, 1% Triton X-100, 150 mM NaCl and 1 mM EDTA was applied to each slide to dissolve the adsorbed protein. A 96-well plate protein assay kit (Life Technologies) was used to quantify protein concentration according to the manufacturer's protocol. Experimental samples and solutions of protein standards with known concentrations were pipetted into microplate wells and 1x dye reagent was added to each well, mixed, and incubated at room temperature for 5 min. Absorbance was measured by a microplate reader (Thermo

Max). A standard curve was generated using the absorption values from the protein standards. Protein concentration of the experimental samples was calculated based on the standard curve. Each condition was performed in triplicate and repeated three times.

### Polymer Characterization

Photopatterned surface morphology was characterized primarily with white light interferometry with subsequent scanning electron microscopy (SEM) and atomic force microscopy (AFM) characterization as needed. Micropattern feature spacing and depth were measured by white light interferometry (Dektak Wyko 1100 Optical Profiling System, Veeco) (Fig 3.3). Feature amplitude was measured as the difference between a

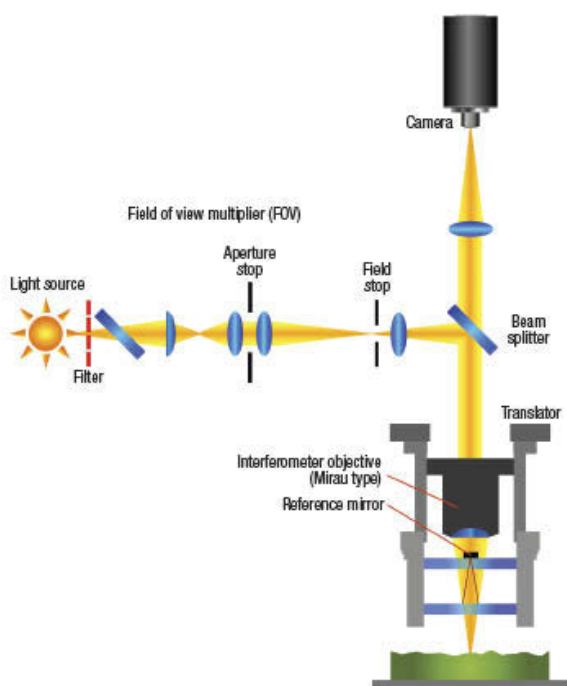


**Figure 3.3** Schematic of white light interferometer used to analyze photopatterned micro- and nano-scale physical guidance cues. A coherent beam is split with part of the beam going to the detector and another portion being reflected off the sample. Using the destructive interference of wave superposition, the detector takes a stack of images and puts them together to generate a depth profile. Image courtesy of Veeco Metrology.

maximum ridge value and an adjacent minimum groove value. For each composition and exposure time, average feature height was determined by measuring channel amplitude in nine different areas across the surface ( $n \geq 3$ ). Feature spacing or periodicity was measured as the distance between the highest points on adjacent ridges and was consistent with photomask band spacing. Measurements and 3D images were generated using Vision software associated with the instrument.

Micropattern morphology of each composition was further characterized by scanning electron microscopy (SEM, S-4800, Hitachi) (Fig 3.4). Conductive silver paint

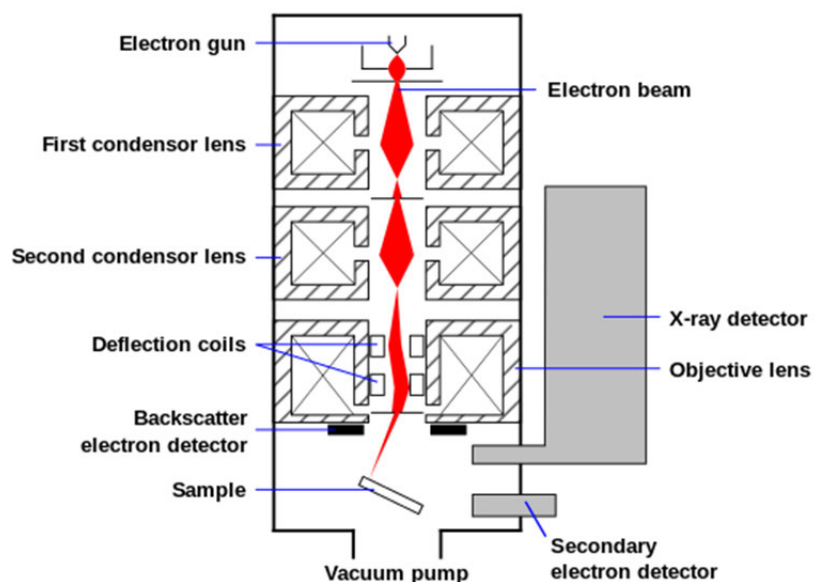


**Figure 3.4** Schematic of scanning electron microscope used to further characterize microfeature surface morphology and polymer cross sections. An electron beam is accelerated, focused, and then rastered across a substrate surface. Secondary electrons emitted by the sample are picked up by the microscope detectors and used to generate a three-dimensional image.<sup>5</sup>

was applied to the bottom of glass substrates modified with micropatterned methacrylate thin films for mounting on aluminum SEM stubs to acquire top-down images. For cross-sectional images, a glass etcher was used to etch the sample on the side opposite the thin

polymer film and patterned polymers were then fractured and mounted vertically on specimen stages. The SEM specimen stage was rotated using automated stage and software controls. Each polymer surface was sputter coated with gold prior to examination by SEM. Electron accelerating voltage was set at 2 kV.

Atomic force microscopy (AFM, Asylum Atomic Force Microscope, Asylum Research) was used to accurately assess the transitional slope between grooves and ridges on micropatterned polymers. A silicon-nitride microscope cantilever with a force constant of 46 N/m and a tuning frequency of 316.62 kHz was used. Samples were scanned at a rate of 5  $\mu\text{m/s}$  with 512 points taken per scan line across 50  $\mu\text{m}$ . X and Y position data were obtained from the instrument software from 2D profiles ( $n = 3$ ) taken at different locations on pattern surfaces. Average and maximum slopes were calculated from profile data.

Polymer thin film surface polarity was measured by water contact angle goniometry. Water contact angles were measured on unpatterned surfaces for each polymer composition using a sessile drop method at room temperature ( $\sim 21^\circ\text{C}$ ) with a Ramé-Hart NRL 100-00 goniometer (Ramé-Hart Instrument Co.). For each composition, three samples were analyzed with repeats in six different spots for a total of 18 measurements per composition. Drops of  $\text{H}_2\text{O}$  were dispensed as 1  $\mu\text{L}$  volumes.

Dynamic mechanical analysis (DMA) was used to characterize polymer mechanical properties. Specifically, tensile tests were performed with a dynamic mechanical analyzer (DMA-Q800, TA Instruments) to measure the Young's modulus of each composition as a measure of substrate rigidity encountered by neural tissue. Polymer specimens for tensile tests were prepared by injecting pre-polymer formulations between two untreated glass plates separated by 280  $\mu\text{m}$  thick spacers and held together with clamps. The sample was then irradiated for 10 minutes using the same lamp and intensity used to fabricate micropatterned surfaces. Polymer bars, with dimensions of 25 mm x 6.4 mm x 0.28 mm, were placed in a vertical film tension clamp for tensile tests.

Young's modulus was evaluated at 30° C using controlled force tensile mode with a designated force rate (0.5 N/m). The modulus was calculated using equation 3.1 using the slope of the stress-strain curve in the early linear regime (less than 5% strain) (n = 5):

$$E = \sigma/\varepsilon \quad (3.1)$$

where E is the material modulus,  $\sigma$  is the stress, and  $\varepsilon$  is the strain.

### Cell Culture and Characterization

Rats were used as the source for auditory neuron cultures to generate the neuronal, glial, and neural process data presented in this work. Rats serve as a primary source for spiral ganglia cultures due to a variety of important advantages.<sup>6-12</sup> For example, they have relatively large cochleae which facilitates microdissection of spiral ganglia and their neural tissue is easy to maintain in culture. SGN yields are high compared to other mammalian models which aids in characterization and quantification of neural process and neuronal behavior. Furthermore, they possess many similarities to other mammalian species – including, most importantly, humans. Finally, due to their extensive use in the literature, using rat neural tissue in this work facilitates comparison of experimental results with other work and makes the results the most widely applicable to other studies.

The institutional animal care and use committee at the University of Iowa approved all protocols used in this study. Spiral ganglia (SG) were isolated from postnatal day 4–5 (P4-P5) rats euthanized under cold anesthesia after placing the pups in a cardboard box on ice for 20 min.<sup>13,14</sup> The temporal bone was harvested and the otic capsule was dissected under operating microscope in ice cold PBS. The bony cochlear capsule was removed, followed by the spiral ligament. The organ of Corti was removed,

transecting the outer radial fibers, leaving the SGNs within the modiolus. Modiolar bone and surrounding connective tissue were removed. Ganglia were collected in ice cold Hanks' balanced salt solution with calcium and magnesium (HBSS+/, Gibco, Carlsbad, CA). When used as explants, SGs were cut into 4 pieces and placed onto culture slides.

Polymer substrates attached to glass slides were first sterilized with 70% ethanol and UV irradiation and air-dried in a culture hood. Dissociated SG cultures from P3-5 rat pups were plated in 8 mm cloning cylinders placed on polymer surfaces with sterile silicon grease to seal the edges as previously described.<sup>10,15,16</sup> Cultures were grown on unpatterned polymers both with and without laminin (20 µg/mL) coating. Laminin coated glass slides were used as a control. Cultures were maintained in Dulbecco's Modified Eagle Medium (DMEM) supplemented with N2 Bottenstein additives and 5% fetal bovine serum. Neurotrophin-3 (NT-3) (50 ng/ml) and Brain Derived Neurotrophic Factor (BDNF) (50 ng/ml) were included in medium to promote SGN survival and neurite growth.<sup>15,17</sup> After 72 h, the cultures were fixed with 4% paraformaldehyde and stained with anti-S100 and anti-neurofilament 200 (NF200) antibodies (1:400, Sigma-Aldrich, St. Louis, MO) to label SGSCs and SGNs, respectively, followed by Alexa 488 and Alexa 546 conjugated secondary antibodies.<sup>15</sup> Hoechst 3342 (10 µg/ml) was used for nuclear staining. Slides were cover slipped with ProLong Gold anti-fading reagent with DAPI (Life Technology) and sealed with nail polish. Digital epifluorescent images were captured of the entire polymer surface using the scan slide application of Metamorph software (Molecular Devices, Silicon Valley, CA) on a Leica DMIRE2 microscope (Leica Microsystem, Bannockburn, IL) with a Leica DFC350FX digital camera.

SGN cell survival was determined as before by counting the total number of viable SGNs per cloning cylinder.<sup>16</sup> Only NF200-positive SGNs with non-pyknotic nuclei were considered viable. The total number of NF200-positive neurons with healthy nuclei was counted from the digital images for each polymer surface to determine SGN survival. The experiments were performed in duplicate and repeated at least three times.

Neurite length was determined by measuring the longest process of 100 randomly selected neurites from each slide using the measurement tool in Image J (NIH, Bethesda, MD). SG explants, prepared by cutting each ganglion into 4 segments, were grown in similar conditions and fixed after 3-4 days of growth for staining and analysis. Number of branches extending from SGN neurites was determined by averaging the total number of neurite bifurcations, including bifurcation of branches, for 100 randomly selected neurites from each condition.

Neurite alignment to micropatterned substrates was calculated using equation 3.2:

$$A_R = \frac{T_L - A_L}{T_L} \quad (3.2)$$

where  $A_R$  is the alignment ratio,  $T_L$  is the total neurite length, and  $A_L$  is the aligned length in the pattern direction. Alignment to the pattern was defined as a ratio of unaligned length per neurite length.  $A_L$  was determined by measuring the distance from the neuronal cell body to the neurite terminus in a straight line in the direction of the micropattern (Fig 3.5). The pattern direction was set horizontally prior to measurements. The unaligned length per neurite length ratio is referred to as the alignment ratio throughout the text. A ratio close to zero represents a neurite that closely follows the pattern along its entire length. A wandering neurite, which does not strongly align to the pattern, has a high alignment ratio. To analyze neurite alignment on unpatterned substrates, aligned distance was arbitrarily measured directly along the horizontal plane. It is important to note that for research objectives 1 and 4 the alignment ratio was slightly different with  $T_L/A_L$  serving as the ratio and alignment asymptotically approaching 1 in place of 0.

Dissociated dorsal root ganglion neuron (DRGN), trigeminal ganglion neuron (TGN), and cerebellar granular neuron (CGN) cultures were prepared by modification of

the SG culture method. Briefly, pooled DRG or TG from P3-5 rat pups were dissociated with 0.125% trypsin and 0.1% collagenase for 45 min at 37°C, followed by gentle

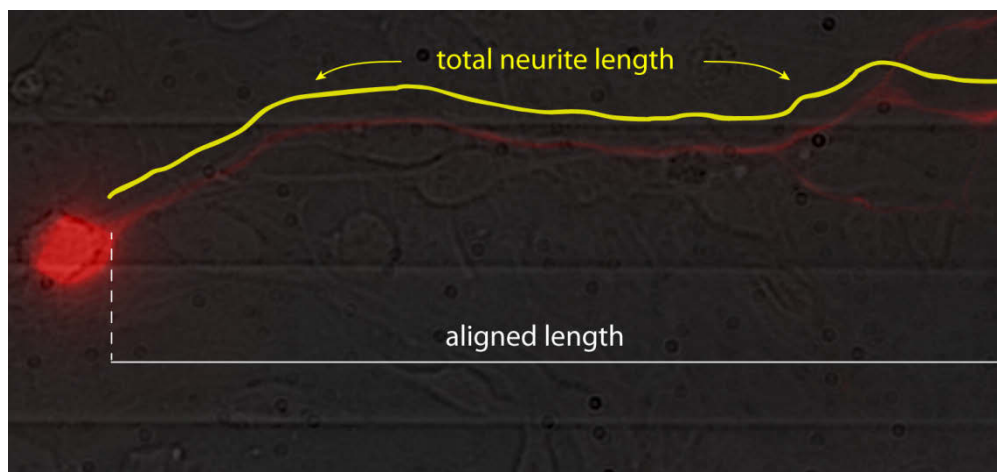


**Figure 3.5** Representation of neurite alignment measurement. Neural processes are stained with fluorescent NF200 antibodies and captured by fluorescence microscopy. Image J is used to measure the total length of the neurite and the aligned length in the pattern direction which is always set horizontally. Neurite alignment is calculated as a ratio as described in equation 3.2.

trituration through fire-polished glass pipettes. For CGN cultures, cerebellar cortices were collected from P3-5 rat pups, stripped of arachnoid membranes, and treated with 0.05% trypsin for 12 min at 37°C followed by gentle trituration. Astrocyte (AC) cultures were prepared and maintained from postnatal cerebral cortex according to the modification of a previously described method<sup>18,19</sup>. All neurons were plated on polymer substrates coated with poly-L-ornithine (100 µg/ml) and laminin (20 µg/ml). TGN and DRGN cultures were maintained in Neurobasal-A medium with B-27 (Invitrogen) and nerve growth factor (NGF, 50 ng/ml). CGN cultures were maintained in Neurobasal-A medium with B-27, 20 µM KCl and NGF 50 ng/ml. AC cultures were maintained as previously described<sup>18</sup>. Cultures were maintained in a humidified incubator with 6.5% CO<sub>2</sub> and fixed

with 4% paraformaldehyde after 48 hr. For TG or DRG neurons, total neurite length was determined by averaging the length of six branches of each neuron for 100 neurons at each condition. Neuronal and neural process behavior was visualized by immunofluorescent microscopy and analyzed with Image J software. SG, TG, and DRG cultures were immunostained with anti-S100 and anti-neurofilament 200 (NF200) antibodies (1:400, Sigma–Aldrich) to label Schwann cells (SCs) and neurons, respectively<sup>15</sup>. CGN cultures were immunostained with anti-MAP2 (1:400, Cell Signaling) and anti-TAU1 (1:200, Cell Signaling) antibodies to label dendritic and axonal neurites, respectively. ACs were immunostained with anti-glial fibrillary acidic protein (GFAP) antibody (1:100, Sigma). Alexa 488 and Alexa 546 conjugated secondary antibodies (Invitrogen) were used to detect primary antibody immunolabeling. Slides were cover slipped with ProLong Gold anti-fading reagent with DAPI (Life Technology).

SC and AC orientation was determined as previously described by drawing the outline of the cell using Image J software and fitting an ellipse to the cell outline.<sup>1</sup> The angle made between the major axis of the ellipse and the pattern ( $\theta$ ) was measured in Image J as glial cell alignment (Fig 3.6). Glial cell alignment was measured from four independent wells on each polymer surface and was repeated three or more times.

To determine the extent that micropatterns influenced neurite turning from inner ear tissue explants, the angle of the neurite relative to the pattern was measured when the neurite first encountered the pattern (initial angle) and compared to the angle of the neurite terminus relative to the pattern (terminal angle). The difference between the initial and terminal angle of the neurite ( $\Delta\theta$ ) was calculated to quantify the extent of turning induced by the micropattern. In some cases, the initial portion of individual neurites remained in bundles as they exited the explant and was not resolvable by epifluorescent microscopy. In each case, the neurites within the bundle traveled in the same trajectory and the angle of the bundle was measured to determine initial angle of the neurites comprising it.

For the multidirectional pattern study, neurite alignment was measured as a distribution of angles relative to the horizontal plane of 10  $\mu\text{m}$  length neurite segments.

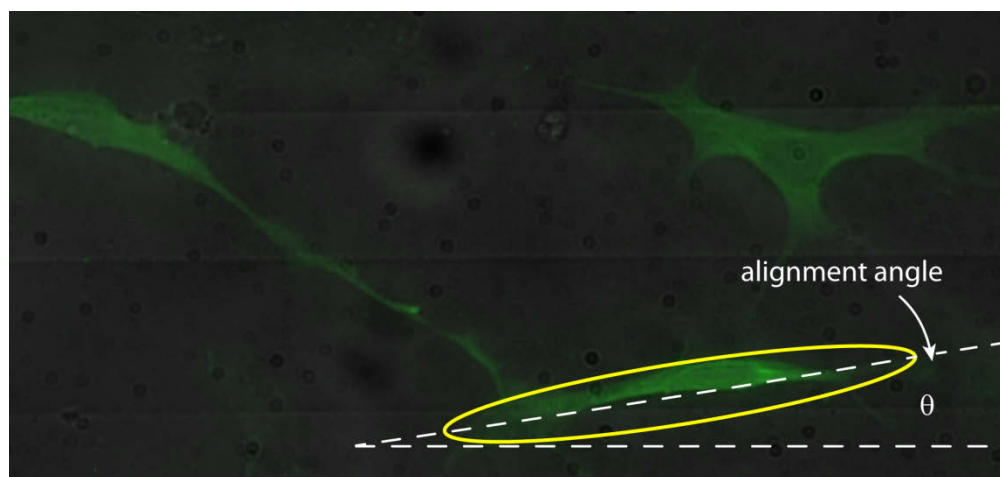


**Figure 3.6** Representation of glial cell alignment measurement. Schwann cells are stained with fluorescent S100 antibodies and captured by fluorescence microscopy. Image J is used to measure the angle made between the major axis of an ellipse fitted around the cell relative to the pattern direction set horizontally.

At least 50 primary neurites from immunolabeled images were traced in Image J for each condition and X-Y distance data were analyzed using Matlab software. The angle of each segment was calculated relative to horizontal and all neurite angles were then binned in 10° segments from 10 - 90°. Random outgrowth would be evidenced by a relatively equal distribution among all angle bins. Strong alignment to the horizontal plane would be demonstrated by high population percentages in bins of 20° or less, while strong alignment to multidirectional patterns, i.e. repeating 90° angle steps, would be evidenced by high percentages around 45° alignment angles since the pattern was rotated 45° during imaging. SGSC alignment was determined as previously described by drawing the outline of the cell using Image J software and fitting an ellipse to the cell outline.<sup>1,2</sup>

Preference of SGN primary neurites for the depressed or raised features of the polymer surface was determined by individual measurement of neurite segments on each feature, summing the length of neurite, and calculating the percentage of primary neurite length on each feature. Lengths were measured from immunolabeled images using the measurement tool in Image J (NIH, Bethesda, MD). Depressed and raised features were differentiated by scanning in the z-plane (vertical) with a Leica TCS SP5 confocal microscope. Percent length of primary neurites on depressed and raised features was averaged for at least 100 randomly chosen neurites from each condition.

Neurite turning capability on multidirectional photopolymerized micropatters was measured using Image J primary neurite traces from immuno-fluorescent digital images that were captured as previously described. Trace data, containing X-Y neurite distance coordinates, was analyzed by measuring the angle of consecutive 10  $\mu\text{m}$  length neurite segments using Matlab. Neurite segment angle was measured relative to the horizontal plane. If three consecutive segments, i.e. 30  $\mu\text{m}$  segment of the neurite, had a trajectory difference of at least  $10^\circ$  from the previous three consecutive segments then it was marked as a turning event. At least 50 neurites were scored for each pattern condition.

### Statistics

Statistical analysis was performed using SigmaStat 3.5 software (Systat Software, Chicago, IL). A two-tailed t-test was used to compare cellular alignment between unpatterned and patterned samples followed by a *post hoc* Mann-Whitney Rank Sum Test when normality criteria were not met. Multiple groups were compared by performing a one-way ANOVA followed by a *post hoc* Kruskal-Wallis analysis of variance on ranks and a Dunn's Method multiple comparison procedure. Results were considered statistically significant if  $p < 0.05$ .

### Notes

1. Clarke, J. C.; Tuft, B. W.; Clinger, J. D.; Levine, R.; Figueroa, L. S.; Guymon, A. C.; Hansen, M. R. Micropatterned methacrylate polymers direct spiral ganglion neurite and Schwann cell growth. *Hear. Res.* **2011**, *278*, 96-105.
2. Tuft, B. W.; Li, S.; Xu, L.; Clarke, J. C.; White, S. P.; Guymon, B. A.; Perez, K. X.; Hansen, M. R.; Guymon, C. A. Photopolymerized microfeatures for directed spiral ganglion neurite and Schwann cell growth. *Biomaterials* **2013**, *34*, 42-54.
3. Bryant, S. J.; Cuy, J. L.; Hauch, K. D.; Ratner, B. D. Photo-patterning of porous hydrogels for tissue engineering. *Biomaterials* **2007**, *28*, 2978-2986.
4. Alcantar, N. A.; Aydil, E. S.; Israelachvili, J. N. Polyethylene glycol-coated biocompatible surfaces. *J. Biomed. Mater. Res.* **2000**, *51*, 343-351.
5. Wikipedia. Scanning Electron Microscope.  
[http://en.wikipedia.org/w/index.php?title=Scanning\\_electron\\_microscope&oldid=608525556](http://en.wikipedia.org/w/index.php?title=Scanning_electron_microscope&oldid=608525556) (accessed June 8, 2014).
6. Zheng, J. L.; Gao, W. Q. Differential damage to auditory neurons and hair cells by ototoxins and neuroprotection by specific neurotrophins in rat cochlear organotypic cultures. *Eur. J. Neurosci.* **1996**, *8*, 1897-1905.
7. Lefebvre, P. P.; Vandewater, T. R.; Weber, T.; Rogister, B.; Moonen, G. Growth-Factor Interactions in Cultures of Dissociated Adult Acoustic Ganglia - Neuronotrophic Effects. *Brain Res.* **1991**, *567*, 306-312.
8. Lefebvre, P. P.; Leprince, P.; Weber, T.; Rigo, J. M.; Delree, P.; Moonen, G. Neuronotrophic Effect of Developing Otic Vesicle on Cochleovestibular Neurons - Evidence for Nerve Growth-Factor Involvement. *Brain Res.* **1990**, *507*, 254-260.
9. Malgrange, B.; Lefebvre, P.; Vandewater, T. R.; Staecker, H.; Moonen, G. Effects of neurotrophins on early auditory neurones in cell culture. *Neuroreport* **1996**, *7*, 913-917.
10. Hegarty, J.; Kay, A.; Green, S. Trophic support of cultured spiral ganglion neurons by depolarization exceeds and is additive with that by neurotrophins or cAMP and requires elevation of  $[Ca^{2+}]_i$  within a set range. *J. Neurosci.* **1997**, *17*, 1959-1970.
11. Ripoll, C.; Rebillard, G. A simple technique to efficiently dissociate primary auditory neurons from 5 day-old rat cochleas. *J. Neurosci. Methods* **1997**, *73*, 123-128.
12. Marzella, P. L.; Gillespie, L. N.; Clark, G. M.; Bartlett, P. F.; Kilpatrick, T. J. The neurotrophins act synergistically with LIF and members of the TGF-beta superfamily

- to promote the survival of spiral ganglia neurons in vitro. *Hear. Res.* **1999**, *138*, 73-80.
13. Danneman, P. J.; Mandrell, T. D. Evaluation of five agents/methods for anesthesia of neonatal rats. *Lab. Anim. Sci.* **1997**, *47*, 386-395.
  14. Phifer, C. B.; Terry, L. M. Use of Hypothermia for General-Anesthesia in Prewaning Rodents. *Physiol. Behav.* **1986**, *38*, 887-890.
  15. Hansen, M. R.; Vijapurkar, U.; Koland, J. G.; Green, S. H. Reciprocal signaling between spiral ganglion neurons and Schwann cells involves neuregulin and neurotrophins. *Hear. Res.* **2001**, *161*, 87-98.
  16. Hansen, M. R.; Zha, X. M.; Bok, J.; Green, S. H. Multiple distinct signal pathways, including an autocrine neurotrophic mechanism, contribute to the survival-promoting effect of depolarization on spiral ganglion neurons in vitro. *J. Neurosci.* **2001**, *21*, 2256-2267.
  17. Roehm, P. C.; Xu, N.; Woodson, E. A.; Green, S. H.; Hansen, M. R. Membrane depolarization inhibits spiral ganglion neurite growth via activation of multiple types of voltage sensitive calcium channels and calpain. *Mol. Cell. Neurosci.* **2008**, *37*, 376-387.
  18. Jeon, E.; Xu, N.; Xu, L.; Hansen, M. R. Influence of central glia on spiral ganglion neuron neurite growth. *Neuroscience* **2011**, *177*, 321-334.
  19. McCarthy, K.; DeVellis, J. Preparation of Separate Astroglial and Oligodendroglial Cell-Cultures from Rat Cerebral Tissue. *J. Cell Biol.* **1980**, *85*, 890-902.

## CHAPTER 4

### MICROPATTERNED METHACRYLATE POLYMERS DIRECT SPIRAL GANGLION NEURITE AND SCHWANN CELL GROWTH<sup>1\*</sup>

Significant advances in the functional outcomes achieved with cochlear implantation will likely require tissue-engineering approaches to improve the neural prosthesis interface. One strategy is to direct spiral ganglion neuron (SGN) axon growth in a highly organized fashion to approximate or contact stimulating electrodes. Here we assessed the ability of micropatterns induced by photopolymerization in methacrylate (MA) polymer systems to direct cultured neonatal rat SGN neurite growth and alignment of SG Schwann cells (SGSCs). SGN survival and neurite length were comparable among various polymer compositions. Remarkably, there was no significant difference in SGN survival or neurite length between laminin and non-laminin coated MA polymer substrates, suggesting high biocompatibility with SG tissue. Micropatterning with photopolymerization generated microchannels with a ridge periodicity of 50  $\mu\text{m}$  and channel depths of 0.6-1.0  $\mu\text{m}$ . SGN neurites grew within the grooves of the microchannels. These topographies strongly induced alignment of dissociated SGN neurites and SGSCs to parallel the pattern. By contrast, fibroblasts failed to align with the micropattern suggesting cell specific responses to topographical cues. SGN neurites extending from explants turned to parallel the pattern as they encountered the microchannels. The extent of turning was significantly correlated with angle at which the neurite initially encountered the pattern. These results indicate that SGN neurites respond to microtopographical features and that these features can be used to direct neurite growth in a highly organized fashion.

---

\* Clarke, J. C.; Tuft, B. W.; Guymon, A. C.; Hansen, M. R. *Hear. Res.* **2011**, 278, 96-105.

## Introduction

Neural Deafness typically results from irreversible cochlear hair cell (HC) death followed by degeneration of the associated afferent spiral ganglion (SG) axons and the eventual death of the spiral ganglion neurons (SGNs) themselves.<sup>2-4</sup> Electrical stimulation of SGNs by cochlear implant (CI) electrodes replaces mechanosensory transduction of sound providing hearing sensation for deaf patients. However, current CI technologies provide a limited number of independent channels due to interaction of nearby channels.<sup>5,6</sup> These channel interactions are due, at least in part, to the distance between the neural elements in the modiolus and the stimulating electrodes in the scala tympani. The limited number of channels contributes to the poor spatial and temporal resolution of CIs and limits performance, especially for complex sounds or in environments with competing noise. Given these limitations, there is lively interest in improving the neural prosthesis interface by directing SGN axon regeneration to approximate or even contact the stimulating electrodes.<sup>7-12</sup> However, to be effective, such axonal regrowth would need to be radial, recapitulating the normal pattern of afferent innervation. If successful, such tissue engineering stands to dramatically enhance the neural prosthesis interface and increase the fidelity provided by stimulating electrodes.

Strategies to direct neurite growth have typically relied on the use of micropatterned bioactive molecules.<sup>13-18</sup> Examples include micropatterned stripes of laminin, fibronectin, or poly-L-lysine or stripes coated with EphA1/IgG-Fc-chimera that direct neurite growth from cultured spiral ganglion explants.<sup>19,20</sup> In these cases, neurites grew preferentially on the high concentration laminin stripes and avoided the EphA1/IgG-Fc-chimera stripes. Other studies used soluble neurotrophic or chemoattractive/repulsive factors to guide neurite growth. For instance, SGN neurites grow towards a concentration gradient of neurotrophin.<sup>21-25</sup> In addition to biochemical cues, many cellular processes including growth cones respond to three-dimensional

topographical features in the environment.<sup>26,27</sup> Recently, patterned topographies have emerged as another method to direct cellular patterning such as axon growth.<sup>28,29</sup> To begin to understand how SGN neurites respond to environmental topographical features we assessed the ability of stable topographic microfeatures in methacrylate polymers to guide SGN neurite growth.

Methacrylates (MAs) were among the first successful polymer systems to serve as functional biomaterials.<sup>30</sup> Their biocompatibility was first demonstrated during the development of the intraocular lens<sup>31,32</sup> and has since been confirmed in contact lens applications,<sup>33</sup> dental resins,<sup>34</sup> cellular encapsulation,<sup>35</sup> and bone cements.<sup>36</sup> Beyond biocompatibility, MAs also provide a versatile range of chemistries that allows for the design of materials with tailored chemical and mechanical properties to suit intended biological interfaces. While various methods exist to generate these biomaterials, photopolymerization, i.e. the use of light to produce polymers, has emerged as a production platform of choice due to its mild reaction conditions and high reaction rates.

Moreover, photopolymerization offers unique advantages over other polymerization techniques that include: reaction environments free of volatile organic compounds or other potentially cytotoxic species, low energy input, and spatial control of the polymerization.<sup>37</sup> Recent studies demonstrated the versatility of this technique for biological applications. For example, a photopolymerization reaction is mild enough to coencapsulate plasmid DNA and cells in a degradable, methacrylate hydrogel. Subsequent transfection of either encapsulated or plated cells is demonstrated upon release of the plasmid DNA from the gel.<sup>38</sup> Further, 3D tissue engineering scaffolds with a range of pore sizes and architectures are generated through a single photopolymerization step in order to determine the effect of substrate geometry and porosity on cell behavior and *in vivo* reaction.<sup>39</sup>

Interestingly, specific surface topographic features such as those that could be formed via photopolymerization influence a variety of cellular responses including

alignment and growth of Schwann cells (SCs) and fibroblasts.<sup>40-42</sup> SCs support and guide axon regeneration and regenerating SGNs closely align with SCs.<sup>43</sup> Furthermore, micropatterning of biomolecules to direct SC orientation also enhances and guides dorsal root ganglion neurite growth.<sup>44</sup>

Our study focuses on the use of mixtures of two MA monomers: hexyl methacrylate (HMA) and 1,6-hexanediol dimethacrylate (HDDMA), polymerized in varied proportions. These polymers, with or without laminin coating, supported SGN survival and neurite growth in culture. Photopolymerization allowed generation of micropatterns in the polymers that directed neurite growth in SG explants and dissociated cultures. We also found that micropatterned polymers promoted alignment of spiral ganglion Schwann cells (SGSCs) but not fibroblasts. Taken together these results demonstrate the biocompatibility of MA polymers with SG tissue and the ability of micropatterned topographic features to direct SGSC alignment and SGN neurite growth.

## Experimental

### Photopolymerization of Physical Guidance Cues

Monomer mixtures of HMA and HDDMA (Aldrich) were prepared with 1 wt% of 2, 2'-dimethoxy-2-phenylacetophenone as the photoinitiator (Ciba, Tarrytown, NY). A sample volume of 20  $\mu$ L was pipetted onto glass microscope slides and was covered with a 50  $\mu$ m periodicity glass-chrome Ronchi rule photomask (Applied Image Inc., Rochester, NY) for patterned samples, or with a glass coverslip for unpatterned samples. Polymer samples were cured under a medium pressure mercury arc lamp (Ace Glass) for 1 to 3 minutes (Fig 4.1). Following polymerization the samples were rinsed copiously with 95% ethanol to remove residual monomer and allowed to air dry before use.

Polymer topography was characterized with a Wyko NT 1100 optical profiling system (Veeco, Plainview, NY) with 20X and 50X objectives (Fig 4.3). Nine channel

amplitude measurements were taken at random locations for each sample, and the average value was reported as the general amplitude of the substrate.

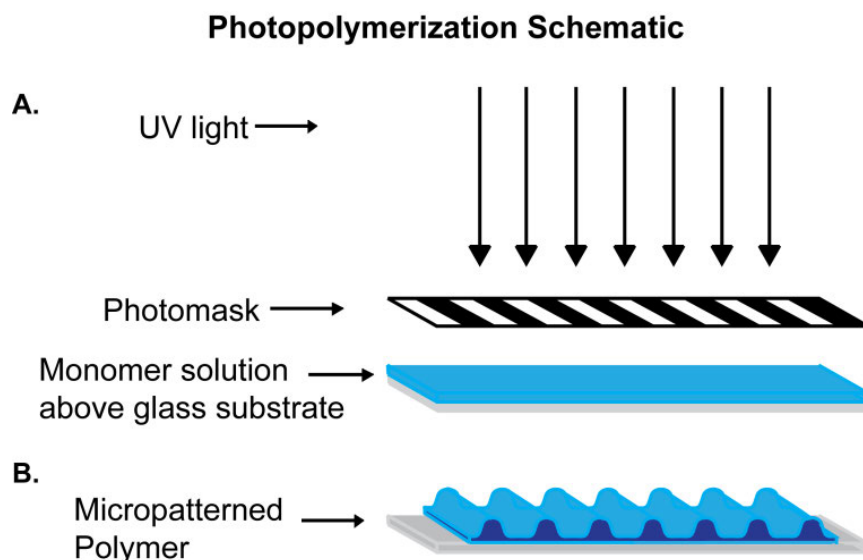


**Figure 4.1.** Schematic of a photopatterning process. **A)** Monomer solution is spread over a glass substrate. UV light passes through the mask photoinitiating the system. **B)** Monomer that is exposed to UV polymerizes quickly and forms ridges while monomer in shadowed regions polymerizes slowly to form grooves between ridges.

### Spiral Ganglia Dissection and Culture

The institutional animal care and use committee at the University of Iowa approved all protocols used in this study. Spiral ganglia (SG) were isolated from postnatal day 4–5 (P4-P5) rats euthanized under cold anesthesia after placing the pups in a cardboard box on ice for 20 min.<sup>45,46</sup> The temporal bone was harvested and the otic capsule was dissected under operating microscope in ice cold PBS. The bony cochlear capsule was removed, followed by the spiral ligament. The organ of Corti was removed, transecting the outer radial fibers, leaving the SGNs within the modiolus. Modiolar bone

and surrounding connective tissue were removed. Ganglia were collected in ice cold Hanks' balanced salt solution with calcium and magnesium (HBSS+/, Gibco, Carlsbad, CA). When used as explants, SGs were cut into 4 pieces and placed onto the prepared culture slides.

Dissociated SG cultures from P3-5 rat pups, prepared as previously described were plated in 8 mm cloning cylinders placed on polymer surfaces with sterile silicon grease to seal the edges.<sup>47-49</sup> Cultures were grown on unpatterned polymers both with and without laminin (20  $\mu\text{g}/\text{mL}$ ) coating. Laminin coated glass slides were used as a control. Cultures were maintained in Dulbecco's Modified Eagle Medium (DMEM) supplemented with N2 additives and 5% fetal bovine serum. Neurotrophin-3 (NT-3) (50 ng/ml) and Brain Derived Neurotrophic Factor (BDNF) (50 ng/ml) were included in medium to promote SGN survival and neurite growth.<sup>48-50</sup> After 72 h, the cultures were fixed with 4% paraformaldehyde and stained with anti-S100 and anti-neurofilament 200 (NF200) antibodies (1:400, Sigma-Aldrich, St. Louis, MO) to label SGSCs and SGNs, respectively, followed by Alexa 488 and Alexa 546 conjugated secondary antibodies. Hoechst 3342 (10  $\mu\text{g}/\text{ml}$ ) was used for nuclear staining. Digital epifluorescent images were captured on a Leica DMIRE2 microscope (Leica Microsystems, Bannock, IL) with Leica DFC350FX digital camera and Metamorph software (Molecular Devices, Silicon Valley, CA). SGN cell survival was determined as before by counting the total number of viable SGNs per cloning cylinder.<sup>47</sup> Only NF200-positive SGNs with non-pyknotic nuclei were considered viable. Neurite length was calculated from digital images of epifluorescence staining by measuring the longest process of 30 randomly selected SGNs per well using the measurement tool in Image J (NIH, Bethesda, MD). Spiral ganglion explants, prepared by cutting each ganglion into 4 segments, were grown in similar conditions and fixed after 3-4 days of growth for immunofluorescent staining and analysis.

### Spiral Ganglion Schwann Cell and Fibroblast Cultures

To determine the influence of the micropatterns on fibroblasts and SC alignment in the absence of neurites, dissociated SG cultures lacking neurons were prepared as previously described.<sup>48</sup> Briefly, spiral ganglia from P3-5 rat pups were enzymatically and mechanically dissociated and plated onto patterned or unpatterned HMA/HDDMA polymers in DMEM/N2 media lacking neurotrophic factors with 5% FCS to support the fibroblasts. After 2 days, the cultures were fixed and immunostained with anti-S100 antibodies. Cell orientation was determined by drawing the outline of the cell using Image J software and fitting an ellipse to the cell outline. The angle of the long axis of the ellipse relative to the pattern ( $\theta$ ) was then measured in Image J.

### Determination of SGN Neurite Alignment to Patterns

To determine the alignment of neurites to micropatterns in dissociated SG cultures, neurite length was measured in Image J as previously described.<sup>50</sup> This measurement was then compared to the distance from the cell body to the nerve terminus in a straight line along the micropattern (Fig. 4.4A). The neurite length divided by the end-to-end distance along the polymer was calculated to represent the alignment to the pattern. A number closer to unity (1) represents a neurite that closely follows the pattern. A wandering neurite, not aligned to the pattern, would have a higher ratio of neurite length to end-to-end distance. In order to analyze neurite alignment on unpatterned polymer substrates, neurite length was compared to end-to-end distance along the horizontal plane (Fig. 4.4).

To determine the extent that micropatterns influenced neurite turning in explants, the angle of the neurite relative to the pattern was measured when the neurite first encountered the pattern (initial angle) and compared to the angle of the neurite terminus relative to the pattern (terminal angle). The difference between the initial and terminal angle of the neurite ( $\Delta\theta$ ) was calculated to quantify the extent of turning induced by the

micropattern (Fig. 4.8A). In some cases, the initial portion of individual neurites remained in bundles as they exited the explant and was not resolvable by epifluorescent microscopy. In each case, the neurites within the bundle traveled in the same trajectory and the angle of the bundle was measured to determine initial angle of the neurites comprising it.

### Statistics

For statistical analysis of SGN survival and SG neurite growth a one-way ANOVA was performed with post hoc Tukey test using SigmaStat software (Systat Software, Chicago, IL). A two-tailed t-test was used to compare neurite alignment on unpatterned vs patterned polymers. To compare SGSC, fibroblast alignment on patterned and unpatterned polymers, a one way ANOVA with post-hoc Dunn's test was used.

## **Results**

### MA Polymers Support SGN Survival and Neurite Growth

Varying the relative proportion of HMA and HDDMA monomer determines the cross-link density and polarity of the polymer. These properties are known to influence cell-material interactions.<sup>51,52</sup> Thus, we first assessed the ability of varied proportions of HMA and HDDMA polymer without micropatterns to support SGN survival and neurite growth (Fig 4.2). Polymer composition ranged from 20% - 80% HMA with the remaining percentage composed of HDDMA. A subset of polymers were coated with laminin. Equal volumes of dissociated SG cultures were grown in 8 mm cloning cylinders placed on the polymer surfaces. Control cultures were maintained on laminin-coated glass slides. After 72 hrs, the cultures were fixed and immunostained with anti-NF200 antibodies. SGN and SGSC growth was robust on all compositions of HMA/HDDMA polymers both with and without laminin coating (Fig. 4.2B). There was no significant difference in SGN survival

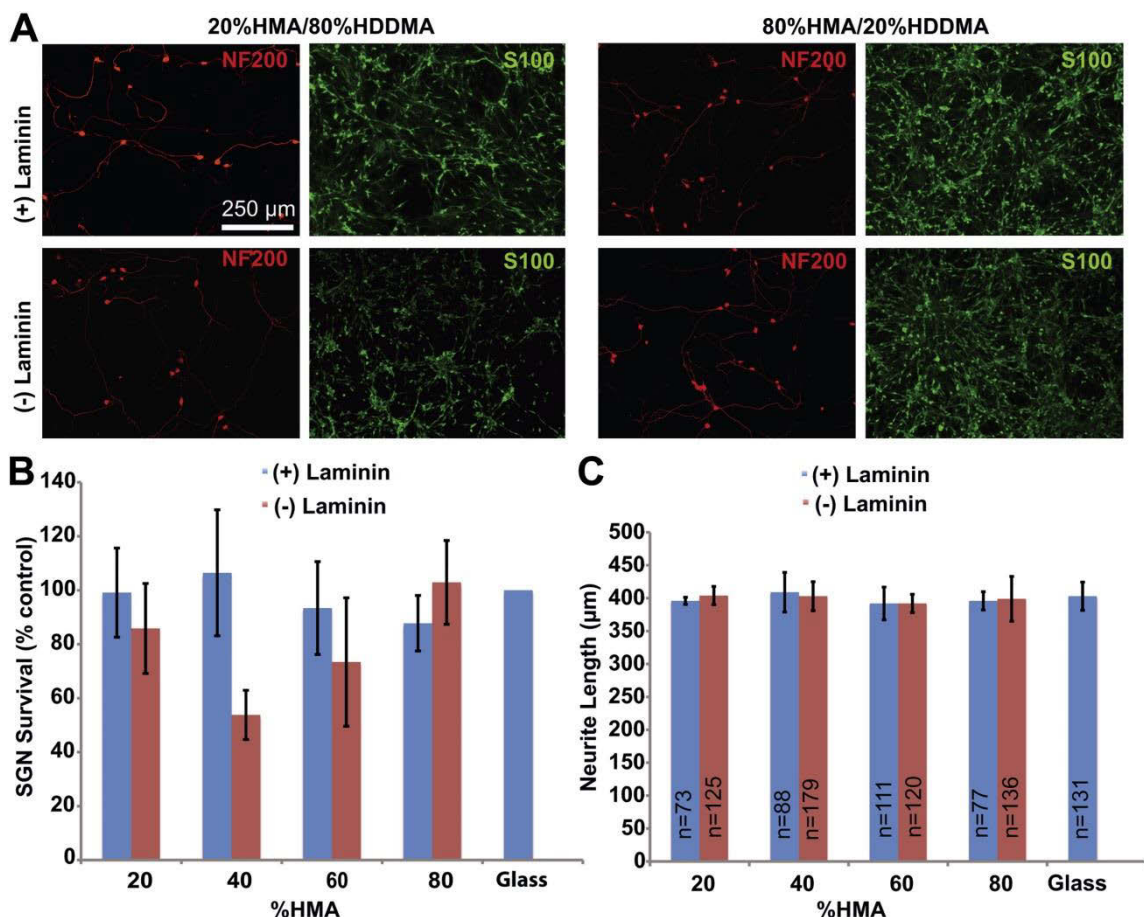


**Figure 4.2.** SGN survival and neurite growth on HMA/HDDMA unpatterned polymer with and without laminin. **A)** Dissociated SG cultures grown on 20%HMA/80%HDDMA (left) and 80%HDDMA/20%HMA (right) and immunostained with anti-NF200 (red) and anti-S100 (green) antibodies. Scale bar = 250  $\mu\text{m}$ . The top row represents cultures on laminin-coated polymer and the bottom row represents cultures on polymers without laminin coating. **B)** SGN survival on indicated MA polymer composition with or without laminin coating. Legend indicates percent of HMA in HMA/HDDMA mixture. Neurons were cultured in three cloning cylinders for each condition with laminin coated glass used as control. Experiments were repeated in triplicate and survival was determined relative to control for each set of cultures. The average number of viable neurons counted across all controls was 521  $\pm$  258 (mean  $\pm$  SD) per well. There was no statistically significance difference in neurite survival among the different conditions ( $p = 0.306$ , one way ANOVA). **C)** SGN neurite length on indicated MA polymer composition with or without laminin coating. Legend indicates percent of HMA in HMA/HDDMA mixture and “n” represents the number of neurites measured in each condition. There was no statistically significance difference in neurite length among the different conditions ( $p = 0.608$ , one way ANOVA)

between any of the individual polymer compositions and control cultures, nor between the various polymer compositions ( $p = 0.306$  one way ANOVA). While SGN morphology appeared similar on laminin and non-laminin coated polymers and glass, SGSCs exhibited a decrease in spindle morphology on polymers without laminin coating when compared to those grown on laminin coated polymer or glass.

Similar to neuronal survival, there was no significant difference in neurite length with variations in polymer composition ( $p = 0.608$  one way ANOVA) (Fig. 4.2C). Further, MA polymers, including those without laminin coating, supported neurite growth to the same extent as laminin-coated glass. These results confirm that MA polymers support SGN survival, neurite growth and SGSC growth. Remarkably, polymers lacking laminin coating supported SGN survival and neurite growth comparable to laminin-coated substrates.

#### Photopatterning of Physical Guidance Cues

Micropatterns were generated on sample surfaces by using the spatial control afforded by the photopolymerization process. Polymerization principally occurs in regions exposed to light irradiance and proceeds more slowly in shadowed regions. Therefore, spatial control of the reaction is achieved by directing the light to areas intended for the polymerization while blocking or reducing the amount of light absorbed at others. In this study, UV light was directed by placing a simple photomask, with 25  $\mu\text{m}$  wide alternating bands (periodicity of 50  $\mu\text{m}$ ) that either transmit or reflect light, between the light source and monomer solution (Fig 4.1). Polymerization occurs rapidly under transparent bands that nearly transmit the full light intensity from the source which results in raised ridges. Reflected light within the sample and migration of reactive chains cause slow polymerization in areas under the reflective bands and generate grooves between ridges. As a result, a pattern of parallel micro-ridges and grooves of uniform width and amplitude rapidly develop across the entire substrate surface in a single

fabrication step (Fig 4.1). As expected, each ridge and groove was approximately 25  $\mu\text{m}$  wide. Smooth transitions between the ridges and grooves were observed in place of sharp features generated by other photolithographic methods. Typical sample amplitude, from the highest point on ridges to the lowest point in adjacent grooves, ranged from 0.6 to 1.8  $\mu\text{m}$  depending on polymerization conditions (Fig 4.3).

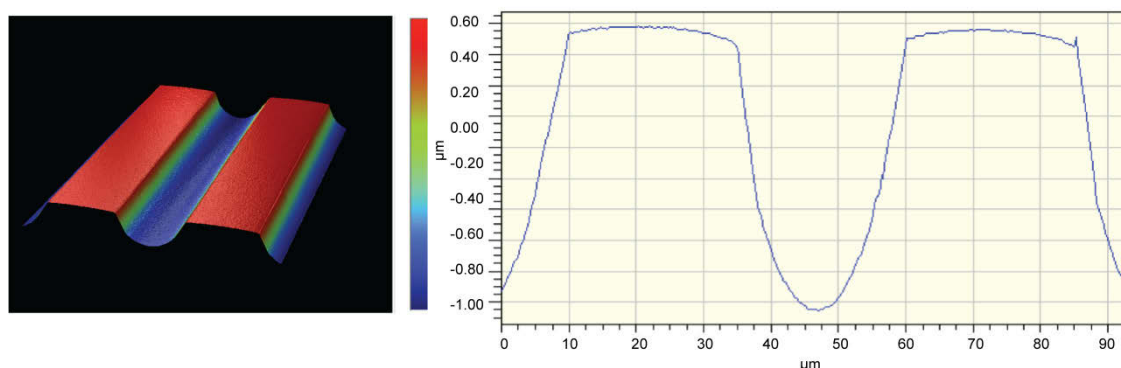


**Figure 4.3.** Examples of a multicolor 3D (left) and graphical (right) schematic derived by interferometry characterizing photopolymerized microridges in methacrylate polymers with channel depth of  $\sim 1.8 \mu\text{m}$ .

#### Micropatterned Polymers Direct SGN Neurite Growth

Having demonstrated the ability of MA polymers to support SG cell growth and survival, we next examined the influence of micropatterning on *de novo* neurite growth. Dissociated spiral ganglion cultures were plated on patterned or unpatterned 40%HMA/60%HDDMA polymers and maintained in BDNF and NT-3 for two days. In these experiments, the ridge periodicity was 50  $\mu\text{m}$  and the channels were between 0.6 and 1  $\mu\text{m}$  deep. Fixed cultures were immunostained with anti-NF200 antibody and digital epifluorescence images were captured. Dissociated SGN neurites wandered randomly on unpatterned HMA/HDDMA (Fig. 4.4A), similar to neurites on laminin coated slides.<sup>50</sup>

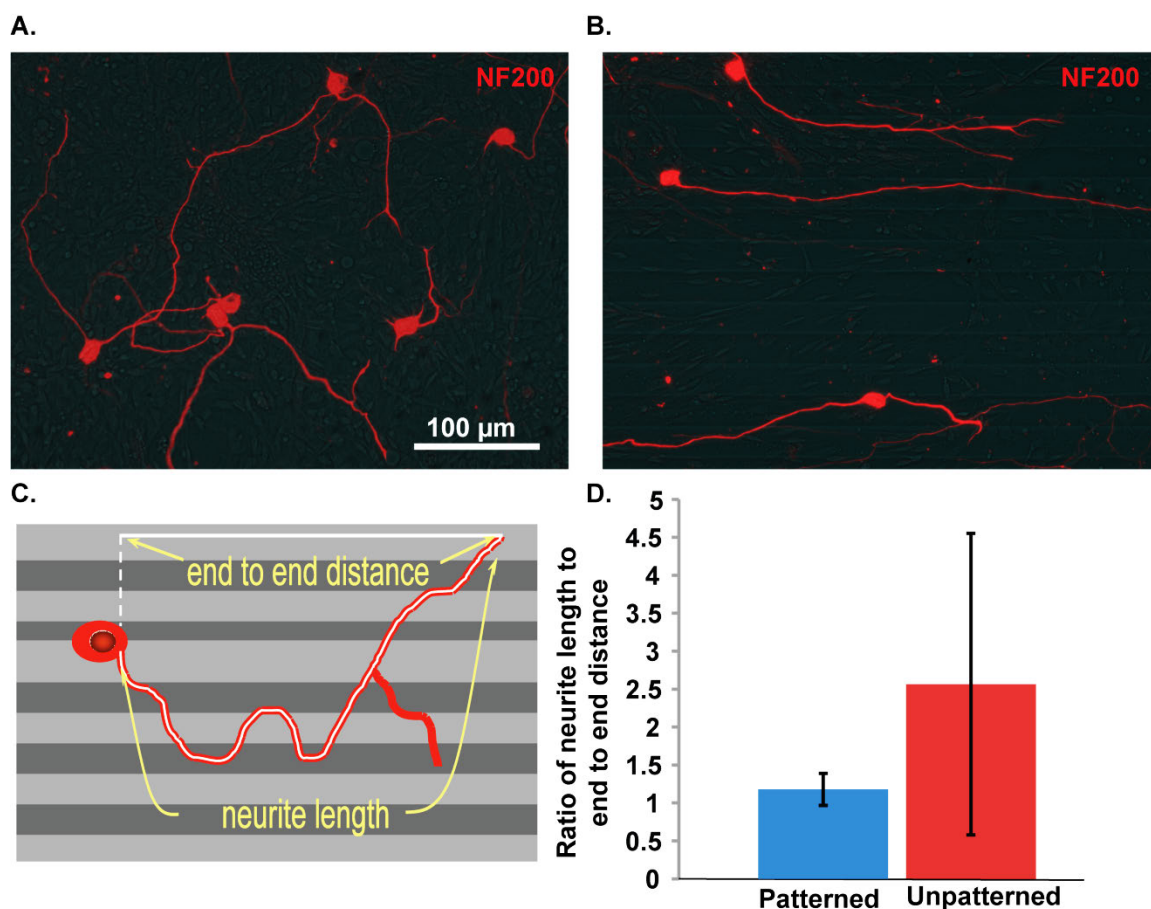


**Figure 4.4.** Dissociated SGN neurite growth on unpatterned or patterned HMA/HDDMA. **A,B)** Dissociated SG cultures grown on unpatterned or patterned HMA/HDDMA and immunostained with anti-NF200 antibody. Neurite growth on unpatterned polymer is random whereas neurites on micropatterned polymers parallel the pattern. **C)** Drawing represents measurement of neurite length as well as the measurement of cell body to nerve terminus parallel to the pattern used to assess the extent of neurite alignment to pattern. **D)** Mean ( $\pm$  SD) ratios of neurite length to end-to-end distance for neurites on unpatterned or patterned HMA/HDDMA are significantly different by Student's unpaired two-tailed t-test ( $p < 0.001$ ).

By contrast, dissociated SGN neurites closely aligned with micropatterned HMA/HDDMA (Fig. 4.4B). To evaluate the extent of alignment to the pattern, we compared the ratio of the overall neurite length with the end-to-end distance of a straight line drawn from the cell body to the neurite terminus in parallel with the micropattern. A

ratio of neurite length to end-to-end distance with values close to unity implies that the neurite closely follows the pattern whereas a ratio significantly greater than one implies that the neurite deviates from the pattern. The ratio of neurite length to end-to-end distance was  $1.20 \pm 0.32$  (mean  $\pm$  SD) on patterned HMA/HDDMA and  $2.64 \pm 2.34$  (mean  $\pm$  SD) on unpatterned HMA/HDDMA ( $p < 0.001$ , Student's unpaired two tailed t-test). Thus, neurites on unpatterned HMA/HDDMA tend to grow in random directions reflected by the increased mean ratio of neurite length to end-to-end distance and the larger standard deviation. By contrast, nearly all neurites on patterned polymer closely align with the pattern. Thus, micropatterns with channel depth between 0.6 and 1  $\mu\text{m}$  strongly direct dissociated SGN neurite growth *in vitro*.

#### SGSC Alignment in the Absence of Neurites

We noted close alignment of SGSCs with SGN neurites and with the pattern. Since growing SGN neurites closely align with SCs,<sup>53,54</sup> it was difficult to determine whether the SC alignment was due to the influence of the pattern and/or the neurites. Thus, we next sought to determine the extent to which micropatterned MA polymers influence the alignment of SGSCs in the absence of neurites. Dissociated SG cultures were maintained in the absence of neurotrophic factors. In these conditions, over 90% of the neurons die.<sup>48,49</sup> Cultures were immunostained with anti-S100 antibody to identify SCs and anti-NF200 antibody to verify lack of SGN processes in the vicinity. Fibroblasts were identified based on typical broad based stellate morphology and lack of S100-immunoreactivity. Subsets of cultures were immunostained with anti-vimentin antibodies to verify the fibroblastic morphology. Cell orientation was determined by drawing the outline of the cell using Image J software and fitting an ellipse to the cell outline. The angle of the long axis of the ellipse relative to the pattern ( $\theta$ ) was then measured in Image J (Fig. 4.5). The mean ellipse angle was  $42.1 \pm 24.1$  (mean  $\pm$  SD) for SCs on unpatterned

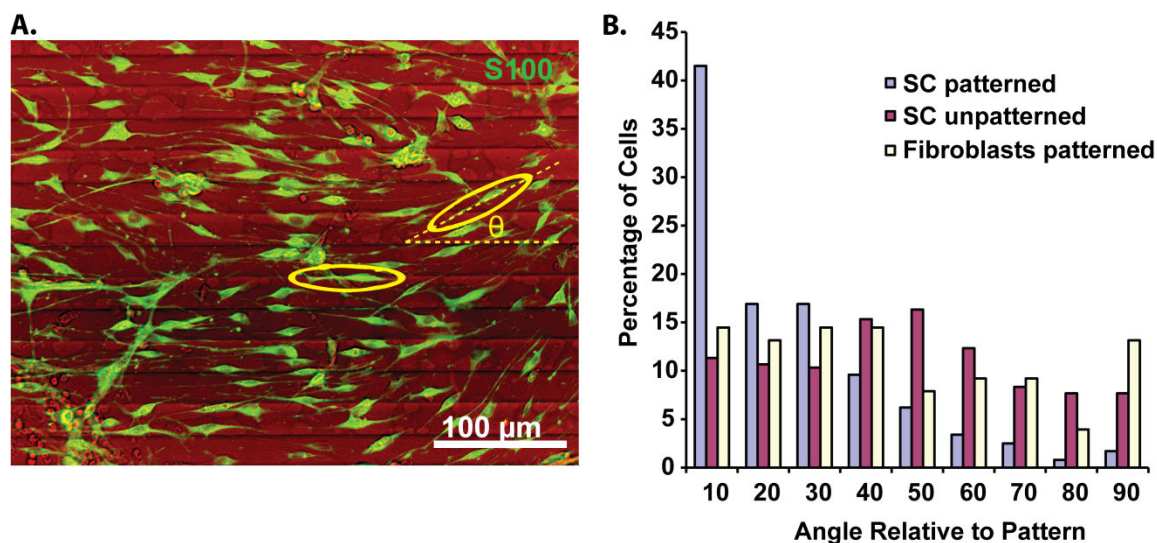


**Figure 4.5.** Spiral ganglion Schwann cells, but not fibroblasts, align with micropatterns in the absence of neurites. **A)** Cell alignment was determined by measuring the angle ( $\theta$ ) of an ellipse fitted to the major axis of the cell relative to the pattern. **B)** Histogram of orientation angle for SCs and fibroblasts on patterned or unpatterned polymers ( $n = 354$ , 300 and 76 for SC on patterned polymer, SC on unpatterned polymer and fibroblasts on patterned polymer respectively). Over 75% of SCs on patterned polymer were oriented within 30 degrees to the pattern. The difference in alignment of SCs on patterned polymers vs SC's on unpatterned polymers and fibroblasts on patterned polymers was significant ( $p < 0.001$ , ANOVA with post-hoc Dunn's Method).

HMA/HDDMA,  $40.4 \pm 26.9$  (mean  $\pm$  SD) for fibroblasts on patterned HMA/HDDMA, and  $20.3 \pm 19.9$  (mean  $\pm$  SD) for SCs on patterned HMA/HDDMA ( $p < 0.001$ , ANOVA with post-hoc Dunn's Method revealing significant difference between orientation of SCs on patterned polymer with that of SCs on unpatterned polymer as well as fibroblasts on patterned polymer). We considered cells with an ellipse angle less than 10 to be aligned with the pattern. On unpatterned HMA/HDDMA, only 11.3% of the SCs aligned to the horizontal whereas 41.5% of SCs on patterned HMA/HDDMA were aligned to the pattern (Fig. 4.5). Fibroblasts failed to align with patterned HMA/HDDMA. Thus, SCs and fibroblast behave differently on the micropatterned HMA/HDDMA polymers used

here implying that the ability of these micropatterns to induce cell alignment depends on cell-type.

#### SGSCs Remain Aligned to SGN Neurites

Although most SGN neurites and SGSCs remain closely aligned with the micropatterns, there are occasional primary neurites or branches that fail to parallel the pattern. We asked whether the SCs associated with these wandering neurites would

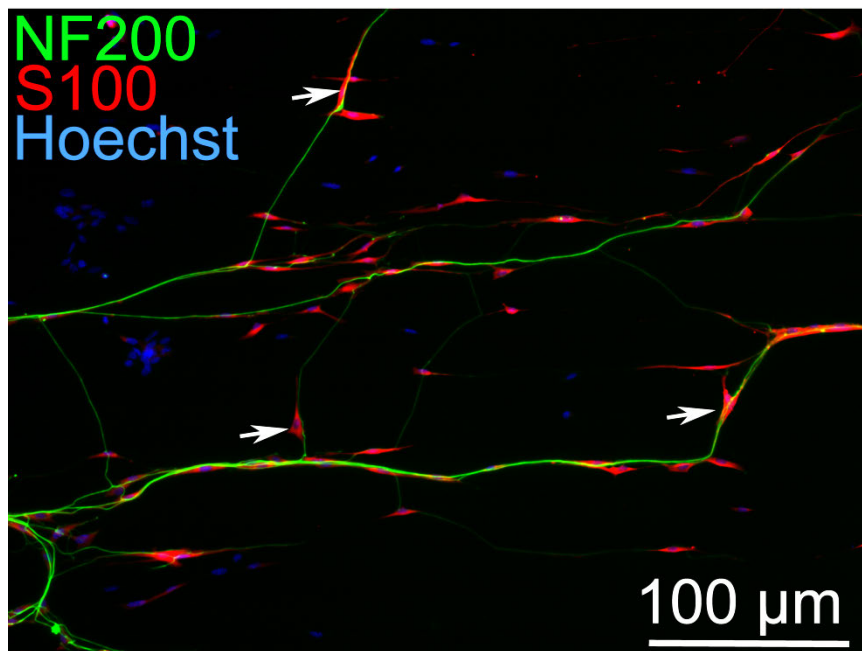


**Figure 4.6.** Spiral ganglion Schwann cells remain closely associated with neurites even when they are not in line with the pattern. Dissociated SG culture on patterned HMA/HDDMA and immunostained with anti-NF200 (red) and anti-S100 (green) antibodies. Arrows denote SCs aligned with neurites that fail to follow the pattern, which is parallel to the horizontal plane.

parallel the pattern or whether they would align themselves with the neurites. In cultures immunolabeled with anti-NF200 and anti-S100 antibodies, we examined the relationship

between neurite and SC when neurites do not follow the micropattern. In each case, the SCs associated with the neurites remained aligned to the direction of the neurite rather than the pattern (Fig. 4.6).

#### Turning of Neurites from SG Explants *in vitro*

Above we demonstrated that MA micropatterns strongly promote alignment of *de novo* neurite growth from dissociated SGNs. To determine whether the micropattern could induce turning of an already existing neurite we used SG explants. These were placed in a central area lacking patterned polymer allowing the neurites to extend out from the explant until they encountered the pattern. Control explants were grown on unpatterned polymers or laminin-coated glass. As shown in Figure 4.7, HMA/HDDMA polymers supported robust neurite outgrowth. Neurites extend radially from explants initially until encountering the micropattern which induces neurites to turn parallel to the pattern. Together with the neurites, SGSCs extended several hundred microns from the explant, however, S100-negative cell outgrowth was restricted, traveling only a fraction of the distance from the explant when compared to S100-positive SGSCs and their associated neurites (Fig 4.7).

To quantify the influence of the pattern on SGN neurite growth, we measured the angle of neurites relative to the pattern as described in the methods section. On glass (n = 69 neurites) and unpatterned polymers (n = 150), neurites extended radially with no consistent directional turning, whereas neurites on patterned polymers (n = 108) consistently turned to parallel the pattern.

Scatterplots of the angle of the initial neurite segment relative to the pattern compared with the difference between the initial and terminal angle relative to the pattern ( $\Delta\theta$ ) illustrate the influence of the pattern on neurite growth (Fig. 4.8). If neurites grow radially and do not turn relative to the pattern, the  $\Delta\theta$  is low and does not correlate with the initial angle to the pattern. Turning of a neurite to parallel the pattern results in strong

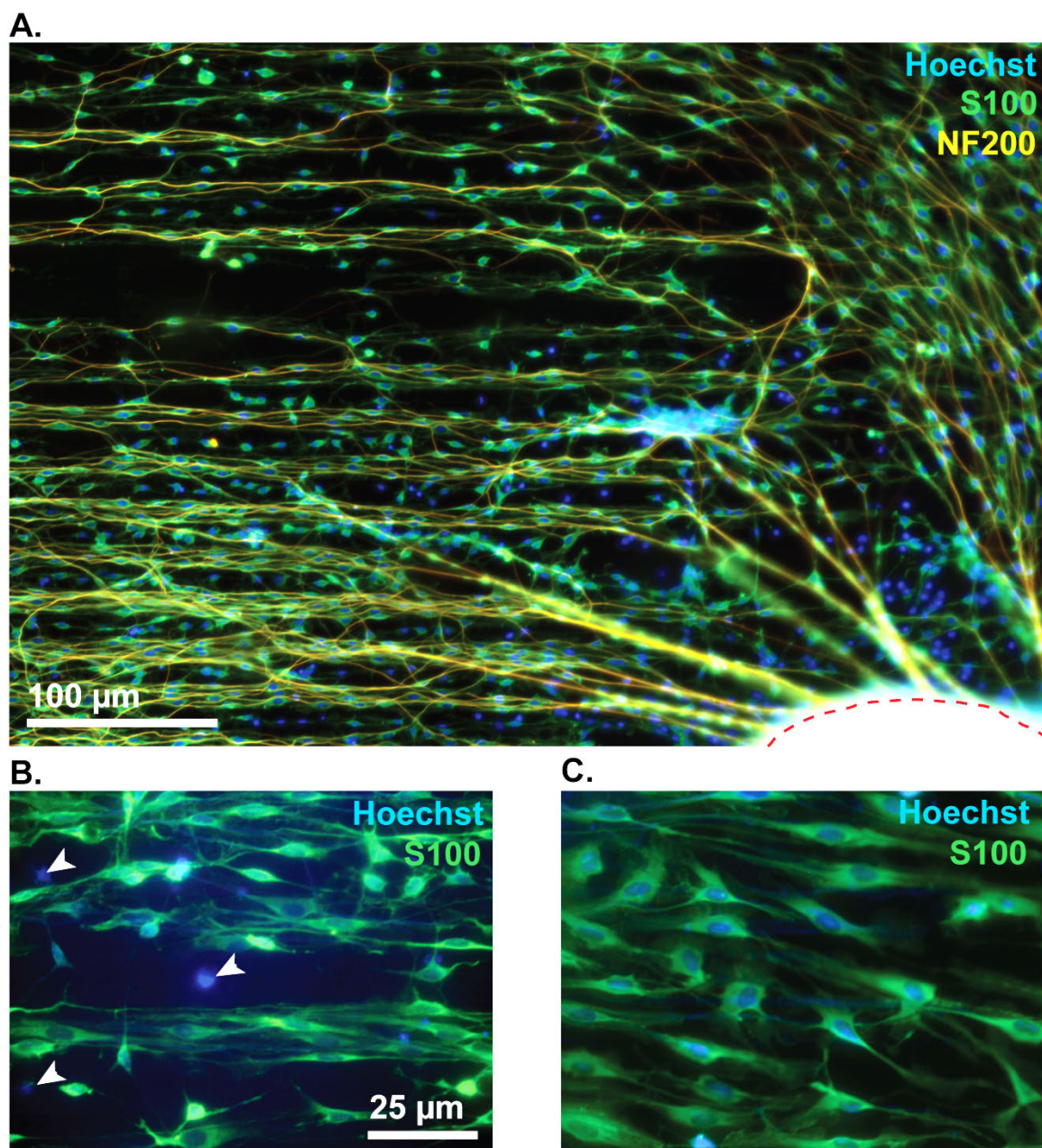


**Figure 4.7.** Spiral ganglion explant on patterned HMA/HDDMA polymer. **A)** The explant body is outlined with a dashed red line on the bottom right corner. NF200-labeled neurites (yellow) extend initially from the explant in a radial fashion and are subsequently induced to turn parallel to the pattern which is oriented along the horizontal plane. Anti-S100 antibody (green) and Hoechst (blue) were used to label SCs and nuclei respectively. Notably, there are several S100-negative cell nuclei clustered close to the explant, as exemplified in the higher magnification images below. **B)** White arrowheads indicate S100-negative cell nuclei. **C)** Image taken further away from the explant ( $\sim 200 \mu\text{m}$ ) demonstrating that all nuclei are associated with S100-positive cells. The

#### Figure 4.7. Continued

micropatterned MAs support SC outgrowth more favorably than S100-negative cells such as fibroblasts.

correlation of the  $\Delta\theta$  with the initial angle. As shown in the scatterplots (Fig. 4.8), the extent of neurite turning ( $\Delta\theta$ ) strongly correlates with the initial angle on patterned polymer ( $r = 0.89$ ,  $p < 0.001$ ), but not on unpatterned polymer or glass ( $r = 0.05$ ,  $p = 0.56$  and  $r = 0.20$ ,  $p = 0.1$ , respectively). Thus, on patterned polymers, the extent of neurite turning depends directly on the angle at which the neurite encounters the pattern. For example, neurites that encounter the pattern with a large initial angle (close to perpendicular) eventually turn to parallel the pattern as exhibited by their large degree of turning (Fig 4.8D). Therefore, on the described topographic features, final alignment of terminal neurite segments appears to be independent of their initial angle relative to the pattern. These results demonstrate that micropatterned methacrylate polymers strongly direct neurite growth and induce turning of established neurites independent of the original growth direction.

#### Neurites Grow within Microchannel Grooves

To determine the location of neurites in the micropatterns, we used laser scanning confocal microscopy to create z-stacks of cultures grown on micropatterned MA polymers and immunostained with anti-NF200 and anti-S100 antibodies. Images were collected every 0.3  $\mu\text{m}$  beginning in the unpatterned area of the polymer and continuing through the thickness of the pattern (typically  $\sim 3 \mu\text{m}$ ). In these stacks, it is easy to distinguish the ridges from the grooves since the ridges appear as acellular stripes lacking S100 immunoreactivity whereas the grooves are the stripes that first appear in the stack with cellular labeling. As shown in Fig. 4.9, SGN neurites grew within the grooves of the

micropatterned HMA/HDDMA polymers. The darker stripes running horizontally across Fig. 4.9 denote acellular regions, which represent ridges. The NF200 positive neurite remained in the cell-filled groove between ridges. This point is also illustrated in a stack of images rotated to view down the x-axis through the depth of the channels (Fig. 4.9). The NF200 positive neurite (red) remained in the groove.

### Discussion

Significant further advances in cochlear implant technology will likely require tissue-engineering approaches to enhance the neural prosthesis interface.<sup>55</sup> Use of defined substrate patterns has recently emerged as a potential tool to precisely control patterns of neural growth and circuitry. Here we leveraged the biocompatibility of MA polymers coupled with our ability to induce stable microchannels by photopolymerization to begin to explore the response of SGNs and SGSCs to specific topographical features. Our results demonstrate the ability of SG explants and dissociated cultures to survive and grow on various polymethacrylate substrates both with and without laminin extracellular matrix coating. These results are consistent with the well-established biocompatibility of MA polymer systems. Further, our data indicate that SGNs tolerate changes in the monomer proportions without substantial impact on survival or neurite outgrowth. This broad biocompatibility with neural cells may prove advantageous in future application by allowing engineers to maximize the physical characteristics of a potential polymer without compromising the tissue interface.<sup>7</sup>

In addition to biocompatibility, MAs are useful for cellular studies that require control of spatial features since they readily undergo photopolymerization in the presence of a photoinitiator.<sup>39</sup> The spatial and temporal control afforded by photopolymerization, in addition to its mild reaction conditions make it a facile fabrication method to generate designed microtopographic features for the study of cellular response and alignment to

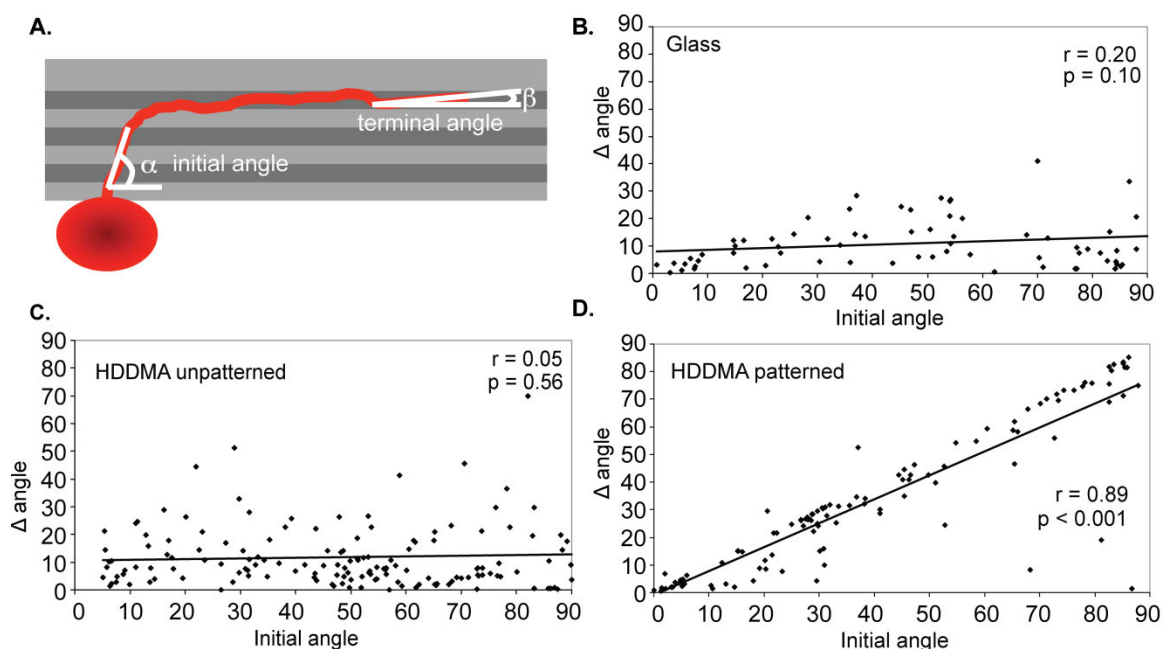


**Figure 4.8.** Micropatterned HDDMA induced turning of SGN neurites from SG explants. **A)** The initial neurite angle relative to the pattern was compared to the angle change from initial to terminal segment ( $\Delta\theta$ ) to determine the extent of turning by neurites in patterned and unpatterned polymer environments. **B-D)** Scatterplots of SGN neurite growth on glass (B), unpatterned HDDMA (C) and HDDMA with micropatterning (D) demonstrate that neurite growth on micropatterned HDDMA has a direct correlation between the initial angle to the pattern and the angle change between the initial and terminal neurite segment.

patterned polymer substrates. Furthermore, process parameters such as light intensity and photoinitiator concentration of this single fabrication step can be modified to create a range of channel widths, depths, and curvatures that may be tailored to elicit varied cellular responses. For example, the width of the parallel micro-ridges and grooves can be modulated by varying the periodicity or band spacing of the photomasks. Moreover, topographic features such as total ridge amplitude and ridge-groove curvature can be manipulated by the temporal control enabled by photopolymerization in the form of total light dosage to the substrate or duration of light application. This spatial and temporal

control will allow future investigations to develop and characterize critical topographic features that guide SGN neurite growth and SC alignment in order to improve the neural interface.

Enhancement of the CI prosthesis neural interface will likely require regrowth of peripheral SGN axons towards a stimulating electrode in an organized, radial pattern reflecting the normal afferent cochlear innervation.<sup>11,55</sup> Our results demonstrate a strong influence on SGN neurite guidance provided by micropatterns. Previous studies found that laminin patterned stripes result in SC alignment and hence enhanced neurite regeneration.<sup>13-15,17,18,56</sup> Consistent with our results, topographical microfeatures generated by physical stamps (e.g. PDMS) promote alignment of PC12 cell processes.<sup>57</sup> Further, a combination of microgrooves and laminin coating in the grooves acted synergistically to direct dorsal root ganglion neurite growth.<sup>56,57</sup> Thus, impregnation of micropatterned methacrylate polymers with one or more species of bioactive molecules may further enhance SG neurite regeneration and provide additional directional cues.

In contrast to the sharply defined microfeatures generated by physical stamps, the photopolymers used here provide unique gradually sloped, shallow channeled characteristics that nevertheless induced SGSC alignment and SG neurite guidance in both explants and dissociated cultures. Further studies shall elicit the manner and order in which they align. The SG neurite growth cone could be influenced by the subtle topographical changes in the center of the channel, or it could respond to the channel walls, inducing a directional change back to the center of the trough as the neurite meanders within the confines of the channel.

Alternative strategies to guide neurite regeneration include the use of soluble factors.<sup>10,22,23,58</sup> These present potential hurdles in the context of CIs, such as maintaining a precise concentration gradient of bioactive molecules in the direction of the CI electrode and the need to maintain bioactivity and stability through the production process. The use of physical cues overcomes many of these potential limitations.

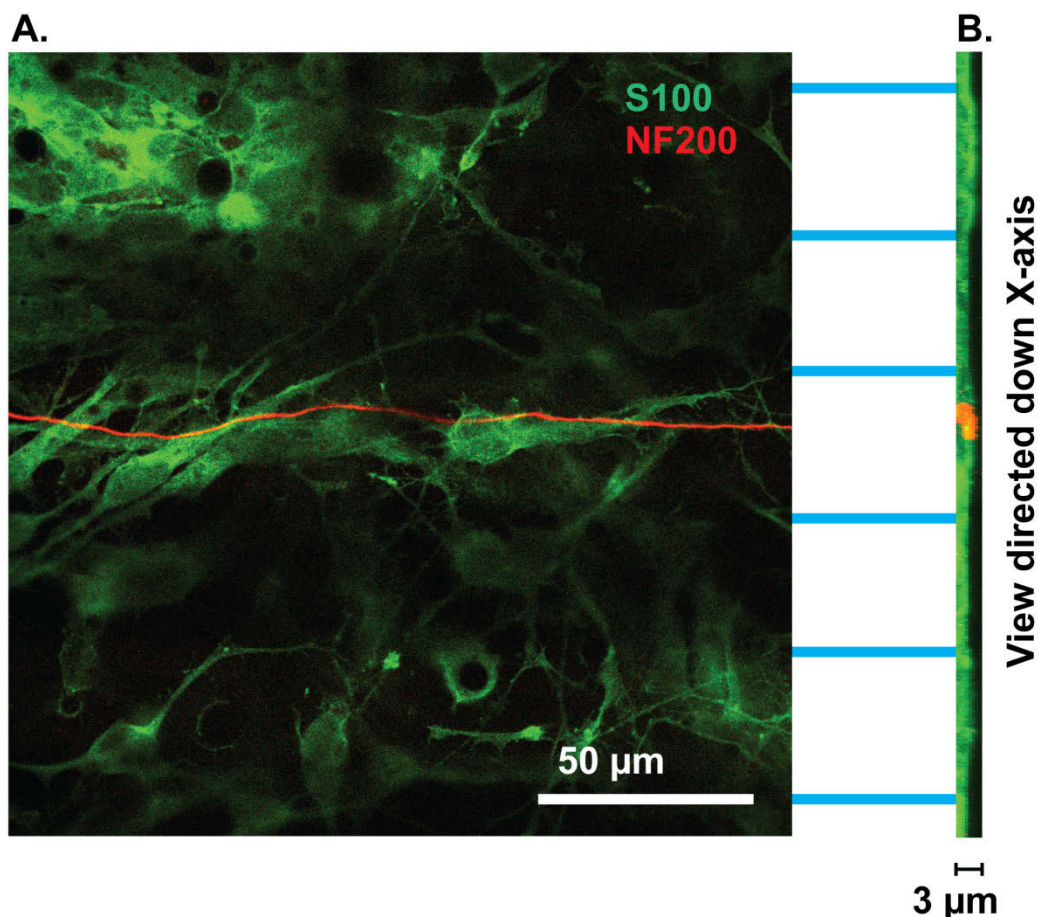


**Figure 4.9.** SGN neurite grow within the microgrooves of patterned HMA/HDDMA. **A)** Section of confocal z-stack from SG culture immunostained with anti-S100 (green) and anti-NF200 (red) antibodies. The neurite grows within the groove, demonstrated as a cellular stripe between acellular ridges. Scale bar = 50 µm. **B)** Ninety degree rotation of the stack to allow viewing down the x-axis. The grooves are evident as the regions with thicker S100 labeling compared with the ridges. The neurite (red) remains confined to the groove region. Scale bar = 3 µm.

Regeneration of functional auditory nerve fibers will likely require appropriate myelination; significantly, we found that the same topographic features that direct SGN neurite growth also promote alignment of SGSCs in the absence of neurites suggesting that both neural and glial elements respond to similar microfeatures. Given the ability of SCs to promote and direct axon regeneration, this influence of the topography on SGSCs could certainly enhance the guidance cues for SG neurites provided by micropatterns as

seen in previous studies.<sup>59</sup> In the case of dissociated SGN cultures, one could imagine the SGSCs adjacent to SGN cell bodies aligning with the pattern prior to SG neurite regeneration. This would result in experimental conditions seen in previous studies in which substrates covered with SCs aligned with laminin stripes directed neurite growth.<sup>18</sup> The tendency of neurites and SCs to remain aligned to one another even when not conforming to the direction of the micropattern further highlights the significance of the mutual influence these cells exert on each other.

In contrast to SCs, we found that fibroblasts in the SG cultures did not align to the micropattern. The micropattern's directing effect on SGSCs and neurites but not on fibroblasts could translate into a clinical advantage. CI performance can be limited by fibrous encapsulation resulting in increased impedance and subsequent increased current requirements.<sup>60,61</sup> Indeed, efforts are underway to manipulate current electrode designs to limit fibroblast growth and subsequent encapsulation.<sup>60,62</sup> We observed SGSCs and SG neurite growth outpacing fibroblasts across the polymer surface. Future *in vivo* experiments will reveal the impact of this effect on fibrous encapsulation.

### Conclusions

These results demonstrate the overall compatibility of MA polymers with cells derived from the SG and the profound influence of topographic microfeatures to differentially direct growth of these cells. The versatility of photopolymerization to create a variety of specific topographies will allow future studies to identify those features most critical for axon guidance. Such features may ultimately prove helpful in improving the neural prosthesis interface in future CI technology.

### Notes

1. Clarke, J. C.; Tuft, B. W.; Clinger, J. D.; Levine, R.; Figueroa, L. S.; Guymon A. C.; Hansen, M. R. Micropatterned methacrylate polymers direct spiral ganglion neurite and Schwann cell growth. *Hear. Res.* **2011**, *278*, 96-105.
2. Leake, P. A.; Hradek, G. T. Cochlear Pathology of Long-Term Neomycin Induced Deafness in Cats. *Hear. Res.* **1988**, *33*, 11-34.
3. Alam, S. A.; Robinson, B. K.; Huang, J.; Green, S. H. Prosurvival and proapoptotic intracellular signaling in rat spiral ganglion neurons in vivo after the loss of hair cells. *J. Comp. Neurol.* **2007**, *503*, 832-852.
4. Spoenclin, H. Retrograde Degeneration of Cochlear Nerve. *Acta Otolaryngol.* **1975**, *79*, 266-275.
5. Rubinstein, J. T. How cochlear implants encode speech. *Curr. Opin. Otolaryngol. Head Neck Surg.* **2004**, *12*, 444-8.
6. Shannon, R. V.; Fu, Q. J.; Galvin, J. The number of spectral channels required for speech recognition depends on the difficulty of the listening situation. *Acta Otolaryngol. Suppl.* **2004**, (552), 50-54.
7. Brors, D.; Aletsee, C.; Schwager, K.; Mlynski, R.; Hansen, S.; Schäfers, M.; Ryan, A. F.; Dazert, S. Interaction of spiral ganglion neuron processes with alloplastic materials in vitro. *Hear. Res.* **2002**, *167*, 110-121.
8. Evans, A. J.; Thompson, B. C.; Wallace, G. G.; Millard, R.; O'Leary, S. J.; Clark, G. M.; Shepherd, R. K.; Richardson, R. T. Promoting neurite outgrowth from spiral ganglion neuron explants using polypyrrole/BDNF-coated electrodes. *J. Biomed. Mater. Res. A* **2009**, *91A*, 241-250.
9. Pettingill, L. N.; Richardson, R. T.; Wise, A. K.; O'Leary, S. J.; Shepherd, R. K. Neurotrophic factors and neural prostheses: Potential clinical applications based upon findings in the auditory system. *IEEE Trans. Biomed. Eng.* **2007**, *54*, 1138-1148.
10. Richardson, R. T.; Wise, A. K.; Thompson, B. C.; Flynn, B. O.; Atkinson, P. J.; Fretwell, N. J.; Fallon, J. B.; Wallace, G. G.; Shepherd, R. K.; Clark, G. M.; O'Leary, S. J. Polypyrrole-coated electrodes for the delivery of charge and neurotrophins to cochlear neurons. *Biomaterials* **2009**, *30*, 2614-2624.
11. Roehm, P.; Hansen, M. Strategies to preserve or regenerate spiral ganglion neurons. *Curr. Opin. Otolaryngol. Head Neck Surg.* **2005**, *13(5)*, 294-300.

12. Miller, J. M.; Le Prell, C. G.; Prieskorn, D. M.; Wys, N. L.; Altschuler, R. A. Delayed neurotrophin treatment following deafness rescues spiral ganglion cells from death and promotes regrowth of auditory nerve peripheral processes: Effects of brain-derived neurotrophic factor and fibroblast growth factor. *J. Neurosci. Res.* **2007**, *85*, 1959-1969.
13. Branch, D. W.; Wheeler, B. C.; Brewer, G. J.; Leckband, D. E. Long-term stability of grafted polyethylene glycol surfaces for use with microstamped substrates in neuronal cell culture. *Biomaterials* **2001**, *22*, 1035-1047.
14. Branch, D. W.; Corey, J. M.; Weyhenmeyer, J. A.; Brewer, G. J.; Wheeler, B. C. Microstamp patterns of biomolecules for high-resolution neuronal networks. *Med. Biol. Eng. Comput.* **1998**, *36*, 135-141.
15. Gustavsson, P.; Johansson, F.; Kanje, M.; Wallman, L.; Linsmeier, C. E. Neurite guidance on protein micropatterns generated by a piezoelectric microdispenser. *Biomaterials* **2007**, *28*, 1141-1151.
16. Miller, C.; Jeftinija, S.; Mallapragada, S. Micropatterned Schwann cell-seeded biodegradable polymer substrates significantly enhance neurite alignment and outgrowth. *Tissue Eng.* **2001**, *7*, 705-715.
17. Oliva, A. A.; James, C. D.; Kingman, C. E.; Craighead, H. G.; Banker, G. A. Patterning axonal guidance molecules using a novel strategy for microcontact printing. *Neurochem. Res.* **2003**, *28*, 1639-1648.
18. Schmalenberg, K. E.; Uhrich, K. E. Micropatterned polymer substrates control alignment of proliferating Schwann cells to direct neuronal regeneration. *Biomaterials* **2005**, *26*, 1423-1430.
19. Evans, A. R.; Euteneuer, S.; Chavez, E.; Mullen, L. M.; Hui, E. E.; Bhatia, S. N.; Ryan, A. F. Laminin and fibronectin modulate inner ear spiral ganglion neurite outgrowth in an in vitro alternate choice assay. *Devel. Neurobiol.* **2007**, *67*, 1721-1730.
20. Brors, D.; Bodmer, D.; Pak, K.; Aletsee, C.; Schafers, M.; Dazert, S.; Ryan, A. F. EphA4 provides repulsive signals to developing cochlear ganglion neurites mediated through ephrin-B2 and-B3. *J. Comp. Neurol.* **2003**, *462*, 90-100.
21. Altschuler, R. A.; Cho, Y.; Ylikoski, J.; Pirvola, U.; Magal, E.; Miller, J. M. Rescue and regrowth of sensory nerves following deafferentation by neurotrophic factors. *Ototox. Basic Sci. Clin. App.* **1999**, *884*, 305-311.
22. Wise, A. K.; Richardson, R.; Hardman, J.; Clark, G.; O'Leary, S. Resprouting and survival of guinea pig cochlear neurons in response to the administration of the neurotrophins brain-derived neurotrophic factor and neurotrophin-3. *J. Comp. Neurol.* **2005**, *487*, 147-165.

23. Wise, A.; Hume, C.; Flynn, B.; Jeelall, Y.; Suhr, C.; Sgro, B.; O'Leary, S.; Shepherd, R.; Richardson, R. Effects of Localized Neurotrophin Gene Expression on Spiral Ganglion Neuron Resprouting in the Deafened Cochlea. *Mol. Ther.* **2010**.
24. Wittig, J. H.; Ryan, A. F.; Asbeck, P. M. A reusable microfluidic plate with alternate-choice architecture for assessing growth preference in tissue culture. *J. Neurosci. Methods* **2005**, *144*, 79-89.
25. Dazert, S.; Kim, D.; Luo, L.; Aletsee, C.; Garfunkel, S.; Maciag, T.; Baird, A.; Ryan, A. F. Focal delivery of fibroblast growth factor-1 by transfected cells induces spiral ganglion neurite targeting in vitro. *J. Cell. Physiol.* **1998**, *177*, 123-129.
26. Curtis, A.; Wilkinson, C. Topographical control of cells. *Biomaterials* **1997**, *18*, 1573-1583.
27. Dalby, M. J.; Riehle, M. O.; Yarwood, S. J.; Wilkinson, C. D.; Curtis, A. S. Nucleus alignment and cell signaling in fibroblasts: response to a micro-grooved topography. *Exp. Cell Res.* **2003**, *284*, 274-282.
28. Fozdar, D. Y.; Lee, J. Y.; Schmidt, C. E.; Chen, S. Hippocampal neurons respond uniquely to topographies of various sizes and shapes. *Biofabrication* **2010**, *2*, 035005.
29. Johansson, F.; Carlberg, P.; Danielsen, N.; Montelius, L.; Kanje, M. Axonal outgrowth on nano-imprinted patterns. *Biomaterials* **2006**, *27*, 1251-1258.
30. Ratner, B.; Hoffman, A.; Schoen, F.; Lemons, J. In *An Introduction to Materials in Medicine*; Academic Press: **2004**; pp 10-11.
31. Apple, D. J.; Sims, J. Harold Ridley and the invention of the intraocular lens. *Surv. Ophthalmol.* **1996**, *40*, 279-292.
32. Ridley, N. Intraocular acrylic lenses. *Trans. Ophthalmol. Soc. U. K.* **1951**, 617-621.
33. Kapoor, Y.; Thomas, J. C.; Tan, G.; John, V. T.; Chauhan, A. Surfactant-laden soft contact lenses for extended delivery of ophthalmic drugs. *Biomaterials* **2009**, *30*, 867-878.
34. Pameijer, C. H.; Zmener, O. Resin Materials for Root Canal Obturation. *Dent. Clin. North Am.* **2010**, *54*, 325-344.
35. Uludag, H.; De Vos, P.; Tresco, P. A. Technology of mammalian cell encapsulation. *Adv. Drug Deliv. Rev.* **2000**, *42*, 29-64.
36. Kenny, S. M.; Buggy, M. Bone cements and fillers: A review. *J. Mater. Sci. Mater. Med.* **2003**, *14*, 923-938.

37. Lee, T. Y.; Guymon, C. A.; Jonsson, E. S.; Hait, S.; Hoyle, C. E. Synthesis, initiation, and polymerization of photoinitiating monomers. *Macromolecules* **2005**, *38*, 7529-7531.
38. Quick, D. J.; Anseth, K. S. Gene Delivery in Tissue Engineering: A Photopolymer Platform to Coencapsulate Cells and Plasmid DNA. *Pharm. Res.* **2003**, *20*, 1730-1737.
39. Bryant, S. J.; Cuy, J. L.; Hauch, K. D.; Ratner, B. D. Photo-patterning of porous hydrogels for tissue engineering. *Biomaterials* **2007**, *28*, 2978-2986.
40. Clark, P.; Connolly, P.; Curtis, A. S. G.; Dow, J. A. T.; Wilkinson, C. D. W. Cell Guidance by Ultrafine Topography In vitro. *J. Cell. Sci.* **1991**, *99*, 73-77.
41. Dunn, G. A.; Brown, A. F. Alignment of Fibroblasts on Grooved Surfaces Described by a Simple Geometric Transformation. *J. Cell. Sci.* **1986**, *83*, 313-340.
42. Hsu, S.; Chen, C.; Lu, P. S.; Lai, C.; Chen, C. Oriented Schwann cell growth on microgrooved surfaces. *Biotechnol. Bioeng.* **2005**, *92*, 579-588.
43. Whilton, D. S.; Tieu, D.; Grover, M.; Reilly, B.; Coulson, M. T. Spontaneous Association of Glial Cells with Regrowing Neurites in Mixed Cultures of Dissociated Spiral Ganglia. *Neuroscience* **2009**, *161*, 227-235.
44. Song, M.; Uhrich, K. E. Optimal micropattern dimensions enhance neurite outgrowth rates, lengths, and orientations. *Ann. Biomed. Eng.* **2007**, *35*, 1812-1820.
45. Danneman, P. J.; Mandrell, T. D. Evaluation of five agents/methods for anesthesia of neonatal rats. *Lab. Anim. Sci.* **1997**, *47*, 386-395.
46. Phifer, C. B.; Terry, L. M. Use of Hypothermia for General-Anesthesia in Prewanling Rodents. *Physiol. Behav.* **1986**, *38*, 887-890.
47. Hansen, M. R.; Zha, X. M.; Bok, J.; Green, S. H. Multiple distinct signal pathways, including an autocrine neurotrophic mechanism, contribute to the survival-promoting effect of depolarization on spiral ganglion neurons in vitro. *J. Neurosci.* **2001**, *21*, 2256-2267.
48. Hansen, M. R.; Vijapurkar, U.; Koland, J. G.; Green, S. H. Reciprocal signaling between spiral ganglion neurons and Schwann cells involves neuregulin and neurotrophins. *Hear. Res.* **2001**, *161*, 87-98.
49. Hegarty, J.; Kay, A.; Green, S. Trophic support of cultured spiral ganglion neurons by depolarization exceeds and is additive with that by neurotrophins or cAMP and requires elevation of  $[Ca^{2+}]_i$  within a set range. *J. Neurosci.* **1997**, *17*, 1959-1970.

50. Roehm, P. C.; Xu, N.; Woodson, E. A.; Green, S. H.; Hansen, M. R. Membrane depolarization inhibits spiral ganglion neurite growth via activation of multiple types of voltage sensitive calcium channels and calpain. *Mol. Cell. Neurosci.* **2008**, *37*, 376-387.
51. Bryant, S. J.; Chowdhury, T. T.; Lee, D. A.; Bader, D. L.; Anseth, K. S. Crosslinking density influences chondrocyte metabolism in dynamically loaded photocrosslinked poly(ethylene glycol) hydrogels. *Ann. Biomed. Eng.* **2004**, *32*, 407-417.
52. Kim, S. H.; Ha, H. J.; Ko, Y. K.; Yoon, S. J.; Rhee, J. M.; Kim, M. S.; Lee, H. B.; Khang, G. Correlation of proliferation, morphology and biological responses of fibroblasts on LDPE with different surface wettability. *J. Biomater. Sci. Polym. Ed.* **2007**, *18*, 609-622.
53. Whilton, D. S.; Tieu, D.; Grover, M.; Reilly, B.; Coulson, M. T. Spontaneous Association of Glial Cells with Regrowing Neurites in Mixed Cultures of Dissociated Spiral Ganglia. *Neuroscience* **2009**, *161*, 227-235.
54. Bostrom, M.; Khalifa, S.; Bostrom, H.; Liu, W.; Friberg, U.; Rask-Andersen, H. Effects of Neurotrophic Factors on Growth and Glial Cell Alignment of Cultured Adult Spiral Ganglion Cells. *Audiol. Neurootol.* **2010**, *15*, 175-186.
55. Pettingill, L. N.; Richardson, R. T.; Wise, A. K.; O'Leary, S. J.; Shepherd, R. K. Neurotrophic factors and neural prostheses: Potential clinical applications based upon findings in the auditory system. *IEEE Trans. Biomed. Eng.* **2007**, *54*, 1138-1148.
56. Miller, C.; Jeftinija, S.; Mallapragada, S. Micropatterned Schwann cell-seeded biodegradable polymer substrates significantly enhance neurite alignment and outgrowth. *Tissue Eng.* **2001**, *7*, 705-715.
57. Foley, J. D.; Grunwald, E. W.; Nealey, P. F.; Murphy, C. J. Cooperative modulation of neuritogenesis by PC12 cells by topography and nerve growth factor. *Biomaterials* **2005**, *26*, 3639-3644.
58. Wittig, J. H.; Ryan, A. F.; Asbeck, P. M. A reusable microfluidic plate with alternate-choice architecture for assessing growth preference in tissue culture. *J. Neurosci. Methods* **2005**, *144*, 79-89.
59. Hsu, S.; Lu, P. S.; Ni, H.; Su, C. Fabrication and evaluation of microgrooved polymers as peripheral nerve conduits. *Biomed. Microdevices* **2007**, *9*, 665-674.
60. Paasche, G.; Tasche, C.; Stoeber, T.; Lesinski-Schiedat, A.; Lenarz, T. The Long-Term Effects of Modified Electrode Surfaces and Intracochlear Corticosteroids on Postoperative Impedances in Cochlear Implant Patients. *Otol. Neurotol.* **2009**, *30*, 592-598.

61. Tykocinski, M.; Cohen, L. T.; Cowan, R. S. Measurement and analysis of access resistance and polarization impedance in cochlear implant recipients. *Otol. Neurotol.* **2005**, *26*, 948-956.
62. Rebscher, S. J.; Hetherington, A.; Bonham, B.; Wardrop, P.; Whinney, D.; Leake, P. A. Considerations for design of future cochlear implant electrode arrays: Electrode array stiffness, size, and depth of insertion. *J. Rehabil. Res. Devel.* **2008**, *45*, 731-747.

## CHAPTER 5

### PHOTOPOLYMERIZED MICROFEATURES CONTROL THE EXTENT OF SPIRAL GANGLION NEURITE AND SCHWANN CELL ALIGNMENT<sup>1\*</sup>

Cochlear implants (CIs) provide auditory perception to individuals with severe hearing impairment, however, their ability to encode complex auditory stimuli is limited due, in part, to poor spatial resolution caused by electrical current spread in the inner ear. Directing nerve cell processes towards target electrodes may reduce the problematic current spread and improve stimulatory specificity. In this work, photopolymerization was used to fabricate micro- and nano-patterned methacrylate polymers to probe the extent of spiral ganglion neuron (SGN) neurite and Schwann cell (SGSC) contact guidance based on variations in substrate topographical cues. Micropatterned substrates are formed in a rapid, single-step reaction by selectively blocking light with photomasks which have parallel line-space gratings with periodicities of 10 – 100  $\mu\text{m}$ . Channel amplitudes of 250 nm – 10  $\mu\text{m}$  are generated by modulating UV exposure time, light intensity, and photoinitiator concentration. Gradual transitions are observed between ridges and grooves using scanning electron and atomic force microscopy. Alignment of neural elements increases significantly with increasing feature amplitude and constant periodicity, as well as with decreasing periodicity and constant amplitude. SGN neurite alignment strongly correlates ( $r = 0.93$ ) with maximum feature slope. Multiple neuronal and glial types orient to the patterns with varying degrees of alignment. The work presents a method to fabricate gradually-sloping micropatterns for cellular contact guidance studies and demonstrates spatial control of inner ear neural elements in response to micro- and nano-scale surface topography.

---

\* Tuft, B. W.; Li, S.; Xu, L.; White, S. P.; Hansen, M. R.; Guymon, C. A. *Biomaterials* **2013**, *34*, 42-54.

## Introduction

Neural prosthetics are intended to replace or substantially augment motor and sensory functions of neural pathways that have been lost or damaged due to physical trauma, disease, or genetics. Ongoing developments in the fields of neurobiology, materials science, and tissue engineering are enabling innovative device designs and modifications that may considerably expand the functional potential of such complex medical devices. However, much of this functional potential remains unrealized due to poor host tissue integration that significantly limits the performance of most neural prostheses.<sup>2</sup>

In particular, neural prosthetic performance is limited by low spatial signal resolution at the neural-electrode interface.<sup>3, 4</sup> Consequently, prostheses fail to recapitulate the intimate, precise interactions inherent to neural networks and therefore fail to provide precise motor or sensory stimulation. For example, visual resolution provided by retinal prostheses is limited to few sensory pixels, at least in part, by electrical signal overlap caused by spatial separation of stimulating electrodes from the target neurons in the retina.<sup>4</sup> Similarly, the cochlear implant (CI) enables basic auditory perception to individuals with severe hearing loss but provides limited tonal information due to comparable limitations in spatial signal control. For CIs, spatial limits to tonal fidelity occur due to electrical signal spread across the neural-electrode interface that excites neurons which are outside of the preferred area of stimulation. As a result, non-specific signaling causes CI patients to struggle with complex auditory stimuli such as music appreciation, voice comprehension in environments with noise, and voice intonations.<sup>5, 6</sup> Furthermore, because the nervous system is generally dependent upon signaling that is location specific, analogous signal resolution challenges are expected for all devices that interact with the nervous system. Precise spatial signal control will,

therefore, be critical to achieve significant performance improvements in next generation neural-prosthetics.

To address spatial resolution challenges, significant research interest has focused on guiding sensory neurites to approach or even contact prosthesis electrodes.<sup>3, 7-13</sup> Spatial proximity to stimulating electrodes would allow for lower stimulation thresholds that would reduce problematic signal overlap, enable higher stimulatory specificity, and may lead to greater precision in both signal input and biological functional output. Recent research illustrates a variety of methods used to direct the outgrowth of regenerative neural processes, including aligned microfibers,<sup>14</sup> parallel micro- and nano-channel morphology,<sup>15, 16</sup> axonal conduits,<sup>17</sup> cyto-mimetic patterning,<sup>18</sup> bioactive molecule patterning,<sup>19-22</sup> diffusion gradients of chemo-attractants,<sup>23</sup> and electrical fields.<sup>24, 25</sup> However, the principle focus of many of these studies is to induce neurites, particularly those of the sciatic nerve, to optimally extend in one direction to bridge large gaps typical of nerve injuries. Similar guidance techniques may also be advantageous to address spatial resolution challenges at the neural-prosthetic interface by enabling spatial control of regenerative sensory neurites specific to the prosthesis.

Among the various methods used to direct cell growth, controlling cell-material interactions based on surface topography, or contact guidance, is of particular interest due to the stability, reproducibility, and high degree of control over surface physical features via well-established micro- and nano-scale patterning techniques. Additionally, contact guidance is a versatile technique used to induce specific morphologies of multiple cell types, including epithelial cells,<sup>26</sup> fibroblasts,<sup>27</sup> stem cells,<sup>28</sup> osteoblasts,<sup>29</sup> as well as neuronal and glial cells.<sup>30</sup> Epithelial cells elongate and align on silicon oxide substrates with ridge and groove depths as small as 70 nm.<sup>26</sup> In addition to controlling cell morphology, contact guidance has been shown to regulate gene expression that may be advantageous for neural regeneration. For example, Schwann cells increase neurotrophin expression when cultured on microgrooved chitosan and poly(D,L-lactide) compared to

those grown on smooth substrates.<sup>31</sup> Micropattern dimensions such as ridge width, groove depth, and pattern shape can be tuned to influence cellular outgrowth and spatial orientation as well.<sup>32, 33</sup> Consequently, recent neural contact guidance studies inspire confidence that neuritic processes relevant to current or developing prosthetics, such as those of spiral ganglion neurons (SGNs) or retinal ganglion neurons, may be spatially oriented towards stimulating electrodes for increased signal specificity and enhanced prosthetic performance.

Accordingly, in this study, we show that photopolymerization enables facile and rapid generation of micro- and nano-patterned methacrylate substrates for contact guidance studies and also demonstrate the extent to which inner ear neural elements, namely SGN neurites and spiral ganglion Schwann Cells (SGSCs), spatially orient to 3D topographical cues. We have previously reported that SGNs and SGSCs adhere to and survive on copolymer methacrylates similar to those used for this study.<sup>34</sup> Micropattern feature spacing is controlled using Ronchi rule optics with varied band-spacing as photomasks and feature amplitude is tuned by terminating the reaction at specific time increments to temporally arrest amplitudes as they develop throughout the reaction. Feature amplitude is also tuned by modulating photoinitiator concentration and UV light intensity. Gradually sloping features produced by this method stand in contrast to the majority of contact guidance studies which use lithographic procedures that produce features with very defined or vertical edges.<sup>31, 35</sup> Variations in the extent of SGN neurite and SGSC alignment are demonstrated using gradually sloping, parallel ridge-groove patterns that have periodicities of 10 – 50  $\mu\text{m}$  and amplitudes of 250 nm – 8  $\mu\text{m}$ . Alignment behavior of astrocytes (ACs) as well as neurites from dorsal root ganglion neurons (DRGNs), trigeminal neurons (TGNs), and cerebellar granular neurons (CGNs) serve as glial and neuronal comparisons, respectively. The extent of neurite alignment is also shown to strongly correlate with maximum feature slope.

## Experimental

### Photopolymerization of Micropatterned Substrates

Standard 1 in x 3 in glass microscope slides were functionalized with a methacrylated silicon bonding agent to prevent delamination of polymer substrates from the glass during sample characterization and cellular studies. The slides were first treated under vacuum with O<sub>2</sub> plasma for 3 min at 30 W RF power (PDC-001 Harrick Plasma Expanded Cleaner, Ithaca, NY). Immediately following removal from the plasma chamber, the slides were immersed in a 1/100 v/v solution of 3-(trimethoxysilyl)propyl methacrylate (Aldrich) and n-hexane (Aldrich) overnight in a covered container at room temperature (~21°C). Upon removal, each slide was rinsed with fresh hexanes and allowed to dry in a fume hood before being placed in a sealed container. Functionalized slides were observed to have a slightly translucent appearance following the hexane rinse. The slides were immediately used as a substrate for polymerization when removed from the sealed container.

Monomer mixtures of 40 wt% hexyl methacrylate (HMA, Aldrich) and 59 wt% 1,6 – hexanediol dimethacrylate (HDDMA, Aldrich) were prepared with 1 wt% of 2,2-dimethoxy-2- phenylacetophenone (DMPA, BASF) as the photoinitiator unless otherwise specified. A sample volume of 20 µL was pipetted onto the center of a functionalized glass slide and was subsequently covered with a 2.54 cm x 2.54 cm glass-chrome Ronchi rule photomask (Applied Image Inc., Rochester, NY) for patterned samples, or with a cut untreated glass slide of the same dimensions for unpatterned samples. Pre-polymer formulations spread evenly under the photomasks due to capillary forces. Polymer samples were cured with a high-pressure mercury vapor arc lamp (Omnicure S1500, Lumen Dynamics, Ontario, Canada) and a 365 nm light intensity of 16 mW/cm<sup>2</sup>. The curing module had an 8 mm diameter liquid light guide that was equipped with an 8 mm aperture x 50 mm length beam homogenizing fused silica light pipe (Edmund Optics). A

collimating lens (RLQ-1, Asahi Spectra) was attached to the end of the light guide. UV radiation was shuttered at specific time. Following polymerization, photomasks were removed from polymer surfaces and samples were washed with 95% ethanol to remove all residual monomer. Samples were allowed to air dry before use.

### Topographic Characterization

Micropattern periodicity and absolute channel amplitude were measured by white light interferometry (Dektak Wyko 1100 Optical Profiling System, Veeco). Channel amplitude was reported as the difference between the maximum ridge value and the adjacent minimum groove value. Average feature height was determined by measuring channel amplitude in nine different areas across each sample ( $n = 3$  or more). Periodicity was measured as the distance between the highest points on adjacent ridges and was consistent with photomask band spacing. 2D profiles and 3D images were generated using *Vision* software associated with the instrument.

Patterned polymer morphology was examined by scanning electron microscopy (SEM, S-4800, Hitachi). For top down images, patterned samples were mounted with the glass side down on aluminum SEM stubs using conductive silver paint. For cross-sectional images, glass substrates and patterned polymers were fractured and then mounted vertically on specimen stages. The SEM specimen stage was angled using an automated stage and software controls to capture angled cross-sectional images. Prior to examination by SEM, each polymer surface was sputter coated with gold. Electron accelerating voltage was set at 2 kV.

The slope between grooves and ridges was determined by atomic force microscopy (AFM, Asylum Atomic Force Microscope, Asylum Research). A microscope cantilever with a force constant of 46 N/m and a tuning frequency of 316.62 kHz was used. Samples were scanned at a rate of 5  $\mu\text{m/s}$  with 512 points taken per scan line across 50  $\mu\text{m}$ . X and Y position data were obtained from the instrument software from 2D

profiles ( $n = 3$ ) taken at different locations on pattern surfaces. Average and maximum slopes were calculated from profile data.

### Cell Culture and Immunostaining

Dissociated spiral ganglion (SG) cultures from P3-5 rat pups were prepared as previously described.<sup>36, 37</sup> Dissociated dorsal root ganglion neuron (DRGN), trigeminal ganglion neuron (TGN), and cerebellar granular neuron (CGN) cultures were prepared by modification of the SG culture method. Briefly, pooled DRG or TG from P3-5 rat pups were dissociated with 0.125% trypsin and 0.1% collagenase for 45 min at 37°C, followed by gentle trituration through fire-polished glass pipettes. For CGN cultures, cerebellar cortices were collected from P3-5 rat pups, stripped of arachnoid membranes, and treated with 0.05% trypsin for 12 min at 37°C followed by gentle trituration. Astrocyte (AC) cultures were prepared and maintained from postnatal cerebral cortex according to the modification of a previously described method.<sup>38, 39</sup> All neurons were plated on polymer substrates coated with poly-L-ornithine (100 µg/ml) and laminin (20 µg/ml).

SGN cultures were maintained in Dulbecco's Modified Eagle Medium (DMEM) supplemented with N2 additives, 5% fetal bovine serum, neurotrophin-3 (NT-3, 50 ng/ml) and brain derived neurotrophic factor (BDNF, 50 ng/ml). TGN and DRGN cultures were maintained in Neurobasal-A medium with B-27 (Invitrogen) and nerve growth factor (NGF, 50 ng/ml). CGN cultures were maintained in Neurobasal-A medium with B-27, 20 µM KCl and NGF 50 ng/ml. AC cultures were maintained as previously described.<sup>38</sup> Cultures were maintained in a humidified incubator with 6.5% CO<sub>2</sub> and fixed with 4% paraformaldehyde after 48 hr.

SG, TG, and DRG cultures were immunostained with anti-S100 and anti-neurofilament 200 (NF200) antibodies (1:400, Sigma–Aldrich) to label SCs and neurons, respectively.<sup>36</sup> CGN cultures were immunostained with anti-MAP2 (1:400, Cell Signaling) and anti-TAU1 (1:200, Cell Signaling) antibodies to label dendritic and axonal

neurites, respectively. ACs were immunostained with anti-glial fibrillary acidic protein (GFAP) antibody (1:100, Sigma). Alexa 488 and Alexa 546 conjugated secondary antibodies (Invitrogen) were used to detect primary antibody immunolabeling. Slides were cover slipped with ProLong Gold anti-fading reagent with DAPI (Life Technology).

#### Characterization of Neurite and Glial Cell Alignment

Digital epifluorescent images were captured on a Leica DMIRE2 microscope (Leica Microsystems, Bannockburn, IL) with Leica DFC350FX digital camera and Metamorph software (Molecular Devices, Silicon Valley, CA). SGN total neurite length was determined from digital images by measuring the longest process of 100 randomly selected neurites from each condition using the measurement tool in Image J (NIH, Bethesda, MD) as previously described.<sup>40</sup> For TG or DRG neurons, total neurite length was determined by averaging the length of six branches of each neuron for 100 neurons for each condition. Neurite alignment was calculated with a modification of our prior method.<sup>34</sup> Briefly, the aligned length ( $A_L$ ) was determined by measuring the distance from the neuronal cell body to the neurite terminus in a straight line in the direction of the micropattern, which was always set horizontally prior to measurements. Alignment to the pattern was defined as the unaligned length per neurite length, or total neurite length ( $T_L$ ) minus the aligned distance ( $A_L$ ), divided by  $T_L$ . The final unaligned length per neurite length ratio is represented as  $[(T_L - A_L)/T_L]$  and is referred to as the alignment ratio in the text. A ratio close to zero represents a neurite that closely follows the pattern along its entire length. A wandering neurite, which does not strongly align to the pattern, has a high alignment ratio. To analyze neurite alignment on unpatterned substrates, aligned distance was arbitrarily measured directly along the horizontal plane.

SC and AC orientation was determined as previously described by drawing the outline of the cell using Image J software and fitting an ellipse to the cell outline.<sup>34</sup> The

angle made between the major axis of the ellipse and the pattern ( $\theta$ ) was measured in Image J as glial cell alignment.

### Statistics

Statistical analysis was performed using SigmaStat 3.5 software (Systat Software, Chicago, IL). A two-tailed t-test was used to compare cellular alignment between unpatterned and patterned samples followed by a *post hoc* Mann-Whitney Rank Sum Test when normality criteria were not met. Multiple groups were compared by performing a one-way ANOVA followed by a *post hoc* Kruskal-Wallis analysis of variance on ranks and a Dunn's Method multiple comparison procedure. Results were considered statistically significant if  $p < 0.05$ .

## **Results and Discussion**

### Photopolymerization of Surface Patterned Substrates

To generate micropatterns suitable for contact guidance studies of inner ear neural elements, Ronchi rule photomasks were used to spatially control the polymerization of a 40 wt% hexyl methacrylate (HMA) and 59 wt% 1,6 – hexanediol dimethacrylate (HDDMA) mixture with 1 wt% 2,2-dimethoxy-2-phenylacetophenone (DMPA) as the photoinitiator (Fig 5.1). Ronchi rule optics, typically used for optical testing, have alternating transparent (glass) and reflective (chrome) bands of equal size which, during photopolymerization, direct light to areas intended for polymerization and block irradiation at adjacent areas (Fig 5.1A). Spatially controlling the UV irradiation in this manner varies polymerization speed locally in the substrate and leads to repeating, raised micro-scale physical features useful for cellular contact guidance studies. Ruling band size is used to control micro-feature width and frequency, with mask bands ranging from 5 – 50  $\mu\text{m}$  wide. Periodicity for this study is defined as the distance between two

repeating points while tracing a line normal to the bands and ranges from 10 – 100  $\mu\text{m}$ , or double the band width.

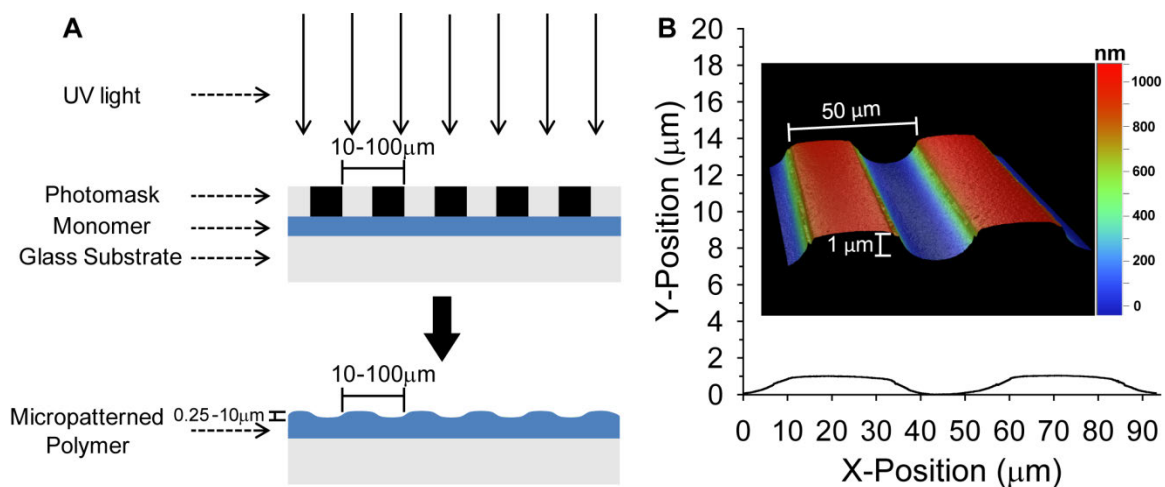


**Figure 5.1.** Schematic of photopatterning process. **A)** Photopolymerizable monomer is selectively exposed to UV light through a photomask resulting in raised microfeatures across the surface. **B)** A 2D profile is shown of a micropatterned HMA-co-HDDMA substrate with a 50  $\mu\text{m}$  periodicity and a channel amplitude of 1  $\mu\text{m}$ . Inset: 3D representation of a 100  $\mu\text{m}^2$  area derived by white light interferometry.

Fabricating micropatterns using photomasking techniques in conjunction with photopolymerization has also been leveraged for other biomaterial applications. For example, 3D hydrogels have been selectively functionalized with biochemical patterns (i.e. gradients) of defined magnitude and slope by using spatially controlled thiol-ene photopolymerization.<sup>41</sup> Additionally, tissue engineering constructs have been fabricated with both micro- and macro-porous structure that is spatially tunable through photopolymerization.<sup>42</sup> However, these studies used photomasks and photopolymerization to control chemical composition or structure of 3D matrices rather than to generate surface features for cell contact guidance. Polymer adhesion to glass substrates is facilitated by covalently bonding methacrylated silicon bonding agents to the

substrate glass via silanization.<sup>43-45</sup> Free methacrylate moieties on the surface then form covalent bonds with the newly formed polymer during photopolymerization and prevent delamination events.

During UV exposure, polymerization occurs rapidly under transparent bands that transmit most of the intensity from the light source. Under irradiated regions, polymer chain concentration increases while unreacted monomer concentration quickly decreases. Consequently, a local concentration gradient at the interface with masked regions develops for both species. Small molecule monomers diffuse rapidly down the concentration gradient and polymerize in the reactive region exposed to full light intensity. The net positive mass transfer to irradiated regions results in raised, micro-scale surface features. Masked regions still undergo polymerization but do so more slowly than unmasked areas. Polymerization under masked regions principally occurs due to angled diffraction of light as it passes through narrow (micro-scale) slits,<sup>46, 47</sup> reflections from the glass substrate, and diffusion of propagating polymer chains into shadowed regions. Consequently, light intensity varies under masked regions and generally decreases, which also decreases the polymerization rate, as distance from the original transparent band increases. Larger, propagating polymer chains diffuse more slowly toward masked regions than do unreacted monomers to irradiated areas.

As a result of the masked photopolymerization, a pattern of gradually sloping parallel micro-ridges and grooves of uniform width and amplitude rapidly develop across the entire substrate surface in a single fabrication step. White light interferometry was used to characterize the micropatterns, including measurements of channel amplitude and feature spacing, in both 2D and 3D (Fig 5.1B). As expected, the distance between repeating points, e.g. a ridge peak to an adjacent ridge peak, closely matches photomask periodicity. Channel amplitudes range from ~250 nm – 10  $\mu$ m on HMA-co-HDDMA materials polymerized by this method depending on reaction parameters. Any residual

monomer under masked regions was removed by an ethanol wash following detachment of the photomask.

Parallel ridges and grooves, or micro-channels, have been used in a wide variety of contact guidance studies, including those used for neurite outgrowth.<sup>48-51</sup> Linear micro-channels are advantageous because they are geometrically simple and facilitate pattern production and characterization as well as analysis of cellular behavior, particularly in the direction of the micro-features. However, the majority of parallel ridge-groove contact guidance studies use various lithographic techniques to fabricate micron and sub-micron features.<sup>31, 49, 52-56</sup> The resultant pattern features have sharp zero-one transitions with a virtually infinite slope. As a contrast to zero-one features, generating micropatterns by photopolymerizing directly under a photomask leads to smooth, gradually sloping transitions between ridges and grooves.

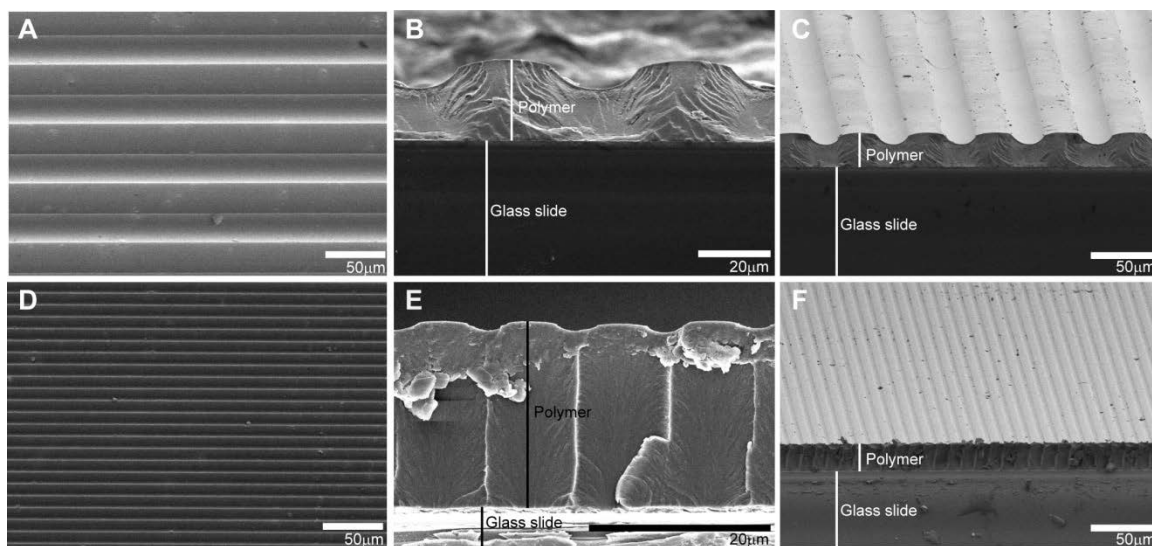


**Figure 5.2.** Representative SEM images of micropatterned HMA-co-HDDMA polymers. **A-C)** SEM images are shown of a pattern with a 50  $\mu\text{m}$  periodicity and a channel amplitude of 8  $\mu\text{m}$ . **D-F)** SEM images are shown of a pattern with a 10  $\mu\text{m}$  periodicity and a channel amplitude of 1  $\mu\text{m}$ . Top down view (A),(D); Cross-sectional view (B),(E); Angled cross-sectional view (C),(F). Note the gradual transitions between ridges and grooves.

To demonstrate gradually sloping transitions between ridges and grooves generated via photopolymerization and photomasking, and to confirm interferometric measurements, scanning electron microscopy (SEM) was used to further characterize patterned substrate morphology (Fig 5.2). Repeating features are seen across the entire substrate surface and vary in frequency based on photomask band spacing (Fig 5.2 A,D). Polymer film thickness is 18  $\mu\text{m}$  and absolute channel amplitude changes as a percentage of the thickness according to reaction conditions such as photoinitiator concentration and UV exposure time. The smooth transitions observed by SEM are likely to more realistically represent physical features of *in vivo* environments compared with sharp or abrupt features, and could be pertinent to contact guidance studies of other neural elements or for different cells (e.g. stem cells).

Furthermore, because transitional slope can be adjusted by altering feature frequency or height, cellular behavior that is not apparent on zero-one patterns may be more readily observed and understood. For example, a critical feature slope may induce a desired cellular behavior, such as neurite alignment, gene expression, cell motility, or stem cell differentiation. Additionally, careful tuning of feature slope may facilitate studies aimed at identifying the mechanisms by which cells sense and respond to physical features. Such studies require the ability to inhibit or enhance pattern-induced cellular alignment by manipulating the underlying signaling events. Quantitative changes in alignment are more likely to be apparent on smooth transitions compared with zero-one patterns which have sharp physical features that dominate cellular morphological responses. Such an approach would enable targeted probing of contact guidance mechanisms.

To investigate the extent of spiral ganglion Schwann cell (SGSC) and spiral ganglion neuron (SGN) neurite alignment to variations in surface topography, microfeature frequency and amplitude were tuned by varying photomask band spacing and by modulating photopolymerization reaction parameters, respectively (Fig 5.3).

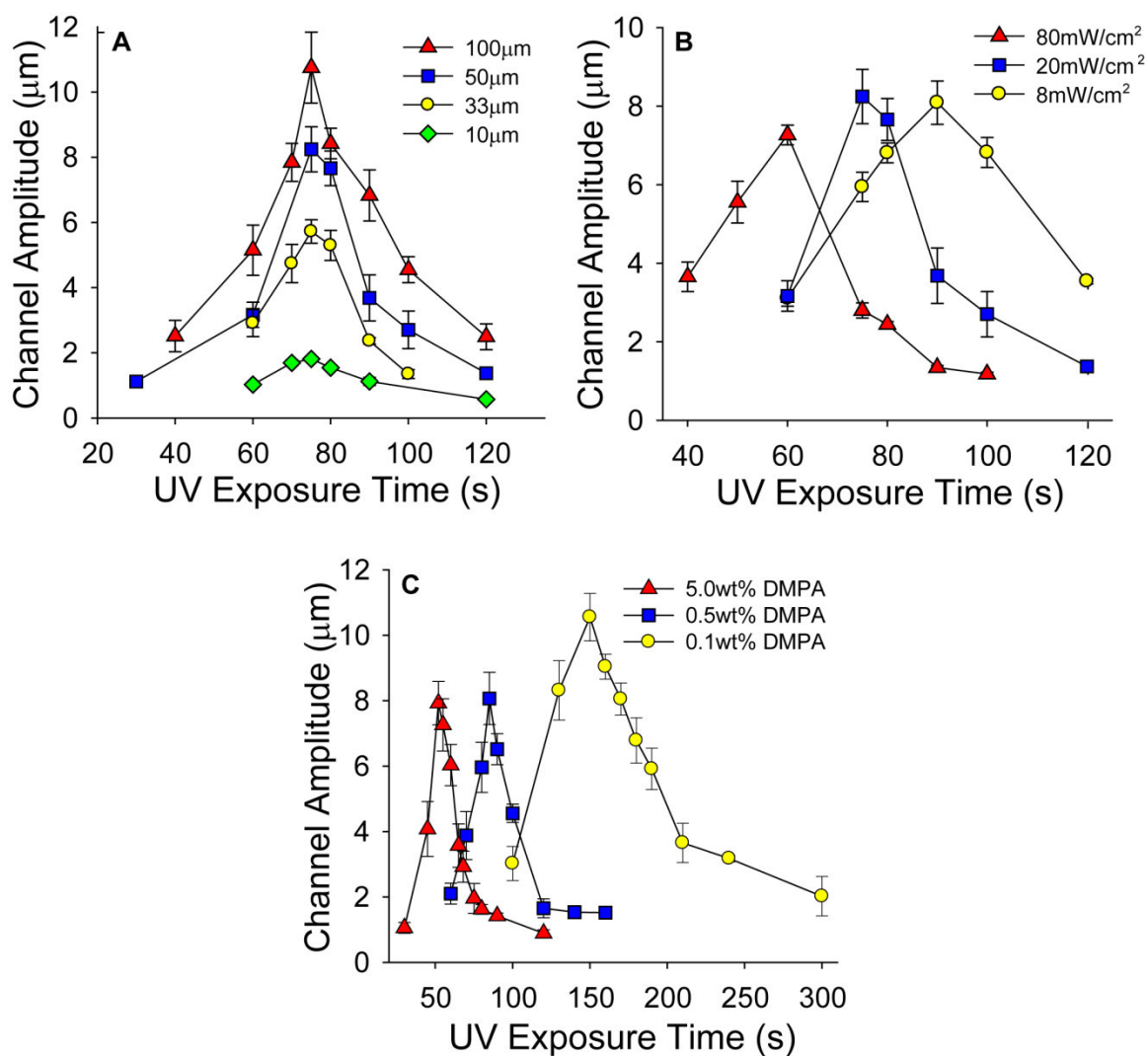


**Figure 5.3.** Tuning of micropattern features by variations in photomask band sizing, light intensity, photoinitiator concentration, and UV exposure time. **A)** Feature frequency is controlled by photomask design. Amplitude profiles represent photomasks with periodicities of 100, 50, 33, and 10  $\mu\text{m}$ . Maximum attainable amplitude is limited as periodicity (mask band size) decreases. **B)** Channel amplitude is controlled by varying initiating light intensity and UV exposure time. **C)** Channel amplitude is also tuned by varying photoinitiator concentration as well as UV exposure time. Periodicity for all trials in (B) and (C) is 50  $\mu\text{m}$ . Each point indicates mean $\pm$ SD.

Specifically, ridge and groove width, which also dictates pattern periodicity, was controlled by using Ronchi rule photomasks with band spacings of 5 – 50  $\mu\text{m}$ . Faithful reproduction of band spacing was observed for all gratings. However, maximum attainable amplitude becomes more limited at smaller periodicities due to increasing diffraction angles of initiating radiation as band space narrows which increases polymerization in masked regions. Also, smaller reaction volumes beneath narrow high intensity bands decrease mass available for diffusion to reactive areas, thus, limiting maximum feature size (Fig 5.3A). For example, the maximum amplitude attained with a 100  $\mu\text{m}$  periodicity mask is approximately 11  $\mu\text{m}$  compared to about 2  $\mu\text{m}$  using a 10  $\mu\text{m}$  periodicity mask. Furthermore, channel amplitude is generally lower at any given time increment for patterns polymerized under photomasks with smaller periodicities (i.e. more frequent bands). Therefore, to enable meaningful neurite alignment for comparison across multiple feature spacings, only periodicities of 10  $\mu\text{m}$  or higher were used for cell studies.

Micro-channel amplitude for the HMA-co-HDDMA system can be varied by almost two orders of magnitude from 250 nm – 10  $\mu\text{m}$  through modulation of reaction parameters of the polymerization reaction (results are only shown for the 1 – 10  $\mu\text{m}$  regime). Amplitudes smaller than 1  $\mu\text{m}$  are readily generated with 10  $\mu\text{m}$  periodicity masks but are not achieved even at long exposure times with masks that have a 50  $\mu\text{m}$  periodicity or higher. However, generating sub-micron amplitudes for patterns with higher periodicities is achieved by increasing the spacing between the pre-polymer solution and the photomask.

To demonstrate the effect of UV exposure time on channel amplitude, pattern samples were cured at controlled time increments (Fig 5.3). Temporal control of the polymerization is achieved by shuttering the initiating light source at specific time steps, which prevents further initiation events leading to rapid termination of propagating kinetic chains and, hence, a termination of the polymerization reaction. Temporal control

is crucial to pattern formation because it enables arrest of specific micropattern feature sizes as the reaction progresses. Channel amplitude steadily increases to a maximum amplitude as unreacted monomer continues to diffuse into irradiated regions with high reaction rates. At some point during the polymerization, grooves begin to backfill due to polymerization in masked regions. Continued irradiation subsequently leads to smaller and smaller amplitudes until a final amplitude is reached that is approximately 10% of the maximum amplitude. The final pattern is set as diffusion becomes significantly limited due to the vitrification of polymerization and the gelling effect of crosslinked networks. UV exposure time strongly correlates to channel amplitude under the described parameters (Fig 5.3). Patterned samples were either tacky or exhibited insufficient mechanical strength for characterization and cellular experiments if polymer conversion is too low, i.e. less than 40s exposure under the given conditions. The correlation between UV exposure time and final feature size demonstrates how quickly and readily multiple sizes, and subsequently slopes, of micro-features can be generated via this facile photopolymerization method.

Modulation of initiating light intensity also serves as a method to control channel amplitude as well as to shift amplitude profiles to different UV exposure times due to changes in reaction rate (Fig 5.3B). For example, an increase in light intensity raises polymerization reaction rate and shifts final amplitude profiles to earlier polymerization times. At the highest intensity of  $80 \text{ mW/cm}^2$ , the maximum average amplitude decreases to approximately  $7 \mu\text{m}$  compared to  $8 \mu\text{m}$  when cured at a lower intensity of  $8 \text{ mW/cm}^2$ . This decrease suggests that polymer gelation or vitrification may inhibit feature size at high reaction rates. Maximum attainable amplitude occurs at an exposure time of 60 s while curing with an  $80 \text{ mW/cm}^2$  light intensity which is 30 s faster than the UV exposure time required to reach maximum amplitude with an  $8 \text{ mW/cm}^2$  light intensity.

To illustrate the effect of photoinitiator concentration on final channel amplitude, pre-polymer formulations were mixed with 0.1, 1, and 5 wt% DMPA with corresponding

reductions in both HMA and HDDMA wt% (Figure 5.3C). Similar to changes in light intensity, altering polymerization speed by modulating photoinitiator concentration also enables tuning of feature amplitude. For example, maximum average channel amplitude increases by 30% from 8  $\mu\text{m}$  at 1 wt% photoinitiator to 11  $\mu\text{m}$  at 0.1 wt% photoinitiator. While maximum amplitude increases with low photoinitiator concentration, exposure time to reach a maximum increases by 180% as concentration decreases from 5 wt% to 0.1 wt%. The final channel amplitude at long exposure times is also lower for high DMPA concentrations at approximately 0.9  $\mu\text{m}$  and 2  $\mu\text{m}$  for 5wt% and 0.1 wt%, respectively. Furthermore, the entire amplitude profile broadens to larger time increments at low DMPA concentration. Similar broadening of the amplitude profile occurs while using a low ( $8 \text{ mW/cm}^2$ ) irradiation intensity. Increases in feature amplitude at low photoinitiator concentrations support the observation that speed of reaction should be considered when targeting a specific feature size due to gelation constraints. Decreases in channel amplitude at UV exposure times above the maximum amplitude time step are likely caused by backfilling of masked regions. Continued diffusion of propagating species as well as generation of new active centers by diffracted as well as internally reflected light may enable masked or groove regions to polymerize, thus, resulting in a decrease of the final measured amplitude. Even with these differences, final channel amplitude is still about 10% of the maximum channel amplitude at high light intensity and long curing times ( $> 500 \text{ s}$ ).

#### Alignment of Neuronal and Glial Cell Types

Our labs have previously demonstrated robust growth of SGNs on unpatterned, as well as some alignment on patterned, HMA-co-HDDMA polymers similar to that used for this study.<sup>34</sup> However, to determine if gradually sloping micro-channels induce general sensory neurite alignment, alternative sensory neuronal populations were cultured on patterned polymers as well as on unpatterned controls (Fig 5.4). Specifically, SGN

neurite alignment was compared to DRGN and TGN neurite alignment, which are also sensory neurons of the peripheral nervous system (PNS). Each neuronal population was cultured on a micropattern with a periodicity of 50  $\mu\text{m}$  and channel amplitude of 3  $\mu\text{m}$ .

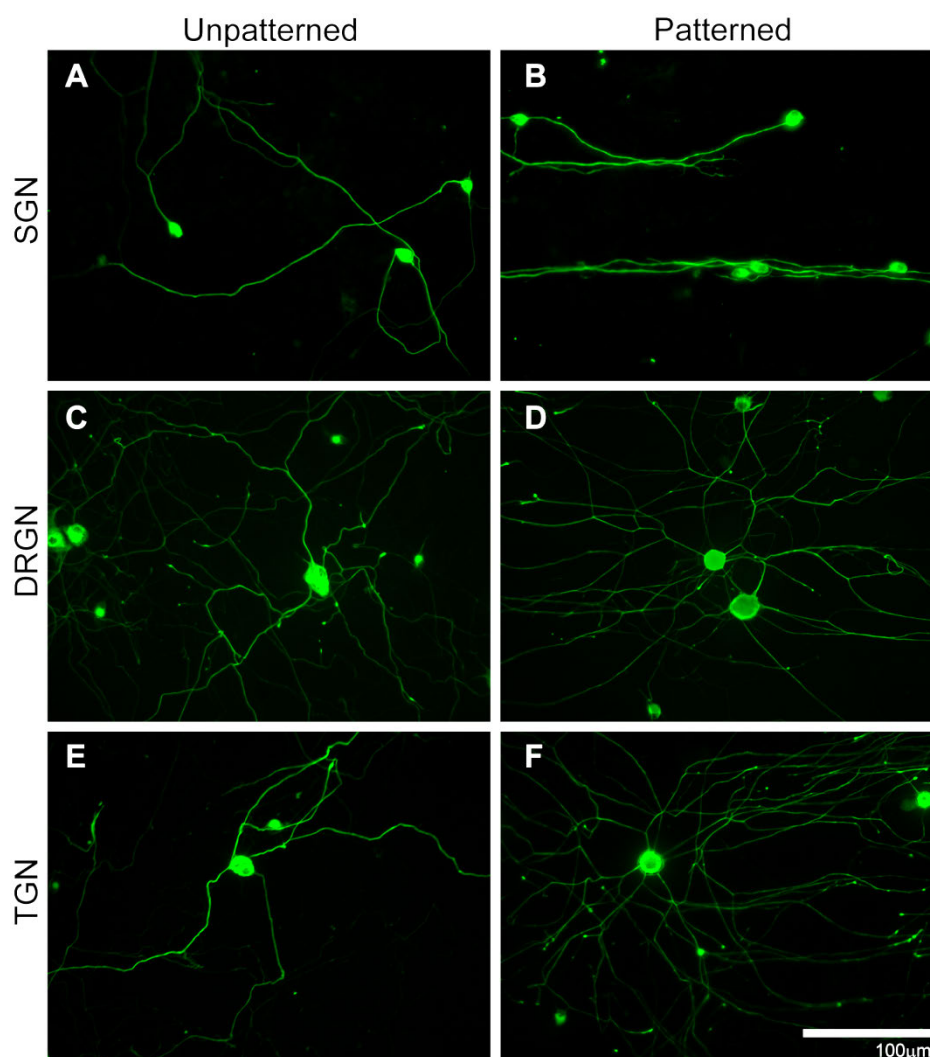


**Figure 5.4.** Neurite growth from dissociated SGNs (A),(B), DRGNs (C),(D), and TGNs (E),(F) on unpatterned (left column) and patterned (right column) HMA-co-HDDMA polymers. Neurite growth extends randomly on unpatterned substrates but aligns to topographic features on patterned substrates. Cultures were stained with anti-NF200 antibodies. Micropatterned substrates have periodicities of 50  $\mu\text{m}$  and channel amplitudes of 3  $\mu\text{m}$ . The pattern is oriented horizontally.

As seen in Figure 5.4, *de novo* neurite growth for each sensory neuronal type extends randomly on unpatterned HMA-co-HDDMA which is analogous to neuritic process growth on laminin coated glass.<sup>40</sup> Conversely, gradually sloping microchannels formed by the described photopolymerization method induce general neurite alignment among each neuronal population. SGN neurites strongly align to the pattern along the majority of their path length. SGNs show a typical monopolar or bipolar morphology in culture (i.e. one to two primary neurites). DRGNs and TGNs extend multiple primary neuritic processes which is also typical of their standard morphology. While neuritic processes from DRGNs and TGNs align to the micropattern, they do not align as strongly along the entire process length compared with SGN neurites. DRGN and TGN neurites initially extend radially from the soma on patterned substrates with apparently little sensitivity to the pattern direction. However, given sufficient distance, the majority of primary neurites turn and align to the pattern direction along the terminal portion of the neurite.

For quantitative analysis, neurite alignment to the pattern was measured and expressed as an alignment ratio of unaligned length per length of neurite. Specifically, unaligned length is determined by subtracting aligned length ( $A_L$ ) from total neurite path length ( $T_L$ ). Aligned length was measured as distance traveled by the neurite only in the direction of the pattern. Pattern direction was always aligned horizontally during epifluorescent imaging. Consequently,  $A_L$  for unpatterned substrates was measured as distance traveled solely in the horizontal direction. Unaligned length ( $T_L - A_L$ ) is then divided by  $T_L$  to yield unaligned distance per length of neurite,  $(T_L - A_L)/T_L$ . An alignment ratio close to zero represents a neurite that strongly aligns to the pattern along its entire length while higher ratios represent neurites with a significant amount of unaligned length.

To evaluate sensory neurite response to micropatterns, alignment was measured on unpatterned and patterned substrates using the previously described ratio (Fig 5.5).

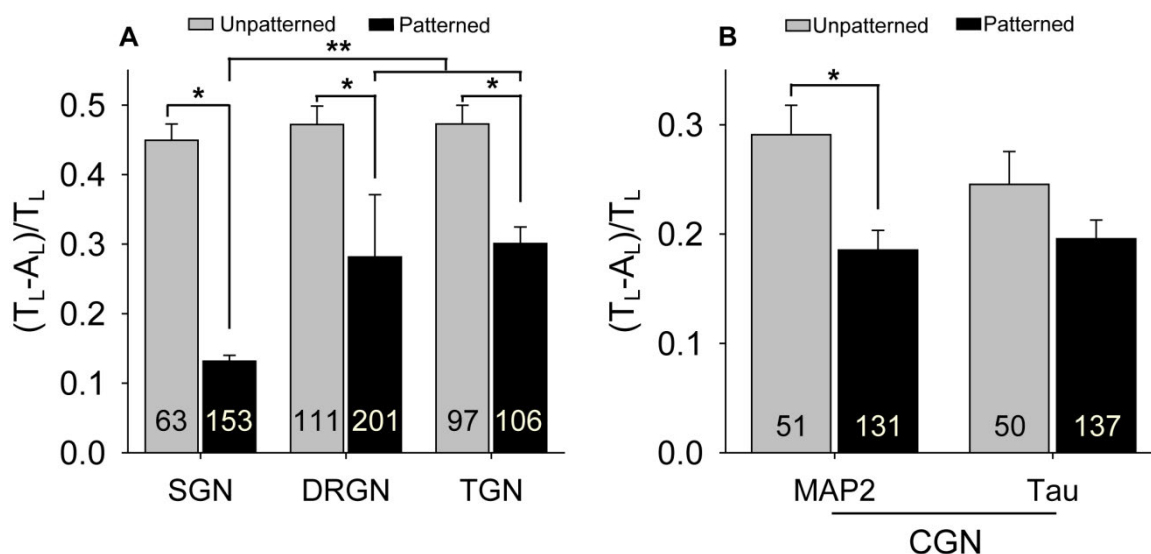


**Figure 5.5.** Unaligned length per neurite length ratios (mean $\pm$ SE) for multiple neuronal types cultured on unpatterned and patterned substrates. **A)** Neurite alignment from dissociated SGNs, DRGNs, and TGNs is statistically different on patterned substrates compared to unpatterned controls (\* $p < 0.005$ , Mann-Whitney Rank Sum test). SGN neurites align more strongly to the pattern than DRGN and TGN neurites (\*\* $p < 0.001$ , one way ANOVA). **B)** Dendritic neurite (MAP 2-positive) alignment from dissociated CGNs is statistically different on patterned substrates compared to an unpatterned control (\* $p < 0.005$ , Mann-Whitney Rank Sum test). However, axonal neurite (Tau-positive) alignment from dissociated CGNs is not statistically different ( $p = 0.135$ ) from an unpatterned control. Micropatterns used for each neuronal culture have periodicities of 50  $\mu\text{m}$  and channel amplitudes of 3  $\mu\text{m}$ . The number in each bar represents the number of neurites measured. Error bars represent standard error of the mean (SE).

Differences between neuritic process alignment on unpatterned compared to alignment on patterned samples are significantly different for each sensory neuronal population. As observed from epifluorescent digital images, SGN neurites align more strongly to patterned substrates than neurites from DRGNs and TGNs. SGN neurites exhibited less than half of the unaligned length per length of neurite shown by the other sensory neurites. The alignment ratios of each type of sensory neurite on unpatterned substrates are not statistically different. Neurite alignment from cerebellar granular neurons (CGN), which are part of the central nervous system (CNS), was also evaluated. CGN MAP 2-

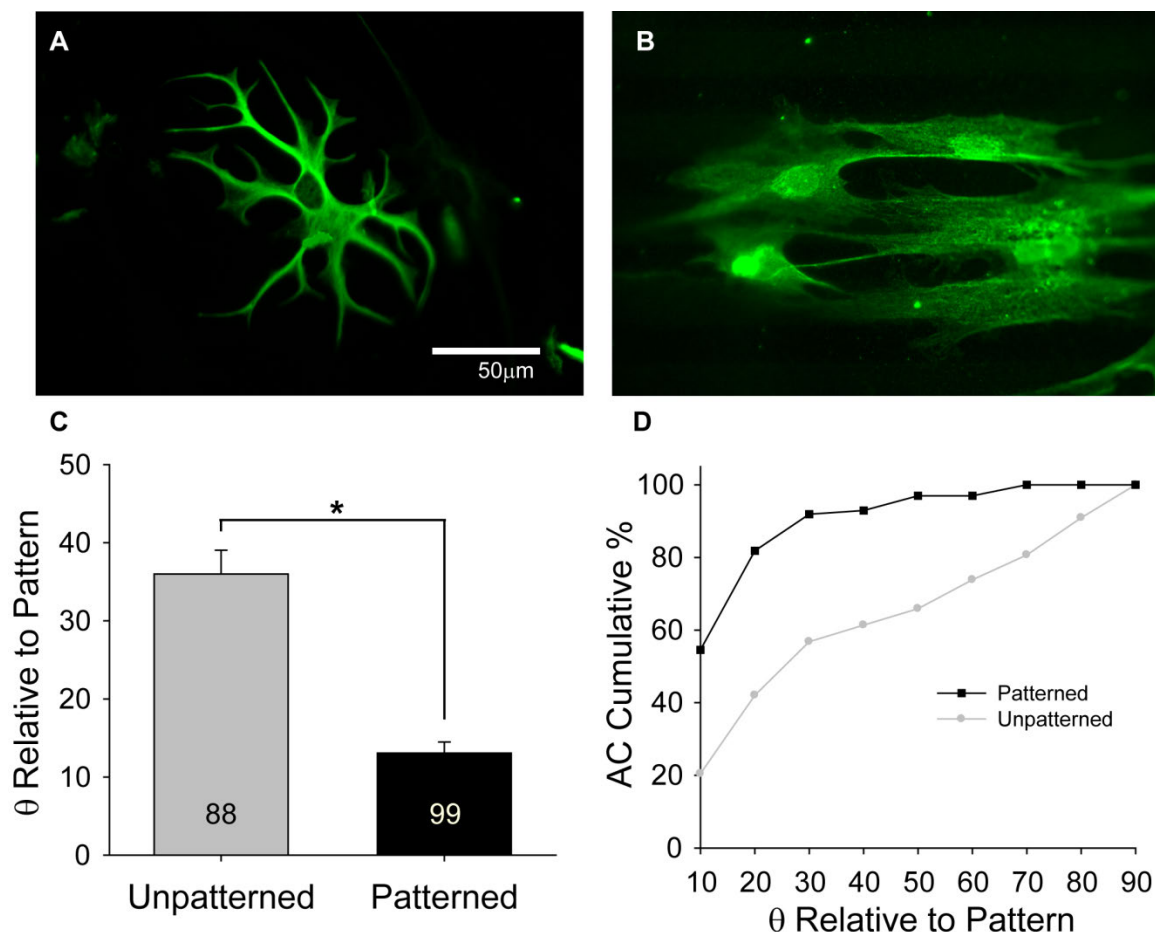


**Figure 5.6.** AC alignment on unpatterned and patterned substrates. **A-B)** ACs demonstrate typical morphology on unpatterned polymers. However, ACs elongate and align on patterned (B) polymers. **C)** The alignment angle (mean $\pm$ SE) of ACs on unpatterned substrates is statistically different from the alignment angle on patterned substrates (\* $p < 0.005$ , Mann-Whitney Rank Sum test). The number in each bar represents the number of ACs measured. **D)** Representation of the cumulative percent of ACs at or below the angle relative to the pattern direction indicated in the x-axis. 55% of ACs align to the pattern (angle of  $10^\circ$  or less) and greater than 90% of ACs are within  $30^\circ$  or less of the pattern direction. Micropatterns used for AC alignment have periodicities of  $50\ \mu\text{m}$  and channel amplitudes of  $3\ \mu\text{m}$ .

positive dendritic neurites align to patterned substrates and show random growth on unpatterned surfaces (Fig 5.5B). However, CGN Tau-positive axonal neurites do not significantly align to micropatterns of the given dimensions. While regenerative neurites from various neuronal types align to microfeatures, differences in neurite alignment indicate that specific neural populations, and even neural process types, respond to physical cues to varying degrees.

Having previously demonstrated basic SGSC alignment on micropatterned HMA-co-HDDMA polymers,<sup>34</sup> astrocytes (ACs) from the CNS were cultured on unpatterned and patterned polymers as a glial cell alternative to determine if similar micro-features induce general glial cell alignment (Fig 5.6). AC cultures were prepared from P5 rat cerebral cortex and were plated on substrates coated with poly-lysine. ACs demonstrate typical morphology on unpatterned substrates. By contrast, ACs elongate and align in the direction of micro-channels on patterned samples with the same dimensions of 50  $\mu\text{m}$  periodicity and 3  $\mu\text{m}$  amplitude as used for neuronal studies. As described previously, SGSC and AC alignment to pattern features was evaluated by measuring the angle made between the major axis of a cell outline and the pattern direction (horizontal).<sup>34</sup> Glial cells that made an angle of  $10^\circ$  or less with the pattern are considered aligned. The mean ellipse angle of ACs cultured on unpatterned polymers is almost three times the mean angle on patterned samples. As a population, 55% of ACs align (i.e.  $10^\circ$  or less) to microfeatures (Fig 5.6D) with a 50  $\mu\text{m}$  periodicity and 3  $\mu\text{m}$  amplitude, which is even greater than the 40% of SGSCs that align to similar features (Fig 5.7F). Interestingly, while ACs and SGSCs align to the described features, fibroblasts do not strongly align to features on a similar size scale.<sup>34</sup>

#### Controlling the Extent of Neurite and Glial Alignment

Pattern shapes ultimately dictate the final direction taken by SGN neurites or SGSCs that orient to the micro-features. However, to evaluate the influence of channel

amplitude on the extent of SGN neurite and SGSC alignment, the cells were cultured on micropatterns with varied amplitude but constant periodicity (Fig 5.7). Specifically, SGSCs and dissociated SGNs were cultured on patterns with a constant periodicity of 50  $\mu\text{m}$  but with varying channel amplitudes of  $1.0 \pm 0.1$ ,  $3.1 \pm 0.3$ , and  $8.1 \pm 0.8$   $\mu\text{m}$ , which will be referred to as 1, 3, and 8  $\mu\text{m}$ , respectively. To tune channel amplitude, the irradiation source was shuttered at specific time intervals to temporally arrest the polymerization during pattern development. SGN neurite length does not appear to change with different amplitudes. In addition to maintaining similar average lengths, the spread of neurite lengths for SGNs cultured on patterned substrates with each amplitude shows no observable effect of channel amplitude on absolute SGN neurite length (Fig 5.7B).

Conversely, SGN neurite alignment increases significantly with increasing channel depth. SGN neurites have a low average alignment ratio of 0.045 on 8  $\mu\text{m}$  deep channels, which is approximately three times more aligned than neurites on 1 and 3  $\mu\text{m}$  amplitude samples with ratios of 0.16 and 0.13, respectively (Fig 5.7C). The low alignment ratio on 8  $\mu\text{m}$  amplitude channels also indicates that the neurites strongly align to the pattern along their entire path length. Alignment along the length of a neurite may be crucial to preserve signal fidelity by limiting interaction with adjacent neurites since unaligned regions of a neurite are more likely to encounter other neurites. Furthermore, to limit inaccurate spatial signaling, it may be necessary to maintain tight control over a population of tens to thousands of neurites within a specific region. It is therefore important to note that greater than 90% of the SGN population cultured on the 8  $\mu\text{m}$  deep channels exhibit alignment ratios of 0.10 or lower while 100% of the neurites produce alignment ratios less than 0.25. Approximately 60% of neurites on 1  $\mu\text{m}$  and 70% on 3  $\mu\text{m}$  channels align fairly well to the pattern with a ratio of 0.15 or lower, however, a significant percentage remains with ratios higher than 0.30 (Fig 5.7D). While wandering neurites may align to the pattern throughout some of their length, a significant portion

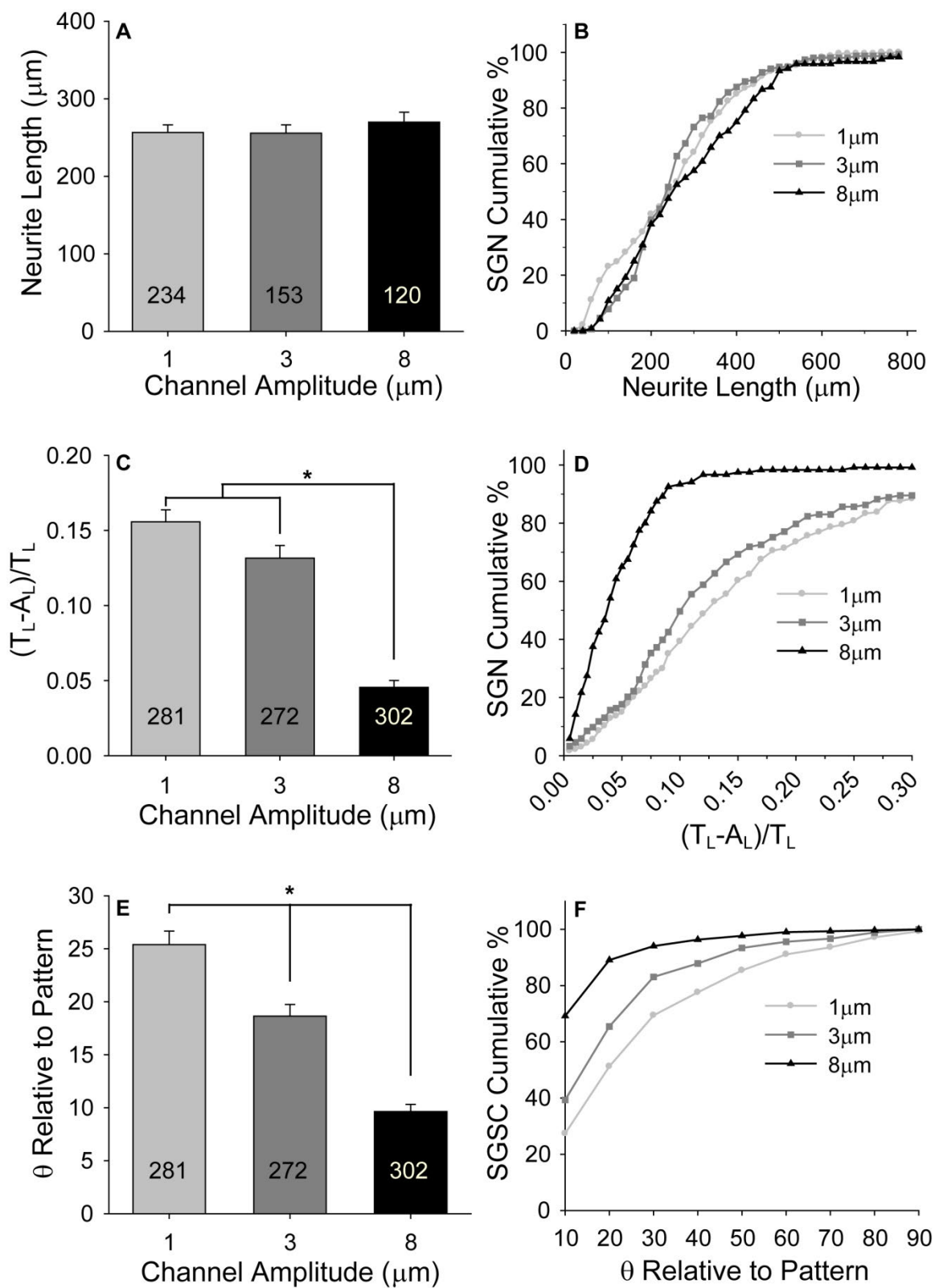


**Figure 5.7.** SGN neurite and SGSC alignment on patterns with constant periodicity

Figure 5.7. Continued

(50  $\mu\text{m}$ ) but varying amplitude. **A)** SGN neurite length is not statistically different when cultured on patterns that have channel amplitudes of 1, 3, and 8  $\mu\text{m}$ . **B)** Representation of the cumulative percent of neurites at or below the length indicated in the x-axis. The spread of neurite lengths for the population of SGN neurites is also not affected by the given channel amplitudes. **C)** SGN neurite alignment (mean $\pm$ SE) increases significantly with increasing channel amplitude (\* $p < 0.001$ , one way ANOVA). SGN neurite alignment was measured as a ratio of unaligned length per neurite length,  $[(T_L - A_L)/T_L]$ . Ratios that approach zero indicate the highest degree of alignment. **D)** Representation of the cumulative percent of neurites at or below the unaligned length per neurite length ratio indicated in the x-axis. 93% of the SGN neurite population cultured on 8  $\mu\text{m}$  deep channels falls within a low unaligned length per neurite length ratio of 0.10 compared to 39% and 50% on 1 and 3  $\mu\text{m}$  channels, respectively. **E)** SGSC alignment (mean $\pm$ SE) increases significantly with increasing channel depth (\* $p < 0.005$ , one way ANOVA). SGSC orientation was measured as the angle made between the pattern and the major axis of an ellipse fitted around the cell. **F)** Representation of the cumulative percent of SGSCs at or below the angle relative to the pattern direction indicated in the x-axis. 70% of SGSCs align (i.e. angle of  $10^\circ$  or less) to patterns with channels that are 8  $\mu\text{m}$  in amplitude compared to 30% and 40% that align to 1  $\mu\text{m}$  and 3  $\mu\text{m}$  deep channels, respectively.

may not track in the pattern direction which could ultimately lead to a loss of stimulatory specificity and resolution. Accordingly, microtopography fabricated for neurite alignment should be designed to quickly orient and maintain spatial control of neuritic processes along their entire length.

Along with SGN neurite contact guidance, it may also be advantageous to develop an understanding of SGSC response to cell relevant physical features due to their close association with SGNs and their processes.<sup>34, 57, 58</sup> For example, SGSCs closely associate with regenerative neurites *in vitro* and express neurotrophins such as BDNF and NT-3 that provide crucial trophic support to maintain SGN viability and support neurite growth.<sup>36, 57, 58</sup> Accordingly, the extent of SGSC alignment in response to patterns with constant periodicity but varied feature amplitude was evaluated by co-culturing SGSCs with SGNs on micropatterned HMA-co-HDDMA polymers with 1, 3, and 8  $\mu\text{m}$  channel amplitudes and 50  $\mu\text{m}$  periodicity (Fig 5.7E,F). SGSC alignment was quantified by the

same method used for AC alignment. Similar to SGN neurite alignment, SGSC alignment to parallel line-space gratings with gradual slopes also significantly increases with increasing channel amplitude (Fig 5.7E). Taken as a population, the percentage of SGSCs that align within  $10^\circ$  to the pattern direction is 25%, 40%, and 70% for 1, 3, and 8  $\mu\text{m}$  channels, respectively.

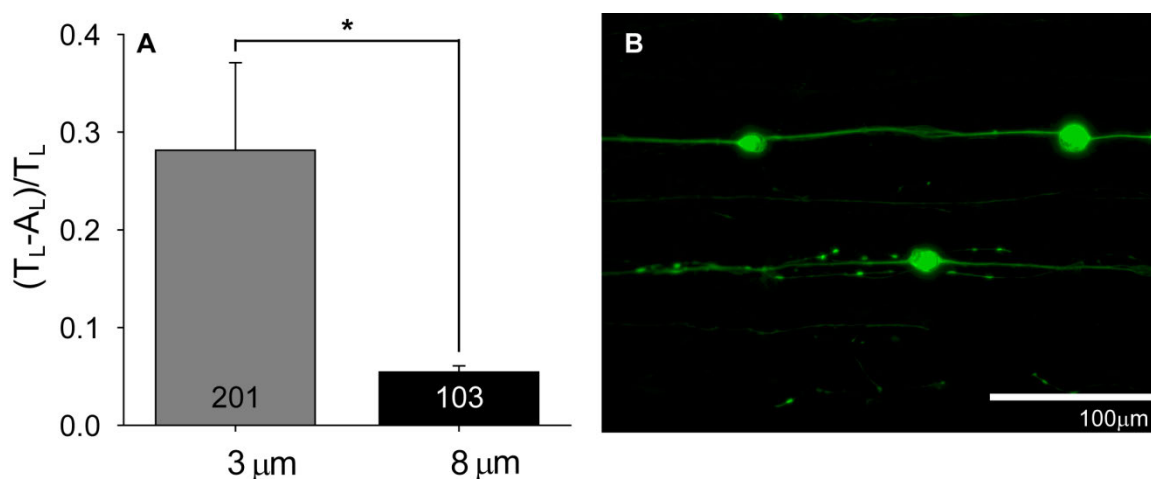


**Figure 5.8.** DRGN neurite alignment on patterns with constant periodicity (50  $\mu\text{m}$ ) but varying amplitude. **A)** DRGN neurite alignment (mean  $\pm$  SE) increases significantly with increasing channel amplitude ( $*p < 0.005$ , one way ANOVA). DRGN neurite alignment was measured as a ratio of unaligned length per neurite length,  $[(T_L - A_L) / T_L]$ . Ratios that approach zero indicate the highest degree of alignment. **B)** Dissociated neurite growth from DRGNs on a pattern with 8  $\mu\text{m}$  deep channels and a 50  $\mu\text{m}$  periodicity. DRGN primary neurites and their branches strongly align to the pattern direction on 8  $\mu\text{m}$  deep channels compared to the spread of neurite growth near the cell body on 3  $\mu\text{m}$  deep channels (Fig 5.4C).

To verify if the change in neurite alignment in response to channel depth was specific to SGN neurites, DRGN neurite alignment was also evaluated on patterns with increasing micro-channel amplitude (Fig 5.8). It was previously noted that DRGN neurites had two times as much unaligned length per length of neurite compared to SGN

neurites on patterns with a 50  $\mu\text{m}$  periodicity and a 3  $\mu\text{m}$  depth. However, on patterns with an 8  $\mu\text{m}$  channel amplitude and 50  $\mu\text{m}$  periodicity, DRGN neurite alignment (ratio of 0.054) is not significantly different from SGN neurite alignment (ratio of 0.045) on the same features (Fig 5.8A). Additionally, DRGN neurites branch extensively as well as cross over pattern features several times at the proximal end of the neurite (i.e. near the soma) on patterns with a 50  $\mu\text{m}$  periodicity and a 3  $\mu\text{m}$  amplitude. However, DRGN primary neurites and their branches appear to be maintained within micropattern features due to strong alignment effects from physical surface cues on patterns with the same periodicity but deeper channels (8  $\mu\text{m}$ ). Therefore, while different neurons may respond to physical guidance cues to varying degrees at one size scale, they appear to exhibit similar guidance behavior after reaching a critical feature slope or amplitude.

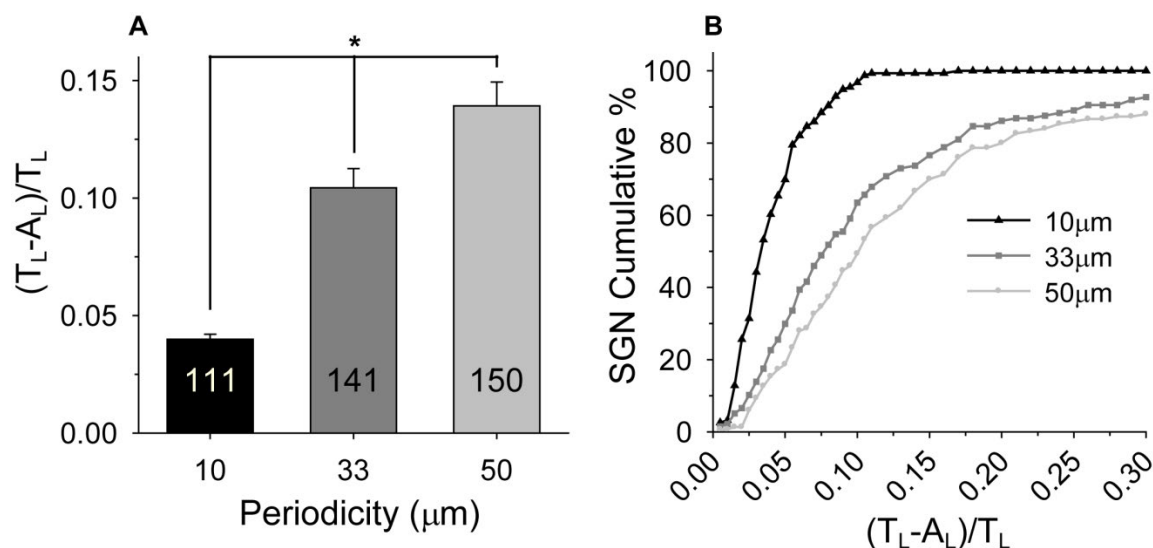


**Figure 5.9.** SGN neurite alignment on patterns with constant amplitude (1  $\mu\text{m}$ ) but varying periodicity. **A)** SGN neurite alignment (mean $\pm$ SE) increases significantly with decreasing periodicity (\* $p < 0.005$ , one way ANOVA). SGN neurite alignment was measured as a ratio of unaligned length per neurite length,  $[(T_L - A_L) / T_L]$ . Ratios that approach zero indicate the highest degree of alignment. **B)** Representation of the cumulative percent of neurites at or below the unaligned length per neurite length ratio indicated in the x-axis. 97% of the SGN neurite population cultured on patterns with a 10  $\mu\text{m}$  periodicity falls within a low unaligned length per neurite length ratio of 0.10 compared to 63% and 49% on patterns with 33 and 50  $\mu\text{m}$  periodicities, respectively.

To determine the effect of feature frequency, or periodicity, on the extent of neural process alignment, SGN neurite alignment was measured on patterns with a constant amplitude of 1  $\mu\text{m}$  but with periodicities of 10, 33.3, and 50  $\mu\text{m}$  (Fig 5.9). Micropattern periodicity is controlled using Ronchi rule photomasks with various band spacings, while consistent amplitude for various periodicities is achieved by controlling UV exposure time. SGN neurites are three times more aligned on patterns with a 10  $\mu\text{m}$  periodicity compared to patterns with 50  $\mu\text{m}$  periodicities (Fig 5.9A). Interestingly, SGN neurite alignment on a 10  $\mu\text{m}$  periodicity and relatively shallow 1  $\mu\text{m}$  amplitude pattern is not statistically different than their alignment on a 50  $\mu\text{m}$  periodicity and 8  $\mu\text{m}$  deep amplitude pattern. Additionally, over 95% of the population of SGN neurites cultured on patterns with a 10  $\mu\text{m}$  periodicity but shallow amplitude of 1  $\mu\text{m}$  fall below the low alignment ratio of 0.10 (Fig 5.9B). While approximately 60% of neurites on patterns with a 33.3  $\mu\text{m}$  periodicity and 50% of neurites on patterns with a 50  $\mu\text{m}$  periodicity also fall below a ratio of 0.10, there still remains a large percentage of the population that weakly aligns. The strong alignment observed on 1  $\mu\text{m}$  amplitude samples with frequent features may be due to several contributing factors. Specifically, patterns that have smaller periodicities present more opportunities for a regenerative neuritic process to encounter a physical feature and orient to the pattern direction over a given distance than those with larger periodicities. Moreover, decreasing pattern periodicity while maintaining channel amplitude increases the slope magnitude between minimum groove depths and the adjacent maximum ridge heights. Photopolymerization of micropatterned topography is, therefore, a useful and facile method to determine cellular response to feature slope and spacing.

#### Neurite Alignment on Nano-scale Features

Having determined that SGN neurites strongly align to shallow (1  $\mu\text{m}$ ) but frequent (10  $\mu\text{m}$ ) features, we next sought to determine, by extension, the extent to which

SGN neurites align to nano-scale ( $< 1 \mu\text{m}$ ) and frequent features (Fig 5.10). Nano-scale features are fabricated by curing samples with long UV exposure times ( $> 100\text{s}$ ) under  $10 \mu\text{m}$  periodicity masks. Narrower bands increase the angle of diffracted light and, therefore, increase polymerization under masked regions leading to greater backfilling and shallower features. Narrow band spacing also decreases reaction volume of each irradiated region which allows for less mass transfer to produce raised regions. Uniform and reproducible amplitudes of approximately  $250 \text{ nm}$  and  $500 \text{ nm}$  were generated using UV exposure increments of  $300 \text{ s}$  and  $125 \text{ s}$ , respectively. SEM confirms that overall polymer thickness remained constant ( $\sim 18 \mu\text{m}$ ) and that the pattern depth is only a small fraction of the film thickness from vertical examination based on cross-sectional imaging (Fig 5.10A,B). SGN neurites strongly align to patterns with channel amplitudes of  $250 \text{ nm}$  and  $500 \text{ nm}$  and show random growth on unpatterned controls (Fig 5.10). Interestingly, SGN neurite alignment on  $250 \text{ nm}$  amplitude channels with a  $10 \mu\text{m}$  periodicity was not statistically different from alignment on  $8 \mu\text{m}$  amplitude channels with a  $50 \mu\text{m}$  periodicity. As indicated by their low alignment ratio, regenerative SGN neurites on  $250 \text{ nm}$  deep channels align along their entire path length which is similar to SGN neurite alignment on channels with an  $8 \mu\text{m}$  amplitude and  $50 \mu\text{m}$  periodicity (Fig 5.10C, D).

Other neuritic processes, namely those from sympathetic and DRG neurons, also align to nano-scale line-space gratings (depth  $300 \text{ nm}$ , width  $100 - 400 \text{ nm}$ ).<sup>16</sup> However, the vertical slopes inherent to lithographic techniques contrast with the sloped transitions between ridges and grooves developed by photopolymerization in this study. In either case, both for SGNs and sympathetic neurons, neuritic growth cones that are several microns in diameter are sensitive enough to respond and align to features that are smaller by an order of magnitude. Accordingly, it is evident that nano-scale features should be considered for alignment of neurites for both *in vitro* contact guidance studies as well as for future applications intended to improve neural-implant interfaces.

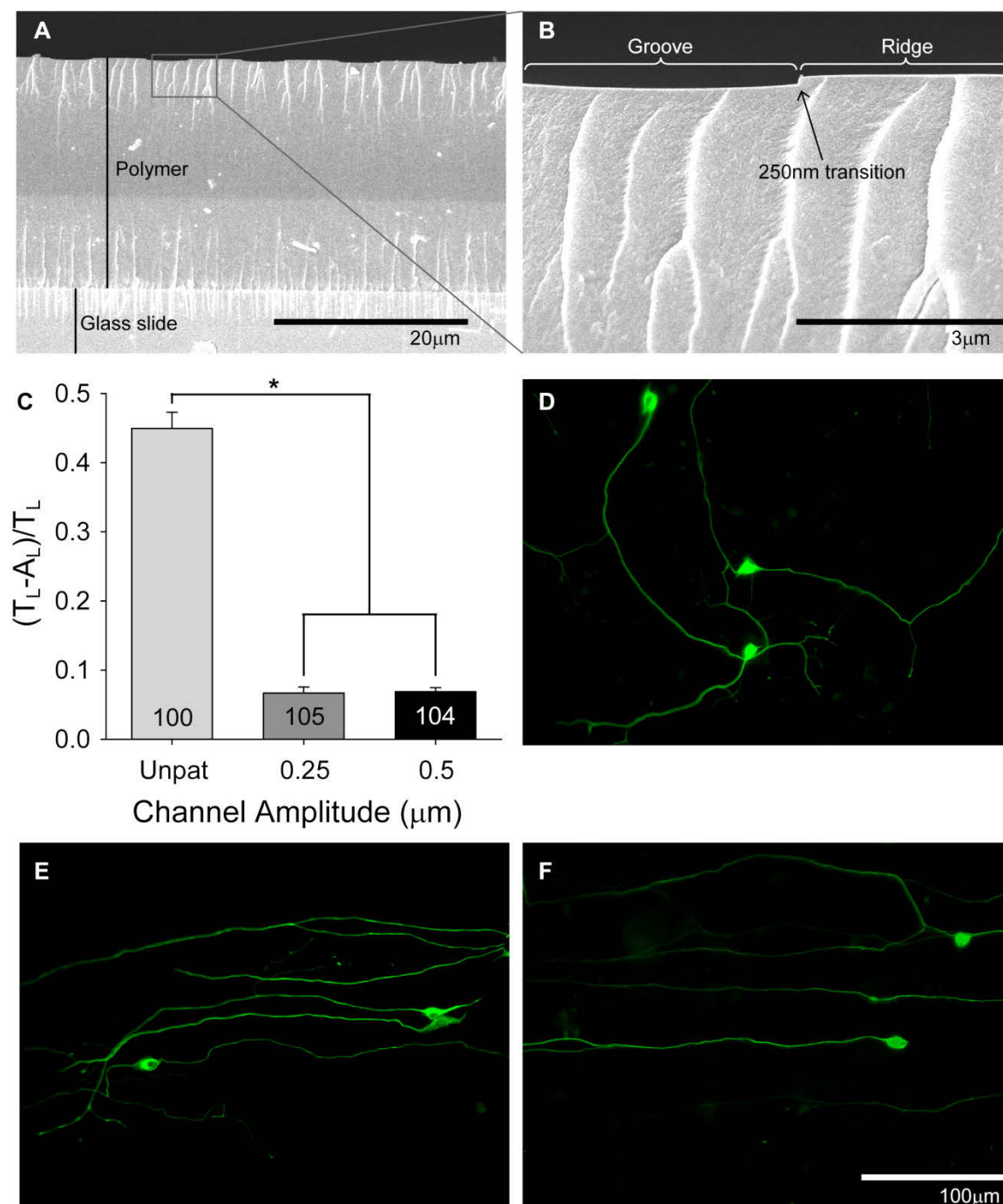


**Figure 5.10.** SGN neurite alignment to nano-scale ( $<1 \mu\text{m}$ ) features. **A-B)** Cross-sectional SEM images demonstrate the depth of the pattern features compared to the thickness of the polymer film. **C)** SGN neurites strongly align to patterns with  $10 \mu\text{m}$  periodicities and  $250 \text{ nm}$  and  $500 \text{ nm}$  amplitudes ( $*p < 0.005$ , one way ANOVA). **D)** SGN neurite growth extends randomly on unpatterned HMA-co-HDDMA polymers. **E-F)** SGN neurite growth strongly aligns to patterns with  $10 \mu\text{m}$  periodicity and  $250 \text{ nm}$  amplitudes (E) as well as to patterns with  $50 \mu\text{m}$  periodicities and  $8 \mu\text{m}$  amplitudes (F).

Figure 5.10. Continued

Interestingly, there is no statistical difference ( $p = 0.369$ ) between SGN neurite alignment on the patterns described in E and F. Cultures were stained with anti-NF200 antibodies (D-F). The pattern is oriented horizontally.

#### Correlation of Neurite Alignment to Microfeature Slope

SGN neurite alignment improves as amplitude increases with constant periodicity and also improves as periodicity decreases with constant amplitude. In both cases, the slope grade that transitions between grooves and ridges also steepens. Accordingly, to determine if changes in neurite alignment correlate to feature slope, AFM was used to quantify the average and maximum slope that occur between groove minimums and adjacent ridge maximums of each pattern used for neurite contact guidance (Table 5.1).

Table 5.1

Summary of micropattern dimensions, transitional slope, and neurite alignment

Periodicity ( $\mu\text{m}$ )	Amplitude* ( $\mu\text{m}$ )	Avg Slope* ( $\mu\text{m}/\mu\text{m}$ )	Max Slope* ( $\mu\text{m}/\mu\text{m}$ )	$(T_L - A_L)/T_L^{**}$ ( $\mu\text{m}/\mu\text{m}$ )
10	0.25 $\pm$ 0.01	0.057 $\pm$ 3e-4	1.12 $\pm$ 0.13	0.063 $\pm$ 9e-3
10	0.51 $\pm$ 0.02	0.095 $\pm$ 2e-4	1.22 $\pm$ 0.15	0.070 $\pm$ 6e-3
10	1.0 $\pm$ 0.1	0.180 $\pm$ 4e-4	1.57 $\pm$ 0.01	0.044 $\pm$ 2e-3
33.3	1.1 $\pm$ 0.1	0.058 $\pm$ 2e-4	0.90 $\pm$ 0.07	0.100 $\pm$ 8e-3
50	1.0 $\pm$ 0.1	0.059 $\pm$ 2e-4	0.74 $\pm$ 0.07	0.156 $\pm$ 9e-3
50	3.1 $\pm$ 0.3	0.098 $\pm$ 4e-4	0.89 $\pm$ 0.09	0.132 $\pm$ 9e-3
50	8.1 $\pm$ 0.8	0.233 $\pm$ 2e-4	1.37 $\pm$ 0.23	0.045 $\pm$ 5e-3

\* mean $\pm$ SD \*\* mean $\pm$ SE

As indicated in Table 5.1, average and maximum slope increase as channel amplitude increases for a given periodicity and neurite alignment correspondingly increases. Figure 5.11 illustrates the correlation between neurite alignment and average feature slope as well as neurite alignment and maximum feature slope on a linear regression plot. Average slope between ridge-groove transitions moderately correlates with SGN alignment ( $r = 0.67$ ) but is not considered significant ( $p > 0.05$ ). However, maximum slope strongly correlates with neurite alignment ( $r = 0.93$ ) and is significant ( $p < 0.005$ ). In fact, slope appears to be a much stronger predictor of alignment than either periodicity or amplitude.

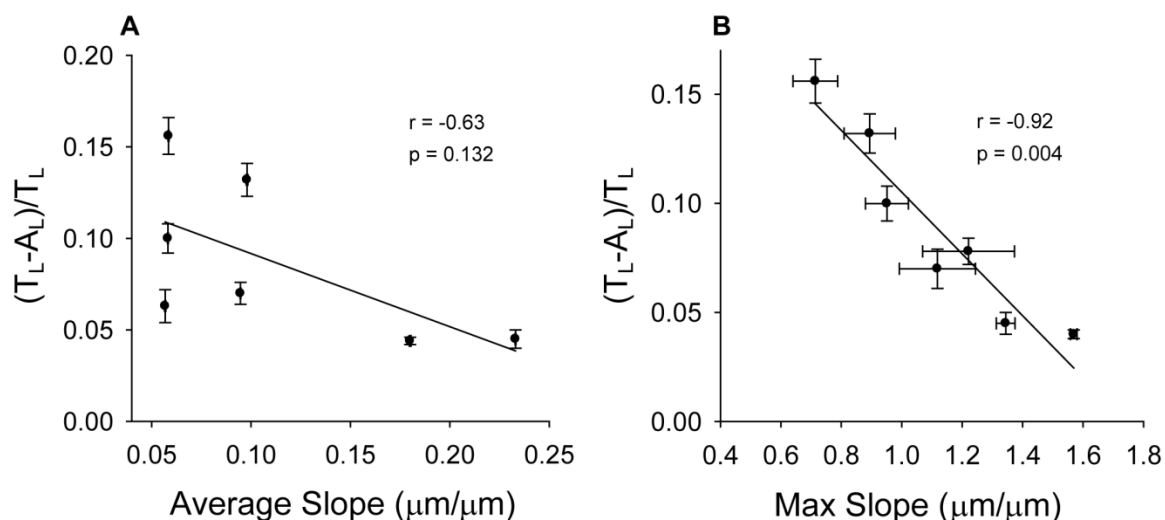


**Figure 5.11.** Linear regression correlation of SGN neurite alignment with average (A) and maximum slope (B) of groove-ridge transitions. SGN neurite alignment strongly correlates with maximum feature slope.

Interestingly, an average diameter of an SGN growth cone is approximately  $5 \mu\text{m}$  but features as small as  $250 \text{ nm}$  cause significant neurite contact guidance when maximum feature slope is sufficiently steep. Therefore, neurite alignment and subsequent spatial

control by physical cues may depend more strongly on feature contrast rather than on absolute feature height.

### Conclusions

Spatially directing regenerative sensory neurites to stimulative prostheses elements may serve as a viable method to improve neural prosthetic performance including enhanced tonal resolution for cochlear implants. Accordingly, in this study we describe a facile photopolymerization method to fabricate tunable methacrylate micropatterns that align inner ear neural elements, namely, regenerative spiral ganglion neuron (SGN) neurites and spiral ganglion Schwann cells (SGSCs), based on physical surface cues. Gradually sloping micro- and nano-scale features generated by this method were tuned to investigate the extent of SGN neurite alignment in response to modulations in feature amplitude, frequency, and slope. Channel amplitude can be controlled from 250 nm – 10  $\mu$ m by modulating UV exposure time, initiating light intensity, and photoinitiator concentration, while pattern periodicity is regulated by grating dimensions. Glial cells as well as neurites from SGNs, DRGNs, TGNs, and CGNs align to the photopolymerized micropatterns, but alignment varies among cell types. Alignment of neural elements increases significantly with increasing feature amplitude as well as with decreasing periodicity. SGN neurites, which are typically several microns in diameter, also strongly align to patterns with nano-scale (250 and 500 nm) channel amplitudes and more frequent features. Furthermore, SGN neurite alignment strongly correlates ( $r = 0.93$ ) with maximum feature slope that can be tuned by feature amplitude and periodicity. This photopolymerization fabrication method serves as an additional surface engineering tool that enables investigation of cell-material interactions in response to slope of micron and sub-micron scale features. The research also informs efforts to direct nerve growth for improved performance of neural prosthetics that currently provide low stimulatory specificity due to spatial resolution challenges.

### Notes

1. Tuft, B. W.; Li, S.; Xu, L.; Clarke, J. C.; White, S. P.; Guymon, B. A.; Perez, K. X.; Hansen, M. R.; Guymon, C. A. Photopolymerized microfeatures for directed spiral ganglion neurite and Schwann cell growth. *Biomaterials* **2013**, *34*, 42-54.
2. Leach, J. B.; Achyuta, A. K.; Murthy, S. K. Bridging the Divide between Neuroprosthetic Design, Tissue Engineering and Neurobiology. *Front. Neuroeng* **2010**, *2*, 18.
3. O'Leary, S. J.; Richardson, R. R.; McDermott, H. J. Principles of design and biological approaches for improving the selectivity of cochlear implant electrodes. *J. Neural Eng.* **2009**, *6*, 055002.
4. Winter, J. O.; Cogan, S. F.; Rizzo, J. F., III Retinal prostheses: current challenges and future outlook. *J. Biomater. Sci. Polym. Ed.* **2007**, *18*, 1031-1055.
5. Rubinstein, J. T. How cochlear implants encode speech. *Curr. Opin. Otolaryngol. Head Neck Surg.* **2004**, *12*, 444-8.
6. Shannon, R. V.; Fu, Q. J.; Galvin, J., The number of spectral channels required for speech recognition depends on the difficulty of the listening situation. *Acta Otolaryngol. Suppl.* **2004**, (552), 50-54.
7. Brors, D.; Aletsee, C.; Schwager, K.; Mlynski, R.; Hansen, S.; Schäfers, M.; Ryan, A. F.; Dazert, S. Interaction of spiral ganglion neuron processes with alloplastic materials in vitro. *Hear. Res.* **2002**, *167*, 110-121.
8. Evans, A. J.; Thompson, B. C.; Wallace, G. G.; Millard, R.; O'Leary, S. J.; Clark, G. M.; Shepherd, R. K.; Richardson, R. T. Promoting neurite outgrowth from spiral ganglion neuron explants using polypyrrole/BDNF-coated electrodes. *J. Biomed. Mater. Res. A* **2009**, *91A*, 241-250.
9. Roehm, P. C.; Hansen, M. R. Strategies to preserve or regenerate spiral ganglion neurons. *Curr. Opin. Otolaryngol. Head Neck Surg.* **2005**, *13*, 294-300.
10. Leng, T.; Wu, P.; Mehenti, N. Z.; Bent, S. F.; Marmor, M. F.; Blumenkranz, M. S.; Fishman, H. A. Directed retinal nerve cell growth for use in a retinal prosthesis interface. *Invest. Ophthalmol. Vis. Sci.* **2004**, *45*, 4132-4137.
11. Mehenti, N. Z.; Peterman, M. C.; Leng, T.; Marmor, M. F.; Blumenkranz, M. S.; Bent, S. F. A retinal interface based on neurite micropatterning for single cell stimulation. *Invest. Ophthalmol. Vis. Sci.* **2003**, *44*, U704-U704.
12. Guenther, E.; Troger, B.; Schlosshauer, B.; Zrenner, E. Long-term survival of retinal cell cultures on retinal implant materials. *Vision Res.* **1999**, *39*, 3988-3994.

13. Cui, X. Y.; Wiler, J.; Dzaman, M.; Altschuler, R. A.; Martin, D. C. In vivo studies of polypyrrole/peptide coated neural probes. *Biomaterials* **2003**, *24*, 777-787.
14. Hurtado, A.; Cregg, J. M.; Wang, H. B.; Wendell, D. F.; Oudega, M.; Gilbert, R. J.; McDonald, J. W. Robust CNS regeneration after complete spinal cord transection using aligned poly-L-lactic acid microfibers. *Biomaterials* **2011**, *32*, 6068-6079.
15. Miller, C.; Jęftinija, S.; Mallapragada, S. Synergistic effects of physical and chemical guidance cues on neurite alignment and outgrowth on biodegradable polymer substrates. *Tissue Eng.* **2002**, *8*, 367-378.
16. Johansson, F.; Carlberg, P.; Danielsen, N.; Montelius, L.; Kanje, M. Axonal outgrowth on nano-imprinted patterns. *Biomaterials* **2006**, *27*, 1251-1258.
17. Wangenstein, K. J.; Kalliainen, L. K. Collagen Tube Conduits in Peripheral Nerve Repair: A Retrospective Analysis. *Hand* **2009**, *5*, 273-277.
18. Richardson, J. A.; Rementer, C. W.; Bruder, J. M.; Hoffman-Kim, D. Guidance of dorsal root ganglion neurites and Schwann cells by isolated Schwann cell topography on poly(dimethyl siloxane) conduits and films. *J. Neural Eng.* **2011**, *8*, 046015.
19. Schmalenberg, K. E.; Uhrich, K. E. Micropatterned polymer substrates control alignment of proliferating Schwann cells to direct neuronal regeneration. *Biomaterials* **2005**, *26*, 1423-1430.
20. Branch, D. W.; Wheeler, B. C.; Brewer, G. J.; Leckband, D. E. Long-term stability of grafted polyethylene glycol surfaces for use with microstamped substrates in neuronal cell culture. *Biomaterials* **2001**, *22*, 1035-1047.
21. Gustavsson, P.; Johansson, F.; Kanje, M.; Wallman, L.; Linsmeier, C. E. Neurite guidance on protein micropatterns generated by a piezoelectric microdispenser. *Biomaterials* **2007**, *28*, 1141-1151.
22. Oliva, A. A.; James, C. D.; Kingman, C. E.; Craighead, H. G.; Banker, G. A. Patterning axonal guidance molecules using a novel strategy for microcontact printing. *Neurochem. Res.* **2003**, *28*, 1639-1648.
23. Wittig, J. H.; Ryan, A. F.; Asbeck, P. M. A reusable microfluidic plate with alternate-choice architecture for assessing growth preference in tissue culture. *J. Neurosci. Methods* **2005**, *144*, 79-89.
24. Li, S.; Li, H.; Wang, Z. Orientation of spiral ganglion neurite extension in electrical fields of charge-balanced biphasic pulses and direct current in vitro. *Hear. Res.* **2010**, *267*, 111-118.
25. Yao, L.; Pandit, A.; Yao, S.; McCaig, C. D. Electric Field-Guided Neuron Migration: A Novel Approach in Neurogenesis. *Tissue Eng. Part B Rev.* **2011**, *17*, 143-153.

26. Teixeira, A. I.; Abrams, G. A.; Bertics, P. J.; Murphy, C. J.; Nealey, P. F. Epithelial contact guidance on well-defined micro- and nanostructured substrates. *J. Cell. Sci.* **2003**, *116*, 1881-1892.
27. Chou, L.; Firth, J.; Uitto, V.; Brunette, D. Substratum surface topography alters cell shape and regulates fibronectin mRNA level, mRNA stability, secretion and assembly in human fibroblasts. *J. Cell. Sci.* **1995**, *108*, 1563-1573.
28. Dalby, M. J.; Gadegaard, N.; Tare, R.; Andar, A.; Riehle, M. O.; Herzyk, P.; Wilkinson, C. D.; Oreffo, R. O. The control of human mesenchymal cell differentiation using nanoscale symmetry and disorder. *Nat. Mater.* **2007**, *6*, 997-1003.
29. Anselme, K.; Bigerelle, M.; Noel, B.; Dufresne, E.; Judas, D.; Iost, A.; Hardouin, P. Qualitative and quantitative study of human osteoblast adhesion on materials with various surface roughnesses. *J. Biomed. Mater. Res.* **2000**, *49*, 155-166.
30. Spivey, E. C.; Khaing, Z. Z.; Shear, J. B.; Schmidt, C. E. The fundamental role of subcellular topography in peripheral nerve repair therapies. *Biomaterials* **2012**, *33*, 4264-4276.
31. Hsu, S.; Lu, P. S.; Ni, H.; Su, C. Fabrication and evaluation of microgrooved polymers as peripheral nerve conduits. *Biomed. Microdevices* **2007**, *9*, 665-674.
32. Song, M.; Uhrich, K. E. Optimal micropattern dimensions enhance neurite outgrowth rates, lengths, and orientations. *Ann. Biomed. Eng.* **2007**, *35*, 1812-1820.
33. Rajnicek, A. M.; Britland, S.; McCaig, C. D. Contact guidance of CNS neurites on grooved quartz: influence of groove dimensions, neuronal age and cell type. *J. Cell. Sci.* **1997**, *110*, 2905-2913.
34. Clarke, J. C.; Tuft, B. W.; Clinger, J. D.; Levine, R.; Figueroa, L. S.; Guymon A. C.; Hansen, M. R. Micropatterned methacrylate polymers direct spiral ganglion neurite and Schwann cell growth. *Hear. Res.* **2011**, *278*, 96-105.
35. Jeon, S.; Menard, E.; Park, J.; Maria, J.; Meitl, M.; Zaumseil, J.; Rogers, J. Three-dimensional nanofabrication with rubber stamps and conformable photomasks. *Adv Mater* **2004**, *16*, 1369-1373.
36. Hansen, M. R.; Vijapurkar, U.; Koland, J. G.; Green, S. H. Reciprocal signaling between spiral ganglion neurons and Schwann cells involves neuregulin and neurotrophins. *Hear. Res.* **2001**, *161*, 87-98.
37. Hegarty, J.; Kay, A.; Green, S. Trophic support of cultured spiral ganglion neurons by depolarization exceeds and is additive with that by neurotrophins or cAMP and requires elevation of  $[Ca^{2+}]_i$  within a set range. *J. Neurosci.* **1997**, *17*, 1959-1970.

38. Jeon, E.; Xu, N.; Xu, L.; Hansen, M. R. Influence of central glia on spiral ganglion neuron neurite growth. *Neuroscience* **2011**, *177*, 321-334.
39. McCarthy; DeVellis, J. Preparation of separate astroglial and oligodendroglial cell-cultures from rat cerebral tissue. *J. Cell Biol.* **1980**, *85*, 890-902.
40. Roehm, P. C.; Xu, N.; Woodson, E. A.; Green, S. H.; Hansen, M. R. Membrane depolarization inhibits spiral ganglion neurite growth via activation of multiple types of voltage sensitive calcium channels and calpain. *Mol. Cell. Neurosci.* **2008**, *37*, 376-387.
41. DeForest, C. A.; Sims, E. A.; Anseth, K. S. Peptide-functionalized click hydrogels with independently tunable mechanics and chemical functionality for 3D cell culture. *Chem. Mater.* **2010**, *22*, 4783-4790.
42. Bryant, S. J.; Cuy, J. L.; Hauch, K. D.; Ratner, B. D. Photo-patterning of porous hydrogels for tissue engineering. *Biomaterials* **2007**, *28*, 2978-2986.
43. Stermann, S.; Marsden, J. G. Silane coupling agents. *Ind. Eng. Chem. Res.* **1966**, *58*, 33-&.
44. Walba, D. M.; Liberko, C. A.; Korblova, E.; Farrow, M.; Furtak, T. E.; Chow, B. C.; Schwartz, D. K.; Freeman, A. S.; Douglas, K.; Williams, S. D.; Klitnick, A. F.; Clark, N. A. Self-assembled monolayers for liquid crystal alignment: simple preparation on glass using alkyltrialkoxysilanes. *Liq. Cryst.* **2004**, *31*, 481-489.
45. Weetall, H. H. Preparation of immobilized proteins covalently coupled through silane coupling agents to inorganic supports. *Appl. Biochem. Biotechnol.* **1993**, *41*, 157-188.
46. Abbe, E. Contributions to the theory of the microscope and the microscopic perception (translated from German). *Arch. Mikr. Anat* **1873**, *9*, 413-468.
47. Garini, Y.; Vermolen, B. J.; Young, I. T. From micro to nano: recent advances in high-resolution microscopy. *Curr. Opin. Biotechnol.* **2005**, *16*, 3-12.
48. Liliensiek, S. J.; Wood, J. A.; Yong, J.; Auerbach, R.; Nealey, P. F.; Murphy, C. J. Modulation of human vascular endothelial cell behaviors by nanotopographic cues. *Biomaterials* **2010**, *31*, 5418-5426.
49. Mattotti, M.; Alvarez, Z.; Ortega, J. A.; Planell, J. A.; Engel, E.; Alcántara, S. Inducing functional radial glia-like progenitors from cortical astrocyte cultures using micropatterned PMMA. *Biomaterials* **2012**, *33*, 1759-1770.
50. Hsu, S. H.; Chen, C. Y.; Lu, P. S.; Lai, C. S.; Chen, C. J. Oriented Schwann cell growth on microgrooved surfaces. *Biotechnol. Bioeng.* **2005**, *92*, 579-588.

51. Yao, L.; Wang, S.; Cui, W.; Sherlock, R.; O'Connell, C.; Damodaran, G.; Gorman, A.; Windebank, A.; Pandit, A. Effect of functionalized micropatterned PLGA on guided neurite growth. *Acta Biomater.* **2009**, *5*, 580-588.
52. Gasiorowski, J. Z.; Liliensiek, S. J.; Russell, P.; Stephan, D. A.; Nealey, P. F.; Murphy, C. J. Alterations in gene expression of human vascular endothelial cells associated with nanotopographic cues. *Biomaterials* **2010**, *31*, 8882-8888.
53. Ferrari, A.; Cecchini, M.; Serresi, M.; Faraci, P.; Pisignano, D.; Beltram, F. Neuronal polarity selection by topography-induced focal adhesion control. *Biomaterials* **2010**, *31*, 4682-4694.
54. Miyoshi, H.; Adachi, T.; Ju, J.; Lee, S. M.; Cho, D. J.; Ko, J. S.; Uchida, G.; Yamagata, Y. Characteristics of motility-based filtering of adherent cells on microgrooved surfaces. *Biomaterials* **2012**, *33*, 395-401.
55. Charest, J.; Eliason, M.; Garcia, A.; King, W. Combined microscale mechanical topography and chemical patterns on polymer cell culture substrates. *Biomaterials* **2006**, *27*, 2487-2494.
56. Francisco, H.; Yellen, B. B.; Halverson, D. S.; Friedman, G.; Gallo, G. Regulation of axon guidance and extension by three-dimensional constraints. *Biomaterials* **2007**, *28*, 3398-3407.
57. Bostrom, M.; Khalifa, S.; Bostrom, H.; Liu, W.; Friberg, U.; Rask-Andersen, H. Effects of neurotrophic factors on growth and glial cell alignment of cultured adult spiral ganglion cells. *Aud. Neurootol.* **2010**, *15*, 175-186.
58. Whilton, D. S.; Tieu, D.; Grover, M.; Reilly, B.; Coulson, M. T. Spontaneous association of glial cells with regrowing neurites in mixed cultures of dissociated spiral ganglia. *Neuroscience* **2009**, *161*, 227-235.

## CHAPTER 6

### NEURAL PATHFINDING ON UNI- AND MULTIDIRECTIONAL PHOTOPOLYMERIZED MICROPATTERNS<sup>1\*</sup>

Overcoming signal resolution barriers of neural prostheses, such as the commercially available cochlear implant (CI) or the developing retinal implant, will likely require spatial control of regenerative neural elements. To rationally design materials that direct nerve growth, it is first necessary to determine pathfinding behavior of *de novo* neurite growth from prosthesis-relevant cells such as spiral ganglion neurons (SGNs) in the inner ear. Accordingly, in this work, repeating 90° turns were fabricated as multidirectional micropatterns to determine SGN neurite turning capability and pathfinding. Unidirectional micropatterns and unpatterned substrates are used as comparisons. Spiral ganglion Schwann cell alignment (SGSC) is also examined on each surface type. Micropatterns are fabricated using the spatial reaction control inherent to photopolymerization with photomasks that have either parallel line spacing gratings for unidirectional patterns or repeating 90° angle steps for multidirectional patterns. Feature depth is controlled by modulating UV exposure time by shuttering the light source at given time increments. Substrate topography is characterized by white light interferometry and scanning electron microscopy (SEM). Both pattern types exhibit features that are 25 μm in width and  $7.4 \pm 0.7$  μm in depth. SGN neurites orient randomly on unpatterned photopolymer controls, align and consistently track unidirectional patterns, and are substantially influenced by, but do not consistently track, multidirectional turning cues. Developing methods to understand neural pathfinding and to guide *de novo* neurite growth to specific stimulatory elements will enable design of

---

\* Tuft, B.; Hansen, M.; Guymon, C. *ACS Appl. Mater Inter.* **2014**, <http://dx.doi.org/10.1021/am501622a>

innovative biomaterials that improve functional outcomes of devices that interface with the nervous system.

## Introduction

The interface between a biomaterial and biological tissue is a complex, dynamic microcellular environment that dictates the ultimate performance of a clinical device or material. Continuing advances in materials science, micro- and nano-fabrication, and tissue engineering enable design of 2D and 3D constructs that allow researchers to probe and even drive specific cell-material interactions along this crucial interface.<sup>2</sup> For example, many studies illustrate that stem cell phenotype can be manipulated by altering the material characteristics of the nascent environment.<sup>3-5</sup> Further, biomaterial mechanical or chemical properties and surface morphologies can be tailored to address requirements of a given cellular niche to improve functional outcomes of the biomaterial. Because of the innate ability that neurons have to explore and respond to their microenvironment – via *de novo* neurite growth during development or regeneration – and due to their importance in sensory, motor, and autonomic functions, they are the focus of substantial effort in cell-biomaterial interaction studies.<sup>6-9</sup>

In particular, a diverse array of methods is employed to direct the outgrowth of regenerative neural processes to span and repair damage in the peripheral nervous system. Nerve autografts remain the gold standard in clinical settings for these types of repairs, but recent advances in fabrication of multifaceted synthetic nerve conduits enable satisfactory neural regeneration and functional recovery even across large nerve gaps (> 10 cm).<sup>9</sup> Typical methods used to direct regenerative neurite outgrowth include: aligned microfibers,<sup>10</sup> bioactive molecule patterning,<sup>11-14</sup> parallel micro- and nano-channel morphology,<sup>15, 16</sup> diffusion gradients of chemo-attractants,<sup>17</sup> electrical fields,<sup>18</sup> intraluminal guidance structures,<sup>19</sup> and oriented glial cells.<sup>20</sup> The primary objective of

many neurite guidance studies is to effect maximal unidirectional outgrowth to bridge large gaps typical of nerve injuries. However, analogous neurite guidance techniques may also serve to address spatial resolution challenges that limit functional outcomes of neural prostheses by directing neurite growth to specific stimulatory elements.<sup>21-23</sup>

Neural prostheses electrically stimulate neural tissue to restore or augment remaining motor and sensory functions of neural pathways that were lost or damaged due to disease or physical trauma. Partly due to spatial resolution limitations, prostheses fail to recapitulate the detailed interactions of neural networks and subsequently fail to precisely simulate motor and sensory signaling. For example, retinal prosthesis simulation is limited to a few sensory pixels due, in part, to electrical signal overlap among target neurons in the retina caused by spatial separation of stimulating electrodes from the neural tissue.<sup>23</sup> The cochlear implant (CI), which is currently the only sensory prosthesis in routine clinical use, enables basic speech perception but suffers from comparable spatial signaling limitations. Nonspecific excitation of spiral ganglion neurons (SGNs) within the cochlea precludes simulation of high fidelity tonal information for the user. Subsequently, CI patients struggle with complex auditory stimuli such as voice comprehension in noisy environments and music appreciation.<sup>24,25</sup>

Driving regenerative neural processes into closer spatial proximity of specific stimulating electrodes would allow for lower current trigger thresholds that would reduce problematic signal overlap, enable higher stimulatory specificity, and perhaps lead to greater precision in both signal input and biological functional output.<sup>26-32</sup> Moreover, since the nervous system depends on location specific signaling, similar spatial resolution limitations are anticipated for any device that interfaces with the nervous system. Consequently, determining neural pathfinding behavior in response to directional cues and precisely directing spatial regeneration will be crucial to realize the functional potential of next-generation neural prostheses.

Among the variety of methods reported to orient neurite outgrowth, directing cell-material interactions using engineered surface topography is of particular interest due to the stability, reproducibility, and high degree of control over surface physical features inherent to the process. The most widely reported patterning techniques used to fabricate micro- and nano-scale actionable physical cues require a photopatterning step, i.e. radiative exposure through a photomask, during the process due to the excellent spatial reaction control afforded by masked light exposure. Typically, variations of traditional photolithography accompanied by subsequent soft lithography casting of an elastomer over patterned silicon masters constitute the primary fabrication methods for cell contact guidance studies.

For example, electron-beam lithography was used to fabricate nano-scale ridge and groove topography that caused epithelial cells to elongate and align on silicon oxide substrates with depths as small as 70 nm.<sup>33</sup> Soft lithography casting of poly(dimethylsiloxane) was used in conjunction with photolithography methods to generate microgrooved chitosan conduits that oriented Schwann cell growth and increased neurotrophin expression compared to smooth substrates.<sup>34</sup> Further, photo- and soft lithography are used to generate master templates with variations in pattern shape, ridge width, and groove depth to influence cellular behavior and spatial outgrowth.<sup>35, 36</sup>

In place of traditional photo- and soft lithography patterning methods, direct photopatterning of 2D surfaces or 3D constructs via photo-functionalization or photocrosslinking reactions has emerged as a prominent alternative production platform for cell-material interaction studies. Patterning materials in this way avoids use of expensive or highly reactive reagents required for traditional photolithography methods and is often accomplished in fewer processing steps. For example, a polyfluorene derivative was directly photopatterned on a poly(ethyleneimine) substrate by spatially controlling crosslinking reactions prior to washing steps to generate cyto-adhesive and non-adhesive stripes.<sup>37</sup> Sequential photopolymerization steps were employed to create

trapping and sorting wells to isolate single cells based on imaged phenotype.<sup>38</sup> Direct photopatterning methods have also been utilized to generate cytocompatible hydrogels with tunable degradation profiles<sup>39</sup> and with controlled microarchitecture<sup>40</sup> for tissue regeneration and cell encapsulation applications. Additionally, photopolymerization was used to surface functionalize polymeric substrates with immunosuppressive proteins to provide bioactive protection against activated T cells.<sup>41</sup> Each of these studies illustrates and utilizes specific advantages inherent to UV curing for cellular applications including excellent temporal and spatial control, mild reaction conditions, and few process steps.

In this contribution, we evaluate the turning capability and neural pathfinding behavior of neurites extending from SGNs on photopolymerized, multidirectional micropatterns with repeating 90° turns. The repeating turns are used as a topographical challenge that is compared with neural outcomes on unidirectional micropatterns and unpatterned substrates. SGNs are the sensory elements of the inner ear that enable the sense of hearing and are the target neurons that are electrically stimulated by a CI prosthesis. As we have previously reported, physical micropatterns for neural pathfinding studies are fabricated via direct photopolymerization while microfeature height and directionality are modulated by controlling UV exposure time and by photomasking techniques, respectively.<sup>34,42</sup> SGN neurite response to each pattern type are characterized by total length, alignment of neurite segments, ratio of process path on depressed features, and number of turning points. Because spiral ganglion Schwann cells (SGSCs) play a crucial supportive role for SGN regenerative neurites,<sup>43</sup> their alignment to each pattern type is also reported. Understanding neurite pathfinding behavior and developing methods to guide *de novo* neurite growth to specific stimulatory elements will enable design of innovative biomaterials that improve functional outcomes of devices that interface with the nervous system.

## Experimental

### Uni- and Multidirectional Micropattern Fabrication

Glass slides were used as substrates for thin-film micropatterned polymers to facilitate cellular microscopy studies. To prevent polymer delamination from the substrate, standard glass slides (2.54 cm x 7.62 cm x 0.1 cm) were surface functionalized with a methacrylated silane coupling agent. The slides were first cleaned and oxidized with O<sub>2</sub> plasma for 3 min at 30 W RF power (PDC-001 Harrick Plasma Expanded Cleaner, Ithaca, NY) while under vacuum. Immediately following removal from the plasma chamber, the slides were immersed in a 1/100 v/v solution of 3-(trimethoxysilyl)propyl methacrylate (Aldrich) and n-hexane (Aldrich) overnight in a covered container at room temperature (~21°C). After removal from the solution, each slide was rinsed with fresh hexanes and allowed to dry in a fume hood before being placed in a sealed container. Functionalized slides had a slightly translucent appearance following the hexane rinse. Methacrylated slides were used immediately after functionalization as substrates for polymerization.

Pre-polymer mixtures of 40 wt% hexyl methacrylate (HMA, Aldrich) and 59 wt% 1,6 – hexanediol dimethacrylate (HDDMA, Aldrich) were prepared with 1 wt% of 2,2-dimethoxy-2- phenylacetophenone (DMPA, BASF) as the photoinitiator. As shown in previous work, poly(HMA-co-HDDMA) supports attachment, survival, and growth of SGNs and SGSCs under *in vitro* conditions and works well for control and tuning of photopatterned physical guidance cues.<sup>42, 44</sup> A volume of 20 µL was pipetted onto the center of a methacrylated slide which was then covered with a 2.54 cm x 2.54 cm x 0.1 cm glass-chrome Ronchi rule photomask (Applied Image Inc., Rochester, NY) for parallel patterns, a repeating 90° angle mask (Nano-Fabrication Facility, University of Minnesota, MN) for angled patterns, or with a cut untreated glass slide of the same dimensions for unpatterned samples. Formulations spread evenly under the photomasks

due to capillary forces between the glass plates. Samples were cured with a high-pressure mercury vapor arc lamp (Omniculture S1500, Lumen Dynamics, Ontario, Canada) with 365 nm at a light intensity of 16 mW/cm<sup>2</sup>. Light intensity was measured with a Cole-Parmer Series 9811 radiometer. The curing module was equipped with an 8 mm aperture x 50 mm length beam homogenizing fused silica light pipe (Edmund Optics) and a collimating lens (RLQ-1, Asahi Spectra). Microfeature amplitude was controlled by shuttering UV radiation at specific times. After polymerization, photomasks were removed from polymer surfaces and samples were washed with 95% ethanol to remove all residual monomer. Samples were allowed to air dry before use.

#### Uni- and Multidirectional Micropattern Characterization

White light interferometry (Dektak Wyko 1100 Optical Profiling System, Veeco) was used to measure micropattern periodicity and absolute channel amplitude. Feature amplitude was reported as the difference between the maximum ridge value and the adjacent minimum groove value. Average feature height for a given polymerization condition was determined by measuring channel amplitude in nine different areas across each sample ( $n \geq 3$ ). Periodicity was measured as the distance between the highest points on adjacent ridges and was consistent with photomask band spacing. Measurements and 3D images were generated using *Vision* software associated with the instrument.

Micropattern morphology was further characterized by scanning electron microscopy (SEM, S-4800, Hitachi). Polymer samples were mounted on aluminum SEM stubs using conductive silver paint to acquire top-down images. For cross-sectional images, glass substrates and patterned polymers were fractured and then mounted vertically on specimen stages. The SEM specimen stage was angled using automated stage and software controls. Each polymer surface was sputter coated with gold prior to examination by SEM. Electron accelerating voltage was set at 2 kV.

### Cell Culture and Immunostaining

Dissociated spiral ganglia (SG) cultures from P3-5 rat pups were prepared as previously described.<sup>45, 46</sup> SGN cultures were maintained in Dulbecco's Modified Eagle Medium (DMEM) supplemented with N2 additives, 5% fetal bovine serum, neurotrophin-3 (NT-3, 50 ng/ml) and brain derived neurotrophic factor (BDNF, 50 ng/ml). Cultures were maintained in a humidified incubator with 6.5% CO<sub>2</sub> and fixed with 4% paraformaldehyde after 48 hr. SGNs were plated on polymer substrates coated sequentially with poly-L-ornithine (100 µg/ml) and laminin (20 µg/ml). To quantify SGN survival, cultures were fixed with 4% paraformaldehyde at 4 °C for 20 min, permeabilized and blocked with 5% goat serum, 2% BSA, 0.1% Triton X in phosphate buffered saline (PBS), and immunostained with anti-neurofilament 200 (NF200) antibodies (1:400, Sigma-Aldrich) at 37 °C for 2 hrs. Alexa 488 conjugated secondary antibody (1:800, Invitrogen) was used to detect the primary antibody immunolabeling at room temperature for 1 hr. Slides were cover slipped with ProLong Gold anti-fading reagent with DAPI (Life Technology) and sealed with nail polish. Digital epifluorescent images were captured of the entire polymer surface using the scan slide application of Metamorph software (Molecular Devices, Silicon Valley, CA) on a Leica DMIRE2 microscope (Leica Microsystem, Bannockburn, IL) with a Leica DFC350FX digital camera. The total number of NF200-positive neurons with healthy nuclei was counted for each polymer surface to determine SGN survival. Experiments were performed in duplicate and repeated at least three times.

Spiral ganglia cultures were immunostained with anti-S100 and anti-neurofilament 200 (NF200) antibodies (1:400, Sigma–Aldrich) to label Schwann cells and neurons, respectively.<sup>45</sup> Alexa 488 and Alexa 546 conjugated secondary antibodies (Life Technology) were used to detect primary antibody immunolabeling. Slides were cover slipped with ProLong Gold anti-fading reagent with DAPI (Life Technology). Digital epifluorescent images were captured on a Leica DMIRE2 microscope (Leica

Microsystems, Bannockburn, IL) with Leica DFC350FX digital camera and Metamorph software (Molecular Devices, Silicon Valley, CA). Images of the entire well were captured using the scan slide feature in MetaMorph to eliminate imaging bias to short neurites. Spiral ganglion neuron (SGN) total neurite length was determined from digital images by measuring the longest process of 100 randomly selected neurites from each condition using the measurement tool in Image J (NIH, Bethesda, MD) as previously described.<sup>47</sup> Number of branches extending from SGN neurites was determined by averaging the total number of neurite bifurcations, including bifurcation of branches, for 100 randomly selected neurites from each condition.

#### Characterization of Neurite Alignment

Neurite alignment was measured as a distribution of angles relative to the horizontal plane of 10  $\mu\text{m}$  length neurite segments. At least 50 primary neurites from immunolabeled images were traced in Image J for each condition and X-Y distance data were analyzed using Matlab software. The angle of each segment was calculated relative to horizontal and all neurite angles were then binned in 10° segments from 10 - 90°. Random outgrowth would be evidenced by a relatively equal distribution among all angle bins. Strong alignment to the horizontal plane would be demonstrated by high population percentages in bins of 20° or less. Strong alignment to multidirectional patterns, i.e. repeating 90° angle steps, would be evidenced by high percentages around 45° alignment angles since the pattern was rotated 45° during imaging.

SGSC alignment was determined as previously described by drawing the outline of the cell using Image J software and fitting an ellipse to the cell outline.<sup>42, 44</sup> The angle made between the major axis of the ellipse and the pattern ( $\theta$ ) was measured in Image J.

Preference of SGN primary neurites for the depressed or raised features of the polymer surface was determined by individual measurement of neurite segments on each feature, summing the length of neurite, and calculating the percentage of primary neurite

length on each feature. Lengths were measured from immunolabeled images using the measurement tool in Image J (NIH, Bethesda, MD). Depressed and raised features were differentiated by scanning in the z-plane (vertical) with a Leica TCS SP5 confocal microscope. Percent length of primary neurites on depressed and raised features was averaged for at least 100 randomly chosen neurites from each condition.

Neurite turns were measured using Image J primary neurite traces from immunofluorescent digital images that were captured as previously described. Trace data, containing X-Y neurite distance coordinates, was analyzed by measuring the angle of consecutive 10  $\mu\text{m}$  length neurite segments using Matlab. Neurite segment angle was measured relative to the horizontal plane. If three consecutive segments, i.e. 30  $\mu\text{m}$  segment of the neurite, had a trajectory difference of at least  $10^\circ$  from the previous three consecutive segments then it was marked as a turning event. At least 50 neurites were scored for each pattern condition.

### Statistics

Statistical analysis was performed using SigmaStat 3.5 software (Systat Software, Chicago, IL). A two-tailed t-test was used to compare cellular alignment between unpatterned and patterned samples followed by a *post hoc* Mann-Whitney Rank Sum Test when normality criteria were not met. Multiple groups were compared by performing a one-way ANOVA followed by a *post hoc* Kruskal-Wallis analysis of variance on ranks and a Dunn's Method multiple comparison procedure. Significance if  $p < 0.05$ .

## **Results and Discussion**

### Photopolymerization of Uni/Multidirectional Patterns

To evaluate neural pathfinding behavior of SGN neurites, the inherent spatial and temporal control of photopolymerization were used to fabricate uni- and multidirectional

micropattern substrates for contact guidance studies. Spatial control is achieved by masking the pre-polymer formulation from initiating light and temporal control is afforded through shuttering of the light source at specific time increments. For a typical photo-initiated radical chain growth polymerization, a small concentration of photo-initiator in the pre-polymer formulation absorbs photons and undergoes cleavage of a C-C bond that results in the generation of reactive free radicals. For this particular system, 2,2-dimethoxy-2-phenylacetophenone (DMPA) undergoes a Norrish type I reaction i.e. photochemical hemolysis of the alpha C-C bond of the ketone.<sup>48</sup> The free radical species then react with electron rich C-C double bonds on methacrylate moieties of the surrounding monomer which initiates the polymerization reaction. Propagation continues through polymerizable methacrylate groups until the growing kinetic chain is terminated via recombination with another radical or through hydrogen abstraction and disproportionation. Because the rate of initiation for a photo-initiation reaction depends on absorbance of light, local reaction speeds can be modulated across a substrate surface by selectively masking incident irradiation.

Accordingly, unidirectional parallel line-space gratings were made by masking the pre-polymer formulation with Ronchi rule optics that have alternating transparent (glass) and reflective (chrome) bands (Fig 6.1). Each band is a straight line with a width of 25  $\mu\text{m}$  and extends across the entire length of the mask. Multidirectional, or angled patterns, were generated by masking the reaction with repeating reflective angles. Masking the photopolymerization reaction in this manner locally modulates polymerization kinetics<sup>49, 50</sup> which results in micro-scale periodic raised and depressed features that match the width of the photomask bands. Surface depressions occur beneath reflective bands and raised features appear beneath transparent bands. Final thin film surface topography is composed of uniform, gradually transitioning microfeatures that

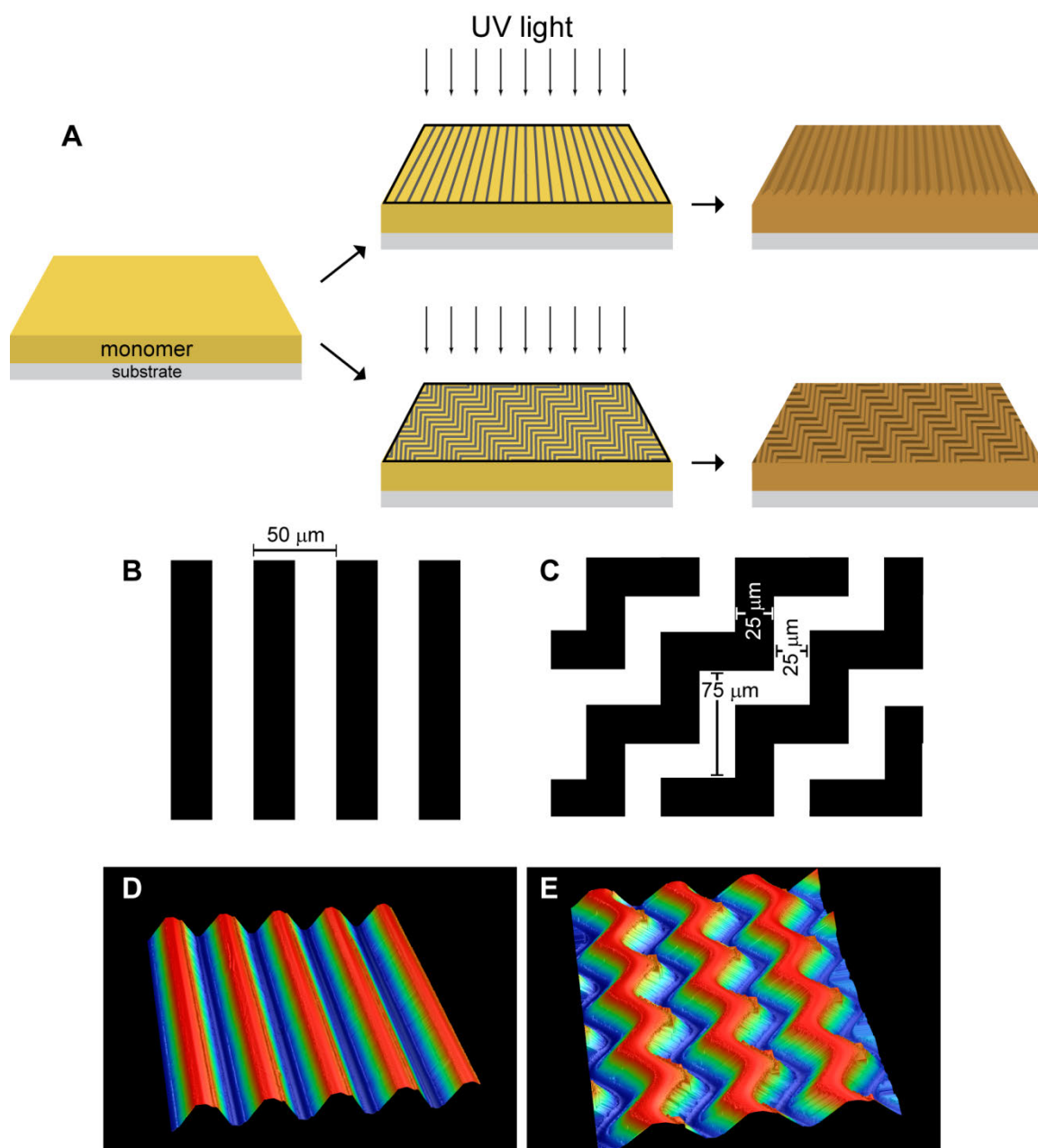


**Figure 6.1.** Schematic of micropattern fabrication process for neural pathfinding studies. **A)** Photopolymerizable monomer is selectively exposed to UV light through a photomask resulting in micropatterns across the substrate surface. **B,C)** Representation of transparent (white) and reflective (black) band size of the photomasks. **D,E)** White light optical profiling 3D images of parallel and 90° angled micropatterned HMA-co-HDDMA substrates representing  $100 \mu\text{m}^2$  areas and channel amplitudes of  $7 \mu\text{m}$ .

contrast with stark, on-off type features generated via multi-step lithographic etching methods.<sup>34, 42, 51</sup> The gradual transitions between microfeatures are likely due to the diffraction of light as it passes through micro-scale photomask bands<sup>52, 53</sup> and due to diffusion of monomer towards reactive regions as demonstrated in interference patterning holographic photopolymerization.<sup>54</sup> Once the light source is shuttered, the reaction rate rapidly decreases as no new radicals are generated via photon absorption.<sup>55</sup> Uni- and multidirectional micropatterns were measured and characterized by white light interferometry (Fig 6.1D-E). As expected, micropattern spacing closely matches photomask band spacing.

For all substrates, the pre-polymer formulation consisted of a 40 wt% hexyl methacrylate (HMA) and 59 wt% 1,6 – hexanediol dimethacrylate (HDDMA) mixture with 1 wt% 2,2-dimethoxy-2-phenylacetophenone (DMPA) as the photoinitiator. In previous work, we demonstrated that poly(HMA-co-HDDMA) is sufficiently biocompatible to enable attachment, survival, and growth of SGNs under *in vitro* conditions.<sup>44</sup> We also illustrated that the comethacrylate can be photopatterned and that microfeature dimensions of the system are readily tunable by modulating photopolymerization parameters.<sup>42</sup>

### Reaction Controlled Feature Modulation

Scanning electron microscopy (SEM) was used to characterize substrate morphology, and to confirm white light interferometric measurements (Fig 6.2). For unidirectional patterns, continuous, 25  $\mu\text{m}$  wide parallel ridges and grooves run the length of the masked area with feature height remaining uniform across the surface. Multidirectional or repeating angle topographies also closely match micro-fabricated photomask band spacings with microfeatures spanning the entirety of the masked region. For both pattern types, photocured substrates have a film thickness of 18  $\mu\text{m}$  and a feature depth approximately 40% of the total thickness at  $7.4 \pm 0.7 \mu\text{m}$  for the given

reaction conditions. Both patterns also have gradual transitions between raised and depressed features due to reactive species diffusion and diffraction of light during the photopolymerization.

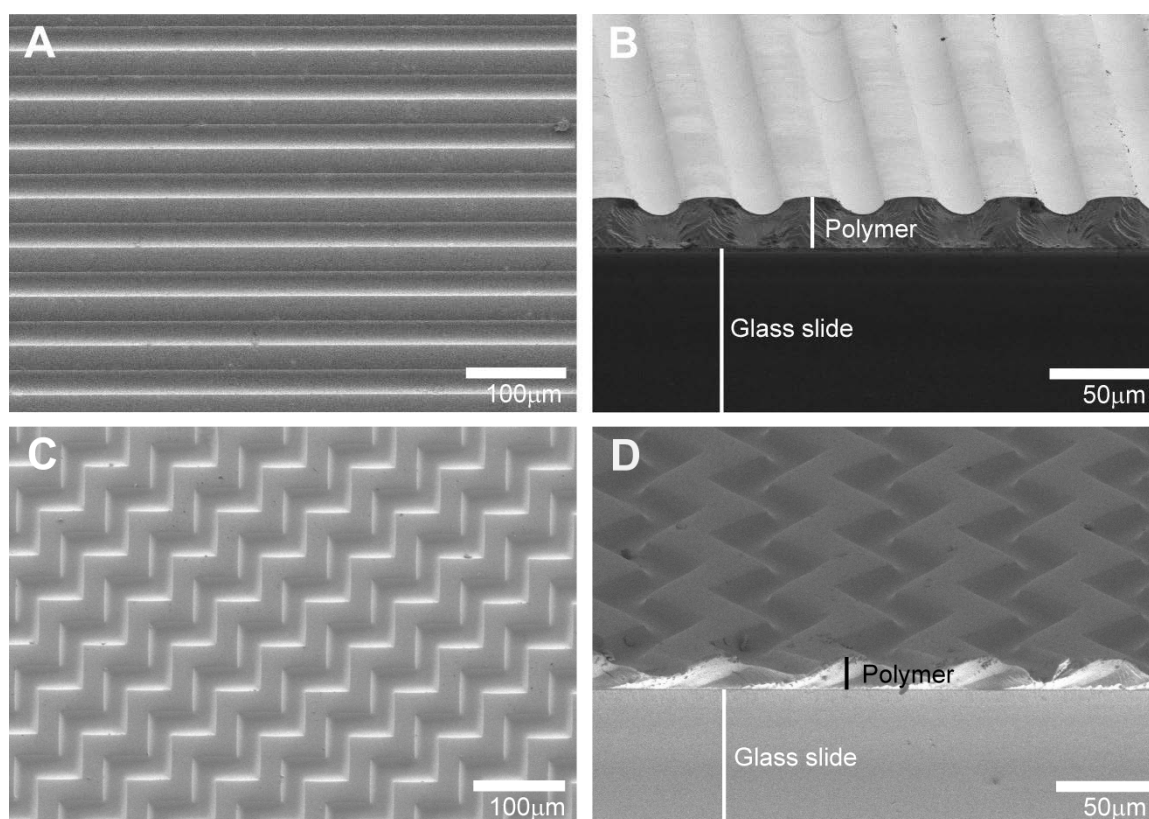


**Figure 6.2.** Representative SEM micrographs of micropatterned HMA-co-HDDMA thin films. **A)** A top-down view of a parallel or unidirectional micropattern with a 50  $\mu\text{m}$  feature spacing and 7  $\mu\text{m}$  amplitude. **B)** A tilted-cross sectional view of a parallel pattern demonstrating film thickness and gradual transitions between raised and depressed features. **C,D)** Top-down and tilted-cross sectional views of repeating 90° angle or multidirectional micropattern with a 7  $\mu\text{m}$  amplitude.

Smooth transitions between photopolymerized microfeatures stand in contrast to infinite slope type features generated via etching lithographic methods. Cell-material interaction studies on topographies fabricated by etching methods illustrate important cell

behavior such as polarization and alignment along the axis of parallel features, differences in alignment to identical microfeatures based on cell type, and sensitivity to nanotopographical noise.<sup>56-58</sup> However, patterns without sharp features are advantageous for some studies in that they more closely mimic native cellular niche morphologies. They may also be used in physical-biochemical cue combination studies to prevent domination of contact guidance cues over biochemical signaling events. The single step photopolymerization of micropatterns is also advantageous because it is fast, low cost, and readily tunable between each sample run whereas etched features require a much longer multi-step process, expensive reagents and microfabrication equipment, and different master templates for each desired feature height. Though, it should also be noted that direct, single step photopolymerization of micro- and nano-topography is limited in lateral feature resolution due to reactive species diffusion constraints and is also limited in ultimate feature depth based on monomer chemistry and reaction kinetics. Tuning of pre-polymer formulation viscosity, photoinitiator choice, irradiation source, and monomer chemistries may mitigate, but likely will not eliminate, these potential disadvantages.

To compare neural pathfinding on both uni- and multidirectional patterns, microfeature amplitude was controlled by shuttering the photopolymerization reaction at specific UV exposure times (Fig 6.3). Polymerization rate rapidly decreases upon shuttering of the radiation source as no new radicals are formed to initiate propagation reactions and as existing radicals terminate by combination and disproportionation reactions. Temporal control of the reaction, thus afforded, enables kinetic trapping of specific microchannel amplitudes that allow for direct comparisons between pattern directionalities. To generate channel amplitudes of  $7.4 \pm 0.7 \mu\text{m}$  for both pattern types, UV light exposure was shuttered at 77 s and 85 s for unidirectional and multidirectional patterns, respectively. Under the given reaction conditions, parallel pattern amplitude ranged from approximately  $1.3 \mu\text{m}$  to  $8 \mu\text{m}$  and  $90^\circ$  angle pattern amplitude ranged from

2  $\mu\text{m}$  to 9  $\mu\text{m}$ . Amplitude profiles as a function of UV exposure time for both pattern types are very similar, with slight variations likely being attributable to differences in light diffraction patterns that alter incident light intensities locally at the substrate surface. Microfeature amplitude increase and subsequent decrease occur nearly symmetrically around a maximum amplitude UV exposure time step. Decreases in amplitude are likely due to backfilling of masked regions as reactive species diffuse into shadowed areas and as more photons are allowed to reach the area through light diffraction and internal reflectance within the system.

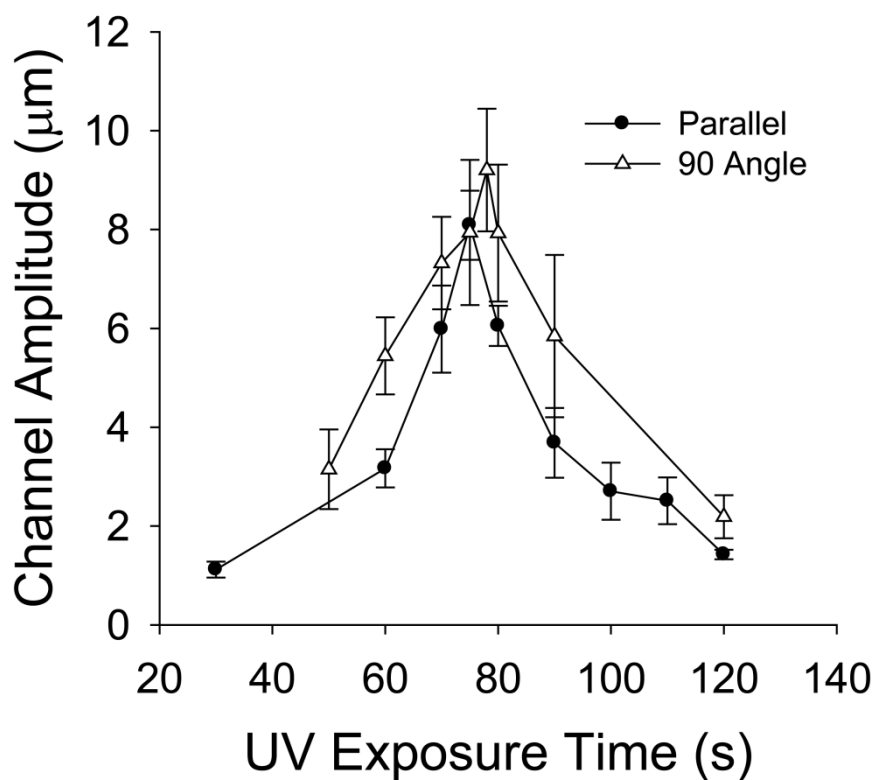


**Figure 6.3.** Channel amplitude is modulated by shuttering the UV light source at specific time increments. Feature depth for parallel and 90° angle patterns is similar at each exposure. Each point indicates mean  $\pm$  SD.

### Neurite Length and Branching

To compare differences in neurite behavior on varied directional surface cues, dissociated SGNs were cultured on unpatterned controls, unidirectional (parallel) patterns, and repeating angle (90° angle) patterns. Neuronal survival, and neurite length

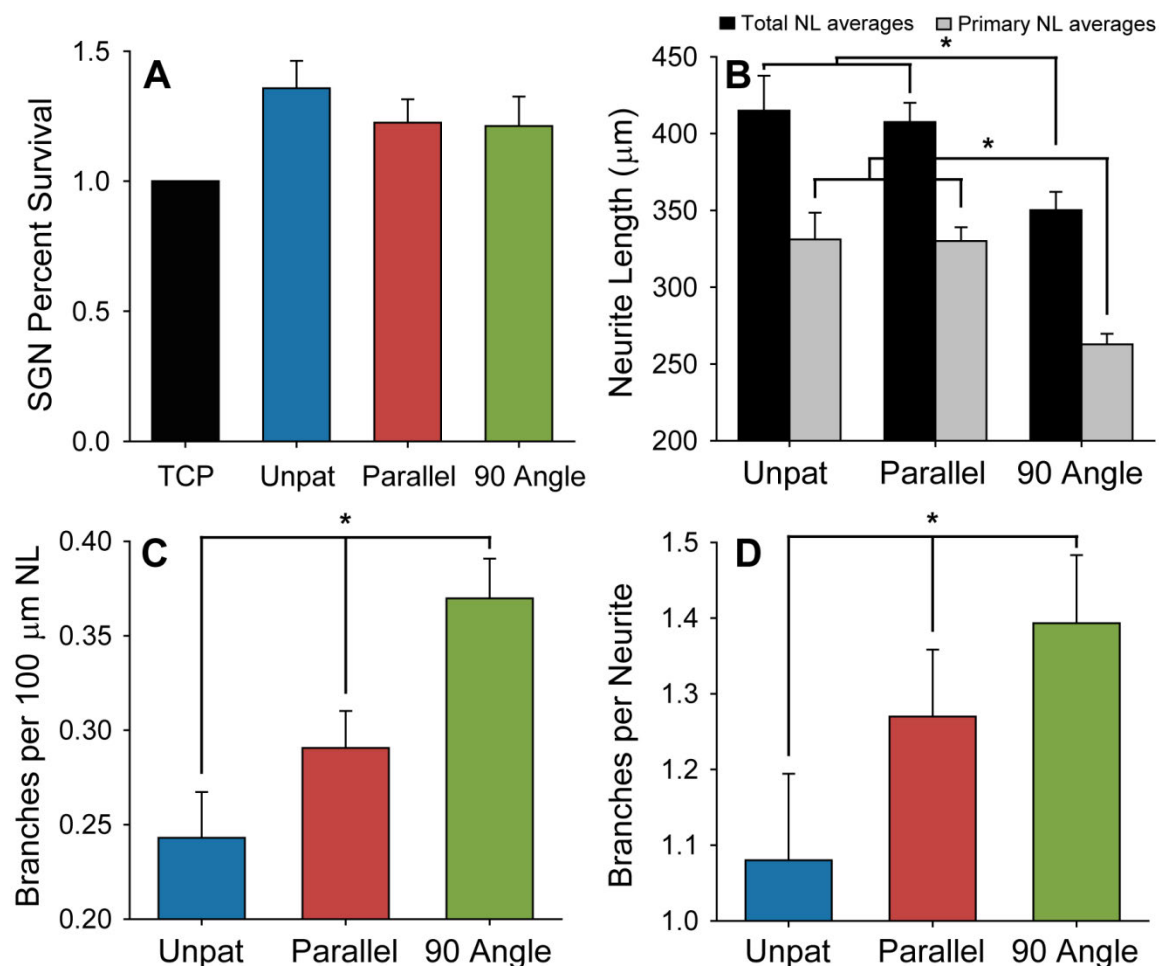


**Figure 6.4.** SGN survival, total and primary neurite length (NL), and branching on unpatterned controls and on parallel and 90° angle micropatterns of HMA-co-HDDMA polymer substrates. **A)** SGN survival on unpatterned and micropatterned substrates normalized to a tissue culture plastic (TCP) control. **B)** Total and primary SGN neurite lengths are significantly shorter than corresponding lengths on parallel patterns and unpatterned controls (\* $p < 0.05$ , ANOVA). **C,D)** Significantly more branches per neurite length and per neurite on 90° angle patterns are observed compared to neurites on parallel patterns and unpatterned controls (\* $p < 0.05$ , ANOVA). Error bars represent standard error of the mean (SE).

and branching were examined as an initial comparison (Fig 6.4). SGN survival on unpatterned and micropatterned poly(HMA-co-HDDMA) is comparable to survival on a tissue culture plastic (TCP) control ( $p > 0.05$ ). Further, no significant difference is evident between primary neurite length, i.e. the longest neurite from each neuron, on unpatterned controls compared to unidirectional micropatterns. Total neurite length, i.e. primary neurite length plus branch length, on unpatterned and unidirectional substrates is also similar.

However, both primary and total neurite lengths are approximately 20% shorter on repeating angle patterns, relative to unpatterned and parallel pattern substrates. Neurites on multidirectional surfaces may be shorter due to the presentation of a higher density of potential encounters with feature edges to the advancing neural growth cone compared to fewer such encounters on smooth or unidirectional surfaces. Each encounter with a feature edge is likely associated with growth cone stalling and the underlying focal adhesion formation or removal and cytoskeleton rearrangement events which reduce the rate of neurite extension.<sup>59</sup>

In addition to neurite length, SGN neurite branching also significantly differs on substrates with varied physical surface cues. The degree of branching per neurite and per 100  $\mu\text{m}$  of neurite length is lowest for SGNs cultured on unpatterned substrates. Branching increases on patterned surfaces, suggesting that growth cone encounters with pattern edges induce neurite branch formation. Neurite branching is highest on multidirectional features with a 52% increase in branches per neurite length compared to unpatterned controls. Interestingly, the neurite length and branching results taken together illustrate that neural processes behave differently on physical cues with varied directionality compared to unidirectional micropatterns even when all other experimental conditions are held constant including the spacing and amplitude of the physical guidance cues.

### Neurite Behavior on Uni/Multidirectional Substrates

Developing precise spatial control of *de novo* neurite growth from neurons that are relevant to neural prosthetics, such as inner ear SGNs, will lead to enhanced prosthesis performance and improved functional outcomes for patients. Directing neurite growth in this manner will require multiple types of biologically actionable cues including biophysical cues that can either induce or inhibit neurite turning events. Accordingly, to compare neurite pathfinding ability on varied biophysical cues, SGNs were cultured on unpatterned, unidirectional, and multidirectional photopolymerized substrates (Fig 6.5). Qualitative immunofluorescence imaging illustrates that SGN neurite outgrowth extends randomly on unpatterned substrates with unpredictable turning events. Conversely, neurites on unidirectional patterns are observed to strongly orient to and grow parallel to the microfeature direction (horizontal) while exhibiting few if any turning events per neurite (Fig 6.5B).

Interestingly, while SGN neurites on multidirectional patterns do not extend randomly, they also do not closely track the repeating sequence of 90° turning cues along a micropattern path despite encountering physical microfeatures that are comparable in width and depth to those of the unidirectional patterns (Fig 6.5C). Rather, extending neurites are often observed to align horizontally and elongate down the length of a feature path. It is interesting that the neurites extend in this fashion even though they must cross multiple feature transitions near the angle turning points. Furthermore, neurites on multidirectional patterns also turn much more frequently than on unidirectional substrates with the accompanying behavior of crossing over a sequence of microfeatures prior to realigning to the horizontal plane. These microfeature crossing events are rare in the case of neurite growth on unidirectional patterns, especially over multiple transitions.

Qualitative SGN neurite alignment observations are further supported by sectioning equal lengths of neurite segments for all scored neurites and measuring their

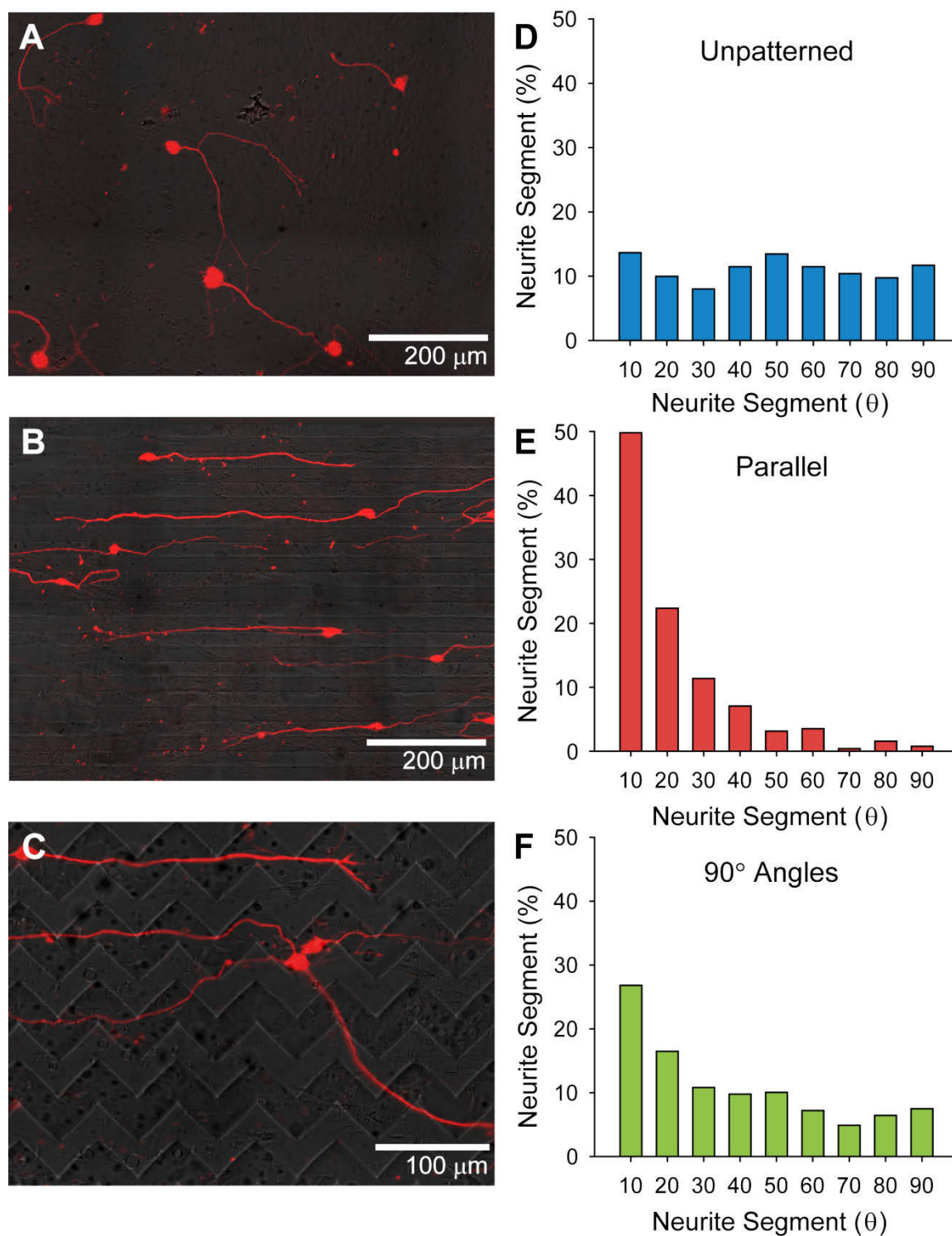


**Figure 6.5.** SGN neurite alignment on variations in topographic cues. **A-C)** Immunofluorescent images of neurite growth from dissociated SGNs on unpatterned (A), parallel (B), and 90° angle (C) substrates. **D-F)** Distribution of SGN neurite segment angles relative to the horizontal plane on unpatterned (D), parallel (E), and 90° angle (F)

## Figure 6.5 Continued.

substrates. Regenerative neurite growth orients randomly on unpatterned substrates as evidenced by a nearly equal distribution of neurite segment angles relative to the horizontal plane. Neurites strongly align to unidirectional topographic cues with 70% of the neurite segment angles at or below  $20^\circ$  from the pattern direction. Neurites on repeating  $90^\circ$  angle patterns do not closely track multidirectional cues as demonstrated by the low incidence of  $45^\circ$  angle neurite segments. They do align somewhat to the horizontal plane, although with a broader distribution of angles than on parallel patterns. Dissociated cultures were stained with anti-NF200 antibodies. Micropatterned substrates have a channel amplitude of  $7\ \mu\text{m}$ .

alignment angle relative to the horizontal plane (Fig 6.5D-F). Neurite segment angles ( $\leq 90^\circ$ ) are binned as a percentage of the total neurite segments measured in  $10^\circ$  increments to represent overall alignment. SGN neurites on unpatterned polymer substrates extend randomly as demonstrated by the relatively equal distribution of neurite segment angles across the  $0 - 90^\circ$  spectrum of alignment. In contrast, neurite segment angles are much more frequent at low angles (i.e.  $< 20^\circ$ ) relative to horizontal on unidirectional, parallel feature micropatterns. Approximately 50% of the neurite segments are considered completely aligned to the pattern direction with an alignment angle of  $10^\circ$  or less and a full 72% of the neurite segment population is within the  $20^\circ$  angle population indicating significant alignment to pattern features.

However, as previously mentioned, neurites on multidirectional substrates do not strongly track the repeating  $90^\circ$  angle patterns as evidenced by low incidence ( $\sim 20\%$ ) of neurite segment angles in the  $40^\circ$  and  $50^\circ$  degree bins. Because the  $90^\circ$  angle features have been rotated  $45^\circ$  for imaging, it could be expected, assuming that neurite growth is strongly and consistently influenced by micropattern physical features on this size scale, that a significant incidence of neurite segment angles at or near  $45^\circ$  relative to the horizontal plane would be evident. Instead, a fairly equal distribution exists across all segment angles in the  $30 - 90^\circ$  population with a relatively high incidence (43%) of

neurite segments at or below  $20^\circ$  from the horizontal plane. Importantly, the parallel and repeating angle micropatterns used for both experiments are quite similar. In both cases the ridge and groove widths are  $25\ \mu\text{m}$  and the channel amplitude or feature height is approximately  $7\ \mu\text{m}$ . Polymerization was halted at similar time steps for both platforms by shuttering the UV light source yielding very similar groove-ridge transitions. All else being equal, it might be expected to see SGN neurites closely tracking the groove paths and, while perhaps not making exact  $90^\circ$  angle turns, there would still be a high incidence of  $45^\circ$  angle neurite segments tracking the groove path. It is clear that the neurite segment distribution does not match the random distribution seen on unpatterned polymer substrates, but that it more closely resembles neurite orientation on unidirectional platforms. However, despite the similarities in neurite alignment to unidirectional patterns, outgrowth complexity increases on multidirectional substrates as neurites are observed to change direction and to cross microfeatures significantly more than on comparable unidirectional features.

To realize functional outcome improvements of neural prosthetics, it may be crucial to direct neurites to specific but separate areas that contain stimulating electrodes.<sup>21</sup> While a variety of neural contact guidance studies demonstrate strong alignment to the long axis of parallel feature micropatterns, their use may be limited to applications that require significant unidirectional growth such as intraluminal patterning of nerve conduits to bridge nerve gaps.<sup>9</sup> Appropriate turning events will be required to spatially segregate and then stimulate specific neurites or groups of neurites. Multidirectional patterns with repeating  $90^\circ$  turns in this work induced greater turning than unidirectional patterns, though neurites are not observed to turn at each encounter of a biophysical cue. Similar behavior occurs when neurites extend between appropriately spaced microposts.<sup>60-62</sup> A lower density in directional changes per area or turns with wider angles may allow for more consistent guidance and predictable turning events throughout the length of a neurite.

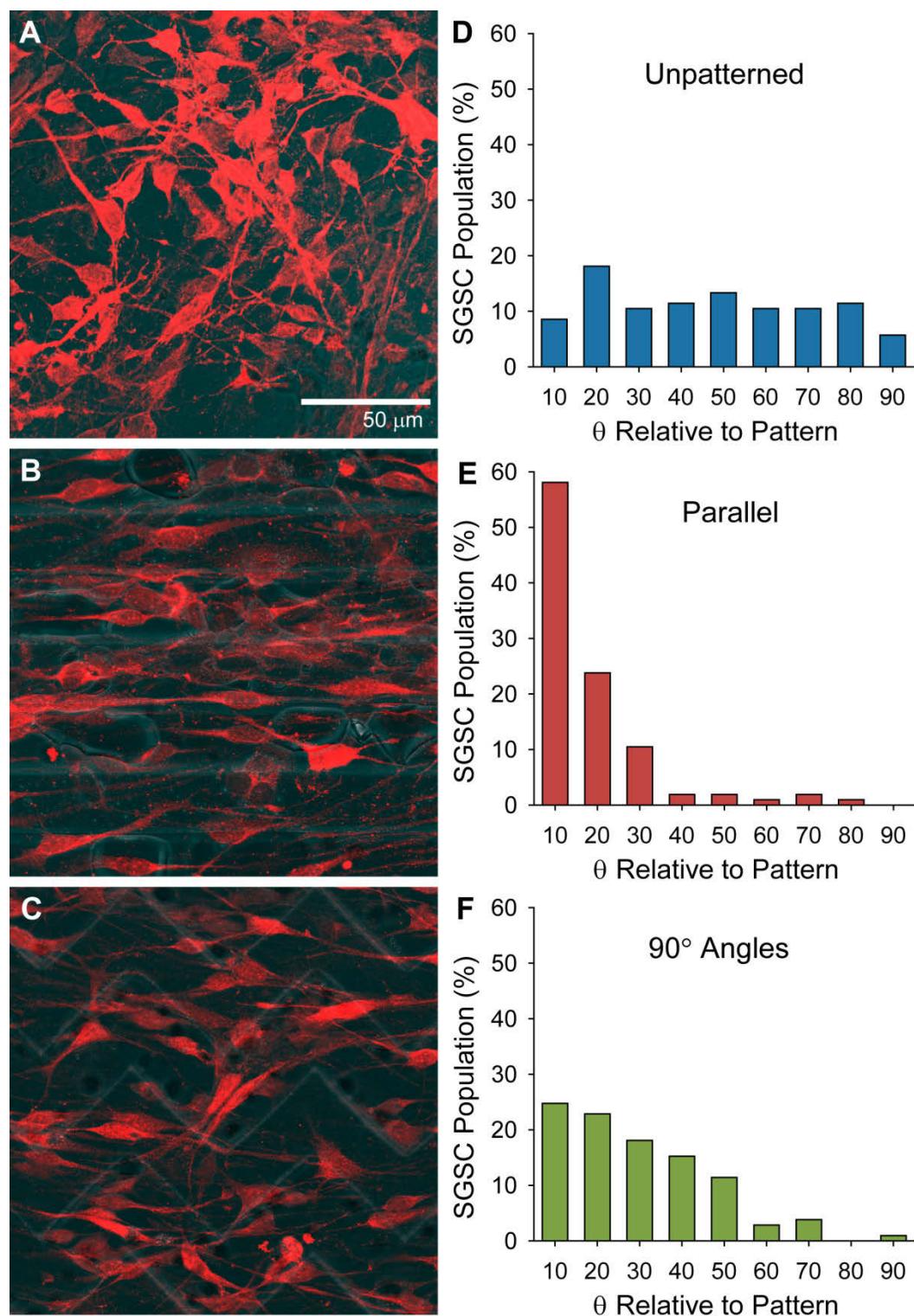


**Figure 6.6.** SGSC alignment on variations in topographic cues. **A-C**) Immunofluorescent images of SGSCs on unpatterned (A), parallel (B), and 90° angle (C) substrates. **D-F**) Distribution of SGSC angles relative to the horizontal plane on unpatterned (D), parallel

Figure 6.6 Continued.

(E), and 90° angle (F) substrates. SGSCs orient randomly on unpatterned substrates and align strongly to unidirectional topographic cues with 80% of the cell angles at or below 20° from the pattern direction. SGSCs on repeating 90° angle patterns do not closely track multidirectional cues as demonstrated by the low incidence of 45° cellular angles. Dissociated cultures were stained with anti-S100 antibodies. Micropatterned substrates have a channel amplitude of 7 μm.

Because glial cells are crucial to the proper function and survival of neuronal cells and because they support and direct neurite growth,<sup>45, 63, 64</sup> the behavior and alignment of SGSCs was also measured and compared on unpatterned and uni/multidirectional micropatterns (Fig 6.6). SGSC alignment mirrors SGN neurite segment alignment. In this case, each scored SGSC was fit with an ellipse and the alignment was measured as the angle between the major axis of the ellipse relative to the horizontal plane. SGSCs orient randomly on unpatterned substrates and strongly align to parallel, unidirectional micropatterns with 82% of SGSCs having an alignment angle of 20° or less. As with SGN neurites on multidirectional platforms, SGSCs do not orient randomly as if on an unpatterned surface but more closely resemble horizontally aligned growth as seen on parallel micropatterns. Again, there is a much lower incidence of 45° alignment angles than would be expected if SGSCs closely tracked repeating 90° angle microfeatures.

The percentage of neurite length in microfeature grooves and the number of feature crossings per neurite length were measured to further characterize differences in neural pathfinding on uni- versus multidirectional surface cues (Fig 6.7). The majority of regenerative SGN neurite length is found in depressed microfeatures (i.e. grooves) on both parallel and repeating angle micropatterns. Nearly 75% of all neurite length tracks surface depressions when SGNs are cultured on parallel feature micropatterns. A few neurites were even observed to turn 180° while remaining sequestered within microgrooves (Fig 6.7B). The quantified preference for depressed features is in contrast to

other research which observed neural processes preferentially growing on elevated features, however, the width of the features used were much narrower (i.e.  $< 1 \mu\text{m}$ ) than the photopolymerized patterns used here.<sup>15</sup> While the majority of neurite length on  $90^\circ$

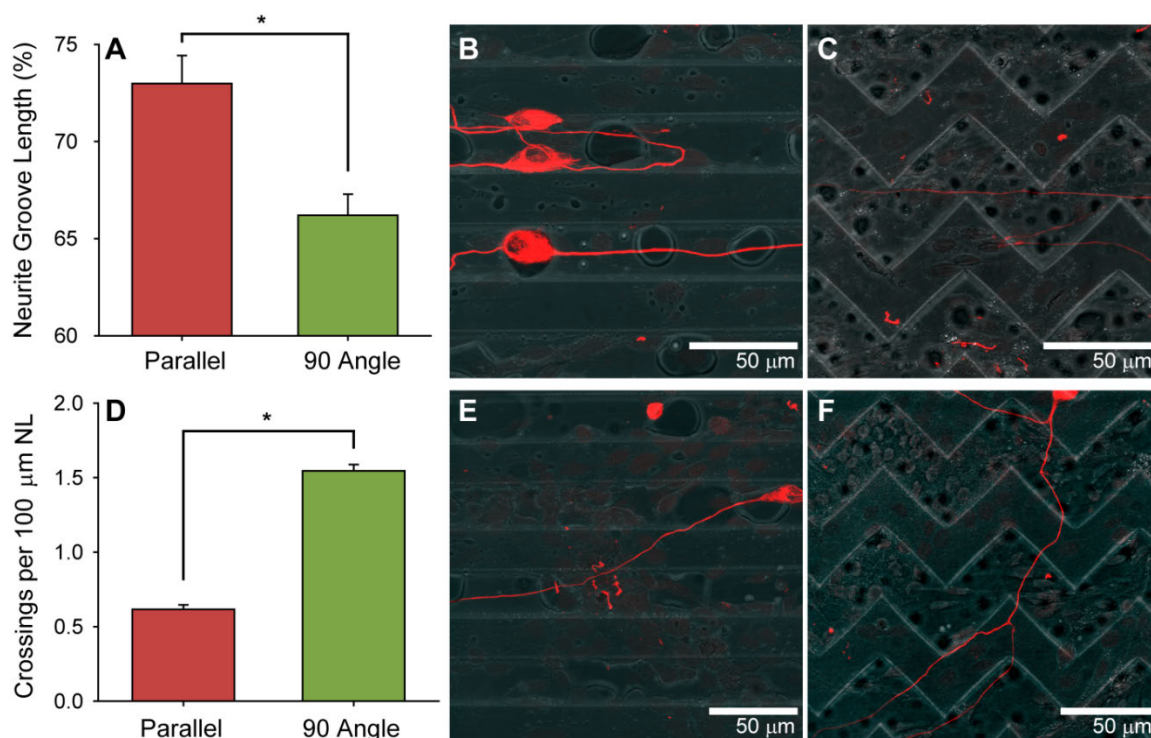


**Figure 6.7.** SGN percent neurite length in depressed microfeatures and feature crossing per neurite length on uni- and multidirectional topographic cues. **A)** The majority of SGN neurite length on both parallel and  $90^\circ$  angle patterns is located in the grooves ( $*p < 0.05$ , Mann-Whitney Rank Sum test). **B,C)** Immunofluorescent images of SGN neurite growth in groove microfeatures. **D)** SGN neurites crossed ridge-groove transitions significantly more on multidirectional patterns compared to unidirectional substrates ( $*p < 0.05$ , Mann-Whitney Rank Sum test). **E,F)** Immunofluorescent images of SGN neurites crossing ridge-groove transitions on various micropatterns. Dissociated cultures were stained with anti-NF200 antibodies. Micropatterned substrates have a channel amplitude of  $7 \mu\text{m}$ .

angle patterns is also found in surface depressions, the percent length in the depressions is still significantly less than that of neurites on unidirectional features. The difference is

likely due to the presentation of multiple directional cues to the advancing growth cone, which increases the number of potential guidance points, and ultimately leads to increased topographic feature crossings.

A crossing event for this study is defined as the transition of the primary neurite from a raised or depressed microfeature to its corresponding opposite. Due to strong alignment on parallel microfeatures, SGN neurite crossing is, on average, very low with many neurites making only one or no feature crossings throughout the entirety of their length. Conversely, micro-feature crossings per neurite length on multidirectional patterns are significantly higher than on unidirectional patterns. Approximately three times the number of crossing events per length of neurite are observed on multidirectional micropatterns (Fig 6.7D-F). Therefore, despite microfeatures for both pattern types having nearly identical widths and depths, SGN neurite pathfinding does not consistently track every change in feature direction as pattern complexity increases. Rather, neurites appear to extend in a manner that minimizes turning events by growing either down the length of a groove path (i.e. horizontally) or directly over multiple feature transitions.

The number of turns per neurite in response to topographic guidance cues was measured as a final comparison of SGN neurite pathfinding ability on uni- and multidirectional patterns and on unpatterned controls (Fig 6.8). Turns are defined as a  $10^\circ$  change in direction over three consecutive  $10\ \mu\text{m}$  length neurite segments relative to the previous three segments. Ultimately, the capacity to guide regenerative neurite growth to spatially specific stimulating elements will require strong adherence to engineered guidance cues and may include precision turning at specific points. SGN neurites turn over five times more on unpatterned substrates compared to unidirectional micropatterns. They also turn significantly more on unpatterned substrates compared to neurites on repeating angle features. The high degree of turning on unpatterned platforms supports the observation that neurite growth is random on unpatterned controls and results in

multiple instances of neural growth cone direction change and, thus, turning points for any given neurite (Fig 6.5).

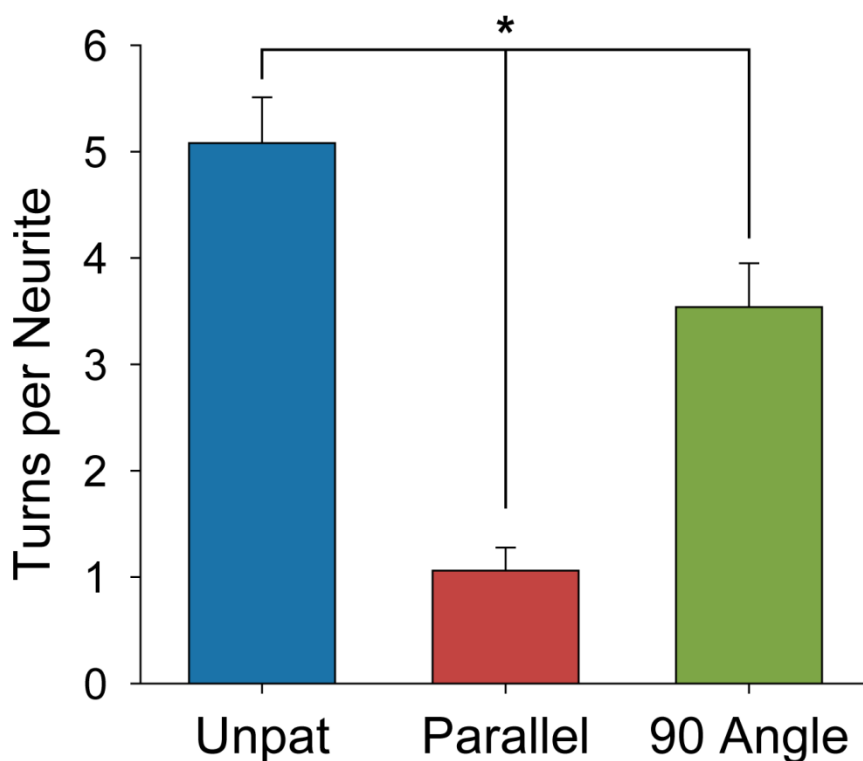


**Figure 6.8.** Number of turns per SGN neurite on substrates with varied topography. SGN neurites turned significantly more on unpatterned surfaces compared to patterned substrates and on patterns that change direction compared to unidirectional morphologies (\* $p < 0.05$ , ANOVA).

The comparatively low number of neurite turns on unidirectional patterns confirms the strong neural alignment data on parallel microfeatures and further supports the observation that there is little to no feature crossing for a given neurite on unidirectional guidance cues. However, while significantly more turning events are evident on multidirectional patterns compared to unidirectional physical guidance cues,

the neurites do not consistently track each 90° turn but can cross over multiple microfeatures before turning to align along portions of them along its path length.

### Conclusions

Directing regenerative neural pathfinding with engineered surface cues to specific stimulatory elements will potentially improve the neural-prosthesis interface and lead to enhanced functional outcomes. In this work we present a versatile photopolymerization method to create an array of patterns that can be used to probe neural pathfinding ability of prosthesis-relevant neurons such as inner ear spiral ganglion neurons (SGNs). Microfeature shape and width are controlled through photomask design, and feature depth is tuned on the micron scale by altering reaction parameters of the photopolymerization. The pathfinding ability of SGNs was compared on unpatterned, unidirectional, and multidirectional micropatterns. Significantly more branching and shorter neurite length are observed on multidirectional patterns compared to unpatterned and unidirectional platforms. SGN neurites extend randomly on unpatterned comethacrylate platforms, orient along the axis of unidirectional micropatterns, and are significantly influenced by but do not strongly track guidance cues on repeating step multidirectional patterns. Spiral ganglion Schwann cells (SGSCs), which provide trophic support to SGNs, mirror the alignment behavior of SGN neurites on each pattern type. On both uni- and multidirectional patterns, the majority of the neurite pathlength is located in depressed surface features but significantly more feature crossing events occur on multidirectional surfaces. This work informs efforts to direct neurite growth to specific stimulatory elements for the purpose of improving functional outcomes of neural prosthetics. Precisely directing neurite growth in this manner will enable fabrication of next generation neural prosthetics with enhanced stimulatory specificity.

## Notes

1. Tuft, B. W.; Xu, L.; White, S. P.; Seline, A. E.; Erwood, A. M.; Hansen, M. R.; Guymon, C. A. Neural pathfinding on uni- and multidirectional photopolymerized micropatterns. *ACS Appl. Mater. Inter.* **2014**, <http://dx.doi.org/10.1021/am501622a>
2. Mata, A.; Kim, E. J.; Boehm, C. A.; Fleischman, A. J.; Muschler, G. F.; Roy, S. A three-dimensional scaffold with precise micro-architecture and surface micro-textures. *Biomaterials* **2009**, *30*, 4610-4617.
3. Kubo, K.; Att, W.; Yamada, M.; Ohmi, K.; Tsukimura, N.; Suzuki, T.; Maeda, H.; Ogawa, T. Microtopography of titanium suppresses osteoblastic differentiation but enhances chondroblastic differentiation of rat femoral periosteum-derived cells. *J. Biomed. Mater. Res. Part A* **2008**, *87A*, 380-391.
4. Yim, E. K.; Pang, S. W.; Leong, K. W. Synthetic nanostructures inducing differentiation of human mesenchymal stem cells into neuronal lineage. *Exp. Cell Res.* **2007**, *313*, 1820-1829.
5. Engler, A. J.; Sen, S.; Sweeney, H. L.; Discher, D. E. Matrix elasticity directs stem cell lineage specification. *Cell* **2006**, *126*, 677-689.
6. Hoffman-Kim, D.; Mitchel, J. A.; Bellamkonda, R. V. Topography, Cell response, and nerve regeneration. *Annu. Rev. Biomed. Eng.* **2010**, *12*, 203-231.
7. Spivey, E. C.; Khaing, Z. Z.; Shear, J. B.; Schmidt, C. E. The fundamental role of subcellular topography in peripheral nerve repair therapies. *Biomaterials* **2012**, *33*, 4264-4276.
8. Straley, K. S.; Foo, C. W.; Heilshorn, S. C. Biomaterial design strategies for the treatment of spinal cord injuries. *J. Neurotrauma* **2010**, *27*, 1-19.
9. Daly, W.; Yao, L.; Zeugolis, D.; Windebank, A.; Pandit, A. A biomaterials approach to peripheral nerve regeneration: bridging the peripheral nerve gap and enhancing functional recovery. *J. R. Soc. Interface* **2012**, *9*, 202-221.
10. Hurtado, A.; Cregg, J. M.; Wang, H. B.; Wendell, D. F.; Oudega, M.; Gilbert, R. J.; McDonald, J. W. Robust CNS regeneration after complete spinal cord transection using aligned poly-L-lactic acid microfibers. *Biomaterials* **2011**, *32*, 6068-6079.
11. Oliva, A. A.; James, C. D.; Kingman, C. E.; Craighead, H. G.; Banker, G. A. Patterning axonal guidance molecules using a novel strategy for microcontact printing. *Neurochem. Res.* **2003**, *28*, 1639-1648.
12. Gustavsson, P.; Johansson, F.; Kanje, M.; Wallman, L.; Linsmeier, C. E. Neurite guidance on protein micropatterns generated by a piezoelectric microdispenser. *Biomaterials* **2007**, *28*, 1141-1151.

13. Schmalenberg, K. E.; Uhrich, K. E. Micropatterned polymer substrates control alignment of proliferating Schwann cells to direct neuronal regeneration. *Biomaterials* **2005**, *26*, 1423-1430.
14. Branch, D. W.; Wheeler, B. C.; Brewer, G. J.; Leckband, D. E. Long-term stability of grafted polyethylene glycol surfaces for use with microstamped substrates in neuronal cell culture. *Biomaterials* **2001**, *22*, 1035-1047.
15. Johansson, F.; Carlberg, P.; Danielsen, N.; Montelius, L.; Kanje, M. Axonal outgrowth on nano-imprinted patterns. *Biomaterials* **2006**, *27*, 1251-1258.
16. Miller, C.; Jefthiniya, S.; Mallapragada, S. Synergistic effects of physical and chemical guidance cues on neurite alignment and outgrowth on biodegradable polymer substrates. *Tissue Eng.* **2002**, *8*, 367-378.
17. Wittig, J. H.; Ryan, A. F.; Asbeck, P. M. A reusable microfluidic plate with alternate-choice architecture for assessing growth preference in tissue culture. *J. Neurosci. Methods* **2005**, *144*, 79-89.
18. Yao, L.; Pandit, A.; Yao, S.; McCaig, C. D. Electric field-guided neuron migration: A novel approach in neurogenesis. *Tissue Eng. Part B Rev.* **2011**, *17*, 143-153.
19. Koh, H. S.; Yong, T.; Teo, W. E.; Chan, C. K.; Puhaindran, M. E.; Tan, T. C.; Lim, A.; Lim, B. H.; Ramakrishna, S. In vivo study of novel nanofibrous intra-luminal guidance channels to promote nerve regeneration. *J. Neural Eng.* **2010**, *7*, 046003.
20. Richardson, J. A.; Rementer, C. W.; Bruder, J. M.; Hoffman-Kim, D. Guidance of dorsal root ganglion neurites and Schwann cells by isolated Schwann cell topography on poly(dimethyl siloxane) conduits and films. *J. Neural Eng.* **2011**, *8*, 046015.
21. O'Leary, S. J.; Richardson, R. R.; McDermott, H. J. Principles of design and biological approaches for improving the selectivity of cochlear implant electrodes. *J. Neural Eng.* **2009**, *6*, 055002.
22. Leach, J. B.; Achyuta, A. K.; Murthy, S. K. Bridging the divide between neuroprosthetic design, tissue engineering and neurobiology. *Front. Neuroeng.* **2010**, *2*, 18.
23. Winter, J. O.; Cogan, S. F.; Rizzo, J. F. Retinal prostheses: current challenges and future outlook. *J. Biomater. Sci. Polym. Ed.* **2007**, *18*, 1031-1055.
24. Shannon, R. V.; Fu, Q. J.; Galvin, J. The number of spectral channels required for speech recognition depends on the difficulty of the listening situation. *Acta Otolaryngol. Suppl.* **2004**, (552), 50-54.
25. Rubinstein, J. T. How cochlear implants encode speech. *Curr. Opin. Otolaryngol. Head Neck Surg.* **2004**, *12*, 444-8.

26. Leng, T.; Wu, P.; Mehenti, N. Z.; Bent, S. F.; Marmor, M. F.; Blumenkranz, M. S.; Fishman, H. A. Directed retinal nerve cell growth for use in a retinal prosthesis interface. *Invest. Ophthalmol. Vis. Sci.* **2004**, *45*, 4132-4137.
27. Evans, A. J.; Thompson, B. C.; Wallace, G. G.; Millard, R.; O'Leary, S. J.; Clark, G. M.; Shepherd, R. K.; Richardson, R. T. Promoting neurite outgrowth from spiral ganglion neuron explants using polypyrrole/BDNF-coated electrodes. *J. Biomed. Mater. Res. Part A* **2009**, *91A*, 241-250.
28. Brors, D.; Aletsee, C.; Schwager, K.; Mlynski, R.; Hansen, S.; Schäfers, M.; Ryan, A. F.; Dazert, S. Interaction of spiral ganglion neuron processes with alloplastic materials in vitro. *Hear. Res.* **2002**, *167*, 110-121.
29. Mehenti, N. Z.; Peterman, M. C.; Leng, T.; Marmor, M. F.; Blumenkranz, M. S.; Bent, S. F. A retinal interface based on neurite micropatterning for single cell stimulation. *Invest. Ophthalmol. Vis. Sci.* **2003**, *44*, U704-U704.
30. Roehm, P. C.; Hansen, M. R. Strategies to preserve or regenerate spiral ganglion neurons. *Curr. Opin. Otolaryngol. Head Neck Surg.* **2005**, *13*, 294-300.
31. Guenther, E.; Troger, B.; Schlosshauer, B.; Zrenner, E. Long-term survival of retinal cell cultures on retinal implant materials. *Vision Res.* **1999**, *39*, 3988-3994.
32. Cui, X. Y.; Wiler, J.; Dzaman, M.; Altschuler, R. A.; Martin, D. C. In vivo studies of polypyrrole/peptide coated neural probes. *Biomaterials* **2003**, *24*, 777-787.
33. Teixeira, A. I.; Abrams, G. A.; Bertics, P. J.; Murphy, C. J.; Nealey, P. F. Epithelial contact guidance on well-defined micro- and nanostructured substrates. *J. Cell. Sci.* **2003**, *116*, 1881-1892.
34. Hsu, S.; Lu, P. S.; Ni, H.; Su, C. Fabrication and evaluation of microgrooved polymers as peripheral nerve conduits. *Biomed. Microdevices* **2007**, *9*, 665-674.
35. Song, M.; Uhrich, K. E. Optimal micropattern dimensions enhance neurite outgrowth rates, lengths, and orientations. *Ann. Biomed. Eng.* **2007**, *35*, 1812-1820.
36. Rajnicek, A. M.; Britland, S.; McCaig, C. D. Contact guidance of CNS neurites on grooved quartz: influence of groove dimensions, neuronal age and cell type. *J. Cell. Sci.* **1997**, *110*, 2905-2913.
37. Baek, N. S.; Kim, Y. H.; Han, Y. H.; Lee, B. J.; Kim, T.; Kim, S.; Choi, Y.; Kim, G. H.; Chung, M.; Jung, S. Facile photopatterning of polyfluorene for patterned neuronal networks. *Soft Matter* **2011**, *7*, 10025-10031.
38. Sun, T.; Kovac, J.; Voldman, J. Image-based single-cell sorting via dual-photopolymerized microwell arrays. *Anal. Chem.* **2014**, *86*, 977-981.

39. Hao, Y.; Shih, H.; Muñoz, Z.; Kemp, A.; Lin, C. Visible light cured thiol-vinyl hydrogels with tunable degradation for 3D cell culture. *Acta Biomater.* **2014**, *10*, 104-114.
40. Nichol, J. W.; Koshy, S. T.; Bae, H.; Hwang, C. M.; Yamanlar, S.; Khademhosseini, A. Cell-laden microengineered gelatin methacrylate hydrogels. *Biomaterials* **2010**, *31*, 5536-5544.
41. Hume, P. S.; Anseth, K. S. Inducing local T cell apoptosis with anti-Fas-functionalized polymeric coatings fabricated via surface-initiated photopolymerizations. *Biomaterials* **2010**, *31*, 3166-3174.
42. Tuft, B. W.; Li, S.; Xu, L.; Clarke, J. C.; White, S. P.; Guymon, B. A.; Perez, K. X.; Hansen, M. R.; Guymon, C. A. Photopolymerized microfeatures for directed spiral ganglion neurite and Schwann cell growth. *Biomaterials* **2013**, *34*, 42-54.
43. Jeon, E.; Xu, N.; Xu, L.; Hansen, M. R. Influence of central glia on spiral ganglion neuron neurite growth. *Neuroscience* **2011**, *177*, 321-334.
44. Clarke, J. C.; Tuft, B. W.; Clinger, J. D.; Levine, R.; Figueroa, L. S.; Guymon, C., A.; Hansen, M. R. Micropatterned methacrylate polymers direct spiral ganglion neurite and Schwann cell growth. *Hear. Res.* **2011**, *278*, 96-105.
45. Hansen, M. R.; Vijapurkar, U.; Koland, J. G.; Green, S. H. Reciprocal signaling between spiral ganglion neurons and Schwann cells involves neuregulin and neurotrophins. *Hear. Res.* **2001**, *161*, 87-98.
46. Hegarty, J.; Kay, A.; Green, S. Trophic support of cultured spiral ganglion neurons by depolarization exceeds and is additive with that by neurotrophins or cAMP and requires elevation of  $[Ca^{2+}]_i$  within a set range. *J. Neurosci.* **1997**, *17*, 1959-1970.
47. Roehm, P. C.; Xu, N.; Woodson, E. A.; Green, S. H.; Hansen, M. R. Membrane depolarization inhibits spiral ganglion neurite growth via activation of multiple types of voltage sensitive calcium channels and calpain. *Mol. Cell. Neurosci.* **2008**, *37*, 376-387.
48. Jaegermann, P.; Lenzian, F.; Rist, G.; Mobius, K. Time-resolved ESR and endor during the photolysis of  $\omega,\omega$ -dimethoxy- $\omega$ -phenyl-acetophenone. *Chem. Phys. Lett.* **1987**, *140*, 615-619.
49. Bryant, S. J.; Hauch, K. D.; Ratner, B. D. Spatial Patterning of Thick Poly(2-hydroxyethyl methacrylate) Hydrogels. *Macromolecules* **2006**, *39*, 4395-4399.
50. Bryant, S. J.; Cuy, J. L.; Hauch, K. D.; Ratner, B. D. Photo-patterning of porous hydrogels for tissue engineering. *Biomaterials* **2007**, *28*, 2978-2986.

51. Mattotti, M.; Alvarez, Z.; Ortega, J. A.; Planell, J. A.; Engel, E.; Alcántara, S. Inducing functional radial glia-like progenitors from cortical astrocyte cultures using micropatterned PMMA. *Biomaterials* **2012**, *33*, 1759-1770.
52. Abbe, E. Contributions to the theory of the microscope and the microscopic perception (translated from German). *Arch. Mikr. Anat* **1873**, *9*, 413-468.
53. Garini, Y.; Vermolen, B. J.; Young, I. T. From micro to nano: recent advances in high-resolution microscopy. *Curr. Opin. Biotechnol.* **2005**, *16*, 3-12.
54. Smith, D. M.; Li, C. Y.; Bunning, T. J. Light-directed mesoscale phase separation via holographic polymerization. *J. Polym. Sci. B Polym. Phys.* **2014**, *52*, 232-250.
55. Odian, G. In *Determination of Absolute Rate Constants; Principles of Polymerization*; John Wiley & Sons Inc: Hoboken, New Jersey, **2004**; 4th Edition, pp 264-271.
56. Hsu, S. H.; Chen, C. Y.; Lu, P. S.; Lai, C. S.; Chen, C. J. Oriented Schwann cell growth on microgrooved surfaces. *Biotechnol. Bioeng.* **2005**, *92*, 579-588.
57. Biela, S. A.; Su, Y.; Spatz, J. P.; Kemkemer, R. Different sensitivity of human endothelial cells, smooth muscle cells and fibroblasts to topography in the nano–micro range. *Acta Biomater.* **2009**, *5*, 2460-2466.
58. Jacchetti, E.; Di Rienzo, C.; Meucci, S.; Nocchi, F.; Beltram, F.; Cecchini, M. Wharton's Jelly human mesenchymal stem cell contact guidance by noisy nanotopographies. *Sci. Rep.* **2014**, *4*, 10.1038/srep03830.
59. Neubrand, V. E.; Thomas, C.; Schmidt, S.; Debant, A.; Schiavo, G. Kidins220/ARMS regulates Rac1-dependent neurite outgrowth by direct interaction with the RhoGEF Trio. *J. Cell Sci.* **2010**, *123*, 2111-2123.
60. Micholt, L.; Gartner, A.; Prodanov, D.; Braeken, D.; Dotti, C. G.; Bartic, C. Substrate determines neuronal polarization and growth in vitro. *PLoS One* **2013**, *8*, e66170.
61. Dowell-Mesfin, N. M.; Abdul-Karim, M.; Turner, A. M.; Schanz, S.; Craighead, H. G.; Roysam, B.; Turner, J. N.; Shain, W. Topographically modified surfaces affect orientation and growth of hippocampal neurons. *J. Neural Eng.* **2004**, *1*, 78-90.
62. Kundu, A.; Micholt, L.; Friedrich, S.; Rand, D. R.; Bartic, C.; Braeken, D.; Levchenko, A. Superimposed topographic and chemical cues synergistically guide neurite outgrowth. *Lab Chip* **2013**, *13*, 3070-3081.
63. Davies, A. M. Neuronal survival: Early dependence on Schwann cells. *Curr. Biol.* **1998**, *8*, R15-R18.
64. Morris, J. K.; Lin, W.; Hauser, C.; Marchuk, Y.; Getman, D.; Lee, K. Rescue of the cardiac defect in ErbB2 mutant mice reveals essential roles of ErbB2 in peripheral nervous system development. *Neuron* **1999**, *23*, 273-283.

## CHAPTER 7

### MATERIAL STIFFNESS EFFECTS ON NEURITE

#### ALIGNMENT TO PHOTOPOLYMERIZED MICROPATTERNS

Directing neurite growth into close proximity of stimulating elements of a neural prosthesis, such as a retinal or cochlear implant (CI), may enhance device performance and overcome current spatial signal resolution barriers. In this work, spiral ganglion neurons (SGNs), which are the target neurons to be stimulated by CIs, were cultured on photopolymerized micropatterns with varied matrix stiffness to determine the effect of rigidity on neurite alignment to physical cues. Micropatterns are generated on methacrylate thin film surfaces in a simple, rapid photopolymerization step by photomasking the pre-polymer formulation with parallel line-space gratings. Two methacrylate series, a non-polar HMA-co-HDDMA series and a polar PEGDMA-co-EGDMA series, with significantly different surface wetting properties were evaluated. Equivalent pattern periodicity is maintained across each methacrylate series based on photomask band spacing, and feature amplitude is tuned to a depth of 2  $\mu\text{m}$  amplitude for all compositions using the temporal control afforded by UV curing methodology. Surface morphology was characterized by scanning electron microscopy (SEM) and white light interferometry. All micropatterned films adsorb similar amounts of laminin from solution and no significant difference in SGN survival is observed when comparing substrate compositions. SGN neurite alignment significantly increases with increasing material modulus for both methacrylate series. Interestingly, SGN neurites respond to material stiffness cues that are orders of magnitude higher (GPa) than what is typically ascribed to neural environments (kPa). Understanding neurite response to engineered physical cues and mechanical properties such as matrix stiffness will allow development of advanced

biomaterials that direct *de novo* neurite growth to address spatial signal resolution limitations of current neural prosthetics.

### Introduction

Matrix stiffness of native extracellular matrices (ECM) or synthetic matrices is a key biophysical cue that regulates cellular functions including migration, differentiation, spreading, and proliferation.<sup>1,2</sup> For example, in a process referred to as durotaxis, NIH 3T3 fibroblast cells are shown to preferentially migrate towards stiffer substrate on polyacrylamide sheets.<sup>3</sup> The number and length of angiogenic sprouts from endothelial cells increases with increasing matrix stiffness which is independent of matrix density.<sup>4</sup> Furthermore, matrix elasticity significantly affects the cell fate of naive mesenchymal stem cells with soft, stiffer, and rigid matrices delineating neurogenic, myogenic, and osteogenic cell lineages, respectively.<sup>5</sup>

Neural processes are also known to sense and respond to biophysical cues including substrate elasticity. For example, primary spinal cord neural processes branch significantly more on softer polyacrylamide gels compared to stiffer matrices.<sup>6</sup> Additionally, neurites from chick dorsal root ganglia grow significantly longer down a stiffness gradient, i.e. harder to softer, than up the gradient in a 3D genipin crosslinked collagen gel.<sup>7</sup> The behavior of neurons and their processes is of particular interest in cell-material interaction studies, including interactions based on matrix stiffness, due to their significance in a host of physiological functions. Accordingly, an array of material modifications or micro-environmental controls have been developed to influence neuronal behavior, particularly regarding neurite outgrowth, including diffusion or patterning of bioactive agents,<sup>8-11</sup> aligned physical features,<sup>11-16</sup> and electrical fields<sup>17</sup>. These methods are often employed as a means to increase ultimate unidirectional outgrowth to bridge gaps representative of nerve injuries.<sup>18-21</sup>

Beyond applications intended to bridge nerve gaps, understanding and controlling the directionality of *de novo* neurite growth based on physical material cues may also enable significant functional improvements of current and developing neural prosthetics. Specifically, directing neural processes into closer spatial proximity of stimulating elements of retinal or cochlear implants (CI) may overcome current spatial signal resolution barriers and enhance prosthesis performance.<sup>22-26</sup> Furthermore, spatially organized neural growth will likely be critical for high resolution performance of any future device that interfaces with the nervous system.

In this work we investigate the effects of material mechanical properties, i.e. matrix rigidity, on spiral ganglion neuron (SGN) neurite alignment to topographical guidance cues. SGNs are nerve cells in the inner ear that are electrically stimulated by CI prostheses. In previous work we demonstrated that *de novo* neurite growth from inner ear SGNs is guided by photopolymerized micropatterns,<sup>27</sup> that the extent of alignment can be tuned based on features dimensions,<sup>28</sup> and that response to uni- and multidirectional cues varies significantly even when neurites are presented with similar topographic features.<sup>29</sup> For this study, micropatterned thin films of hexyl methacrylate (HMA) with 1,6-hexanediol dimethacrylate (HDDMA) and poly(ethylene glycol) dimethacrylate (PEGDMA) with ethylene glycol dimethacrylate (EGDMA) are generated for neural alignment experiments using the spatial reaction control afforded via photopolymerization. Crosslink density is tuned for both methacrylate series to modulate matrix stiffness. Identical surface features are developed on each composition using the unique spatial and temporal reaction control afforded by photopolymerization. Developing advanced biomaterials that direct *de novo* neurite growth will require an improved understanding of neuron-material interactions, including response to substrate stiffness, to improve the spatial signal resolution of existing and future prostheses.

## Experimental

### Fabrication of Patterned Films with Varied Matrix Rigidity

Methacrylate thin films were polymerized on functionalized glass slides to prevent polymer delamination and facilitate cellular microscopy studies. Standard microscope glass slides (2.54 cm x 7.62 cm x 0.1 cm) were functionalized with the silane coupling agent 3-(trimethoxysilyl)propyl methacrylate (Aldrich). Prior to treatment with the coupling agent, slides were first cleaned and oxidized with O<sub>2</sub> plasma for 3 min at 30 W RF power (PDC-001 Harrick Plasma Expanded Cleaner, Ithaca, NY) while under 300 mTorr vacuum. Following removal from the plasma chamber, slides were immersed in a 1/100 v/v solution of the silane coupling agent and n-hexane (Aldrich) overnight in a covered container at room temperature (~21°C). Each slide was then rinsed with fresh hexanes and dried in the fume hood before being placed in a sealed container. Functionalized slides were used immediately as a substrate for polymerization.

All mixtures of hexyl methacrylate (HMA, Aldrich) with 1,6-hexanediol dimethacrylate (HDDMA, Aldrich) and poly(ethylene glycol) dimethacrylate (PEGDMA, Aldrich, M<sub>n</sub> = 600) with ethylene glycol dimethacrylate (EGDMA, Aldrich) were prepared with 1 wt% of 2,2-dimethoxy-2-phenylacetophenone (DMPA, BASF) as the photoinitiator. Copolymer compositions are represented as whole numbers (e.g. 40/60, 50/50) but each polymer fraction is 0.5 wt% less to account for the photoinitiator. 20 μL of pre-polymer solutions were pipetted onto the center of a functionalized slide then covered with a 2.54 cm x 2.54 cm x 0.1 cm glass-chrome Ronchi rule photomask (Applied Image Inc., Rochester, NY) for parallel patterns or with a cut untreated glass slide of the same dimensions for unpatterned samples. Capillary forces caused the formulations to spread evenly under the photomasks. Photopolymerization was carried out with a high-pressure mercury vapor arc lamp (Omniculture S1500, Lumen Dynamics, Ontario, Canada) at a 365 nm light intensity of 16 mW/cm<sup>2</sup>. The curing module was

equipped with an 8 mm aperture x 50 mm length beam homogenizing fused silica light pipe (Edmund Optics) and a collimating lens (RLQ-1, Asahi Spectra). Light intensity was measured with a Cole-Parmer Series 9811 radiometer. Microfeature amplitude was tuned by shuttering UV radiation at specific times thereby preventing further initiation events and resulting in rapid termination of the polymerization. Following the set exposure time, the photomask was removed from the polymer and the sample was washed with 95% ethanol to remove residual surface monomer. Rinsed samples were then post-cured for 10 min under the same light source and intensity without the photomask and under ambient conditions to maximize monomer conversion without reducing surface channel amplitude due to trough back-filling.

#### Topographical Characterization

Micropattern feature spacing and depth were measured by white light interferometry (Dektak Wyko 1100 Optical Profiling System, Veeco). Feature amplitude was measured as the difference between a maximum ridge value and an adjacent minimum groove value. For each composition and exposure time, average feature height was determined by measuring channel amplitude in nine different areas across the surface ( $n \geq 3$ ). Feature spacing or periodicity was measured as the distance between the highest points on adjacent ridges and was consistent with photomask band spacing. Measurements and 3D images were generated using Vision software associated with the instrument.

Micropattern morphology of each composition was further characterized by scanning electron microscopy (SEM, S-4800, Hitachi). Conductive silver paint was applied to the bottom of glass substrates modified with micropatterned methacrylate thin films for mounting on aluminum SEM stubs to acquire top-down images. For cross-sectional images, a glass etcher was used to etch the sample on the side opposite the thin polymer film and patterned polymers were then fractured and mounted vertically on

specimen stages. The SEM specimen stage was rotated using automated stage and software controls. Each polymer surface was sputter coated with gold prior to examination by SEM. Electron accelerating voltage was set at 2 kV.

#### SGN Culture, Survival, and Neurite Length

Polymer substrates attached to glass slides were sterilized with 70% ethanol and UV irradiation and air-dried in a culture hood. Micropatterned surfaces were then coated sequentially with poly-L-ornithine (100 µg/ml) at room temperature and laminin (20 µg/ml) at 4 °C overnight. The following day, dissociated spiral ganglion (SG) cultures from P3-6 rat pups were prepared as previously described.<sup>30,31</sup> Dissociated cultures were plated with equal volumes of the cell suspension and maintained in a humidified incubator with 6.5% CO<sub>2</sub> for 48 hrs. The cultures were maintained in Dulbecco's Modified Eagle Medium (DMEM) supplemented with N2 additives, insulin, 5% fetal bovine serum, neurotrophin-3 (NT-3, 50 ng/ml) and brain derived neurotrophic factor (BDNF, 50 ng/ml).

SGN cultures were fixed with 4% paraformaldehyde at 4 °C for 20 min, permeabilized and blocked with 5% goat serum, 2% BSA, 0.1% Triton X in phosphate buffered saline (PBS), and immunostained with anti-neurofilament 200 (NF200) antibodies (1:400, Sigma-Aldrich) at 37 °C for 2 hrs, as previously described.<sup>30</sup> Alexa 488 conjugated secondary antibody (1:800, Invitrogen) was used to detect the primary antibody immunolabeling at room temperature for 1 hr. Slides were treated with ProLong Gold anti-fading reagent with DAPI (Life Technology) and sealed with nitrocellulose. Digital epifluorescent images were captured of the entire polymer surface using the scan slide application of Metamorph software (Molecular Devices, Silicon Valley, CA) on a Leica DMIRE2 microscope (Leica Microsystem, Bannockburn, IL) with a Leica DFC350FX digital camera. The total number of NF200-positive neurons with healthy nuclei was counted from the digital images for each polymer surface to determine SGN

survival. The experiments were performed in duplicate and repeated at least three different times. Neurite length was determined by measuring the longest process of 100 randomly selected neurites from each slide using the measurement tool in Image J (NIH, Bethesda, MD) as previously described.<sup>32</sup>

#### Material Surface Chemistry and Laminin Adsorption

Polymer substrates were sequentially coated with poly-L-ornithine (100 µg/ml) at room temperature and 10 µg laminin (20 µg/ml, 0.5 ml in Hank's Balanced Salt Solution, Life Technologies) at 4 °C overnight. The laminin solution was removed by pipette and surfaces were washed three times. An equal volume of RIPA buffer containing 50 mM Tris-HCl, 1% NP-40, 1% Triton X-100, 150 mM NaCl and 1 mM EDTA was applied to each slide to dissolve the adsorbed protein. A 96-well plate protein assay kit (Life Technologies) was used to quantify protein concentration according to the manufacturer's protocol. Experimental samples and solutions of protein standards with known concentrations were pipetted into microplate wells and 1x dye reagent was added to each well, mixed, and incubated at room temperature for 5 minutes. Absorbance was measured by a microplate reader (THERMOmax, Molecular Devices). A standard curve was generated using the absorption values from the protein standards. Protein concentration of the experimental samples was calculated based on the standard curve. Each condition was performed in triplicate and then repeated at three different times.

Water contact angles were measured on unpatterned surfaces for each polymer composition using a sessile drop method at room temperature (~21° C) with a Ramé-Hart NRL 100-00 goniometer (Ramé-Hart Instrument Co., Mountain Lakes, NJ). For each composition, three samples were analyzed with repeats in six different spots for a total of 18 measurements per composition. Drops of doubly distilled H<sub>2</sub>O were dispensed as a 1 µL volume.

### Neurite Alignment on Patterns with Varied Matrix Rigidity

Tensile tests were performed with a dynamic mechanical analyzer (DMA- Q800 DMA TA Instruments) to measure the Young's modulus of each composition as a measure of substrate rigidity encountered by neural tissue. Polymer specimens for tensile tests were prepared by injecting pre-polymer formulations between two untreated glass plates separated by 280  $\mu\text{m}$  thick spacers and held together with clamps. The sample was then irradiated for 10 min using the same lamp and intensity used to fabricate micropatterned surfaces. Polymer bars, with dimensions of 25 mm x 6.4 mm x 0.28 mm, were placed in a vertical film tension clamp for tensile tests. Young's modulus was evaluated at 30° C using controlled force tensile mode with a designated force rate (0.5 N/m). The modulus was calculated from the slope of the stress-strain curve in the early linear regime (less than 5% strain) ( $n = 5$ ).

Neurite alignment to micropatterns was measured by determining the ratio ( $T_L/A_L$ ) of the total neurite length ( $T_L$ ) to the aligned length ( $A_L$ ).  $A_L$  is defined as the distance in a straight line along the direction of the micropattern (set horizontally) from the cell body to the nerve terminus. Neurites that closely follow the pattern have a ratio close to unity (1). Wandering neurites that do not strongly align to the pattern have higher ratios. For each sample, neurite alignment was measured for 100 randomly selected SGNs.

### Statistics

Statistical analysis was performed using SigmaStat 3.5 software (Systat Software, Chicago, IL). Groups were compared by performing a one-way ANOVA followed by a post hoc Kruskal-Wallis analysis of variance on ranks and a Dunn's Method or Tukey Test multiple comparison procedure. Results were considered statistically significant if  $p < 0.05$ .

## Results and Discussion

### Matching Feature Amplitude for Different Chemistries

The spatial control inherent to radiation curing was used to generate micro-scale biophysical cues suitable for neural process contact guidance. Specifically, pre-polymer methacrylate monomer and photoinitiator mixtures were selectively exposed to UV irradiation through photomasks which have alternating reflective and transparent 25  $\mu\text{m}$  wide bands (Fig. 7.1). Photomasking the reaction in this way enables modulation of local

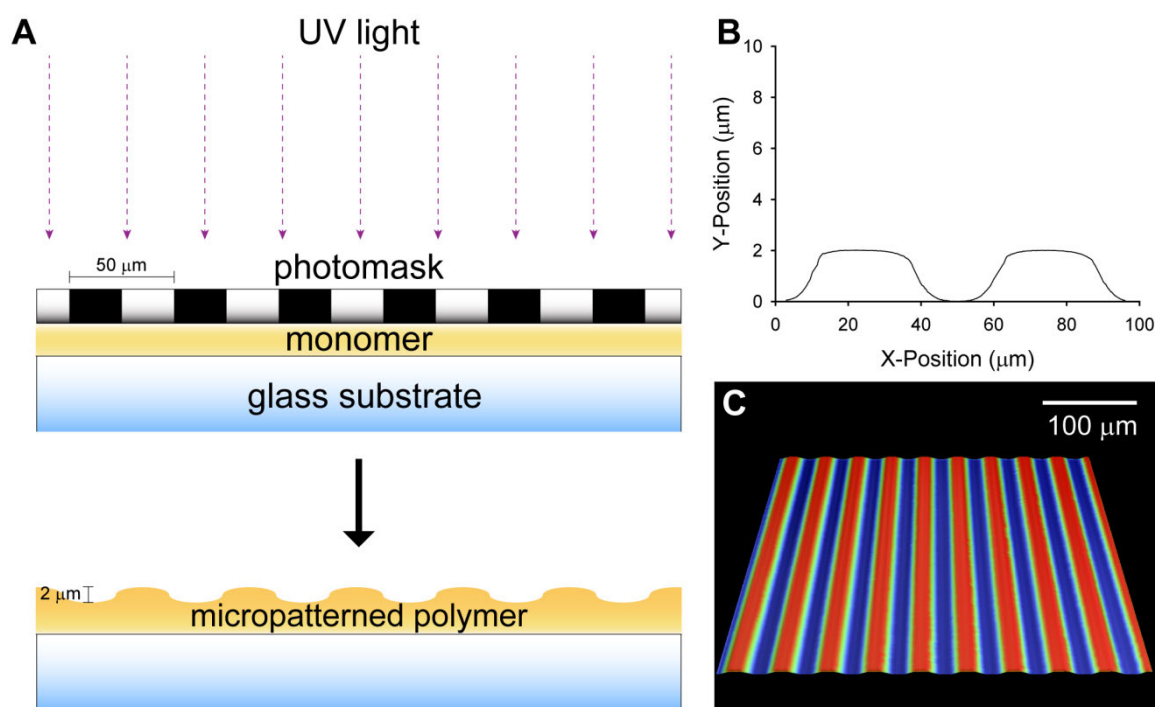


**Figure 7.1.** Photopolymerization of micropatterns on methacrylate thin film surfaces. **A)** UV exposure of the pre-polymer formulation is selectively blocked with a photomask to alter local reaction kinetics on the surface that result in raised or depressed microfeatures. **B)** 2D profile of a 50/50 PEGDMA-co-EGDMA ridge-groove-ridge transition generated by white light interferometry. **C)** 3D representation of a micropatterned methacrylate surface formed during a masked photopolymerization. All patterns used for this study have a 50  $\mu\text{m}$  periodicity and a channel amplitude of 2  $\mu\text{m}$ .

reaction kinetics which leads to formation of a global micropattern across the substrate surface. We have previously demonstrated that this size scale is relevant to spiral ganglion neurons (SGNs), their processes, and associated glial cells.<sup>28</sup> Furthermore, hair cell spacing within the cochlea is also within the feature spacing range which is relevant for future application to improve patient integration with a cochlear prosthetic.<sup>33</sup>

While under UV exposure, the photoinitiator absorbs high energy photons and undergoes photolysis which generates reactive free radicals that initiate polymerization. Polymerization occurs rapidly under transparent bands that transmit full incident light intensity from the source resulting in raised polymer ridges. Polymerization still occurs at some distance below reflective bands due to light diffraction, reflections within the reaction vessel, and diffusion of reactive species. However, regions directly below reflective bands do not undergo polymerization as insufficient photons reach the area to facilitate initiation events and reaction and diffusion constraints prevent reactive species from migrating deep into shadowed regions. As a result, a pattern of parallel micro-ridges and grooves of uniform width and amplitude rapidly develop across the substrate surface in a single fabrication step. The glass substrates used were first oxidized with O<sub>2</sub> plasma and treated with a methacrylated silane coupling agent to improve thin film adhesion and prevent polymer delamination during neurite microscopy studies.

Many cell-contact guidance studies for neurons and other cell types use microfeatures generated directly by photolithography or indirectly via soft lithography casting over etched silicon masters.<sup>34,35</sup> For example, human corneal epithelial cells were shown to align to and migrate in the direction of nanotopography generated by X-ray lithography and reactive ion etching.<sup>36</sup> Bovine aortic endothelial cells exhibited contact guidance to micropatterned polyacrylamide gels that were fabricated via soft lithography on a patterned silicon master template.<sup>37</sup> Furthermore, in an effort to produce cartilage tissue engineering constructs that yield superior mechanical properties of the resultant tissue, micropatterned collagen-glycosaminoglycan membranes were generated using a

combination of photolithography and softlithography to direct mesenchymal stem cell growth and ECM formation.<sup>38</sup> As an alternative patterning method, direct micropattern fabrication by photopolymerization presented here is advantageous as it requires one principle reaction step, few reagents, and simple and inexpensive equipment. By contrast, generation of micropatterns by photolithographic methods often requires a multistep process, hazardous reagents, and expensive substrates and processing equipment. Furthermore, creating a range of gradually transitioning features with direct photopolymerization enables tailored probing of cell contact guidance behavior in response to simultaneous physical and chemical guidance cues. Sharp features generated with traditional photolithography would likely dominate cellular interactions which may mask the effects of bioactive signaling on cellular behaviors. However, it should be noted that the direct photopolymerization method cannot reach the level of complexity afforded by multistep addition or removal processes available in photolithographic methodology.<sup>39</sup> It is, therefore, an additional and advantageous tool to be utilized for the rapid and facile development of surface active substrates for cell-material interaction studies.

To determine if SGN neurite response to matrix stiffness is system dependent, photopolymerized micropatterns were generated on the surface of various compositions of two different methacrylate platforms (Fig. 7.2). The HMA-co-HDDMA system is a relatively non-polar material with HDDMA serving as the crosslinker. As HDDMA content increases crosslinking density increases which stiffens the material including the physical microfeatures generated at the substrate surface. The PEGDMA-co-EGDMA system, by contrast, has a higher surface energy and is more wettable due to repeating polar ether linkages between polymerizable methacrylate moieties on high molecular weight PEGDMA monomers. Both monomers in the PEGDMA-co-EGDMA system undergo crosslinking within the network. However, crosslinking density decreases with increasing PEGDMA content due to larger spacing between polymerizable groups, and hence, fewer crosslinks per unit volume.



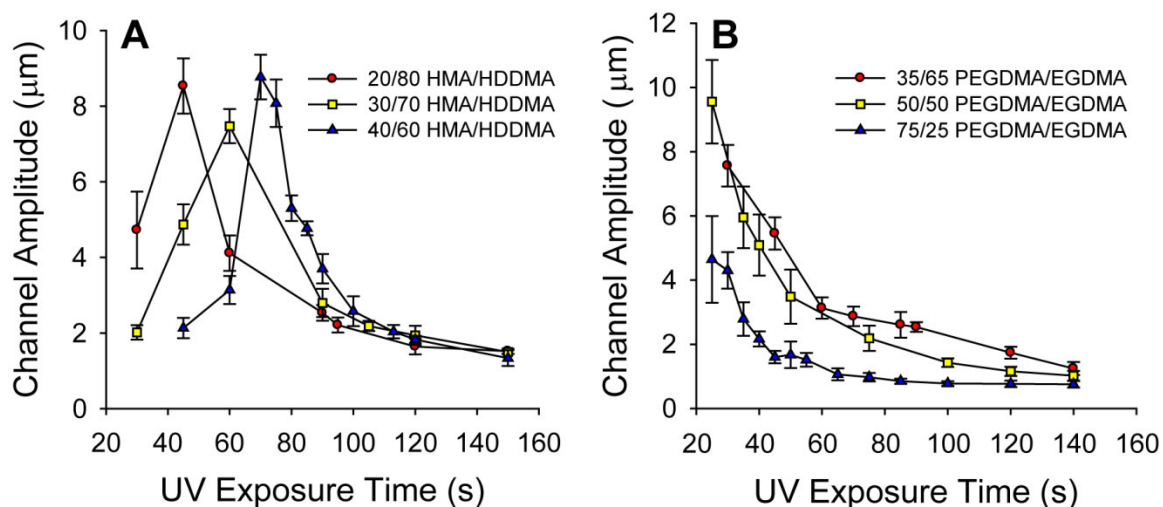


**Figure 7.3.** Micropattern feature height is tuned by modulating UV exposure time as determined by white light interferometry. **A)** HMA-co-HDDMA amplitude profiles for various compositions and exposure times. Maximum channel amplitudes are similar but occur at earlier polymerization times with increased diene concentration. **B)** PEGDMA-co-EGDMA amplitude profiles for various compositions and exposure times. Maximum amplitudes occur early in the reaction due to rapid vitrification caused by polymerization of high molecular weight PEGDMA monomers. Final amplitudes level off at a similar height of approximately 1.5 μm for both series. Each composition was masked with a 50 μm periodicity glass-chrome photomask and was mixed with 1 wt% DMPA as the photoinitiator. Error bars represent standard deviation (SD).

For example, under the given photopolymerization conditions, a microfeature amplitude of 2 μm for the HMA-co-HDDMA series occur at approximately 93 s, 105 s, and 114 s for 20, 30, and 40 HMA wt% compositions, respectively. Accordingly, microfeature amplitude for all compositions was tuned by modulating UV exposure time based on the reaction kinetics of pre-polymer formulations to generate comparable micropatterns. For HMA-co-HDDMA polymers, the amplitude development profile shifts to higher polymerization times with decreasing crosslinker content. However, for the PEGDMA-co-EGDMA system, the amplitude profile, including UV exposure time at the maximum amplitude and the subsequent leveling off at a lower amplitude, occurs at much earlier polymerization times due to rapid onset of system vitrification caused by

polymerization of high molecular weight PEGDMA monomer. As a result, exposure times required to reach a microfeature target amplitude of 2  $\mu\text{m}$  were much shorter than for the HMA-co-HDDMA system at 40 s, 74 s, and 95 s for 35, 50, and 75 wt% PEGDMA, respectively. It should be noted for both methacrylate systems that 2  $\mu\text{m}$  amplitude features were targeted with UV exposure times that occurred after maximum amplitude exposure times. Under the given reaction conditions, polymer conversion prior to generation of a maximum amplitude is generally insufficient to yield mechanically robust surfaces for microfeature characterization or contact guidance studies. Following the initial cure to develop 2  $\mu\text{m}$  amplitude microfeatures, all samples received a 10 min post-cure under the same exposure conditions but without the photomask to maximize methacrylate conversion within the film.

SEM was used to confirm white light interferometry measurements and to enable a more detailed comparison of micropattern morphology of each methacrylate composition (Fig. 7.4). The temporal control of photopolymerization was utilized to generate identical 2  $\mu\text{m}$  amplitude features for all compositions to allow simple comparisons of neurite behavior between systems based on material mechanical properties rather than on microfeature dimensions. Microfeature band spacing of ridges and grooves for all compositions closely matches the periodicity of transparent and reflective bands of the photomask with ridge-ridge spacing on the polymer surface occurring 50  $\mu\text{m}$  apart. Furthermore, SEM cross-sectional images demonstrate that polymer film thickness, surface micropatterns, and feature transitions are nearly identical for each composition. The microfeature similarities for different polymer chemistries indicate that final surface morphology is strongly shaped by constraints of the photopolymerization including light diffraction and reactive species diffusion considerations. Accordingly, neurite alignment to topographic features would be expected to be nearly identical if only the dimensions of the physical cues, but not the mechanical properties of the substrate, are considered as contact guidance factors.

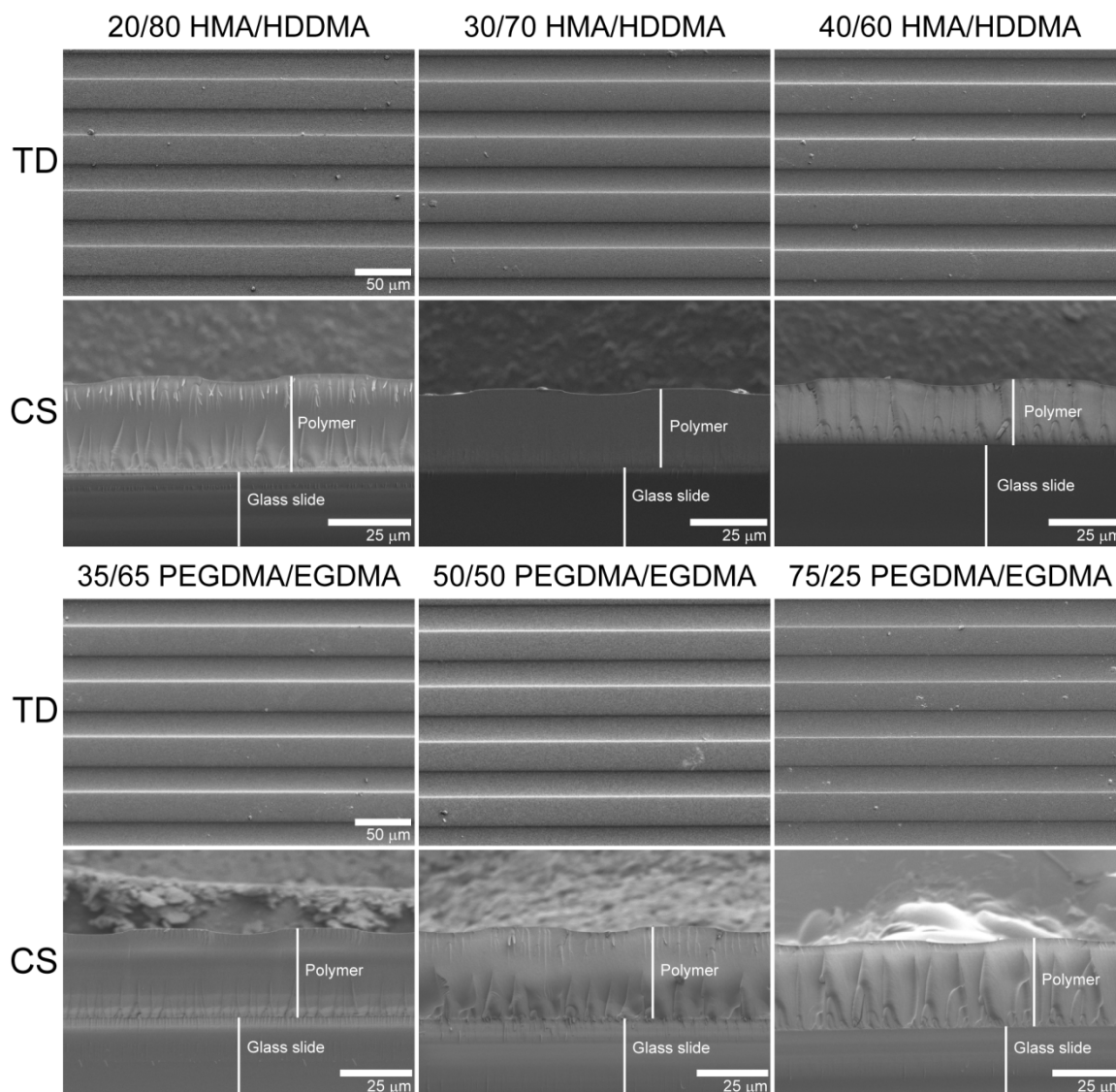


**Figure 7.4.** Representative top down (TD) and cross-section (CS) scanning electron micrographs of micropatterned polymer surfaces of each methacrylate composition.

#### Material Surface Chemistry and Protein Adsorption

To isolate the effect of matrix rigidity on neurite alignment to physical micropatterns, we first quantified HMA-co-HDDMA and PEGDMA-co-EGDMA surface wettability and adsorbed protein content to determine their contribution, if any, to differences in neural behavior (Figs. 7.5 and 7.6). Unpatterned thin films for each

methacrylate composition were photopolymerized using the same reaction conditions as outlined for micropatterned substrates. In place of a photomask, plain glass slides were cut to similar dimensions as the photomasks and used to enable absorption of full incident light intensity across the entire thin film area. Following removal of residual surface monomer with an ethanol wash, unpatterned polymer surface polarity was quantified by measuring water contact angles using a sessile drop method (Fig. 5). For the HMA-co-HDDMA series, the surface becomes slightly more hydrophobic with increasing HMA content with static water contact angles of  $73.8^\circ \pm 1.1$ ,  $76.7^\circ \pm 1.6$ ,  $79.2^\circ \pm 1.4$  for 20, 30, and 40 wt% HMA, respectively. However, while the contact angle difference between the 20 and 40 wt% HMA compositions is significant, it is unlikely that such a small absolute change in surface polarity, i.e.  $\sim 5^\circ$  water contact angle change, would lead to significant differences in neural behavior on the surface. For example, endothelial and epithelial cell adhesion on OH, COOH, and  $\text{NH}_2$  terminated self-assembled monolayers does not significantly change within a  $5^\circ$  range, but does change significantly with larger differences (e.g.  $20 - 80^\circ$ ) in surface wettability.<sup>40</sup> Furthermore, it was illustrated that iridium oxide substrates with a relatively broad distribution of surface energies are suitable for both insect and vertebrate neuronal growth.<sup>41</sup>

Similar to the HMA-co-HDDMA system, surface polarity does not substantially change across the PEGDMA-co-EGDMA series with static water contact angles of  $48.3^\circ \pm 2.9$ ,  $49.5^\circ \pm 1.8$ , and  $49.4^\circ \pm 2.5$  for 35, 50, and 65 wt% PEGDMA, respectively. While little to no change in surface polarity occurs for a given series, a significant difference in surface polarity is observed when comparing both series. The PEGDMA-co-EGDMA series is significantly more polar, i.e. wettable, with average static water contact angles  $\sim 30^\circ$  lower than those on the HMA-co-HDDMA series. Both polymer series have surface polarities that are known to support cellular adhesion and survival.<sup>42,43</sup> The two platforms, therefore, provide surfaces with substantially different chemical properties but

identical microfeature dimensions on which to probe neurite response to material stiffness in relation to topographic cues.

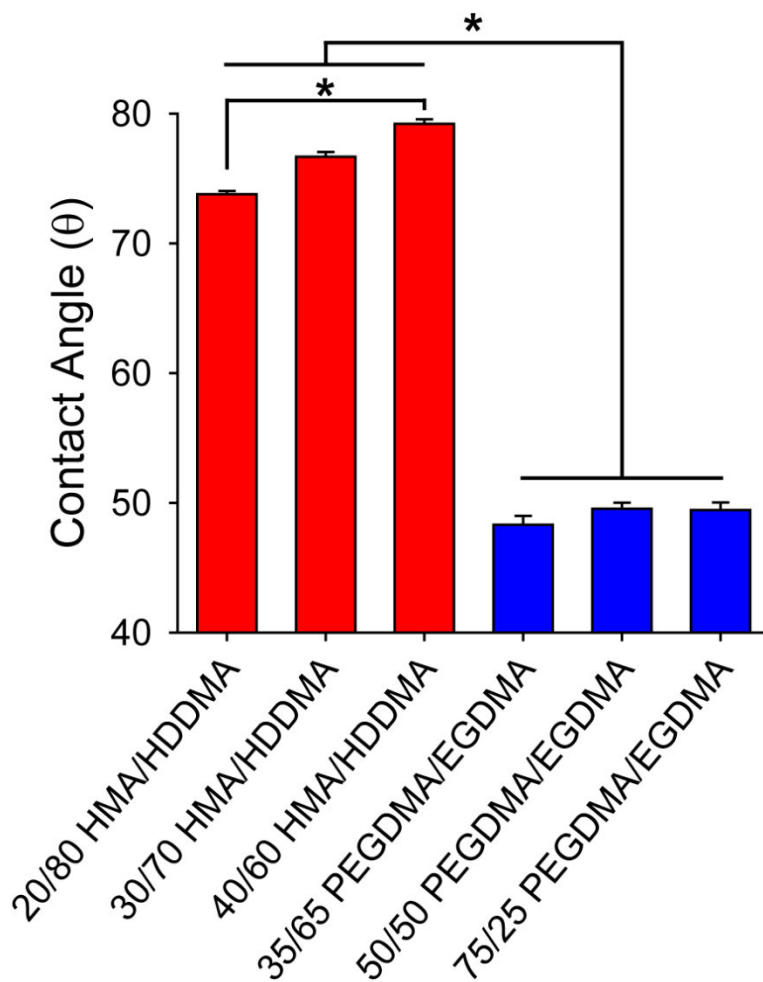


**Figure 7.5.** Static water contact angle on unpatterned methacrylate substrates. Surface polarity increases slightly with increasing HMA concentration for the HMA-co-HDDMA series with a 5° difference between the 20 and 40 wt % compositions. No statistical difference in contact angle is observed across the PEGDMA-co-EGDMA series. The PEGDMA-co-EGDMA series is substantially more polar and wettable with an average contact angle 30° lower than the other methacrylate series (\*  $p < 0.05$  one way ANOVA, Dunn's Method). Error bars represent SD.

In addition to substrate polarity, the amount of adsorbed laminin on each composition was also measured to determine its potential effects on neural outcomes including survival, neurite length, and neurite alignment (Fig. 7.6). Laminin is an

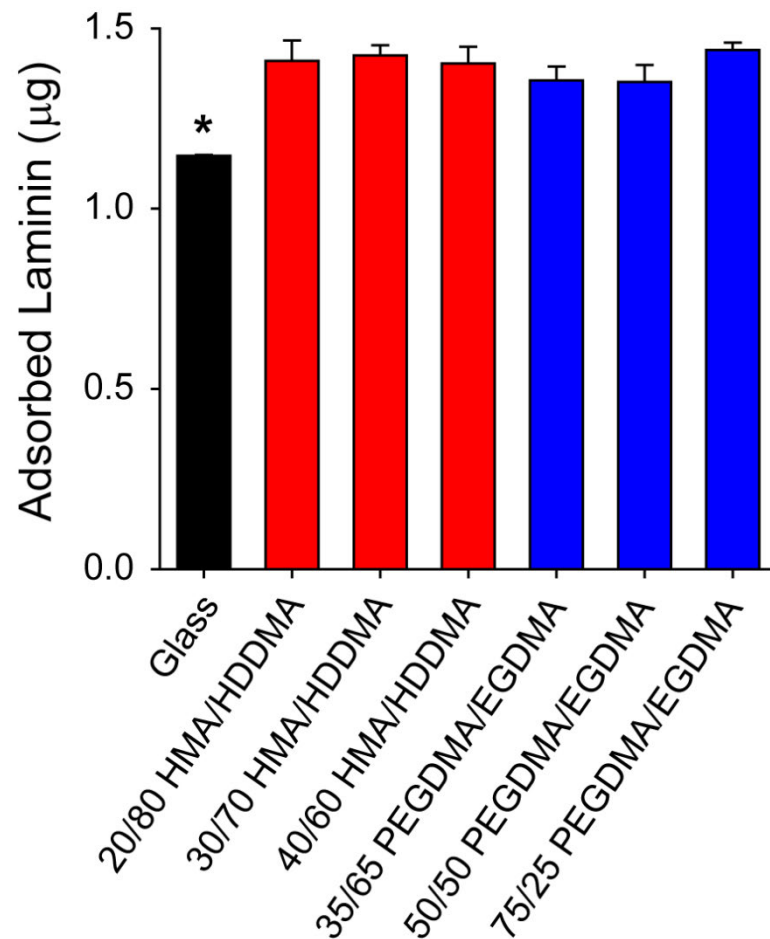


**Figure 7.6.** Laminin adsorption on methacrylate thin films. Laminin adsorption is no different on non-polar HMA-co-HDDMA substrates compared to polar PEGDMA-co-EGDMA substrates. The glass control adsorbed less laminin from solution than did methacrylate films. (\* $p < 0.05$  one way ANOVA, Tukey Test). Error bars represent standard error of the mean (SE).

extracellular glycoprotein that facilitates neuronal adhesion, survival and neurite growth.<sup>44</sup> Glycoproteins are polypeptides, i.e. proteins, that have covalently attached oligosaccharide side chains. A complex variety of pendant groups populate the main polypeptide chain which include aliphatic, polar, and charged groups for electrostatic interactions at neutral pH. Pendant surface moieties largely determine interfacial interactions with material surfaces which can vary based on material chemical properties.<sup>45</sup> However, even with the substantial disparity in surface polarity between the two methacrylate platforms, no significant difference in the concentration of adsorbed laminin is observed. Furthermore, adsorbed protein content for each composition across a given series is also nearly identical.

Protein adsorption on varied thin film compositions is likely similar for several reasons. For example, both surface types are moderately wettable, i.e. 40 – 70° water contact angle, so it is probable that sufficient protein-surface interactions occur with either series to facilitate adhesion. Additionally, while the surface polarity between the two series is substantially different, the functional groups presented by each material are quite similar. Both series present aliphatic backbones of polymer chains that make up the crosslinked network along with polar ester bonds from polymerizable methacrylate groups. The main difference in polarity between the two series is due to the presence of repeating polar ether bonds between crosslinks in the PEGDMA-co-EGDMA platform. Approximately ten percent of the laminin in solution remains adsorbed to micropatterned methacrylate platforms following rinsing steps which is similar to but slightly higher than the amount adsorbed on the glass control. The increase is likely due to greater hydrophobic interactions between the protein and the polymer surface compared to the interactions with a highly polar glass substrate. Laminin function is not compromised following surface adsorption as verified by the healthy outcomes of dissociated neuronal cultures on each composition indicating active surface protein. With little to no change in surface polarity across either series, and because adsorbed functional laminin content for

each composition is similar, a more direct comparison of stiffness effects on neurite alignment to physical features can be realized.

### SGN Survival and Neurite Length on MA Platforms

Dissociated SGNs were cultured on a series of methacrylate substrates with varied matrix stiffness in the MPa to GPa range to compare neuronal and process behavior. Matrix stiffness is modulated by varying crosslink density by either increasing crosslinker concentration in the HMA-co-HDDMA series or by tuning spacing between crosslinks based on high molecular weight monomer concentration in the PEGDMA-co-EGDMA series. As an initial comparison of neural behavior, SGN survival was quantified on a tissue culture plastic (TCP) control and on each micropatterned methacrylate thin film composition (Fig. 7.7). The TCP control and polymer substrates were coated with poly-L-ornithine and laminin to facilitate neuronal adhesion. For both TCP and unpatterned methacrylate polymers, *de novo* neurite growth extended randomly across the substrate surface (Fig 7.7A-C). SGN survival on micropatterned methacrylate substrates is comparable to survival on the TCP control. Furthermore, SGN survival is not significantly different on HMA-co-HDDMA compared to PEGDMA-co-EGDMA substrates or between substrates of the same series but with varied matrix stiffness (Fig. 7.7 D). Similar survival and culture behavior outcomes for SGNs on each methacrylate composition facilitate comparisons of neural behaviors, including neurite length and alignment in response to physical cues, without potential complications in accounting for unhealthy neurons or irregular morphologies. No trend or correlation is observed between SGN survival and methacrylate matrix rigidity under the range of stiffness studied.

To further compare neurite behavior in response to varied matrix stiffness, SGN neurite length was quantified from dissociated neuronal populations cultured on micropatterned polymers for each methacrylate composition (Fig. 7.8). Comparable microfeature spacing and depth is developed for each methacrylate composition using the

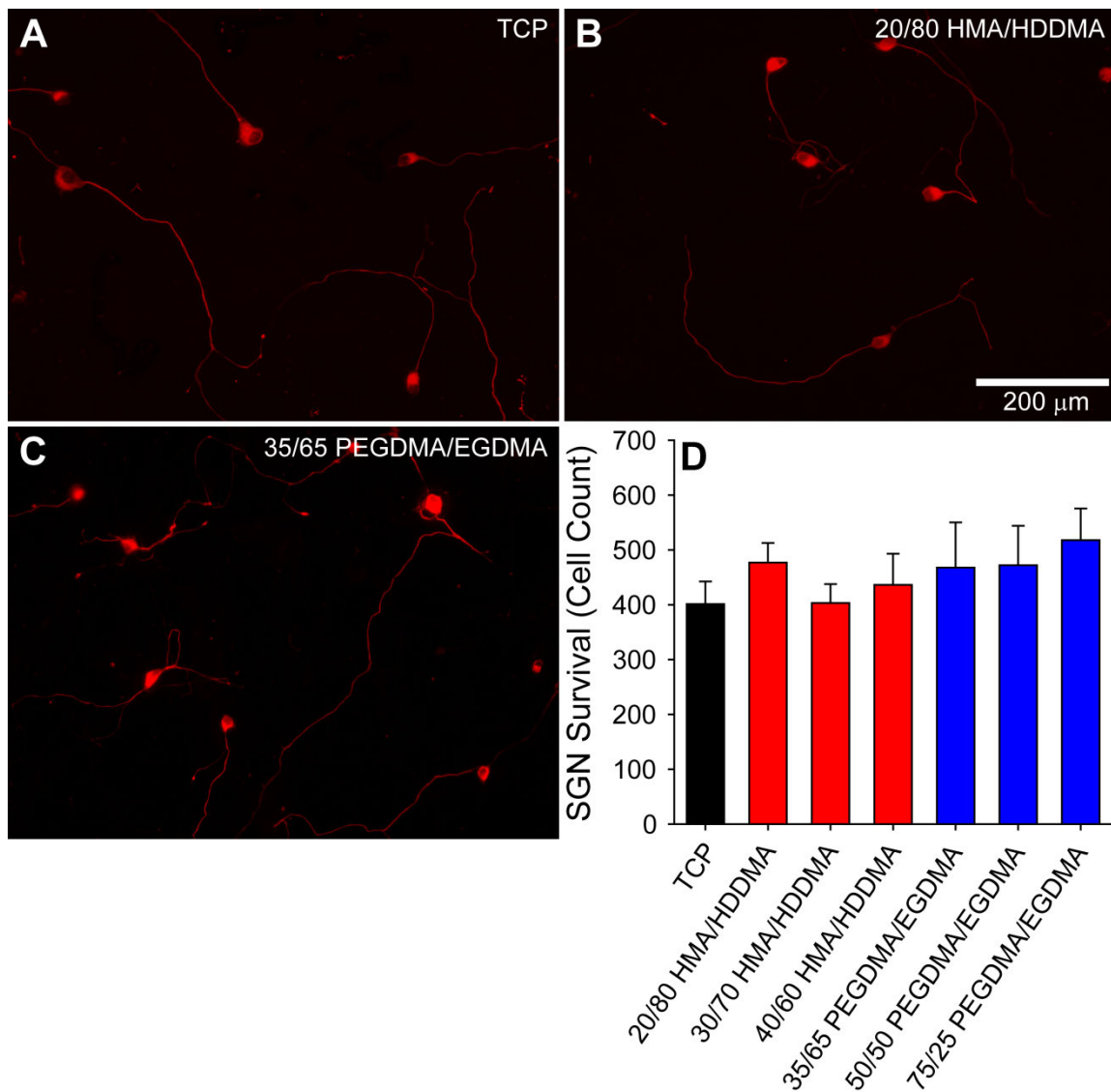


**Figure 7.7.** SGN survival on unpatterned TCP and methacrylate thin films. **A-C)** Immunofluorescent images of *de novo* neurite growth from dissociated SGNs illustrate random neurite outgrowth on unpatterned TCP (A) and on unpatterned HMA-co-HDDMA (B), and PEGDMA-co-EGDMA (C) films. No significant difference in SGN survival is observed when cultured on HMA-co-HDDMA substrates compared to PEGDMA-co-EGDMA substrates. SGN survival on polymer substrates is also similar to survival on a tissue culture plastic (TCP) control ( $p = 0.125$ , one way ANOVA). Error bars represent SE.

compositions were selectively blocked with photomasks that had repeating 25  $\mu\text{m}$  reflective – 25  $\mu\text{m}$  transmissive bands, or a 50  $\mu\text{m}$  periodicity. The widths of photopolymerized microfeatures for all compositions closely match photomask band

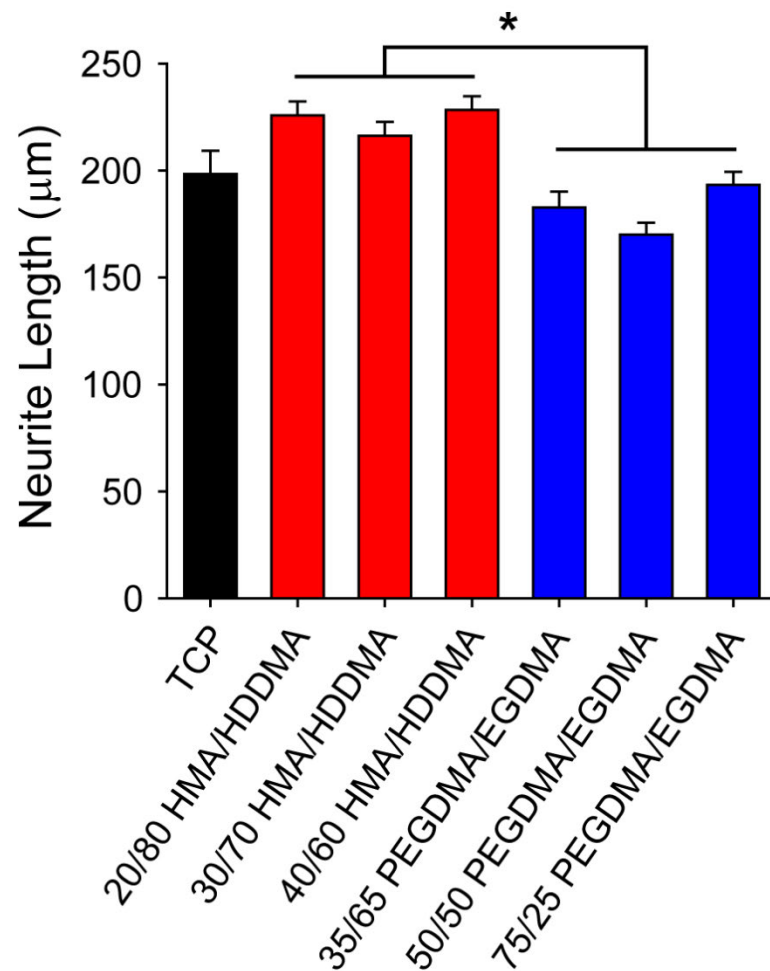


**Figure 7.8.** SGN neurite length on micropatterned methacrylate thin films. Neurite length is significantly shorter on PEGDMA-co-EGDMA substrates compared to HMA-co-HDDMA substrates. The average difference in length between the two series is 40  $\mu\text{m}$ . No significant difference in neurite length is observed between the TCP control and polymer substrates (\* $p < 0.05$ , one way ANOVA, Dunn's Method). Error bars represent SE.

spacing as observed by interferometry and SEM. The temporal control of photopolymerization was utilized to generate identical 2  $\mu\text{m}$  amplitude features for all compositions to allow simple comparisons of neurite behavior between systems based on material mechanical properties rather than on microfeature dimensions.

Similar to neuronal survival, no significant difference is observed between neurite length on TCP compared to neurite length on each polymer composition. SGN survival and neurite length results further illustrate that the photopolymerized methacrylate platforms are amenable to neuronal cultures and that no substantial deviations from typical dissociated SGN culture behavior occur. Furthermore, neurite length on varied compositions of a given series are also similar indicating that matrix rigidity does not significantly influence the rate of neurite outgrowth, at least for the range of stiffness studied.

Other studies have reported differences in neurite length based on mechanical properties of the culture material in certain stiffness ranges. For example, neurites from PC12 cells are longer on stiff PDMS substrates (1.72 MPa) compared to soft substrates (5 kPa) during the first five days of culture.<sup>46</sup> On the other hand, dorsal root ganglia grow longer neurites in very soft (0.5 kPa) elastin-like polypeptide hydrogels compared to stiffer (2 kPa) gels.<sup>47</sup> Furthermore, neurite outgrowth is longer from neuroblast Neuroa-2A cells on stiff matrices (800 kPa) compared to softer substrates (200 kPa).<sup>48</sup> However, each of these studies examines neural response to materials that are orders of magnitude less rigid, i.e. kPa range, than those examined here. Neurite length may not be significantly influenced after reaching a certain threshold of material stiffness.<sup>49</sup> Additionally, neurite length response to matrix stiffness may also be dependent on neuronal type.

While no substantial difference in neurite length is observed between the TCP control and either methacrylate series, neurite length is significantly different when directly comparing both polymer platforms. On average, neurites are approximately 40

$\mu\text{m}$  longer on the HMA-co-HDDMA substrates compared to PEGDMA-co-EGDMA substrates when maintained under the same culture conditions for the same length of time. Neurite length differences can likely be attributed to increased interactions of advancing neural growth cones on PEGDMA-co-EGDMA polymers compared to the HMA-co-HDDMA series. Because the two polymer series have significantly different surface polarity it is possible that laminin, while adsorbing at similar surface concentrations (Fig. 7.6), is presented in a more favorable orientation for trans-membrane receptor binding which increases neurite-substrate interactions and may slow outgrowth. Alternatively, changes in ECM organization and cell membrane response to material surface energy alone may be sufficient cause for the observed difference in neurite length.

#### Neurite Alignment on Patterns with Varied Matrix Rigidity

To determine the effect of rigid matrix stiffness on neurite alignment to physical cues, the crosslink density of each methacrylate platform was modulated while microfeature periodicity and amplitude were maintained across each composition. For the HMA-co-HDDMA series, matrix stiffness increased by raising the concentration of the dimethacrylate monomer – HDDMA – which increases the crosslink density of the network (Fig. 7.9A). However, increasing the concentration of the diene also increases the polymerization rate and leads to faster onset of gelation which alters microfeature formation time. Accordingly, UV exposure time must be adjusted to enable targeting of specific microfeature amplitudes for each composition (see Fig. 7.3). Following the photomasked exposure and subsequent ethanol wash, all micropatterned samples were treated with a 10 min post cure to maximize double bond conversion under the given reaction conditions. While maintaining equivalent microfeature spacing and amplitude for each HMA-co-HDDMA composition, SGN neurite alignment to micropattern features

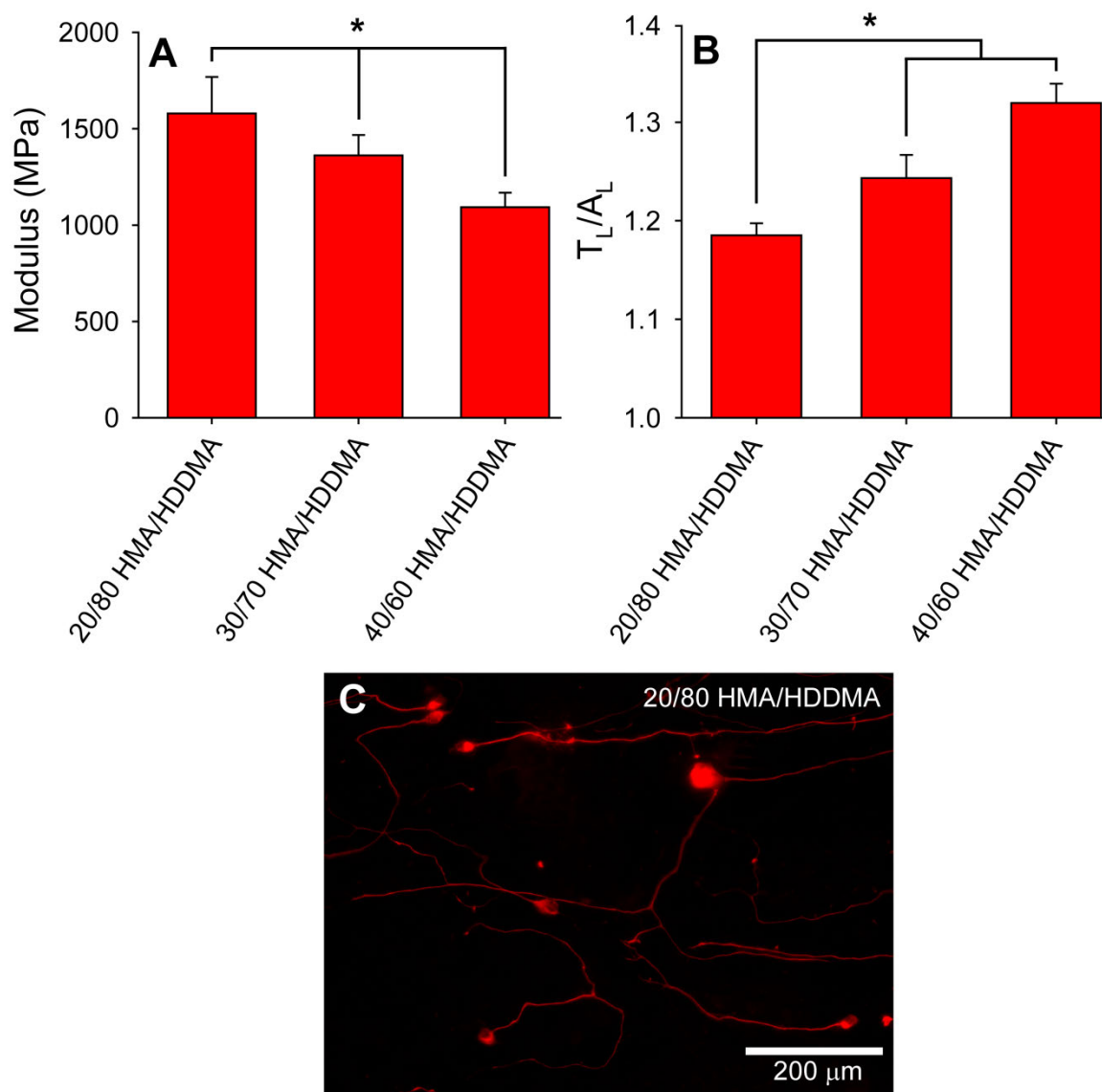


**Figure 7.9.** Modulus and SGN neurite alignment on the HMA-co-HDDMA series. **A)** Material modulus significantly increases with increasing crosslinker concentration ( $*p < 0.05$  one way ANOVA, Tukey Test). Error bars represent SD. **B)** SGN neurite alignment on micropatterned HMA-co-HDDMA substrates. Neurite alignment significantly increases (i.e. alignment ratio  $T_L/A_L$  decreases) with increasing substrate stiffness ( $*p < 0.05$  one way ANOVA, Dunn's Method). **C)** Representative immunofluorescent image of SGN neurite growth on micropatterned HMA-co-HDDMA polymers. Neurite outgrowth orients to the pattern direction which is set horizontally during alignment measurement. Error bars represent SE. The micropattern for each composition has a 50  $\mu$ m periodicity and a 2  $\mu$ m amplitude.

significantly increases with increasing matrix stiffness (Fig. 7.9B). Specifically, micropattern periodicity and amplitude were tuned to 50  $\mu\text{m}$  and 2  $\mu\text{m}$  respectively using the spatial and temporal control inherent to photopolymerization. Furthermore, topographic features for each polymer composition, including feature transitions, were demonstrated by SEM to be nearly identical for both methacrylate series (Fig. 7.4). Modulation of photopolymerization parameters to precisely tune topographic features for each composition enables direct comparison of neurite contact guidance behavior based on material mechanical properties. Neurite alignment ratios ( $T_L/A_L$ ) approaching unity indicate substantial alignment to the pattern direction along the entire length of the neurite while higher ratios are indicative of greater wandering or random growth. For an average neurite that is 225  $\mu\text{m}$  in length for the HMA-co-HDDMA series, the neurite would travel an extra 30  $\mu\text{m}$  of unaligned distance, i.e. outgrowth that is not in the direction of the micropattern features, on the softest substrate with an alignment ratio of 1.32 compared to the stiffest substrate with a neurite alignment ratio of 1.18.

Because both monomers in the PEGDMA-co-EGDMA system undergo crosslinking reactions, tuning of matrix stiffness is realized by modulating the ratio of the high molecular weight PEGDMA monomer relative to the low molecular weight EGDMA monomer (Fig. 7.10A). EGDMA has the same structure as the larger PEGDMA monomer but has only one ethylene glycol repeat unit whereas PEGDMA monomer used for this study has ten repeat units on average. With more flexible ether repeat units between polymerizable moieties, i.e. methacrylates, there are fewer crosslinks per unit volume which significantly reduces the material modulus. Material modulus for the PEGDMA-co-EGDMA system ranged from a maximum of  $1901 \pm 97$  MPa to a minimum of  $649 \pm 35$  MPa for 35 and 75 wt% PEGDMA compositions, respectively. Again, though microfeatures were maintained at equivalent periodicity and amplitude for each composition based on the spatio-temporal reaction control afforded by

photopolymerization, SGN neurite alignment is substantially improved on the stiffest substrate compared to the softest substrate (Fig 7.10B).

For many biomaterial applications that consider matrix stiffness, it is often deemed ideal to match the material modulus to that of the native tissue.<sup>50-54</sup> This approach is particularly appropriate for tissue engineering applications which aim to develop scaffolds that enable regeneration of healthy and functional tissue. For example, isolated embryonic cardiomyocytes are shown to overstrain and stop beating on rigid substrates, beat but do little work on soft materials, and optimally striate and transmit contractile work on substrates that match the stiffness of native matrices.<sup>52</sup> Potential stem cell treatments are also substantially affected by material mechanical properties as their lineage-specific differentiation has been repeatedly linked to matrix stiffness.<sup>55-60</sup> Further, load bearing applications such as cartilage tissue engineering require appropriate mechanical properties, i.e. similar to previously lost or damaged tissue, for successful mechanical function and integration.<sup>53,61</sup> However, our results demonstrate that some biomaterial applications, such as promoting spatial organization of *de novo* neurite growth, require careful consideration of material mechanical property effects on cellular behavior even when the material modulus is several orders of magnitude removed from native matrix stiffness of the target tissue. Part of the physical and biomechanical signals presented to neural growth cones during development and regeneration following injury likely include interactions with high modulus native matrices of bone, i.e. GPa range, or other dense connective tissues that are crucial to formation of spatially organized neural networks.<sup>62,63</sup> For example, SGN growth cones extend through the bony modiolus and along the osseous spiral lamina to reach the organ of Corti. While the exact mechanisms by which different cell types integrate biophysical cues remain unknown, it is evident that SGN neurites sense matrix stiffness on materials that are much more rigid than central neural environments (e.g. brain or spinal cord) and that their alignment to biophysical cues substantially changes based on substrate rigidity.<sup>64-66</sup>

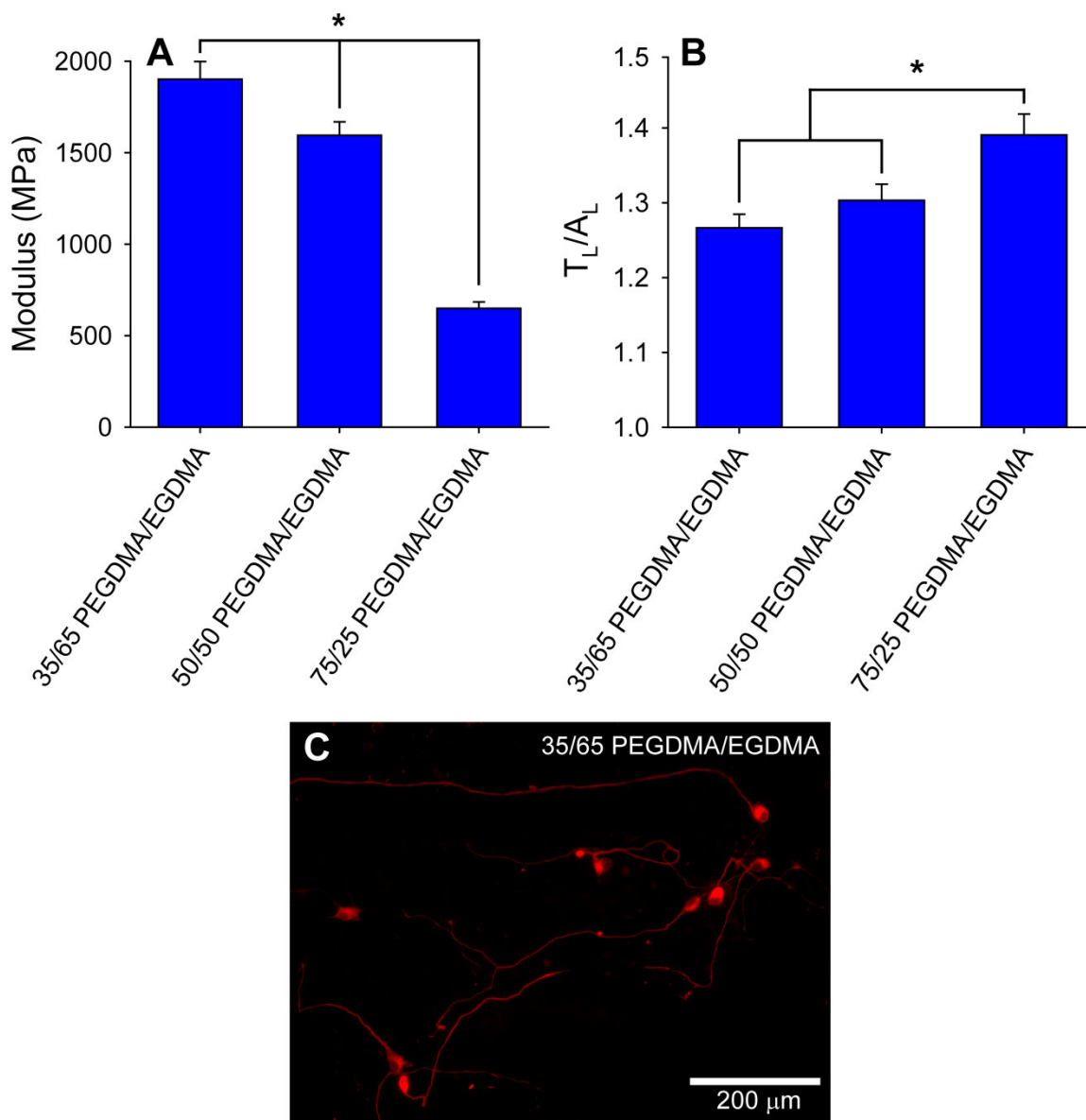


**Figure 7.10.** Modulus and SGN neurite alignment on PEGDMA-co-EGDMA series. **A)** Material modulus significantly decreases with increasing large PEGDMA monomer content (\* $p < 0.05$  one way ANOVA, Tukey Test). Error bars represent SD. **B)** SGN neurite alignment on micropatterned PEGDMA-co-EGDMA substrates. Neurite alignment significantly increases (i.e. alignment ratio  $T_L/A_L$  decreases) with increasing substrate stiffness (\* $p < 0.05$  one way ANOVA, Dunn's Method). **C)** Representative immunofluorescent image of SGN neurite growth on micropatterned PEGDMA-co-EGDMA polymers. Neurite outgrowth orients to the pattern direction which is set horizontally during alignment measurement. Error bars represent SE. The micropattern for each composition has a 50  $\mu\text{m}$  periodicity and a 2  $\mu\text{m}$  amplitude.

## Conclusions

This work illustrates that neurite alignment to physical micropatterns is significantly affected by the matrix stiffness of the underlying network. Specifically, for both the non-polar HMA-co-HDDMA and polar PEGDMA-co-EGDMA series, SGN neurite alignment significantly increases with increasing material stiffness. Interestingly, neurites respond to changes in matrix stiffness that are orders of magnitude higher than what is reported for tissue stiffness in a native neural environment. SGN survival is comparable on both methacrylate series but neurite length is significantly shorter on the polar PEGDMA-co-EGDMA substrates. Furthermore, photopolymerization is demonstrated as a powerful tool to fabricate readily tunable microfeatures across a variety of methacrylate compositions based on the spatial and temporal control of UV curing. Our results add to efforts aimed to enhance neural prosthetic performance by improving spatial signaling resolution and are also applicable to neural pathfinding and cell-material interaction applications.

### Notes

1. Discher, D. E.; Janmey, P.; Wang, Y. L. Tissue cells feel and respond to the stiffness of their substrate. *Science* **2005**, *310*, 1139-1143.
2. Wang, Y.; Chen, C. S. Cell adhesion and mechanical stimulation in the regulation of mesenchymal stem cell differentiation. *J. Cell. Mol. Med.* **2013**, *17*, 823-832.
3. Lo, C. M.; Wang, H. B.; Dembo, M.; Wang, Y. L. Cell movement is guided by the rigidity of the substrate. *Biophys. J.* **2000**, *79*, 144-152.
4. Mason, B. N.; Starchenko, A.; Williams, R. M.; Bonassar, L. J.; Reinhart-King, C. A. Tuning three-dimensional collagen matrix stiffness independently of collagen concentration modulates endothelial cell behavior. *Acta Biomater.* **2013**, *9*, 4635-4644.
5. Engler, A. J.; Sen, S.; Sweeney, H. L.; Discher, D. E. Matrix elasticity directs stem cell lineage specification. *Cell* **2006**, *126*, 677-689.
6. Flanagan, L. A.; Ju, Y. E.; Marg, B.; Osterfield, M.; Janmey, P. A. Neurite branching on deformable substrates. *Neuroreport* **2002**, *13*, 2411-2415.
7. Sundararaghavan, H. G.; Monteiro, G. A.; Firestein, B. L.; Shreiber, D. I. Neurite growth in 3D collagen gels with gradients of mechanical properties. *Biotechnol. Bioeng.* **2009**, *102*, 632-643.
8. Oliva, A. A.; James, C. D.; Kingman, C. E.; Craighead, H. G.; Banker, G. A. Patterning axonal guidance molecules using a novel strategy for microcontact printing. *Neurochem. Res.* **2003**, *28*, 1639-1648.
9. Gustavsson, P.; Johansson, F.; Kanje, M.; Wallman, L.; Linsmeier, C. E. Neurite guidance on protein micropatterns generated by a piezoelectric microdispenser. *Biomaterials* **2007**, *28*, 1141-1151.
10. Schmalenberg, K. E.; Uhrich, K. E. Micropatterned polymer substrates control alignment of proliferating Schwann cells to direct neuronal regeneration. *Biomaterials* **2005**, *26*, 1423-1430.
11. Li, J.; McNally, H.; Shi, R. Enhanced neurite alignment on micro-patterned poly-L-lactic acid films. *J. Biomed. Mater. Res. Part A* **2008**, *87A*, 392-404.
12. Hurtado, A.; Cregg, J. M.; Wang, H. B.; Wendell, D. F.; Oudega, M.; Gilbert, R. J.; McDonald, J. W. Robust CNS regeneration after complete spinal cord transection using aligned poly-L-lactic acid microfibers. *Biomaterials* **2011**, *32*, 6068-6079.
13. Johansson, F.; Carlberg, P.; Danielsen, N.; Montelius, L.; Kanje, M. Axonal outgrowth on nano-imprinted patterns. *Biomaterials* **2006**, *27*, 1251-1258.

14. Miller, C.; Jeftinija, S.; Mallapragada, S. Synergistic effects of physical and chemical guidance cues on neurite alignment and outgrowth on biodegradable polymer substrates. *Tissue Eng.* **2002**, *8*, 367-378.
15. Richardson, J. A.; Rementer, C. W.; Bruder, J. M.; Hoffman-Kim, D. Guidance of dorsal root ganglion neurites and Schwann cells by isolated Schwann cell topography on poly(dimethyl siloxane) conduits and films. *J. Neural Eng.* **2011**, *8*, 046015.
16. Koh, H. S.; Yong, T.; Teo, W. E.; Chan, C. K.; Puhaindran, M. E.; Tan, T. C.; Lim, A.; Lim, B. H.; Ramakrishna, S. In vivo study of novel nanofibrous intra-luminal guidance channels to promote nerve regeneration. *J. Neural Eng.* **2010**, *7*, 046003.
17. Yao, L.; Pandit, A.; Yao, S.; McCaig, C. D. Electric field-guided neuron migration: A novel approach in neurogenesis. *Tissue Eng. Part B Rev.* **2011**, *17*, 143-153.
18. Hoffman-Kim, D.; Mitchel, J. A.; Bellamkonda, R. V. Topography, cell response, and nerve regeneration. *Annu. Rev. Biomed. Eng.* **2010**, *12*, 203-231.
19. Spivey, E. C.; Khaing, Z. Z.; Shear, J. B.; Schmidt, C. E. The fundamental role of subcellular topography in peripheral nerve repair therapies. *Biomaterials* **2012**, *33*, 4264-4276.
20. Straley, K. S.; Foo, C. W.; Heilshorn, S. C. Biomaterial design strategies for the treatment of spinal cord injuries. *J. Neurotrauma* **2010**, *27*, 1-19.
21. Daly, W.; Yao, L.; Zeugolis, D.; Windebank, A.; Pandit, A. A biomaterials approach to peripheral nerve regeneration: bridging the peripheral nerve gap and enhancing functional recovery. *J. R. Soc. Interface* **2012**, *9*, 202-221.
22. O'Leary, S. J.; Richardson, R. R.; McDermott, H. J. Principles of design and biological approaches for improving the selectivity of cochlear implant electrodes. *J. Neural Eng.* **2009**, *6*, 055002.
23. Leach, J. B.; Achyuta, A. K.; Murthy, S. K. Bridging the divide between neuroprosthetic design, tissue engineering and neurobiology. *Front. Neuroeng.* **2010**, *2*, 18.
24. Leng, T.; Wu, P.; Mehenti, N. Z.; Bent, S. F.; Marmor, M. F.; Blumenkranz, M. S.; Fishman, H. A. Directed retinal nerve cell growth for use in a retinal prosthesis interface. *Invest. Ophthalmol. Vis. Sci.* **2004**, *45*, 4132-4137.
25. Winter, J. O.; Cogan, S. F.; Rizzo, J. F., III Retinal prostheses: current challenges and future outlook. *J. Biomater. Sci. Polym. Ed.* **2007**, *18*, 1031-1055.
26. Mehenti, N. Z.; Peterman, M. C.; Leng, T.; Marmor, M. F.; Blumenkranz, M. S.; Bent, S. F. A retinal interface based on neurite micropatterning for single cell stimulation. *Invest. Ophthalmol. Vis. Sci.* **2003**, *44*, U704-U704.

27. Clarke, J. C.; Tuft, B. W.; Clinger, J. D.; Levine, R.; Figueroa, L. S.; Guymon, C. A., Hansen, M. R. Micropatterned methacrylate polymers direct spiral ganglion neurite and Schwann cell growth. *Hear. Res.* **2011**, *278*, 96-105.
28. Tuft, B. W.; Li, S.; Xu, L.; Clarke, J. C.; White, S. P.; Guymon, B. A.; Perez, K. X.; Hansen, M. R.; Guymon, C. A. Photopolymerized microfeatures for directed spiral ganglion neurite and Schwann cell growth. *Biomaterials* **2013**, *34*, 42-54.
29. Tuft, B. W.; Xu, L.; White, S. P.; Seline, A. E.; Erwood, A. M.; Hansen, M. R.; Guymon, C. A. Neural pathfinding on uni- and multidirectional photopolymerized micropatterns. *ACS Appl. Mater. Inter.* **2014**, <http://dx.doi.org/10.1021/am501622a>
30. Hansen, M. R.; Vijapurkar, U.; Koland, J. G.; Green, S. H. Reciprocal signaling between spiral ganglion neurons and Schwann cells involves neuregulin and neurotrophins. *Hear. Res.* **2001**, *161*, 87-98.
31. Hegarty, J.; Kay, A.; Green, S. Trophic support of cultured spiral ganglion neurons by depolarization exceeds and is additive with that by neurotrophins or cAMP and requires elevation of  $[Ca^{2+}]_i$  within a set range. *J. Neurosci.* **1997**, *17*, 1959-1970.
32. Roehm, P. C.; Xu, N.; Woodson, E. A.; Green, S. H.; Hansen, M. R. Membrane depolarization inhibits spiral ganglion neurite growth via activation of multiple types of voltage sensitive calcium channels and calpain. *Mol. Cell. Neurosci.* **2008**, *37*, 376-387.
33. Wright, A.; Davis, A.; Bredberg, G.; Ulehlova, L.; Spencer, H.; Bock, G.; Felix, H.; Iurato, S.; Johnsson, L. G.; Pauler, M. Hair cell distributions in the normal human cochlea. *Acta Otolaryngol.* **1987**, 1-48.
34. Singh, A. V.; Patil, R.; Thombre, D. K.; Gade, W. N. Micro-nanopatterning as tool to study the role of physicochemical properties on cell-surface interactions. *J. Biomed. Mater. Res. Part A* **2013**, *101*, 3019-3032.
35. Schmidt, R. C.; Healy, K. E. Controlling biological interfaces on the nanometer length scale. *J. Biomed. Mater. Res. Part A* **2009**, *90A*, 1252-1261.
36. Diehl, K. A.; Foley, J. D.; Nealey, P. F.; Murphy, C. J. Nanoscale topography modulates corneal epithelial cell migration. *J. Biomed. Mater. Res. Part A* **2005**, *75A*, 603-611.
37. Charest, J. M.; Califano, J. P.; Carey, S. P.; Reinhart-King, C. A. Fabrication of substrates with defined mechanical properties and topographical features for the study of cell migration. *Macromol. Biosci.* **2012**, *12*, 12-20.
38. Chou, C.; Rivera, A. L.; Sakai, T.; Caplan, A. I.; Goldberg, V. M.; Welter, J. F.; Baskaran, H. Micrometer scale guidance of mesenchymal stem cells to form structurally oriented cartilage extracellular matrix. *Tissue Eng. Part A* **2013**, *19*, 1081-1090.

39. Tawfick, S.; De Volder, M.; Copic, D.; Park, S. J.; Oliver, C. R.; Polsen, E. S.; Roberts, M. J.; Hart, A. J. Engineering of micro- and nanostructured surfaces with anisotropic geometries and properties. *Adv. Mater.* **2012**, *24*, 1628-1674.
40. Arima, Y.; Iwata, H. Effect of wettability and surface functional groups on protein adsorption and cell adhesion using well-defined mixed self-assembled monolayers. *Biomaterials* **2007**, *28*, 3074-3082.
41. Göbbels, K.; Kuenzel, T.; van Ooyen, A.; Baumgartner, W.; Schnakenberg, U.; Bräunig, P. Neuronal cell growth on iridium oxide. *Biomaterials* **2010**, *31*, 1055-1067.
42. Lee, J. H.; Lee, J. W.; Khang, G.; Lee, H. B. Interaction of cells on chargeable functional group gradient surfaces. *Biomaterials* **1997**, *18*, 351-358.
43. Tamada, Y.; Ikada, Y. Cell adhesion to plasma-treated polymer surfaces. *Polymer* **1993**, *34*, 2208-2212.
44. Nurcombe, V. Laminin in neural development. *Pharmacol. Ther.* **1992**, *56*, 247-264.
45. Norde, W.; Horbett, T. A.; Brash, J. L. In *Proteins at Interfaces III: Introductory Overview*; American Chemical Society: **2012**; *1120*, pp 1-34.
46. Palchesko, R. N.; Zhang, L.; Sun, Y.; Feinberg, A. W. Development of polydimethylsiloxane substrates with tunable elastic modulus to study cell mechanobiology in muscle and nerve. *PLoS One* **2012**, *7*, e51499.
47. Lampe, K. J.; Antaris, A. L.; Heilshorn, S. C. Design of three-dimensional engineered protein hydrogels for tailored control of neurite growth. *Acta Biomater.* **2013**, *9*, 5590-5599.
48. Chou, S.; Cheng, C.; Chen, C.; LeDuc, P. R. Localized neurite outgrowth sensing via substrates with alternative rigidities. *Soft Matter* **2011**, *7*, 9871-9877.
49. Leach, J. B.; Brown, X. Q.; Jacot, J. G.; DiMilla, P. A.; Wong, J. Y. Neurite outgrowth and branching of PC12 cells on very soft substrates sharply decreases below a threshold of substrate rigidity. *J. Neural Eng.* **2007**, *4*, 26-34.
50. Moglia, R. S.; Robinson, J. L.; Muschenborn, A. D.; Touchet, T. J.; Maitland, D. J.; Cosgriff-Hernandez, E. Injectable polyMIPE scaffolds for soft tissue regeneration. *Polymer* **2014**, *55*, 426-434.
51. Palchesko, R. N.; Zhang, L.; Sun, Y.; Feinberg, A. W. Development of polydimethylsiloxane substrates with tunable elastic modulus to study cell mechanobiology in muscle and nerve. *PLoS One* **2012**, *7*, e51499.

52. Engler, A. J.; Carag-Krieger, C.; Johnson, C. P.; Raab, M.; Tang, H.; Speicher, D. W.; Sanger, J. W.; Sanger, J. M.; Discher, D. E. Embryonic cardiomyocytes beat best on a matrix with heart-like elasticity: scar-like rigidity inhibits beating. *J. Cell. Sci.* **2008**, *121*, 3794-3802.
53. Kemppainen, J. M.; Hollister, S. J. Tailoring the mechanical properties of 3D-designed poly(glycerol sebacate) scaffolds for cartilage applications. *J. Biomed. Mater. Res. Part A* **2010**, *94A*, 9-18.
54. Yu, T. T.; Shoichet, M. S. Guided cell adhesion and outgrowth in peptide-modified channels for neural tissue engineering. *Biomaterials* **2005**, *26*, 1507-1514.
55. Engler, A. J.; Sen, S.; Sweeney, H. L.; Discher, D. E. Matrix elasticity directs stem cell lineage specification. *Cell* **2006**, *126*, 677-689.
56. Wang, Y.; Chen, C. S. Cell adhesion and mechanical stimulation in the regulation of mesenchymal stem cell differentiation. *J. Cell. Mol. Med.* **2013**, *17*, 823-832.
57. Ayala, R.; Zhang, C.; Yang, D.; Hwang, Y.; Aung, A.; Shroff, S. S.; Arce, F. T.; Lal, R.; Arya, G.; Varghese, S. Engineering the cell-material interface for controlling stem cell adhesion, migration, and differentiation. *Biomaterials* **2011**, *32*, 3700-3711.
58. Kim, I. L.; Khetan, S.; Baker, B. M.; Chen, C. S.; Burdick, J. A. Fibrous hyaluronic acid hydrogels that direct MSC chondrogenesis through mechanical and adhesive cues. *Biomaterials* **2013**, *34*, 5571-5580.
59. Engler, A. J.; Griffin, M. A.; Sen, S.; Bonnetmann, C. G.; Sweeney, H. L.; Discher, D. E. Myotubes differentiate optimally on substrates with tissue-like stiffness: pathological implications for soft or stiff microenvironments. *J. Cell Biol.* **2004**, *166*, 877-887.
60. Park, J. S.; Chu, J. S.; Tsou, A. D.; Diop, R.; Tang, Z.; Wang, A.; Li, S. The effect of matrix stiffness on the differentiation of mesenchymal stem cells in response to TGF- $\beta$ . *Biomaterials* **2011**, *32*, 3921-3930.
61. Xiao, Y.; Friis, E. A.; Gehrke, S. H.; Detamore, M. S. Mechanical testing of hydrogels in cartilage tissue engineering: Beyond the compressive modulus. *Tissue Eng. Part B Rev.* **2013**, *19*, 403-412.
62. Rho, J. Y.; Ashman, R. B.; Turner, C. H. Young's modulus of trabecular and cortical bone material: Ultrasonic and microtensile measurements. *J. Biomech.* **1993**, *26*, 111-119.
63. Zysset, P. K.; Guo, X. E.; Hoffler, C. E.; Moore, K. E.; Goldstein, S. A. Elastic modulus and hardness of cortical and trabecular bone lamellae measured by nanoindentation in the human femur. *J. Biomech.* **1999**, *32*, 1005-1012.

64. Lewis, K. J.; Anseth, K. S. Hydrogel scaffolds to study cell biology in four dimensions. *MRS Bull* **2013**, *38*, 260-268.
65. Eyckmans, J.; Boudou, T.; Yu, X.; Chen, C. S. A hitchhiker's guide to mechanobiology. *Dev. Cell* **2011**, *21*, 35-47.
66. Chen, C. S. Mechanotransduction - a field pulling together? *J. Cell. Sci.* **2008**, *121*, 3285-3292.

## CHAPTER 8

### BIOCHEMICAL BORDER CHALLENGES TO NEURITE

#### ALIGNMENT ON PHOTOPOLYMERIZED PHYSICAL MICROPATTERNS

Developing neurites must respond to a variety of biophysical and biochemical cues in their micro-environment or niche to reach target cells for meaningful synapse. Utilizing both types of cues to precisely direct *de novo* neurite growth to specific electrodes of a neural prosthesis may improve neural tissue integration and significantly improve device performance. In this work, bioactive chemical borders are established on photopolymerized physical microfeatures to determine the strength of physical cues when neural growth cones are presented with conflicting cues. Physical micropatterns are fabricated using the photomasking techniques to spatially control photoinitiation events of the polymerization. Temporal control of the reaction is utilized to form microfeatures with the same amplitude across a range of feature frequencies or periodicities. Spiral ganglion neuron (SGN) and trigeminal neuron (TGN) neurites serve as neural process models. Neurite behavior is measured at biochemical borders as cross, turn, stop, or repel events. Both the chemical borders and the physical patterns are shown to significantly affect neurite outgrowth. Importantly, physical cues are illustrated to dominate neurite trajectory at sufficiently high micropattern feature frequencies. Designing prosthesis interfaces with physical cues that induce spatially organized neurite outgrowth even in the presence of conflicting biochemical cues will likely be necessary for *in vivo* applications with inherent biochemical signaling.

## Introduction

Neural sensory prostheses, such as the successful cochlear implant (CI) and the developing retinal implant, are designed to meaningfully interact with the nervous system to replace or substantially augment lost sensory function. Sensory simulation is achieved through use of an artificial sensor, i.e. microphone for auditory loss and cameras for visual impairment, followed by direct electrical stimulation of remaining healthy nerve cells by an electrode array.<sup>1,2</sup> The firing pattern of the prosthesis electrode array is controlled by computer algorithms to selectively modulate nervous system stimulation which alters the final signal transmitted to the brain.

While current neural prostheses provide rudimentary sensory information, such as basic audio or visual perception, their performance is substantially limited by poor integration with the target neural tissue.<sup>1,3</sup> In particular, sensory neural prostheses are constrained to providing few effective signal channels due to spatial resolution limitations which prevent precise stimulation of specific neural populations. For example, electrical current spread in the cochlea results in non-specific excitation of inner ear spiral ganglion neurons (SGNs) and limits tonal information provided by the CI prosthesis.<sup>2</sup> Limited tonal simulation results in poor audio performance in environments with noise and poor music perception.<sup>4-6</sup> Current CI electrode arrays lie in the *scala tympani* and stimulate the SGN cell bodies or central fibers within the *modiolus*. The distance between the stimulating electrodes and the neurons that they activate results in stimulation of SGNs over a broad frequency range and significant interaction of adjacent channels.<sup>4,7,8</sup> Though current CIs have up to 24 distinct electrodes, a maximum of only 8 effective or perceptual channels are achieved with current CI technology.<sup>9</sup> Thus, the tone dependent, or tonotopic, spatial organization inherent to the auditory system is poorly exploited by the implant and limits patient auditory performance.<sup>10,11</sup> Accordingly, increasing the number of effective signal channels provided by the prosthesis would

substantially improve auditory performance outcomes for CI users as the device would make better use of the tonotopic spatial organization within the cochlea.

To improve tissue integration and enhance the stimulatory specificity of neural prostheses, there is lively interest in developing methods to promote regrowth of the sensory neurites into close proximity, or even contact, with the stimulating electrodes.<sup>5,12-16</sup> Precisely directing neurites to specific electrodes in this manner would substantially increase the number of available perceptual signal channels, which would greatly enhance device performance and improve user experience.<sup>1,2,16</sup> To be useful, neurite outgrowth must preserve the precise spatial organization of the nervous system such as the tonotopic neural organization in the cochlea.<sup>17-19</sup> To meaningfully direct neural processes, biomaterials scientists and biomedical engineers have designed or modified materials with chemical or physical micro and nanoscale patterning that guide neurite outgrowth. For example, diode lasers were used to covalently bind a fluorophore conjugated-biotin and laminin binding sequence to a planar surface with high resolution spatial control to direct dorsal root ganglion neurite outgrowth.<sup>20,21</sup> Microcontact printing was used to biofunctionalize polystyrene, glass, and silicon-oxide surfaces with the oligopeptide binding sequence of laminin to spatially direct the formation of hippocampal neuronal networks.<sup>22</sup>

Because favorable cellular interactions at the interface between a biological system and a material often require location specific signaling, photo-dependent processes such as photolithography and photopolymerization are increasingly exploited in biomaterial and tissue engineering studies and device fabrication due to their inherent spatial control.<sup>23-26</sup> Utilizing the reaction control afforded by photo-initiation, our labs previously demonstrated that SGN neurites are directed by photopolymerized microtopographic features and that the extent of neurite alignment strongly correlates with physical feature transitional slope.<sup>27,28</sup> Furthermore, the consistency of SGN neural-pathfinding to microfeatures of specific dimensions was shown to depend on pattern

complexity.<sup>29</sup> In addition to physical surface features, SGN neurite alignment to induced topographies is modulated by the matrix stiffness of the synthetic biomaterial.

While significant progress has been made to induce *de novo* neurite outgrowth from remaining SGNs following deafness, meaningfully directing neural process extension *in vivo* remains a significant obstacle to the proximate growth strategy for improved prosthesis performance.<sup>17,19,30,31</sup> During tissue formation, development, and regeneration, cells – including neurons and their extending neurites – encounter and must respond to a complex milieu of biochemical and biophysical signals in their surrounding microenvironment.<sup>32-38</sup> Because chemical or physical cues in the native environment may induce counterproductive neural outgrowth, it may be necessary to design guidance cues that overcome conflicting directional signals.

Accordingly, in this work, SGN neural process alignment is evaluated on photopatterned materials that are modified with distinct biochemical cues and borders. Neurite alignment and behavior is evaluated at the dynamic biochemical border to determine physical guidance cues that dominate neural process directional growth outcomes. Dissociated SGNs and trigeminal neurons (TGNs) were cultured on photopolymerized micropattern substrates coated with two species of bioactive molecules and neurite outgrowth and pathfinding behavior is characterized at the biochemical border between the species. Bioactive species utilized in the work include: laminin, an integrin binding glycoprotein that facilitates neuronal adhesion and process outgrowth; tenascin-C (TnC), an adhesion modulating glycoprotein that can modify cellular adhesion by binding molecules of a cell's extra cellular matrix; and EphA4 which is a protein kinase important in cell adhesion and migration as well as in neurite guidance. The adsorbed biochemicals form a distinct border across each sample and neurite alignment is characterized at the border as cross, stop, turn, and repel behavior. SGN neurites readily cross from EphA4-Fc coated regions to laminin coated areas on all pattern types, but the extent of crossing for a given neuronal population significantly increases with increasing

feature frequency. Neurites from SGNs and TGNs are also observed to cross a laminin-TnC biochemical border when confronted with sufficiently strong physical guidance cues. However, the border between laminin and TnC generally serves as a repulsive cue that neurites do not readily cross on wider feature spacings. Importantly, biochemical directional cues are shown to be readily overcome when physical guidance cues are designed to have sufficiently narrow spacing at a given amplitude of 1.5  $\mu\text{m}$ . Designing prosthesis interfaces with physical cues that induce spatially organized neurite outgrowth even in the presence of conflicting biochemical cues will likely be necessary for *in vivo* applications with inherent biochemical signaling.

## Experimental

### Physical Patterns for Biochemical Border Studies

Methacrylate thin films were polymerized on functionalized glass slides to prevent polymer delamination and facilitate cellular microscopy studies. Standard microscope glass slides (2.54 cm x 7.62 cm x 0.1 cm) were functionalized with the silane coupling agent 3-(trimethoxysilyl)propyl methacrylate (Aldrich). Prior to treatment with the coupling agent, slides were first cleaned and oxidized with O<sub>2</sub> plasma for 3 min at 30 W RF power (PDC-001 Harrick Plasma Expanded Cleaner, Ithaca, NY) while under 300 mTorr vacuum. Following removal from the plasma chamber, slides were immersed in a 1/100 v/v solution of the silane coupling agent and n-hexane (Aldrich) overnight in a covered container at room temperature ( $\sim 21^\circ\text{C}$ ). Each slide was then rinsed with fresh hexanes and dried in the fume hood before being placed in a sealed container. Functionalized slides were used immediately as a substrate for polymerization.

All mixtures of hexyl methacrylate (HMA, Aldrich) with 1,6-hexanediol dimethacrylate (HDDMA, Aldrich) and were prepared with 1 wt% of 2,2-dimethoxy-2-phenylacetophenone (DMPA, BASF) as the photoinitiator. Copolymer compositions are

represented as whole numbers (e.g. 40/60, 50/50) but each polymer fraction is 0.5 wt% less to account for the photoinitiator. 20  $\mu\text{L}$  of pre-polymer solutions were pipetted onto the center of a functionalized slide then covered with a 2.54 cm x 2.54 cm x 0.1 cm glass-chrome Ronchi rule photomask (Applied Image Inc., Rochester, NY) for parallel patterns or with a cut untreated glass slide of the same dimensions for unpatterned samples. Capillary forces caused the formulations to spread evenly under the photomasks. Photopolymerization was carried out with a high-pressure mercury vapor arc lamp (Omnigore S1500, Lumen Dynamics, Ontario, Canada) at a 365 nm light intensity of 16  $\text{mW}/\text{cm}^2$ . The curing module was equipped with an 8 mm aperture x 50 mm length beam homogenizing fused silica light pipe (Edmund Optics) and a collimating lens (RLQ-1, Asahi Spectra). Light intensity was measured with a Cole-Parmer Series 9811 radiometer. Microfeature amplitude was tuned by shuttering UV radiation at specific times thereby preventing further initiation events and resulting in rapid termination of the polymerization. Following the set exposure time, the photomask was removed from the polymer and the sample was washed with 95% ethanol to remove residual surface monomer. Rinsed samples were then post-cured for 10 min under the same light source and intensity without the photomask and under ambient conditions to maximize monomer conversion without reducing surface channel amplitude due to trough back-filling.

#### Physical Micropattern Characterization

Micropattern feature spacing and depth were measured by white light interferometry (Dektak Wyko 1100 Optical Profiling System, Veeco). Feature amplitude was measured as the difference between a maximum ridge value and an adjacent minimum groove value. For each composition and exposure time, average feature height was determined by measuring channel amplitude in nine different areas across the surface ( $n \geq 3$ ). Feature spacing or periodicity was measured as the distance between the highest points on adjacent ridges and was consistent with photomask band spacing.

Measurements and 3D images were generated using Vision software associated with the instrument.

Micropattern morphology of each composition was further characterized by scanning electron microscopy (SEM, S-4800, Hitachi). Conductive silver paint was applied to the bottom of glass substrates modified with micropatterned methacrylate thin films for mounting on aluminum SEM stubs to acquire top-down images. For cross-sectional images, a glass etcher was used to etch the sample on the side opposite the thin polymer film and patterned polymers were then fractured and mounted vertically on specimen stages. The SEM specimen stage was rotated using automated stage and software controls. Each polymer surface was sputter coated with gold prior to examination by SEM. Electron accelerating voltage was set at 2 kV.

#### SGN and TGN Culture

Polymer substrates attached to glass slides were sterilized with 70% ethanol and UV irradiation and air-dried in a culture hood. Micropatterned surfaces were then coated sequentially with poly-L-ornithine (100 µg/ml) at room temperature and laminin (20 µg/ml) at 4 °C overnight. The following day, dissociated spiral ganglion (SG) cultures from P3-6 rat pups were prepared as previously described.<sup>39,40</sup> Dissociated cultures were plated with equal volumes of the cell suspension and maintained in a humidified incubator with 6.5% CO<sub>2</sub> for 48 hrs. The cultures were maintained in Dulbecco's Modified Eagle Medium (DMEM) supplemented with N2 additives, insulin, 5% fetal bovine serum, neurotrophin-3 (NT-3, 50 ng/ml) and brain derived neurotrophic factor (BDNF, 50 ng/ml).

SGN cultures were fixed with 4% paraformaldehyde at 4 °C for 20 min, permeabilized and blocked with 5% goat serum, 2% BSA, 0.1% Triton X in phosphate buffered saline (PBS), and immunostained with anti-neurofilament 200 (NF200) antibodies (1:400, Sigma-Aldrich) at 37 °C for 2 hrs, as previously described.<sup>39</sup> Alexa

488 conjugated secondary antibody (1:800, Invitrogen) was used to detect the primary antibody immunolabeling at room temperature for 1 hr. Slides were treated with ProLong Gold anti-fading reagent with DAPI (Life Technology) and sealed with nitrocellulose. Digital epifluorescent images were captured of the entire polymer surface using the scan slide application of Metamorph software (Molecular Devices, Silicon Valley, CA) on a Leica DMIRE2 microscope (Leica Microsystem, Bannockburn, IL) with a Leica DFC350FX digital camera.

Dissociated spiral ganglion (SG) cultures from P3-5 rat pups were prepared as previously described<sup>39,41</sup>. Trigeminal ganglion neuron (TGN) cultures were prepared by modification of the SG culture method. Briefly, pooled TG from P3-5 rat pups were dissociated with 0.125% trypsin and 0.1% collagenase for 45 min at 37°C, followed by gentle trituration through fire-polished glass pipettes.

#### Measurement of Neurite Behavior at Biochemical Borders

To characterize SGN and TGN neural outgrowth at biochemical borders, neurite responses were categorized into four distinct behaviors: cross, turn/parallel, repel, and stop. Neurites that extend greater than 10  $\mu\text{m}$  past the border after approaching it from the opposite side are scored as a cross (Fig 8.2A). Processes that reach and then subsequently reorient to align with the direction of the border are scored as turn/parallel (Fig. 8.2A). A neurite is scored as repel if it reaches the border and reverses back in the same direction, and as stop if it does not cross, turn, or repel after encountering the biochemical border

#### Statistics

Statistical analysis was performed using SigmaStat 3.5 software (Systat Software, Chicago, IL). Groups were compared by performing a one-way ANOVA followed by a

post hoc Kruskal-Wallis analysis of variance on ranks and a Dunn's Method or Tukey Test multiple comparison procedure. Results are statistically significant if  $p < 0.05$ .

## Results and Discussion

### Biochemical Borders on Micropatterned Polymers

To determine topographic feature dimensions that overcome contrary biochemical signaling, and to investigate the role of bioactive adhesion molecules on neurite alignment to physical micropatterns, biochemical borders of laminin, EphA4, and tenascin C were developed on photopolymerized topographies (Fig 8.1). Our labs previously demonstrated photopolymerization as an effective method to fabricate and tune topographic guidance cues appropriate for neural process contact guidance.<sup>27-29</sup> Specifically, pre-polymer formulations are exposed to UV light through a photomask. The formulations contain low concentrations of photoinitiator that absorbs UV light and subsequently undergoes photolytic cleavage to generate reactive free radical species. Radicals then react with methacrylate monomers, which are the precursor repeat units of the polymer chains. After reacting with a methacrylate monomer, the reaction propagates by continuously adding monomer units to form large polymer chains as well as crosslinks between chains resulting in a solid macromolecular network.

Selectively exposing the pre-polymer formulation to UV irradiance through a photomask inhibits local initiation events which slows polymerization rates beneath reflective bands of the mask. Consequently, raised features develop beneath transparent bands and surface depression form beneath reflective bands yielding a globally patterned substrate useful for cell-material interaction studies. For these studies, a photomask with parallel reflective and transparent bands was used to generate anisotropic ridge-groove topography to orient spiral ganglion neuron (SGN) and trigeminal neuron (TGN) neurite outgrowth. Feature repeat frequency, or periodicity, is controlled by the band spacing of

the photomask. Parallel micropattern periodicity is defined as the distance between repeat bands on the photomask, e.g. the start of one reflective band to the start of the next.

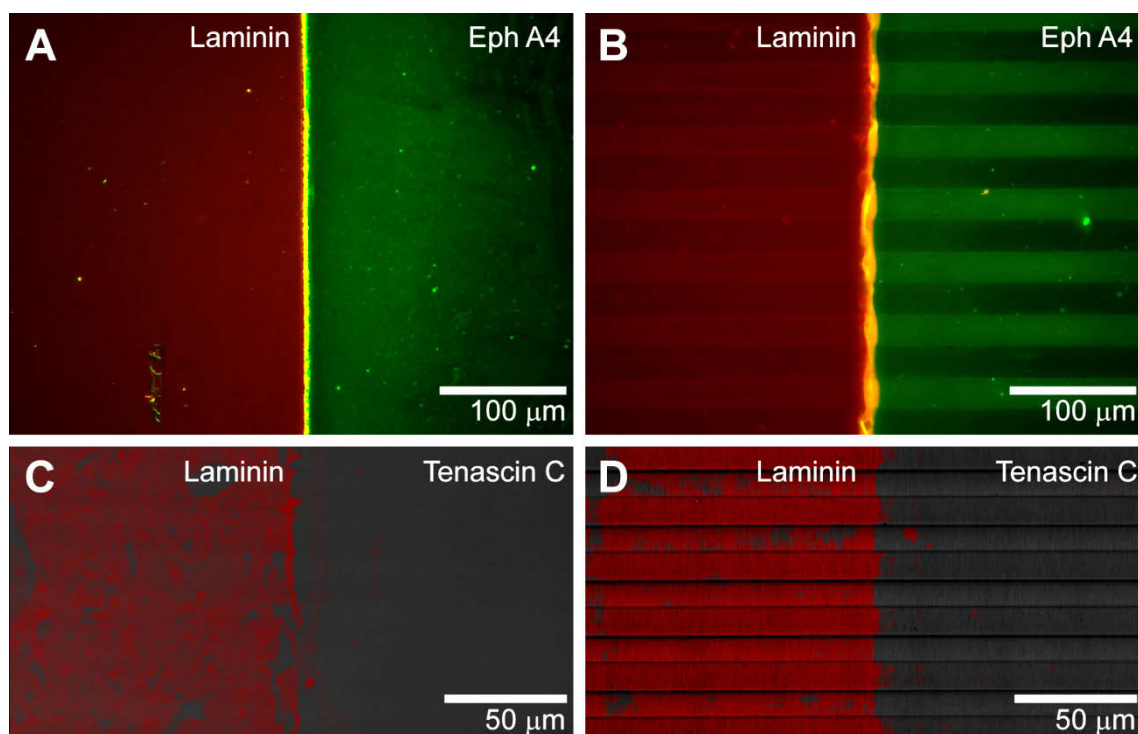


**Figure 8.1.** Fluorescence images of biochemical borders on unpatterned and micropatterned HMA-co-HDDMA polymers. Shown are chemical borders of laminin (red) and ephrin A4 (green) on unpatterned (A) and micropatterned (B) substrates, and of laminin (red) and tenascin C (no stain) on unpatterned (C) and micropatterned (D) substrates. The represented micropatterns have dimensions of 50  $\mu\text{m}$  periodicity and 1.5  $\mu\text{m}$  amplitude (B) and 20  $\mu\text{m}$  periodicity and 1.5  $\mu\text{m}$  amplitude (D). Borders were established by placing coverslips adjacently over respective protein solutions on polymer substrates. The yellow line in (A) and (B) is an artefact from mixed fluorescence at the border.

While feature periodicity is altered by photomask band spacing, feature depth or amplitude is precisely controlled on the micro- and nano-scale by modulation of photopolymerization parameters.<sup>28</sup> Because of light diffraction and reactive species

diffusion constraints, surface feature amplitude varies at a given irradiance exposure time for each periodicity. Accordingly, the temporal control of the photoinitiation event that is achieved by simple shuttering of the UV light source was used to generate  $1.5 \pm 0.2 \mu\text{m}$  amplitude features for each pattern periodicity. Unpatterned controls are generated by exposing photopolymer formulations to UV light beneath glass slides cut in the same dimensions as the photomask but devoid of reflective chrome plating.

Following the generation of unpatterned or micropatterned methacrylate thin-films, adsorbed biochemical borders are created on the surface to investigate their role in neurite pathfinding on physical guidance cues. To create biochemical borders, equal volumes of solutions with different bioactive species, e.g. one solution containing laminin and the other containing EphA4, are separately deposited on a methacrylate polymer surface. A glass coverslip for each solution is placed on the dispensed volume in such a way as to cover half of the polymer film while aligning adjacently to the other coverslip. Bioactive species solutions subsequently spread across the surface due to capillary forces between the glass coverslip and the methacrylate thin-film. A portion of the solubilized biochemical concentration from the solution remains adsorbed to photopolymer substrates following multiple wash steps as evidenced by immunofluorescence microscopy (Fig 8.1). Only a slight bleed was observed between coverslips for a given bioactive species indicating that the advancing growth cone of a neural process encounters a true chemical border rather than a gradient transition between the two bioactive species (Figs 8.1A,B). The adhesion modulating bioactive molecules used in this study all adsorb readily to unpatterned methacrylate films and also evenly coat photopatterned topography (Fig 8.1B,D).

To characterize SGN and TGN neural outgrowth at biochemical borders, neurite responses were categorized into four distinct behaviors: cross, turn/parallel, repel, and stop (Fig. 8.2). Neurites that extend greater than  $10 \mu\text{m}$  past the border after approaching it from the opposite side are scored as a cross (Fig 8.2A). Processes that reach and then

subsequently reorient to align with the direction of the border are scored as turn/parallel (Fig. 8.2A). Interestingly, neurites which grow parallel to the border in this manner must continue to cross multiple physical guidance cues oriented perpendicularly to the biochemical border. A neurite is scored as repel if it reaches the border and reverses back in the same direction, and as stop if it does not cross, turn, or repel after encountering the biochemical border (Fig 8.2) Previous work with photopolymerized micropatterns shows strong neurite alignment on features that are sufficiently steep.<sup>28</sup> In this study, a relatively shallow feature amplitude of 1.5  $\mu\text{m}$  was chosen as it would induce aligned neurite growth but still allow for neural process directional changes upon the encounter of biochemical signaling. Specifically, the physical neurite guidance stimulus is designed to be sufficiently weak to prevent masking of the influence that bioactive species have on neurite alignment to the micropatterns.

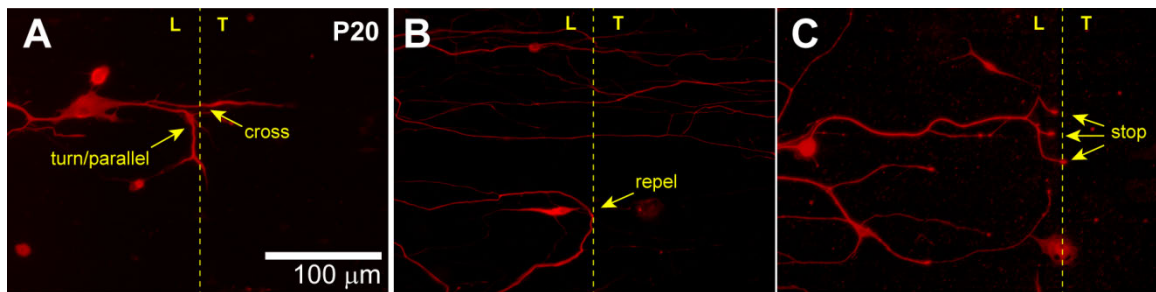


**Figure 8.2.** Immunofluorescence images of TGNs on photopolymerized methacrylate polymers. The images represent neurite behaviors quantified at biochemical borders on micropatterned substrates. **A-C** Neurite cross, turn/parallel (A), repel (B), and stop (C) behaviors are shown. The biochemical border between laminin and tenascin C is represented as a yellow dashed line. Regions coated with laminin and tenascin C are demarcated with a yellow L and T, respectively. Dissociated TGNs are stained with fluorescent anti-NF200 antibody (red). Immunofluorescence of adsorbed biochemical is not shown to facilitate identification of neurite behavior. The pattern for each image is set horizontally and has a periodicity of 20  $\mu\text{m}$  and a channel amplitude of 1.5  $\mu\text{m}$ .

### SGN Neurite Behavior at Laminin-EphA4 Borders

To investigate the role of adhesion modulating biomolecules on neurite guidance, dissociated SGNs were cultured on unpatterned and micropatterned thin-films that were coated with laminin and EphA4 (Fig 8.3). The temporal and spatial control of photopolymerization were utilized to generate micropatterns that have a channel amplitude of 1.5  $\mu\text{m}$  and a periodicity ranging from 10 to 50  $\mu\text{m}$  based on photomask band spacing. Micropatterned HMA-co-HDDMA was subsequently coated with laminin on one half of the substrate and with EphA4 on the other half using the coverslip method previously discussed. Laminin is an extra cellular matrix (ECM) glycoprotein present in all connective tissue of the body that facilitates cellular adhesion by binding to trans-membrane integrins which anchor the cell to its surface.<sup>42-44</sup> EphA4 is expressed in the developing cochlea and has been identified as a chemo-repulsive signal to SGN neurite outgrowth unless expression of the adhesion mediating ephrin-B2 and -B3 is inhibited.<sup>45</sup> The expression of EphA4 is greatest from cells along the osseous spiral lamina which is significant as SGN neurites must pass this through this region to provide afferent innervation of hair cells in the organ of Corti.<sup>46,47</sup> Due to the significant influence of EphA4 on *de novo* SGN neurite growth, it is important to understand how it affects neurite alignment to physical cues as both types of signals are likely involved in inner ear histogenesis. Furthermore, understanding its effects on neurite alignment to topographical guidance may enable the use of EphA4 in patterning applications that direct the development of neural networks or spatially organize neural process outgrowth to improve tissue integration of neural prostheses. It may also be advantageous to identify topographic features that overcome repulsive biochemical cues in the native neural niche to prevent problematic disruption of spatially directed neurite growth.

After coating the photopolymerized micropattern polymers with both laminin and EphA4, dissociated SGNs were cultured on the substrate surface for 72 hrs in neurotrophic media. SGNs were stained with fluorescent NF200 antibody to enable

characterization of outgrowth behavior at the biochemical border between laminin and EphA4 for both unpatterned and micropatterned polymers. SGN neurite outgrowth on unpatterned substrates extends randomly on both laminin and EphA4 coated regions (Fig 8.3A). Though EphA4 has previously been identified as a repulsive cue, dissociated SGNs cultured solely on the EphA4 coated region displayed robust *in vitro* culture behavior and neurite outgrowth with no obvious visual differences between SGNs cultured on the laminin coated region. In contrast to wandering SGN neurite growth on unpatterned substrates, neural processes strongly aligned to parallel ridge-groove topographies generated by photopolymerization with the greatest alignment occurring on patterns with the narrowest feature spacing, i.e. low periodicity (Fig 8.3B,C).

SGN neurites that originate on the laminin coated side and encounter the laminin-EphA4 border on unpatterned polymers extend across the border to the EphA4 side only 31% of the time demonstrating the chemo-repulsive influence of EphA4 (Fig 8.3D). The proportion of neurites crossing from the laminin coated to EphA4 coated regions increases significantly when SGNs are presented with mild physical guidance cues. Specifically, when SGNs are cultured on 50  $\mu\text{m}$  periodicity and 1.5  $\mu\text{m}$  amplitude parallel ridge-groove patterns the neurites are induced to cross the biochemical border to the EphA4 side 20% more often than on the unpatterned substrates with a frequency of nearly 50%. It should be noted that the aspect ratio, i.e. height divided by width, of the 50  $\mu\text{m}$  periodicity pattern is extremely low indicating that *de novo* neurite growth is quite sensitive to even subtle changes in surface topography. A slight increase in biochemical border crossing is observed when using increasingly narrow features with both 33  $\mu\text{m}$  and 20  $\mu\text{m}$  periodicity patterns inducing 56% of the neurites that encounter the border from the laminin side to the EphA4 side. Interestingly, a substantial increase in biochemical border crossing is observed when neurites are challenged with a 10  $\mu\text{m}$  periodicity pattern. Nearly 90% of the SGN neural processes cross to the EphA4 surface

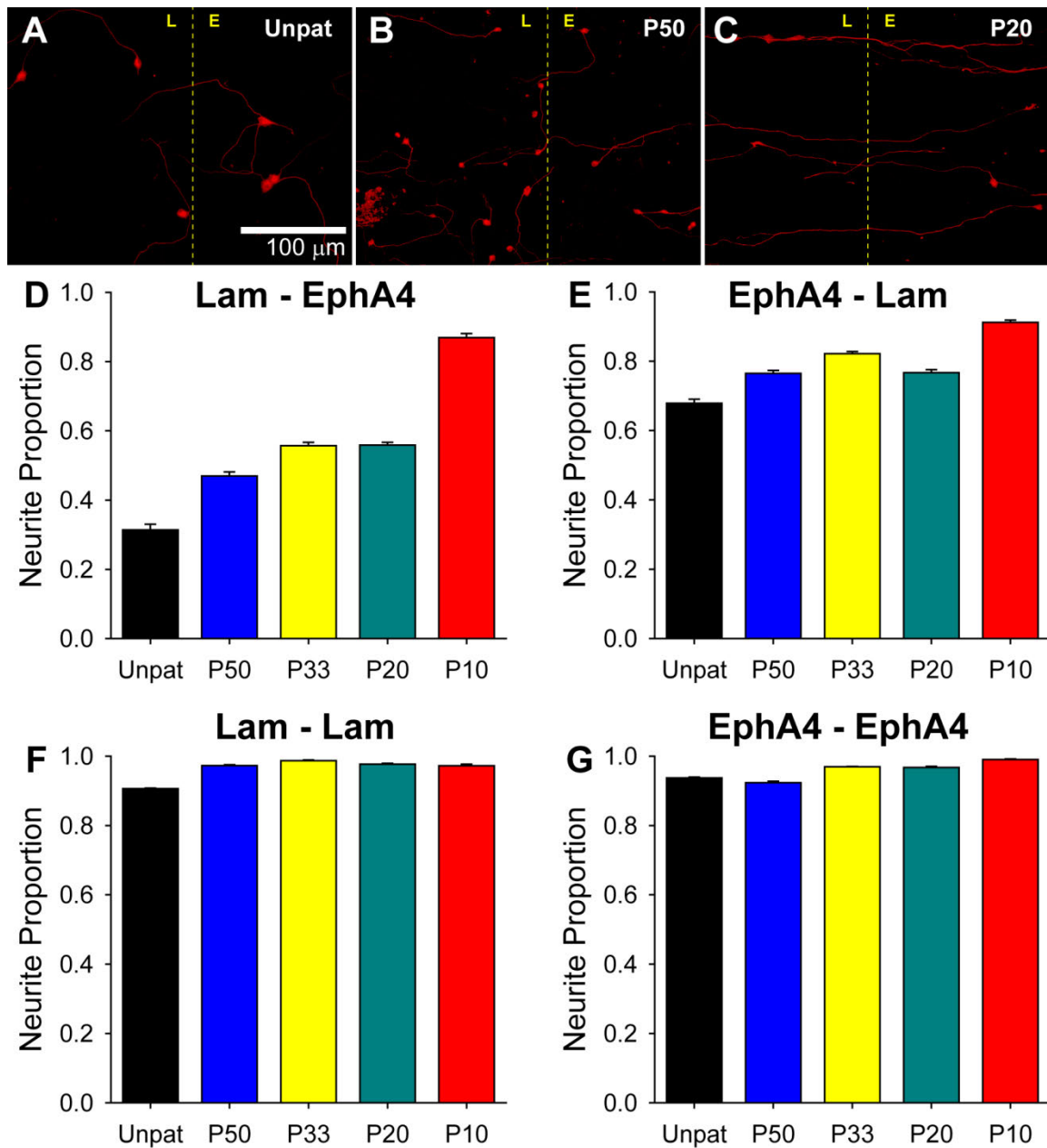


**Figure 8.3.** SGN neurite crossing behavior at the biochemical border between laminin (Lam) and EphA4 on micropatterned polymer substrates. **A-C)** Immuno-fluorescence images of dissociated SGNs cultured on unpatterned (A), 50  $\mu\text{m}$  periodicity (P50) (B), and 20  $\mu\text{m}$  periodicity (P20) (C) parallel micropattern substrates. SGNs are stained with fluorescent NF200 antibody. The biochemical border is marked with a dashed yellow line and the laminin and EphA4 sides are marked with a yellow L or E, respectively. **D-F)** Proportion of scored neurites that cross the biochemical border from laminin to EphA4 (D), from EphA4 to laminin (E), from laminin to laminin (F), and from ephrin A4 to ephrin A4. SGN neurites cross the biochemical border significantly more when cultured on patterns with narrow features (i.e. low periodicities) compared to unpatterned

Figure 8.3. Continued.

substrates and wide features. Neurites are much more likely to cross from ephrin A4 coated substrate to a laminin coating than from laminin to ephrin A4 even on unpatterned surfaces. All patterned substrates have a microfeature amplitude of 1.5  $\mu\text{m}$ .

from the laminin surface while influenced by microfeatures that are more frequent and steep compared to larger periodicity patterns. The strength of the EphA4 repulsive signal can be expressed or represented as the 70% of neurites it prevents from crossing the border on unpatterned polymers. Furthermore, the strength of the underlying physical cue is represented by the difference between the proportion of neurites that cross on the 10  $\mu\text{m}$  periodicity compared to the unpatterned control for a guidance strength of 56%. These results inspire confidence that physical cues can be designed to overcome strong chemo-repulsive cues that could disrupt spatially organized neural regeneration for *in vivo* applications. Moreover, EphA4 could also be used in conjunction with physical cues to strengthen the alignment affect.

The bioactive function of laminin and EphA4 becomes more apparent when comparing SGN process behavior encountering the biochemical border in the reverse order, i.e. from the EphA4 to the laminin coated region (Fig. 8.3E). When comparing neurite populations on unpatterned surfaces a clear preference for laminin adhesion is observed. For SGN neural processes that reach the biochemical border from the EphA4 coated side, 68% readily cross without any other additive guidance cue which is a nearly 40% increase in neurite crossing compared to the opposite transition on unpatterned substrates. As seen with the laminin to EphA4 transition, micropatterns with relatively wide but shallow features increase neurite crossing by approximately 10 – 12% with no significant differences in neurite crossing between the 50, 33, and 20  $\mu\text{m}$  periodicity patterns. An even greater proportion of neurites are induced to cross the biochemical border when presented with a 10  $\mu\text{m}$  periodicity pattern. It appears that the guidance

strength of the physical pattern is not diminished by either bioactive signal presented at the biochemical border as 90% of the neurite population cross the border while approaching it from either side.

To determine if the observed neurite behavior was due to the bioactive function of either laminin or EphA4 at the biochemical border rather than random process growth, SGN neurite behavior was characterized at arbitrary borders made on regions coated with only one bioactive species, i.e. a laminin to laminin or EphA4 to EphA4 border (Fig 8.3F,G). Accordingly, the neuronal soma and the entire length of the SGN neurite were on regions coated only with laminin or EphA4. In both cases, the most striking difference between neurite behavior at the biochemical border of laminin and EphA4 and laminin-laminin and EphA4-EphA4 borders occurs on unpatterned methacrylate thin films. The neurite proportion crossing the biochemical border between the two bioactive species is less than 50% whereas on borders with the same species on either side greater than 90% of the neurites readily cross.

The crossing proportion slightly increases at both borders when neurites are presented with topographical guidance cues. The increase is attributed to greater incidence of neurite growth in a direction that is perpendicular to the biochemical border which increases the chances that a neural process will be observed to cross. It should also be noted that the largest proportion of neurites to cross from laminin to EphA4 or its reverse is 90% whereas the largest proportion of crossing neurites on laminin-laminin and EphA4-EphA4 borders is 97% and 99%, respectively. For all border types, the highest incidence of neurite crossing occurs on 10  $\mu\text{m}$  periodicity micropatterns. It is likely that the observed 10% discrepancy between hetero and homogenous bioactive species borders is due to chemo-repulsion from the adhesion modulating molecules. Even when extending from the repulsive EphA4 cue to the adhesive laminin cue, neurites are less likely to cross the biochemical border than on homogenous transitions.

In addition to neurite crossing behavior at biochemical borders, neurite turn, repel, and stop responses further elucidate neural pathfinding behavior when processes are presented with physical guidance cues of various strengths (Fig 8.4). For example, the remaining 70% of neurites that do not cross the biochemical border on unpatterned, laminin coated substrates are observed to split relatively evenly between the described turn, repel, and stop behaviors (Fig 8.4A). By contrast, SGN neurites that are presented

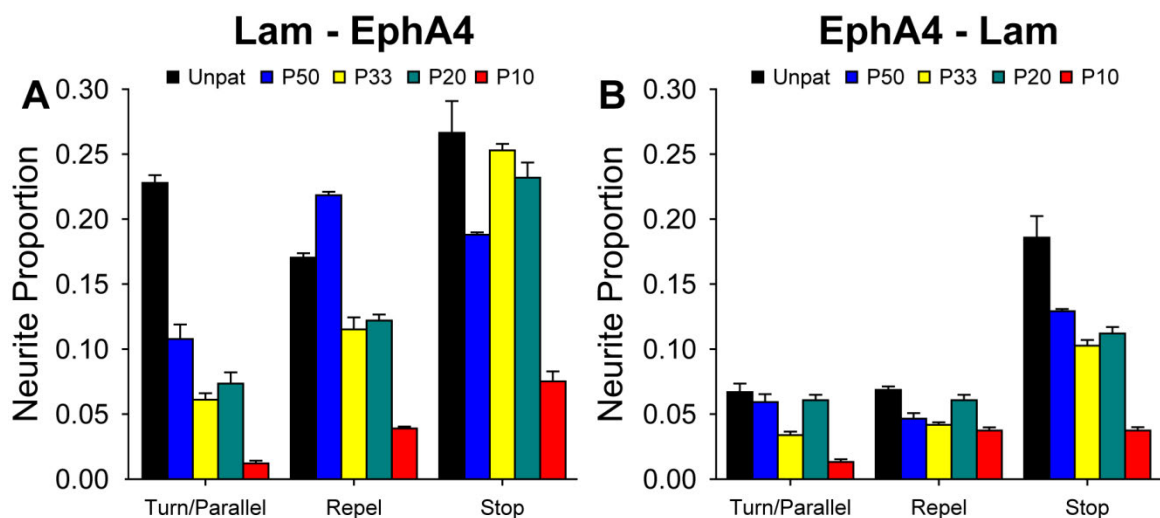


**Figure 8.4.** Non-crossing SGN neurite behavior at the biochemical border between laminin (Lam) and ephrin A4 (EphA4) on micropatterned polymers. A,B) Proportion of scored neurites that exhibit turn/parallel, repel, and stop behaviors when approaching the biochemical border starting from the laminin (A) and ephrin A4 (B) sides, respectively. All patterned substrates have a microfeature amplitude of 1.5  $\mu\text{m}$ .

with physical guidance cues are much more likely to be repelled by or to stop at the border compared to unpatterned controls. The trend to repel or to stop at the border on micropatterned substrates increases with increasing feature frequency for neurites that originate on the laminin coated side (Fig 8.4A). As previously mentioned, the guidance strength of the photopolymerized topographic cues increases with decreasing pattern

periodicity as evidenced qualitatively by immunofluorescence images (Fig. 8.3A-C) and quantitatively by increased SGN neurite crossing of repulsive biochemical cues (Fig. 8.3D,E). The relative increase in the proportion of neurites that is repelled or stopped at border on micropatterned substrates is, therefore, most likely due to the inhibition of neurite turning on physical guidance cues. In other words, significant reduction of turning behavior increases the relative percentage of neurites for the other scored behaviors. Interestingly, for almost all pattern types as well as unpatterned samples, the most common SGN neurite behavior, other than crossing, is to stop after encountering the biochemical border. It is unclear whether the observed stop behavior is due to an actual arrest in neurite outgrowth or if advancing neural growth cones are induced to pause at the biochemical border before transitioning to cross, turn, or repel behavior. A pause or a lag-time in neurite outgrowth at the bioactive border would lead to more frequent capture of the neurite terminus there during immunofluorescence microscopy and increase the frequency of the neurite stop characterization. However, if the rate of neurite growth is not decreased at the border then the actual stop behavior is the most common neural process outcome other than crossing. Stopping *de novo* neurite outgrowth at spatially specific electrodes is identified as a significant obstacle to improving neural prosthetic performance and tissue integration.<sup>1,2</sup> Accordingly, designing material interfaces with biochemical stopping cues that work in conjunction with topographic patterning may potentially provide the necessary guidance as well as stopping signals if appropriately designed for a given neural niche.

The proportion of SGN neurites that do not cross from the EphA4 to the laminin coated side is significantly smaller than the proportion that does not cross the opposite transition (Fig. 8.4B). Accordingly, SGN neurite proportions for this group are all below 20%. Even for the small proportion of non-crossing neurites that meet the biochemical border from the EphA4 side, stopping behavior is still the most common response. For Unpatterned samples and for patterns with periodicities between 20 and 50  $\mu\text{m}$ , the

frequency of stopping behavior doubles from around 5% to 10% or higher. It is likely that a higher incidence of stop behavior would be observed on patterns with a 10  $\mu\text{m}$  periodicity if there wasn't such a large proportion ( $> 90\%$ ) that were induced to cross the border due to the guidance strength of the topographic surface features. SGN non-crossing neurite behavior was not scored on homogeneous chemical borders as the vast majority of neurites ( $> 95\%$ ) are observed to cross the border leaving prohibitively few neurites to be scored for other behaviors.

#### SGN Neurite Behavior at Laminin-TnC Borders

To further elucidate the role of adhesion modulating biomolecules on neurite guidance, and to compare neurite process growth when presented with two cues that are not identified as chemo-repulsive, dissociated SGNs were cultured on unpatterned and micropatterned polymers coated with laminin and tenascin-C (TnC) (Fig 8.5). TnC, like laminin, is a modular or mosaic glycoprotein expressed in the ECM that moderates cellular adhesion.<sup>44</sup> TnC also resembles fibronectin, another ECM adhesion modulating protein, in that over half of the macromolecule consists of fibronectin type III repeat units. Fibronectin and TnC are also colocalized in many tissues, but TnC expression is usually uniquely restricted compared to other adhesion moderators.<sup>48</sup> TnC is known to be expressed transiently during development of organs and the nervous system.<sup>49,50</sup> The restricted and highly regulated expression of TnC has incited significant research interest in delineating its role in cell migration and differentiation, cell-cell interactions, and in tissue development.

Precise micropattern morphology was fabricated for laminin-TnC border experiments using the temporal and spatial control of photopolymerization as previously discussed for fabrication of substrates used in laminin-EphA4 studies. Briefly, feature depth was again tuned to an amplitude of 1.5  $\mu\text{m}$  by controlling UV exposure time, and the same periodicity range of 10 to 50  $\mu\text{m}$  was developed by utilizing photomasks with

the same band spacing to facilitate neurite behavior comparisons with laminin-EphA4 results. Unpatterned and micropatterned HMA-co-HDDMA polymers were subsequently coated with laminin on one half of the substrate and with TnC on the other half using the adjacent coverslip method. Due to the importance of TnC in during histogenesis, and specifically during development of the nervous system, it will likely be significantly important to determine its effects on the spatial organization of *de novo* neurite outgrowth. In particular, as neural prosthetics exhibit poor tissue integration with remaining neural networks, using or overcoming biochemical cues from adhesion modulators such as laminin, EphA4, TnC will likely be part of future device designs that precisely guide the neural outgrowth towards specific stimulating elements of a prosthesis.

After coating the photopolymerized micropattern polymers with both laminin and TnC, dissociated SGNs were cultured on the substrate surface for 72 hrs in neurotrophic media. SGNs were stained with fluorescent NF200 antibody to enable characterization of outgrowth behavior at the biochemical border between laminin and TnC for both unpatterned and micropatterned polymers. Initial, qualitative observations of SGN neural process outgrowth illustrate similar trends seen for neurite extension on substrates modified with laminin-EphA4 chemical borders. Namely, process outgrowth spreads randomly on unpatterned, photopolymerized methacrylate substrates coated either with laminin or with TnC (Fig 8.5A). Further, SGN neurite direction became increasingly aligned with anisotropic uni-directional microfeatures as pattern periodicity decreased (Fig 8.5B,C). Also like the laminin-EphA4 system, SGN soma and neural processes appear healthy and similar whether growing solely on laminin or TnC coatings following *in vitro* culture.

However, in contrast to observed behavior on laminin-EphA4 substrates, SGN neurite crossing of the laminin-TnC border, originating from the laminin coated side, is substantially lower for both unpatterned and patterned substrates (Fig 8.3D,E and Fig

8.5D,E). The proportion of neurites that transitions across the biochemical border on unpatterned substrates is 10% lower than that seen for laminin to EphA4 transitions. Only 21% of SGN neurites that originate on laminin coated substrate cross to the TnC coated region. Furthermore, neurite crossing of laminin-EphA4 borders increases substantially when dissociated SGNs are cultured on 1.5  $\mu\text{m}$  amplitude and 50  $\mu\text{m}$  periodicity photopolymerized topographic guidance cues – going from a 31% cross rate to nearly 50%. Remarkably, SGNs presented with the same microfeature dimensions exhibit only a 4% average increase, which is not statistically significant, in crossing of the biochemical border when transitioning from laminin to TnC. The proportion of SGN neurite crossing of the laminin-TnC border remains lower than 40% on both 33 and 20  $\mu\text{m}$  feature periodicities, though the trend of increased border crossing at narrower periodicities becomes evident on 20  $\mu\text{m}$  periodicity micropatterns. The guidance strength of topographical surface cues is even more evident on 10  $\mu\text{m}$  periodicity features as greater than 60% of neurites which reach the laminin-TnC border are induced to cross despite the strength of the biochemical border that prevents crossing on patterns with wider features and on unpatterned controls. While TnC has many similarities with other adhesion modulating ECM proteins such as laminin and fibronectin, it is apparent that its function to moderate cellular adhesion is functionally quite different than direct adhesion promoters of a similar modular protein class.<sup>9</sup> Interestingly, TnC appears to affect neural adhesion in such a way to act as a stronger chemo-repulsive cue than EphA4 which has previously been demonstrated as a known repulsive cue to SGN process outgrowth.<sup>45</sup>

SGN neurites cross from TnC to laminin coated regions significantly more than going from laminin to TnC (Fig 8.5D,E). However, the difference in neurite crossing is only observed for physically patterned samples. On unpatterned substrates, the extent of SGN neurite biochemical border crossing is nearly identical with 21% of neurites making the transition. With the widest periodicity micropattern, and therefore the weakest physical guidance strength, neurite crossing proportion increases nearly two fold to 37%

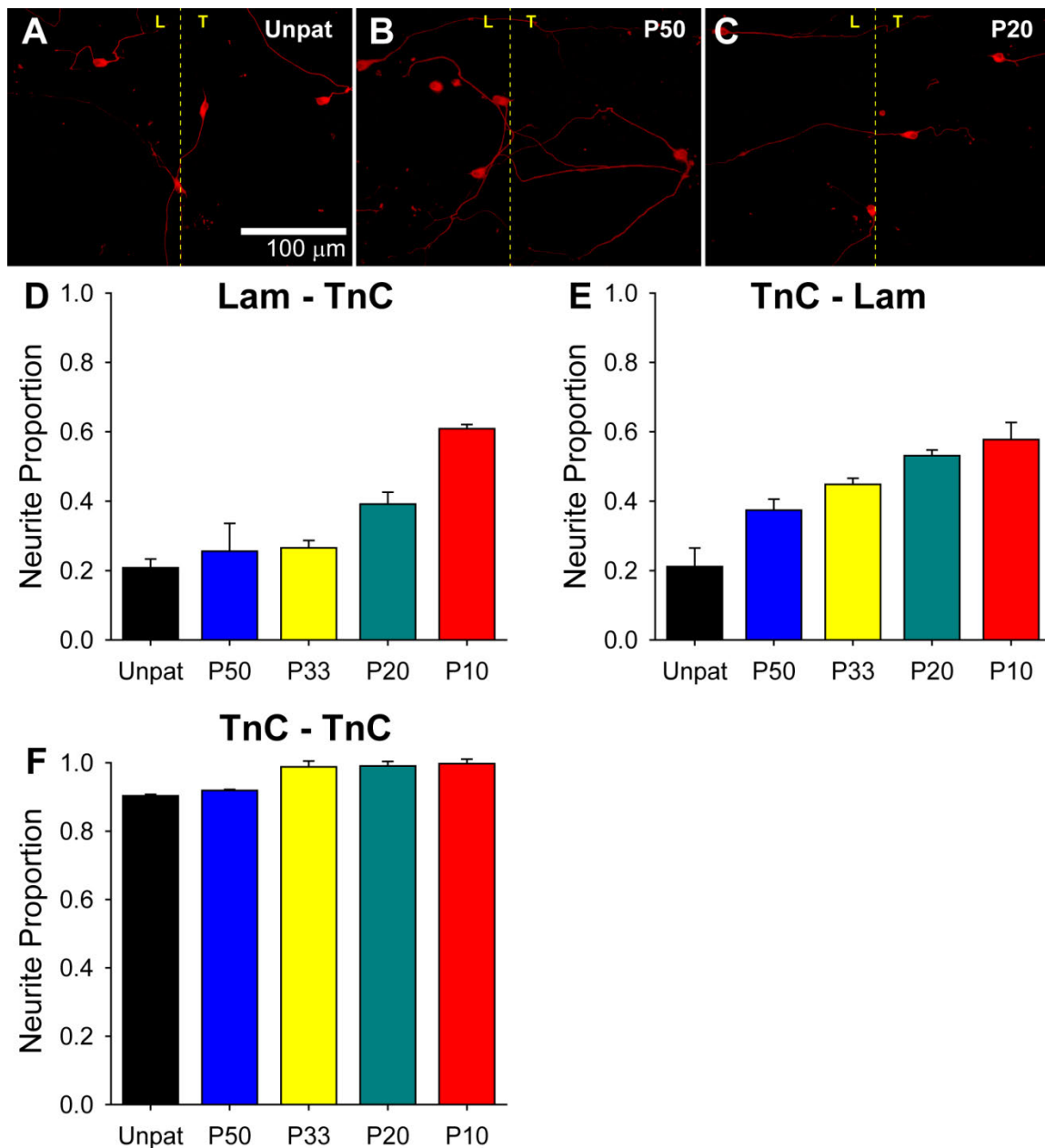


**Figure 8.5.** SGN neurite crossing behavior at the biochemical border between laminin (Lam) and tenascin C (TnC) on micropatterned polymer substrates. **A-C)** Immunofluorescence images of dissociated SGNs cultured on unpatterned (A), 50  $\mu\text{m}$  periodicity (P50) (B), and 20  $\mu\text{m}$  periodicity (P20) (C) parallel micropattern substrates. SGNs are stained with fluorescent NF200 antibody. The biochemical border is marked with a dashed yellow line and the laminin and tenascin C sides are marked with a yellow L or T, respectively. **D-F)** Proportion of scored neurites that cross the biochemical border from laminin to tenascin C (D), from ephrin A4 to laminin (E), from laminin to laminin (F), and from ephrin A4 to ephrin A4. SGN neurites cross the biochemical border significantly more when cultured on patterns with narrow features (i.e. low periodicities)

Figure 8.5. Continued.

compared to unpatterned substrates and wide features. Neurites are much more likely to cross from ephrin A4 coated substrate to a laminin coating than from laminin to ephrin A4 even on unpatterned surfaces. All patterned substrates have a microfeature amplitude of 1.5  $\mu\text{m}$ .

which did not occur for neurite making the opposite transition. Moreover, the proportion of neurites that cross from TnC to laminin coated substrate on 33 and 20  $\mu\text{m}$  periodicity patterns is also significantly higher at 45% and 53% compared to 27% and 39% respectively for laminin to TnC transitions. The trend demonstrating the increasing guidance strength of the underlying physical cues is more readily discernable for TnC to laminin crossing as the average neurite proportion that extends across the border increases with each decrease in pattern periodicity. While SGN neurites are increasingly likely to cross from TnC to laminin coated substrate with narrower features, it is noteworthy to observe that the proportion of SGN neurites that are induced to cross the biochemical border by 10  $\mu\text{m}$  periodicity patterns is nearly the same (~60%) for laminin to TnC crossings as for the opposite transition. Therefore, TnC does not necessarily act as a repulsive cue *per se* as initially implicated by the laminin-TnC results. Rather, TnC may sufficiently alter intracellular biochemical signaling as to strongly inhibit the transition of the neural growth cone either going to or from TnC coated regions.

The strength of the biochemical repulsive signal at the laminin-TnC border can be expressed or represented as the 80% of neurites it prevents from crossing on unpatterned polymers. Similarly, the guidance strength of the underlying surface topography is represented by the difference between the proportion of neurites that cross on the 10  $\mu\text{m}$  periodicity compared to the unpatterned control for a guidance strength of approximately 40% approaching the biochemical border from either direction. As with the laminin-EphA4 results, these data engender confidence that micropattern topography can be

devised to overcome chemical cues that may prevent spatially organized neurite growth for improved neural prosthetic tissue integration.

Culture of dissociated SGNs on TnC alone does not substantially alter neurite pathfinding behavior as evidenced by cross results on homogeneous TnC-TnC borders (Fig 8.5F). SGN neurites cross the homogenous border with a frequency greater than

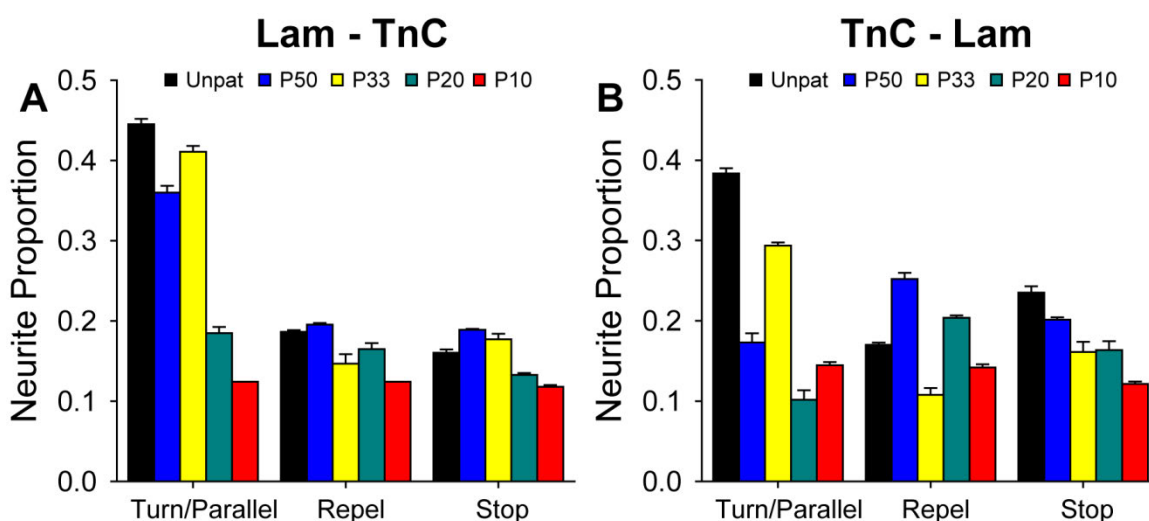


**Figure 8.6.** Non-crossing SGN neurite behavior at the biochemical border between laminin (Lam) and tenascin C (TnC) on micropatterned polymers. **A,B)** Proportion of scored neurites that exhibit turn/parallel, repel, and stop behaviors when approaching the biochemical border starting from the laminin (A) and tenascin C (B) sides, respectively. All patterned substrates have a microfeature amplitude of 1.5  $\mu\text{m}$ .

90% for all patterned conditions and for unpatterned controls. As with laminin-laminin and EphA4-EphA4, the proportion of neurites that cross TnC-TnC borders increases for SGNs presented with anisotropic photopolymerized guidance cues. For 33, 20, and 10  $\mu\text{m}$  periodicity patterns SGN neurite crossing reaches an average of 99% indicating that TnC does not interfere with neural process growth cone guidance response to physical features.

Along with neural process crossing behavior at the laminin-TnC biochemical border, investigating neurite turn, repel, and stop responses increases understanding of SGN neurite pathfinding behavior when challenged with physical guidance cues (Fig 8.6). As previously described, the most common neurite behavior besides crossing for the laminin-EphA4 system is stopping at the biochemical border. However, for laminin-TnC coated substrates, the most common neurite response, for all substrates other than 10  $\mu\text{m}$  periodicity patterns, is not to cross. This behavior is particularly evident on unpatterned substrates as 45% out the remaining 60% of non-crossing neurites turn to parallel the pattern when reaching the biochemical border from the laminin coated side. Similarly, from the TnC coated side, 38% out of the remaining 60% of non-crossing neurites also turn to parallel or align to the biochemical border.

Even the majority of non-crossing SGN neurites challenged with physical guidance cues on 50 and 33  $\mu\text{m}$  periodicity turns at and aligns to the direction of the laminin-TnC border for neurites originating on the laminin side (Fig 8.6A). For the 20 and 10  $\mu\text{m}$  periodicity patterns, the neurite behavior appears to be random as there are even distributions between turn, repel, and stop responses. SGN neurites that meet the TnC-laminin border from the the TnC side do not exhibit any behavioral trends, other than the high proportion of turning on unpatterned and 33  $\mu\text{m}$  periodicity samples, as the neurite distribution spreads relatively evenly among the characterized responses (Fig 8.6B).

The significant tendency for SGN neurites to stop at the biochemical border on laminin-EphA4 coated substrates is markedly diminished on laminin-TnC borders (Fig 8.4 and Fig 8.6). While stops still occur in at least 10% of the neurite population for each type of substrate, the proportion of neurite stops for each population does not make up the largest non-crossing proportion for any condition. Contrasted with EphA4 coated substrates, TnC either does not cause the proposed pause in neurite growth that leads to increased capture stopping behavior, or it does not arrest neural process extension as may

be occurring with EphA4. The strong disruption in SGN neurite crossing of the biochemical border, even for neurites on effective physical guidance cues, suggests that transitioning from either bioactive species to the other on laminin-TnC substrates is a significant obstacle for advancing neural growth cones. Substantial increases in neurite turning and repeling behavior compared to neurite stopping further support this observation as neurites that turn or repel remain anchored to whichever adhesion modulator on which they originated.

#### TGN Neurite Behavior at Laminin-TnC Borders

SGNs are the target neural element to be stimulated by the cochlear prosthesis. Due to their importance in neural prosthetics, their pathfinding behavior in relation to biophysical and biochemical cues is the principal focus of these studies. To determine whether SGN pathfinding behavior is typical for other neuronal types and to verify if the demonstrated results are more broadly applicable to other neural pathfinding work, dissociated trigeminal neurons (TGNs) were also cultured on unpatterned and micropatterned substrates modified with laminin-TnC borders as a comparison to SGNs (Fig 8.7). Qualitative observations of TGN neurite outgrowth by immunofluorescence microscopy demonstrate similar neural pathfinding behavior as SGN neurite growth on laminin-TnC coated unpatterned and photopatterned polymer films (Fig 8.7A-C). Specifically, TGN neurite extension proceeds randomly on unpatterned HMA-co-HDDMA films on both laminin and TnC coated areas (Fig 8.5A). Further, on unidirectional photopolymerized micropatterns, TGN neurite extension increasingly parallels microfeature anisotropy as pattern periodicity decreases (Fig 8.7B,C). Like SGNs on EphA4 or TnC, TGN neural processes and cell bodies are observed to exhibit normal *in vitro* culture behavior while adhered solely to either laminin or TnC coated regions.

TGN neurite crossing behavior at the biochemical border of laminin and TnC on both unpatterned and physically patterned polymer substrates strongly resembles SGN

neural pathfinding (Fig 8.5 D,E and Fig 8.7 D,E). The substantial similarities observed between the two neuronal types indicate that SGN neural process pathfinding behavior in

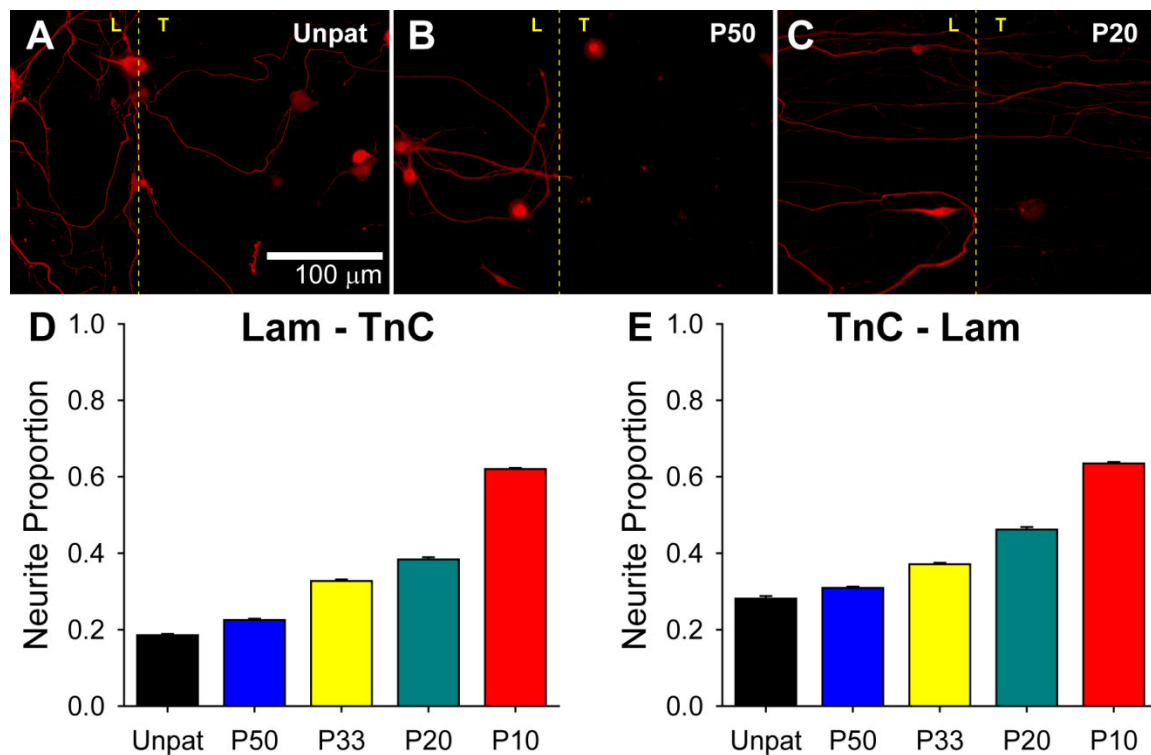


**Figure 8.7.** TGN neurite crossing behavior at the biochemical border between laminin (Lam) and tenascin C (TnC) on micropatterned polymer substrates. **A-C)** Immunofluorescence images of dissociated SGNs cultured on unpatterned (A), 50 μm periodicity (P50) (B), and 20 μm periodicity (P20) (C) parallel micropattern substrates. TGNs are stained with fluorescent NF200 antibody. The biochemical border is marked with a dashed yellow line and the laminin and tenascin C sides are marked with a yellow L or T, respectively. **D-F)** Proportion of scored neurites that cross the biochemical border from laminin to tenascin C (D) and from tenascin C to laminin (E). TGN neurites cross the biochemical border significantly more when cultured on patterns with narrow features (i.e. low periodicities) compared to unpatterned substrates and wide features. All patterned substrates have a microfeature amplitude of 1.5 μm.

response to both biochemical and biophysical cues, as presented in this work, informs and enables future work aimed to spatially direct *de novo* neurite outgrowth. On

unpatterned methacrylate substrates, TGN neurites do not readily cross the laminin-TnC border from either bioactively coated side. Though, the frequency to cross over to the laminin side is higher than the reverse transition with 28% and 19% crossing, respectively.

As observed for SGN neurite extension, the extent of TGN neurite crossing of the biochemical border increases substantially as neurites are presented with physical guidance cues. However, the weakest physical cue, a 50  $\mu\text{m}$  periodicity pattern and a 1.5  $\mu\text{m}$  amplitude provides only negligible change with a 4% and 2% increase in neurite crossing proportion when originating on either laminin or TnC coated sides, respectively. TGN neurite crossing of the laminin-TnC border remains lower than 40% on both 33  $\mu\text{m}$  and 20  $\mu\text{m}$  feature periodicities except for TGN neurites originating on the TnC coated side on 20  $\mu\text{m}$  periodicity substrates. As the topographical surface guidance strength increases on 10  $\mu\text{m}$  periodicity patterns, the majority of TGN neurites are induced to cross the laminin-TnC border when reaching it from either side. Similar to SGN behavior, 10  $\mu\text{m}$  periodicity features cause approximately 60% of neurites that encounter the border to cross despite the strength of the biochemical border that prevents crossing on patterns with wider features and on unpatterned controls. The observation that TnC, while similar to other ECM adhesion modulators, has unique function when moderating neural process adhesion is further confirmed by the strong repulsive behavior observed for both SGN and TGN neurite outgrowth (Fig 8.5 and Fig 8.7).

TGN neurites cross from TnC to laminin coated regions significantly more than going from laminin to TnC (Fig 8.7D,E). The proportion of neurites that cross from TnC to laminin coated substrate on 33 and 20  $\mu\text{m}$  periodicity patterns is significantly higher at 37% and 46% compared to 32% and 38% respectively for laminin to TnC transitions. Though TGN neurites more readily cross from TnC to laminin coated regions, there appears to be a sufficiently strong repulsive biochemical cue as to allow only 60% of

neurites to cross the border when approaching from either direction in spite of the favorable transition to laminin coated substrate.

Biochemical border repulsive signal strength at the laminin-TnC transition for TGN neurites can be expressed as the 70 – 80% neurite proportion that are prevented from crossing on unpatterned substrates (Fig 8.7D,E). Furthermore, maximum topographical surface contact guidance strength is represented by the difference between the proportion of neurites that cross on the 10  $\mu\text{m}$  periodicity patterns compared to unpatterned controls for a guidance strength of 44% and 35% for neurites on the laminin and TnC coated sides, respectively. The similarities of TGN crossing behavior with SGN crossing behavior on the same topographically patterned and bioactively coated substrates supports the conclusion that photopolymerized topographies can be designed to overcome contrary biochemical signals that could disrupt spatially organized neurite growth aimed to improve neural prosthetic tissue integration.

TGN neural process crossing behavior at laminin-TnC biochemical borders is observed to strongly match SGN neurite crossing behavior on the same topographies and bioactive species. To further explore TGN neural pathfinding behavior, and to compare it to observed SGN neural outgrowth, non-crossing TGN neurite responses were measured as turn, repel, and stop responses when challenged with both biochemical and biophysical guidance cues (Fig 8.8). Due to the repulsive strength of the laminin-TnC border presented to TGN neurites, neurite crossing behavior does not describe the majority of neurite behavior unless TGNs are cultured on patterns with the strongest physical guidance cues (Fig 8.7D,E). Like SGN neurites, on unpatterned substrates and on micropatterns with weak guidance strength the most prominent TGN neurite behavior is to turn and align to the border direction. Great than 40% align to the border, rather than cross, for neurites that approach the border from the laminin side and greater than 30% behave similarly when reaching the biochemical transition from the TnC side (Fig 8.8). The 10% discrepancy in turning is likely due to increased favorability of TGN neuronal

adhesion to laminin compared to TnC. However, the chemo-repulsive affect is substantial for unpatterned substrates and for pattern that have topographic cues with weak guidance strength as less than 30% of neurites cross for either condition and approaching the border from either direction.

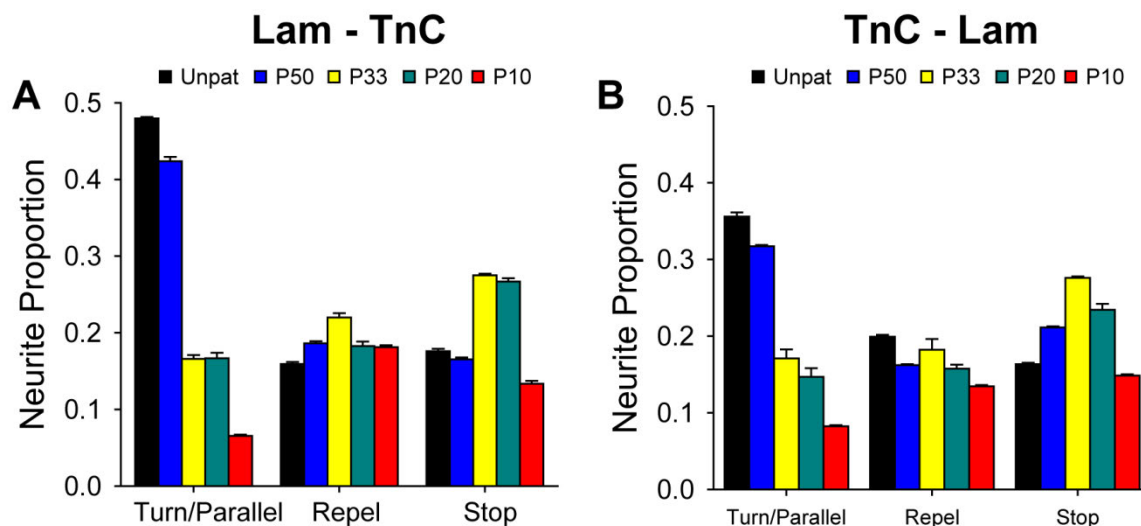


**Figure 8.8.** Non-crossing TGN neurite behavior at the biochemical border between laminin (Lam) and tenascin C (TnC) on micropatterned polymers. **A,B)** Proportion of scored neurites that exhibit turn/parallel, repel, and stop behaviors when approaching the biochemical border starting from the laminin (A) and tenascin C (B) sides, respectively. All patterned substrates have a microfeature amplitude of 1.5  $\mu\text{m}$ .

Even the majority of non-crossing SGN neurites challenged with physical guidance cues on 50 and 33  $\mu\text{m}$  periodicity turns at and aligns to the direction of the laminin-TnC border for neurites originating on the laminin side (Fig 8.6A). For the 20 and 10  $\mu\text{m}$  periodicity patterns, the neurite behavior appears to be random as there are even distributions between turn, repel, and stop responses. SGN neurites that meet the TnC-laminin border from the the TnC side do not exhibit any behavioral trends, other than the high proportion of turning on unpatterned and 33  $\mu\text{m}$  periodicity samples, as the

neurite distribution spreads relatively evenly among the characterized responses (Fig 8.6B). TGN neurites are also observed to have a relatively random distribution of scored non-crossing neurites behaviors other than the increase in turn and parallel behavior as observed for SGN neurites also on laminin-TnC substrates. Accordingly, only SGN neurites on laminin-EphA4 substrates are observed to show a marked increase in stopping behavior as physical pattern guidance strength increases. However, the proportion of neural processing stopping behavior does make up a larger percentage for TGN populations than for SGN populations on the same cues.

### Conclusions

As cells are known to respond to an assortment of physical as well as biochemical cues in their micro-environment, research presented in this work also elucidates appropriate physical microfeature dimensions which induce SGN neurite alignment across conflicting biochemical directional cues. Dissociated SGNs and trigeminal neurons (TGNs) were cultured on photopolymerized micropattern substrates coated with two species of bioactive molecules and neurite outgrowth and pathfinding behavior was characterized at the biochemical border between the species. Bioactive species utilized in the work include: laminin, an integrin binding glycoprotein that facilitates neuronal adhesion and process outgrowth; tenascin-C, an adhesion modulating glycoprotein that can modify cellular adhesion by binding molecules of a cell's extra cellular matrix; and ephrin A4 which is a protein kinase important in cell adhesion and migration as well as in neurite guidance. The adsorbed biochemicals formed a distinct border across each sample and neurite alignment was characterized at the border as cross, stop, turn, and repel behavior. SGN neurites readily crossed from ephrin A4 coated regions to laminin coated areas on all pattern types, but the extent of crossing for a given neuronal population significantly increased with increasing feature frequency. Neurites from SGNs and

trigeminal neurons were also observed to cross a laminin-tenascin C biochemical border when confronted with sufficiently strong physical guidance cues. However, the border between laminin and tenascin C generally served as a repulsive cue that neurites did not readily cross on wider feature spacings. Importantly, biochemical directional cues were shown to be readily overcome when physical guidance cues were designed to have sufficiently narrow spacing at a given amplitude of 1.5  $\mu\text{m}$ . Designing prosthesis interfaces with physical cues that induce spatially organized neurite outgrowth even in the presence of conflicting biochemical cues will likely be necessary for *in vivo* applications with inherent biochemical signaling.

### Notes

1. Leach, J. B.; Achyuta, A. K.; Murthy, S. K. Bridging the divide between neuroprosthetic design, tissue engineering and neurobiology. *Front. Neuroeng* **2010**, *2*, 18.
2. O'Leary, S. J.; Richardson, R. R.; McDermott, H. J. Principles of design and biological approaches for improving the selectivity of cochlear implant electrodes. *J. Neural Eng.* **2009**, *6*, 055002.
3. Winter, J. O.; Cogan, S. F.; Rizzo, J. F. Retinal prostheses: current challenges and future outlook. *J. Biomater. Sci-Poly Ed.* **2007**, *18*, 1031-1055.
4. Rubinstein, J. T. How cochlear implants encode speech. *Curr. Opin. Otolaryngol. Head Neck Surg.* **2004**, *12*, 444-8.
5. Pfungst, B. E.; Bowling, S. A.; Colesa, D. J.; Garadat, S. N.; Raphael, Y.; Shibata, S. B.; Strahl, S. B.; Su, G. L.; Zhou, N. Cochlear infrastructure for electrical hearing. *Hear. Res.* **2011**, *281*, 65-73.
6. Shannon, R. V.; Fu, Q. J.; Galvin, J. The number of spectral channels required for speech recognition depends on the difficulty of the listening situation. *Acta Otolaryngol. Suppl.* **2004**, (552), 50-54.
7. Sly, D. J.; Heffer, L. F.; White, M. W.; Shepherd, R. K.; Birch, M. G. J.; Minter, R. L.; Nelson, N. E.; Wise, A. K.; O'Leary, S. J. Deafness alters auditory nerve fibre responses to cochlear implant stimulation. *Eur. J. Neurosci.* **2007**, *26*, 510-522.
8. Shepherd, R. K.; Roberts, L. A.; Paolini, A. G. Long-term sensorineural hearing loss induces functional changes in the rat auditory nerve. *Eur. J. Neurosci.* **2004**, *20*, 3131-3140.
9. Dorman, M. F.; Loizou, P. C.; Fitzke, J.; Tu, Z. M. The recognition of sentences in noise by normal-hearing listeners using simulations of cochlear-implant signal processors with 6-20 channels. *J. Acoust. Soc. Am.* **1998**, *104*, 3583-3585.
10. Wilson, B. S.; Dorman, M. F. Cochlear implants: A remarkable past and a brilliant future. *Hear. Res.* **2008**, *242*, 3-21.
11. McDermott, H. J. Music perception with cochlear implants: A review. *Trends in Amp.* **2004**, *8*, 49-82.
12. Shibata, S. B.; Budenz, C. L.; Bowling, S. A.; Pfungst, B. E.; Raphael, Y. Nerve maintenance and regeneration in the damaged cochlea. *Hear. Res.* **2011**, *281*, 56-64.

13. Roehm, P. C.; Hansen, M. R. Strategies to preserve or regenerate spiral ganglion neurons. *Curr. Opin. Otolaryngol. Head Neck Surg.* **2005**, *13*, 294-300.
14. Richardson, R. T.; Noushi, F.; O'Leary, S. Inner ear therapy for neural preservation. *Aud. Neurotol.* **2006**, *11*, 343-356.
15. Whilton, D. S.; Tieu, D.; Grover, M.; Reilly, B.; Coulson, M. T. Spontaneous association of glial cells with regrowing neurites in mixed cultures of dissociated spiral ganglia. *Neuroscience* **2009**, *161*, 227-235.
16. Pettingill, L. N.; Richardson, R. T.; Wise, A. K.; O'Leary, S. J.; Shepherd, R. K. Neurotrophic factors and neural prostheses: Potential clinical applications based upon findings in the auditory system. *IEEE Trans. Biomed. Eng.* **2007**, *54*, 1138-1148.
17. Glueckert, R.; Bitsche, M.; Miller, J. M.; Zhu, Y.; Prieskorn, D. M.; Altschuler, R. A.; Schrott-Fischer, A. Deafferentation-associated changes in afferent and efferent processes in the guinea pig cochlea and afferent regeneration with chronic intrascalar brain-derived neurotrophic factor and acidic fibroblast growth factor. *J. Comp. Neurol.* **2008**, *507*, 1602-1621.
18. Altschuler, R. A.; Cho, Y.; Ylikoski, J.; Pirvola, U.; Magal, E.; Miller, J. M. Rescue and regrowth of sensory nerves following deafferentation by neurotrophic factors. *Oto tox.: Basic Sci. Clin. App.* **1999**, *884*, 305-311.
19. Wise, A.; Hume, C.; Flynn, B.; Jeelall, Y.; Suhr, C.; Sgro, B.; O'Leary, S.; Shepherd, R.; Richardson, R. Effects of localized neurotrophin gene expression on spiral ganglion neuron resprouting in the deafened cochlea. *Mol. Ther.* **2010**.
20. Belisle, J. M.; Correia, J. P.; Wiseman, P. W.; Kennedy, T. E.; Costantino, S. Patterning protein concentration using laser-assisted adsorption by photobleaching, LAPAP. *Lab Chip* **2008**, *8*, 2164-2167.
21. Belisle, J. M.; Levin, L. A.; Costantino, S. High-content neurite development study using optically patterned substrates. *PLoS One* **2012**, *7*, e35911.
22. Klein, C. L.; Scholl, M.; Maelicke, A. Neuronal networks in vitro: formation and organization on biofunctionalized surfaces. *J. Mater. Sci-Mater. Med* **1999**, *10*, 721-727.
23. Eisenbarth, E. Biomaterials for tissue engineering. *Adv. Eng. Mater.* **2007**, *9*, 1051-1060.
24. Fisher, J. P.; Dean, D.; Engel, P. S.; Mikos, A. G. Photoinitiated polymerization of biomaterials. *Ann. Rev. Mater. Res.* **2001**, *31*, 171-181.
25. Lin, C.; Anseth, K. S. PEG hydrogels for the controlled release of biomolecules in regenerative medicine. *Pharm. Res.* **2009**, *26*, 631-643.

26. Ainslie, K. M.; Desai, T. A. Microfabricated implants for applications in therapeutic delivery, tissue engineering, and biosensing. *Lab Chip* **2008**, *8*, 1864-1878.
27. Clarke, J. C.; Tuft, B. W.; Clinger, J. D.; Levine, R.; Figueroa, L. S.; Guymon, C. A.; Hansen, M. R. Micropatterned methacrylate polymers direct spiral ganglion neurite and Schwann cell growth. *Hear. Res.* **2011**, *278*, 96-105.
28. Tuft, B. W.; Li, S.; Xu, L.; Clarke, J. C.; White, S. P.; Guymon, B. A.; Perez, K. X.; Hansen, M. R.; Guymon, C. A. Photopolymerized microfeatures for directed spiral ganglion neurite and Schwann cell growth. *Biomaterials* **2013**, *34*, 42-54.
29. Tuft, B. W.; Xu, L.; White, S. P.; Seline, A. E.; Erwood, A. M.; Hansen, M. R.; Guymon, C. A. Neural pathfinding on uni- and multidirectional photopolymerized micropatterns. *ACS Appl. Mater. Interfaces* **2014**.
30. Staecker, H.; Kopke, R.; Malgrange, B.; Lefebvre, P.; VandeWater, T. NT-3 and/or BDNF therapy prevents loss of auditory neurons following loss of hair cells. *Neuroreport* **1996**, *7*, 889-894.
31. Wise, A. K.; Richardson, R.; Hardman, J.; Clark, G.; O'Leary, S. Resprouting and survival of guinea pig cochlear neurons in response to the administration of the neurotrophins brain-derived neurotrophic factor and neurotrophin-3. *J. Comp. Neurol.* **2005**, *487*, 147-165.
32. Chou, L.; Firth, J.; Uitto, V.; Brunette, D. Substratum surface topography alters cell shape and regulates fibronectin mRNA level, mRNA stability, secretion and assembly in human fibroblasts. *J. Cell. Sci.* **1995**, *108*, 1563-1573.
33. Dalby, M. J.; Biggs, M. J.; Gadegaard, N.; Kalna, G.; Wilkinson, C. D.; Curtis, A. S. G. Nanotopographical stimulation of mechanotransduction and changes in interphase centromere positioning. *J. Cell. Biochem.* **2007**, *100*, 326-338.
34. Dalby, M. J.; Gadegaard, N.; Riehle, M. O.; Wilkinson, C. D.; Curtis, A. S. Investigating filopodia sensing using arrays of defined nano-pits down to 35 nm diameter in size. *Int. J. Biochem. Cell Biol.* **2004**, *36*, 2005-2015.
35. Clark, P.; Connolly, P.; Curtis, A. S.; Dow, J. A.; Wilkinson, C. D. Topographical control of cell behavior 1 Simple step cues. *Development* **1987**, *99*, 439-448.
36. Clark, P.; Connolly, P.; Curtis, A. S. G.; Dow, J. A. T.; Wilkinson, C. D. W. Topographical Control of Cell Behavior 2 Multiple grooved substrata. *Development* **1990**, *108*, 635-644.
37. Karuri, N. W.; Liliensiek, S.; Teixeira, A. I.; Abrams, G.; Campbell, S.; Nealey, P. F.; Murphy, C. J. Biological length scale topography enhances cell-substratum adhesion of human corneal epithelial cells. *J. Cell. Sci.* **2004**, *117*, 3153-3164.

38. Karuri, N. W.; Porri, T. J.; Albrecht, R. M.; Murphy, C. J.; Nealey, P. F. Nano- and microscale holes modulate cell-substrate adhesion, cytoskeletal organization, and integrin localization in Sv40 human corneal epithelial cells. *IEEE Trans. NanoBiosci.* **2006**, *5*, 273-280.
39. Hansen, M. R.; Vijapurkar, U.; Koland, J. G.; Green, S. H. Reciprocal signaling between spiral ganglion neurons and Schwann cells involves neuregulin and neurotrophins. *Hear. Res.* **2001**, *161*, 87-98.
40. Roehm, P. C.; Xu, N.; Woodson, E. A.; Green, S. H.; Hansen, M. R. Membrane depolarization inhibits spiral ganglion neurite growth via activation of multiple types of voltage sensitive calcium channels and calpain. *Mol. Cell. Neurosci.* **2008**, *37*, 376-387.
41. Hegarty, J.; Kay, A.; Green, S. Trophic support of cultured spiral ganglion neurons by depolarization exceeds and is additive with that by neurotrophins or cAMP and requires elevation of  $[Ca^{2+}]_i$  within a set range. *J. Neurosci.* **1997**, *17*, 1959-1970.
42. Kam, L.; Shain, W.; Turner, J.; Bizios, R. Axonal outgrowth of hippocampal neurons on micro-scale networks of polylysine-conjugated laminin. *Biomaterials* **2001**, *22*, 1049-1054.
43. Nurcombe, V. Laminin in neural development. *Pharmacol. Ther.* **1992**, *56*, 247-264.
44. Engel, J. Laminins and Other Strange Proteins. *Biochemistry* **1992**, *31*, 10643-10651.
45. Brors, D.; Bodmer, D.; Pak, K.; Aletsee, C.; Schafers, M.; Dazert, S.; Ryan, A. F. EphA4 provides repulsive signals to developing cochlear ganglion neurites mediated through ephrin-B2 and-B3. *J. Comp. Neurol.* **2003**, *462*, 90-100.
46. Pickles, J. O.; Claxton, C.; van Heumen, W. R. Complementary and layered expression of Ephs and ephrins in developing mouse inner ear. *J. Comp. Neurol.* **2002**, *449*, 207-216.
47. van Heumen, W. R.; Claxton, C.; Pickles, J. O. Expression of EphA4 in developing inner ears of the mouse and guinea pig. *Hear. Res.* **2000**, *139*, 42-50.
48. Chiquete-Hrismann, R. What distinguishes tenascin from fibronectin. *Faseb J.* **1990**, *4*, 2598-2604.
49. Erickson, H.; Bourdon, M. Tenascin - an extracellular-matrix protein prominent in specialized embryonic-tissues and tumors. *Annu. Rev. Cell Biol.* **1989**, *5*, 71-92.
50. Erickson, H.; Taylor, H. Hexabrachion proteins in embryonic chicken tissues and human-tumors. *J. Cell Biol.* **1987**, *105*, 1387-1394.

## CHAPTER 9

### CONCLUSIONS AND RECOMMENDATIONS

Use of synthetic organic polymers for medical applications and devices has grown rapidly since their initial development in the early to mid-twentieth century. Many synthetic materials are now identified as part of an expanding biomaterials science field which is increasingly multi-disciplinary and which substantially impacts the economy and human health. Due to significant progress in micro- and nanofabrication, tissue engineering, materials science, cell and molecular biology, and biotechnology, scientists and engineers now design material constructs and devices that address increasingly complex medical challenges. In particular, bioactive materials, or materials that are specifically designed to drive favorable biological interactions, show tremendous potential to save or improve quality of life for millions. The research presented in this thesis explores photopolymer materials and patterning methods to develop bioactive systems with physical cues that direct nerve growth and aid in elucidating neural pathfinding behavior.

Specifically, the spatial and temporal control of UV were used to generate and control the development of micro- and nanoscale physical cues across a substrate surface for neural process contact guidance studies and applications. Precisely directing *de novo* neurite growth in this manner will lead to substantial improvement of sensory-prosthesis performance due to enhanced signaling resolution and specificity. Spatially controlling photochemical initiation events was shown to alter local polymerization kinetics which yielded controllable surface topography. Furthermore, inner ear neural tissue, including SGN neurites and SGSCs, were demonstrated to thrive on photopolymerized methacrylate materials and to align to photopatterned physical cues. The extent of neural alignment was demonstrated to strongly correlate with microfeature dimensions which were readily tuned by altering photopolymerization reaction parameters. SGN neurite

pathfinding and turning capability was explored by developing multidirectional topographic cues using similar methods to fabricate unidirectional patterns. To investigate neurite pathfinding in response to material mechanical properties, two series of methacrylate copolymers were used with variations in crosslink density to alter substrate stiffness while micropattern feature dimensions were held constant across each series using the reaction controlled feature modulation developed in previous research objectives. Finally, neural pathfinding behavior was investigated with bioactive border challenges adsorbed to the surface of photopatterned materials and physical features were elucidated which overcome opposing surface chemical cues. The ultimate goal of this work is to substantially enhance neural prosthetic performance by developing bioactive materials which precisely direct nerve growth to improve the sensory-prosthesis interface. The work presented in this thesis significantly advances this goal.

Methacrylates were used as a model polymer platform for neural contact guidance studies as they have shown excellent biocompatibility in a variety of medical applications. Robust spiral ganglion neuron (SGN) and spiral ganglion Schwann Cell (SGSC) growth was observed on a series of hexyl methacrylate (HMA) and 1,6-hexanediol dimethacrylate (HDDMA) polymers with or without laminin coating illustrating the biocompatibility and suitability of photopolymerizable materials for neural contact guidance studies. To generate microfeatures across the methacrylate copolymer surface, a photomasking reaction method was developed to alter local reaction kinetics throughout the polymerization. Rapidly and directly generating cell-scale physical features with this method substantially expands systems and tools available for cell-material contact guidance research and for biomedical device modification and enhancement. Neuritogenesis, or new neurite growth, neurite length, and neuronal morphology were similar on each polymer composition and on substrates with or without laminin coatings. Furthermore, the results illustrate that the same topographic features which direct SGN neurite growth also promote alignment of SGSCs in the absence of

neurites suggesting that both neural and glial elements respond to similar microfeatures. The tendency of neurites and SCs to remain aligned to one another even when not conforming to the direction of the micropattern further highlights the significance of the mutual influence these cells exert on each other. These results demonstrate that inner ear neural tissue, which is critical to cochlear implant (CI) function, thrives on photopolymer materials, that the spatial and temporal control of photopolymerization can be utilized to generate physical micropatterns for neural pathfinding applications, and that SGN neurites and SGSCs align to micro-scale topographical cues.

Having demonstrated the efficacy of the photopatterning method to generate physical micropatterns for neural contact guidance, the degree of control over pattern formation was explored by modulating photopolymerization parameters such as photoinitiator choice and concentration, UV light intensity, radiation exposure time, and photomask band spacing. Depending on pattern periodicity, a range of channel amplitudes across several orders of magnitude can be generated for cell-material contact guidance applications. White light interferometry serves as a rapid and non-destructive means to characterize surface topography generated with the photopatterning method. Scanning electron microscopy (SEM) and atomic force microscopy (AFM) confirm white light interferometry analysis and enable detailed characterization of thin-film cross sections and microfeature transitional slopes.

Using reaction controlled feature modulation of topographic features enabled detailed probing of the extent of neural alignment to physical cues based on width, height, and transitional slope. Specifically, SGN neurite and SGSC alignment was shown to increase significantly with increasing feature amplitude and constant periodicity and with decreasing periodicity at constant amplitude. SGN neurites, which are typically several microns in diameter, were also demonstrated to strongly align to patterns with nanoscale (250 and 500 nm) channel amplitudes. Neurites from multiple neuronal types and a variety of glial cells from both the central and peripheral nervous system were

shown to align to photopolymerized micropatterns. However, alignment was not the same for each neural type indicating that features would likely need to be tuned for a given cellular niche and biomedical application. Importantly, microfeature transitional slope was identified as a crucial neurite guidance characteristic as the degree of SGN neurite alignment very strongly correlates ( $r = 0.93$ ) to this dimension. The versatility of photopolymerization enables fabrication of a variety of specific topographies that will facilitate identification of features most critical for neurite guidance. Such features may ultimately be used to improve the neural prosthesis interface in future neural prosthetic technology.

Rationally designing a bioactive surface that improves tissue integration of a neural prosthetic will likely require an interface that redirects regenerative nerve growth towards spatially specific electrodes. Accordingly, the photopatterning method developed in this research was used to fabricate multidirectional micropatterns to evaluate SGN neural pathfinding and turning capability. Understanding of SGN neurite pathfinding and SGSC response in relation to multidirectional physical micropatterns will likely aid in the ultimate design of an improved prosthesis interface. Microfeature shape and width are controlled through photomask design, and feature depth is readily tuned on the micron scale by altering reaction parameters of the photopolymerization. The pathfinding ability of SGNs was evaluated on repeating  $90^\circ$  patterns and compared to behavior on unpatterned, and unidirectional micropatterns. SGN neurites extend randomly on unpatterned surfaces and strongly align to and consistently track unidirectional patterns. Interestingly, when presented with multidirectional cues of the same width and height as those of the unidirectional pattern, SGN neurites are substantially influenced by, but do not consistently track, repeating turns. Rather, neurite extension is observed to avoid turning events even to the extent of crossing over multiple feature transitions which is rarely seen on unidirectional patterns. SGSCs which provide trophic support to SGNs, mirror the alignment behavior of SGN neurites on each pattern type. On both uni- and

multidirectional patterns, the majority of the neurite pathlength is located in depressed surface features but significantly more feature crossing events occur on multidirectional surfaces. These results improve understanding of SGN neural pathfinding in relation to physical guidance cues and inform efforts to direct neurite growth towards specific stimulatory elements. Developing methods to understand neural pathfinding and to guide *de novo* neurite growth to specific stimulatory elements will enable design of innovative biomaterials that improve functional outcomes of devices that interface with the nervous system.

As demonstrated in a variety of cell-material action studies, biological systems, including neuronal cells, are also known to respond to mechanical cues of synthetic biomaterial constructs. It will, therefore, ultimately be crucial to understand neurite response to material mechanical properties in relation to their alignment to physical features since final material properties of a medical device could significantly affect neural pathfinding. To determine the effects of material mechanical properties on physical feature contact guidance, methacrylate thin-film stiffness was modulated across two copolymer series by varying the cross-link density of the final material by either increasing the amount of cross-linker in the prepolymer formulation or by increasing the size of the spacer unit between cross-links. Controlling photopolymerization parameters, as established in previous research objectives, enabled production of micropatterns with identical physical features on a variety of polymer compositions despite differences in reaction kinetics due to differences in monomer chemistry or changes in prepolymer formulation. The tensile modulus of each composition was measured with dynamic mechanical analysis as a relative measure of rigidity for contact guidance studies. SGN neurite alignment is shown to increase significantly to physical microfeatures as matrix rigidity increases.

For many biomaterial applications that consider matrix stiffness, it is often deemed ideal to match the material modulus to that of the native tissue. This approach is

particularly appropriate for tissue engineering applications which aim to develop scaffolds that enable regeneration of healthy and functional tissue – particularly for load bearing applications such as cartilage tissue engineering. Remarkably, the results from this research demonstrate that some biomaterial applications, such as promoting spatial organization of *de novo* neurite growth, require careful consideration of material mechanical property effects on cellular behavior even when the material modulus is several orders of magnitude removed from native matrix stiffness of the target tissue. Part of the physical and biomechanical signals presented to neural growth cones during development and regeneration following injury likely include interactions with high modulus native matrices of bone, i.e. GPa range, or other dense connective tissues that are crucial to formation of spatially organized neural networks. For example, SGN growth cones extend through the bony modiolus and along the osseous spiral lamina to reach the organ of Corti. While the exact mechanisms by which different cell types integrate biophysical cues remain unknown, it is evident that SGN neurites sense matrix stiffness on materials that are much more rigid than central neural environments (e.g. brain or spinal cord) and that their alignment to biophysical cues substantially changes based on substrate rigidity.

This work illustrates that neurite alignment to physical micropatterns is significantly affected by the matrix stiffness of the underlying network. Furthermore, photopolymerization is demonstrated as a powerful tool to fabricate readily tunable microfeatures across a variety of methacrylate compositions based on the spatial and temporal control of UV curing. These results add to efforts aimed to enhance neural prosthetic performance by improving spatial signaling resolution and are also applicable to neural pathfinding and cell-material interaction applications.

As cells are known to respond to an assortment of physical as well as biochemical cues in their micro-environment, research presented in this work also elucidates appropriate physical microfeature dimensions which induce SGN neurite alignment

across conflicting biochemical directional cues. Dissociated SGNs and trigeminal neurons (TGNs) were cultured on photopolymerized micropattern substrates coated with two species of bioactive molecules and neurite outgrowth and pathfinding behavior was characterized at the biochemical border between the species. Bioactive species utilized in the work include: laminin, an integrin binding glycoprotein that facilitates neuronal adhesion and process outgrowth; tenascin-C, an adhesion modulating glycoprotein that can modify cellular adhesion by binding molecules of a cell's extra cellular matrix; and ephrin A4 which is a protein kinase important in cell adhesion and migration as well as in neurite guidance. The adsorbed biochemicals formed a distinct border across each sample and neurite alignment was characterized at the border as cross, stop, turn, and repel behavior. SGN neurites readily crossed from ephrin A4 coated regions to laminin coated areas on all pattern types, but the extent of crossing for a given neuronal population significantly increased with increasing feature frequency. Neurites from SGNs and trigeminal neurons were also observed to cross a laminin-tenascin C biochemical border when confronted with sufficiently strong physical guidance cues. However, the border between laminin and tenascin C generally served as a repulsive cue that neurites did not readily cross on wider feature spacings. Importantly, biochemical directional cues were shown to be readily overcome when physical guidance cues were designed to have sufficiently narrow spacing at a given amplitude of 1.5  $\mu\text{m}$ . Designing prosthesis interfaces with physical cues that induce spatially organized neurite outgrowth even in the presence of conflicting biochemical cues will likely be necessary for *in vivo* applications with inherent biochemical signaling.

Future research strategies aimed towards the ultimate goal of improved neural prosthetic performance will include both 2D and 3D approaches for spatially organized neural process outgrowth. To advance 2D approaches, elucidating the effects of monomer chemistry and polymerization kinetics on physical feature formation will potentially broaden both the variety of photopolymerizable materials and the range of feature

dimensions and shapes available for neural and cellular contact guidance applications. For example, in this work photopatternable systems consisted predominantly of small monomer, network forming methacrylates which propagate via radical chain growth. The resultant networks are highly crosslinked, brittle systems that remain in a glassy state below their glass transition temperature ( $T_g$ ) at physiological temperatures ( $\sim 37^\circ \text{C}$ ). Modulating monomer chemistry, crosslinker content, polymerization mechanism, and oligomer to monomer ratios will dramatically affect final material properties of photopatterned biomaterials contact guidance research. A systemic investigation of methacrylate monomer chemistries could include a range of aliphatic chain spacer lengths in dimethacrylate crosslinkers, as well as inclusion of other functional groups such as hydroxyl or amino groups that can participate in hydrogen bonding. For instance, poly(2-hydroxyethyl methacrylate) consists of linear chains but has some physical properties similar to crosslinked networks due to extensive hydrogen bonding within the system. Inclusion of other functional groups will also substantially alter polymerization kinetics which may yield useful advantages in either material chemical and mechanical properties or in pattern formation such as steeper transitions or deeper features. Furthermore, methacrylate or acrylated oligomers with an assortment of molecular weights and functionalities could be included to significantly alter both final material properties as well as reaction kinetics during photopolymerization. Oligomers may be particularly important for a final free-standing device that does not rely on the mechanical stability of glass substrates as were used for many of the *in vitro* studies presented in this research. Furthermore, many biomaterial and tissue engineering studies have demonstrated favorable biological outcomes when using natural biopolymers such as collagen, hyaluronic acid, and chitosan. Accordingly, natural biopolymers could be functionalized with photopolymerizable moieties to enable photopatterning of bioactive cues that direct cellular outcomes.

Previous results demonstrate that pattern formation is significantly affected by changes in photopolymerization parameters such as initiating light intensity, UV exposure time, and photoinitiator concentration. To expand on this work, reaction kinetics should be monitored for a variety of systems, including suggestions for changes in polymer formulation given above, to determine the effects of reaction kinetics on final pattern formation. Photopolymerization kinetics can be monitored and characterized by photo-differential scanning calorimetry (Photo-DSC) as has previously been done in our lab. Identifying key chemical and kinetic factors that impact feature formation will substantially augment the degree of control available over pattern development which will enhance neural contact guidance research and applications. A statistical design of experiments (DOE) strategy is recommended for formulation and kinetics work as it would significantly reduce the number of experiments required to yield crucial response space directional indicators to enable generation of target physical properties and surface guidance cues.

Previous results from this research show that SGN neurites consistently align to and track parallel or unidirectional microfeatures of appropriate dimensions. However, SGN neurites do not consistently align to or track multidirectional turning cues that have the same feature dimensions. It is unclear why *de novo* neurite growth did not more closely follow these cues. To determine the degree of attainable neurite turning in response to physical guidance cues, a series of patterns could be developed with varying feature angle widths using the photopatterning method explored in this work. Furthermore, reaction modulated feature control developed in this work could expand the range of feature periodicities and amplitudes tested in parallel with changes in angle width to identify key parameters that predictably redirect or turn neurite outgrowth. Along with angled neurite directional changes, there may also be methods to generate either curved features or posts to enable spatial redirection of regenerative neural processes. For example, a pattern with cell scale quarter circle features may more readily

effect 90° directional changes than stark 90° steps as were used in previous work. The neural pathfinding studies described here would be facilitated by working with a nano/micro fabrication center that has experience in designing photomasks. Pathfinding studies would be further enhanced by expanding the range of biomaterials and microfeature dimensions available through changes in system chemistry and polymerization kinetics as outlined here.

Many of the contact guidance studies conducted in this work focused primarily on identifying features and parameters that yield high degrees of neurite alignment to parallel microfeatures. However, the work would advance significantly if *de novo* neurite outgrowth could be directed in such a way as to enable spatially specific excitation testing. For example, a neural tissue explant or a group of dissociated neurons could be cultured at one end of a photopatterned material. Physical cues would orient extending neurites towards a microelectrode array with spatially distinct electrodes that could be fired independently. As the neurites approach the electrode array, they would encounter specifically designed directional cues such as angles, curves, or posts that disrupt unidirectional alignment and direct them to spatially specific electrodes. Neuronal excitation could then be measured and correlated with firing of distinct electrodes. If successful, this experiment, though conducted *in vitro*, would demonstrate a critical proof-of-concept result for improved neural prosthetic interface work and would also represent a crucial advance in the research. However, both the design of micropatterns that direct spatially distinct neurite growth and the real time monitoring of neuronal excitation will be challenging.

Another 2D strategy that exploits the unique spatial and temporal reaction control of photo-chemistry is to covalently functionalize material surfaces with bioactive species for neural guidance studies. Preliminary work in our lab demonstrates that laminin, an integrin binding protein found in the majority of connective tissue, can be covalently immobilized on acrylate polymer surfaces through thiol-acrylate chemistry. Laminin, or a

variety of other adhesion promoting proteins or oligomeric peptides, are bound to the surface through free thiols on cysteine amino acid groups. Using photo-initiated and orthogonal chemistry, such as thiol-ene reactions, could also be used to create patterns with different chemical properties, such as surface energy, in place of using bioactives. For example, fluorinated polymers are well known to inhibit protein adhesion which also prevents cellular adhesion. A fluorinated mono-functional thiol could be covalently bound to a polymer with remaining surface acrylate or 'ene' groups in spatially directed patterns to chemically guide neurite outgrowth. Interestingly, this approach would enable investigation of neural pathfinding in response to both chemical and physical guidance cues as the photo-functionalization step could be performed in series with a substrate that is already patterned with induced topography. Chemical cues, whether bioactive such as oligomeric peptides or as simple small molecule modifications, could be oriented as additive or destructive to physically induced neural process alignment.

While 2D neurite guidance strategies will yield important fundamental understanding regarding photopatterning and neurite pathfinding, it is likely that 3D constructs will be necessary for final *in vivo* biomedical devices that enhance neural prosthetic performance. To approach or even contact distinct electrodes on a cochlear prosthesis array, SGN neurite growth must extend through the osseous spiral lamina into the scala tympani where the array is placed. The scala tympani is a hollow canal that extends the length of the cochlea. As SGN neurites may exit the osseous spiral lamina at different locations, it may be prohibitively difficult to place a micropatterned but planar construct in the canal in a way that meaningfully supports and directs neurite outgrowth. A three-dimensional construct which is also patterned through the unique reaction control of photo-chemistry will likely be more practical and efficacious. However, it should be noted that one potential method to employ a patterned 2D micropatterned substrate within the scala tympani would be to use a patterned conduit like those used in peripheral nerve repair. However, rather than being patterned on the inner lumen, the pattern would be

curved around the outer diameter of the conduit and would be placed in contact or very close proximity to the osseous spiral lamina.

As detailed in Chapter 1, hydrogels are used increasingly in biomaterial and tissue engineering applications due to their tissue-like water content and the capacity that materials scientists have to tune their properties to mimic microcellular niches. Designing a hydrogel that supports and spatially directs SGN neurite outgrowth from the osseous spiral lamina to distinct CI electrodes will likely be more feasible to improve the prosthesis interface than trying to manipulate a patterned 2D surface to fit the same purpose. Realizing the objective of improving the CI interface using a 3D matrix will require a multi-step process with many potential research directions. First, inner ear neural tissue should be cultured on and in hydrogels with a range of properties and network densities. The distinction between being on or in the hydrogel may be important since SGN neurites will not initially be in the hydrogel upon exiting the osseous spiral lamina but will need to begin growing through the matrix towards spatially distinct electrodes after making contact with it. Accordingly inner ear tissue explants should be cultured on the surface of a hydrogel to explore initial neurite penetration of the gel. Immunofluorescence staining combined with confocal fluorescence microscopy will facilitate characterization of gel penetration. This process may have multiple iterations as not all hydrogels will have the same physical or chemical properties. Each gel will have variations in water uptake, transport properties, mechanical stiffness, and porosity which will affect both the health of the neural tissue as well as the ease of migration through the gel for extending neurites.

In addition to culture on the gel surface, explants or dissociated neurons could also be encapsulated in hydrogels by placing them in an aqueous solution with a water soluble photoinitiator and pre-polymer formulation. Upon irradiation, a network rapidly forms in the aqueous media entrapping the cells or neural tissue in a synthetic polymer matrix in a process referred to as photo-encapsulation. Photo-encapsulation has already

been shown to have low cytotoxicity under appropriate reaction conditions. Encapsulating neural tissue in this way would allow for investigation of neural pathfinding behavior through matrices with a variety of material properties and porosities.

In conjunction with initial *in vitro* investigation of neural tissue on and in a variety of hydrogel materials, development of a 3D construct appropriately shaped for insertion in the scala tympani would be essential. To design such a construct, accurate physical models of the cochlea would need to be used to develop a casting model to fabricate hydrogels with appropriate physical dimensions. This process may first require accurate physical representation of animal cochleae such as that of the murine inner ear. After fabrication of a mold of appropriate shape and size, hydrogels with various physical properties and swelling ratios would be developed for insertion into the scala tympani of the cochlea. It is likely that the hydrogel will have a teardrop-like shape similar to the scala tympani and that it will not be at its equilibrium swelling ratio for initial insertion. The hydrogel will initially be partially dehydrated to facilitate insertion through the round window in the cochlea and would then expand with gentle hydrodynamic pressure to fill the volume of the scala tympani. The gel should make contact with the osseous spiral lamina to immediately support any exiting SGN neurites, but the pressure the construct exerts on the osseous spiral lamina should be sufficiently low as to avoid trauma that could lead to damage and infection.

Once a suitable hydrogel has been determined for cochlear insertion, an electrode array, or array mimic, could also be encapsulated in the gel in such a way that upon gel swelling the electrodes are perimodiolar, i.e. hug or surround the modiolar, but are spaced far enough away from the osseous spiral lamina to prevent damage. The hydrogel matrix between the spiral lamina and the electrodes would serve as the directing agent to guide *de novo* SGN neurite growth to the electrodes. If neurite growth were successfully directed to CI electrodes in this manner it would likely substantially increase the number

of perceptual channels available which would improve their auditory performance. Accomplishing this objective will likely require collaboration with scientists with expertise in histology to examine cochleae following experimental implantations as well as with researchers that have experience with electrical neural stimulation to test the efficacy of the method.

Guiding SGN neurite growth through the gel to electrodes will also be a significant challenge. Several studies demonstrate that neurites can be induced to extend up a concentration gradient of nerve growth factors called neurotrophins. One way to test this idea for inner ear neural tissue would be to encapsulate inner ear tissue explants in an optimized hydrogel system and pass a gentle flow of a solution that contains neurotrophin through the gel. It is anticipated that neurites would initially extend radially from the explant in all directions but would be induced to turn up the neurotrophin gradient. Indeed, to induce *de novo* neurite growth from SGNs that no longer synapse with cochlear hair cells will require neurotrophin stimulation. One strategy to provide nerve growth factors would be to genetically modify SGSCs to overproduce neurotrophins. SGSCs normally provide trophic support of SGNs in the inner ear so it is likely that their behavior and outcomes will be a significant part of the research. Modifying SGSCs to overproduce nerve growth factors has previously been demonstrated. Photo-encapsulation would enable spatial separation of native neural tissue from genetically modified SGSCs. SGSCs could be injected in one side of the vessel just prior to encapsulating the system and would develop a gradient of neurotrophin through the hydrogel. After several days of culture the cells would be fixed with paraformaldehyde and immunostained with fluorescent anti-NF200 and anti-S100 antibodies to observe neurite outgrowth directionality. It is anticipated that neurite growth will extend toward the genetically modified SGSCs.

A final device made with this approach would encapsulate an electrode array in a hydrogel shaped like the scala tympani with concomitant encapsulation of genetically

modified SGSCs injected near the electrodes immediately before photoencapsulation. The gel would not yet be at its equilibrium water uptake allowing for insertion into the scala tympani. Once in the scala tympani the gel would swell bringing the SGSCs and electrodes in very close proximity to the osseous spiral lamina behind which the remaining SGNs are housed. Neurotrophins from the insert would stimulate *de novo* neurite growth from the SGNs which would penetrate the osseous spiral lamina and come in contact with the synthetic hydrogel construct. Neurites would then penetrate the gel and be guided by a soluble nerve growth factor gradient towards spatially distinct electrodes.

An alternative or additive neurite alignment strategy to the soluble neurotrophin gradient approach is to exploit the spatial and temporal reaction control of photopolymerization to selectively functionalize the 3D hydrogel matrix supporting neurite outgrowth. For example, hydrogel monomers could be modified either with a pendant attachment group between polymerizable moieties or monofunctional polymerizable groups, e.g. mono-(meth)acrylate, could be synthesized with an attachment group for future functionalization of the hydrogel. Following the initial hydrogel formation, groups throughout the 3D matrix would remain for sequential functionalization steps.

One example of the spatially controlled covalent modification method would be to functionalize methacrylate and dimethacrylate monomers with a pendant thiol for future thiol-ene orthogonal photo-chemistry. A dimethacrylate would be modified with a pendant thiol between the polymerizable groups. Thiol radicals do not readily react with methacrylates which would ensure their availability following the initial photopolymerization step. After the thiol modified methacrylate hydrogel has been photopolymerized, it could be swollen in an aqueous media that contains a bioactive functionality bound to an 'ene' that is reactive towards thiols such, e.g. RGD vinyl or allyl ether. RGD is a three amino acid sequence responsible for integrin binding on

various adhesion proteins and facilitates neuronal and neural process attachment and survival. The gel could then be exposed to UV light through a photomask to generate channels of RGD functionalized matrix throughout the gel. Neural tissue would then preferentially attach to and follow an adhesion channel specifically designed in the gel. Many other photochemical schemes and bioactive modifications could be derived from this method. Again, matrix material modification may work synergistically with modified SGSCs which provide trophic support and chemical guidance cues for neurite outgrowth.

The work presented in this thesis significantly advances research objectives aimed to improve neural prosthetic signaling specificity and performance. Specifically, the work demonstrates the efficacy of photopolymerization as a versatile production platform for direct fabrication of physical guidance cues for cell and neural contact guidance studies and applications. Photopatterned feature dimensions such as periodicity, amplitude, and transitional slope were identified as crucial parameters to precisely control the extent of directed neurite outgrowth. Furthermore, modulation of photopolymerization parameters was shown to enable tight control over physical surface features at the micro- and nano-scale. Particular emphasis is given to research outcomes for neural elements of the inner ear which are crucial to cochlear prosthesis performance. Important relationships were also established between neurite alignment to physical cues and the underlying material mechanical properties as well as adsorbed surface bioactive species. Fundamental understanding developed from the completion of this research regarding neural pathfinding to various environmental physical cues serves as a foundation for development of devices and constructs for *in vivo* neural regeneration models including the design of enhanced neuron-prostheses interfaces.

## BIBLIOGRAPHY

- Abbe, E. Contributions to the theory of the microscope and the microscopic perception (translated from German). *Arch. Mikr. Anat* **1873**, *9*, 413-468.
- Adams, D. N.; Kao, E. Y. -.; Hypolite, C. L.; Distefano, M. D.; Hu, W.; Letourneau, P. C. Growth cones turn and migrate up an immobilized gradient of the laminin IKVAV peptide. *J. Neurobiol.* **2005**, *62*, 134-147.
- Ainslie, K. M.; Desai, T. A. Microfabricated implants for applications in therapeutic delivery, tissue engineering, and biosensing. *Lab Chip* **2008**, *8*, 1864-1878.
- Akutsu, T.; Dreyer, B.; Kolff, W. J. Polyurethane artificial heart valves in animals. *J. Appl. Physiol.* **1959**, *14*, 1045-1048.
- Alam, S. A.; Robinson, B. K.; Huang, J.; Green, S. H. Prosurvival and proapoptotic intracellular signaling in rat spiral ganglion neurons in vivo after the loss of hair cells. *J. Comp. Neurol.* **2007**, *503*, 832-852.
- Alcantar, N. A.; Aydil, E. S.; Israelachvili, J. N. Polyethylene glycol-coated biocompatible surfaces. *J. Biomed. Mater. Res.* **2000**, *51*, 343-351.
- Altschuler, R. A.; Cho, Y.; Ylikoski, J.; Pirvola, U.; Magal, E.; Miller, J. M. Rescue and regrowth of sensory nerves following deafferentation by neurotrophic factors. *Ototoxicity: Basic Science and Clinical Applications* **1999**, *884*, 305-311.
- Ameri, H.; Ratanapakorn, T.; Ufer, S.; Eekhardt, H.; Humayun, M. S.; Weiland, J. D. Toward a wide-field retinal prosthesis. *J. Neural Eng.* **2009**, *6*, 035002.
- Anselme, K.; Bigerelle, M.; Noel, B.; Dufresne, E.; Judas, D.; Iost, A.; Hardouin, P. Qualitative and quantitative study of human osteoblast adhesion on materials with various surface roughnesses RID D-8909-2011. *J. Biomed. Mater. Res.* **2000**, *49*, 155-166.
- Apple, D. J.; Sims, J. Harold Ridley and the invention of the intraocular lens. *Surv. Ophthalmol.* **1996**, *40*, 279-292.
- Arima, Y.; Iwata, H. Effect of wettability and surface functional groups on protein adsorption and cell adhesion using well-defined mixed self-assembled monolayers. *Biomaterials* **2007**, *28*, 3074-3082.
- Asher, A.; Segal, W. A.; Baccus, S. A.; Yaroslavsky, L. P.; Palanker, D. V. Image processing for a high-resolution optoelectronic retinal prosthesis. *IEEE Trans. Biomed. Eng.* **2007**, *54*, 993-1004.
- Augustin, A. J.; Kirchhof, J. Inflammation and the pathogenesis of age-related macular degeneration. *Expert Opinion on Therapeutic Targets* **2009**, *13*, 641-651.

- Ayala, R.; Zhang, C.; Yang, D.; Hwang, Y.; Aung, A.; Shroff, S. S.; Arce, F. T.; Lal, R.; Arya, G.; Varghese, S. Engineering the cell-material interface for controlling stem cell adhesion, migration, and differentiation. *Biomaterials* **2011**, *32*, 3700-3711.
- Baek, N. S.; Kim, Y. H.; Han, Y. H.; Lee, B. J.; Kim, T.; Kim, S.; Choi, Y.; Kim, G. H.; Chung, M.; Jung, S. Facile photopatterning of polyfluorene for patterned neuronal networks. *Soft Matter* **2011**, *7*, 10025-10031.
- Balgude, A. P.; Yu, X.; Szymanski, A.; Bellamkonda, R. V. Agarose gel stiffness determines rate of DRG neurite extension in 3D cultures. *Biomaterials* **2001**, *22*, 1077-1084.
- Beebe, D.; Moore, J.; Bauer, J.; Yu, Q.; Liu, R.; Devadoss, C.; Jo, B. Functional hydrogel structures for autonomous flow control inside microfluidic channels. *Nature* **2000**, *404*, 588-+.
- Belisle, J. M.; Correia, J. P.; Wiseman, P. W.; Kennedy, T. E.; Costantino, S. Patterning protein concentration using laser-assisted adsorption by photobleaching, LAPAP. *Lab Chip* **2008**, *8*, 2164-2167.
- Belisle, J. M.; Levin, L. A.; Costantino, S. High-Content Neurite Development Study Using Optically Patterned Substrates. *PLoS One* **2012**, *7*, e35911.
- Bernard, A.; Fitzli, D.; Sonderegger, P.; Delamarche, E.; Michel, B.; Bosshard, H. R.; Biebuyck, H. Affinity capture of proteins from solution and their dissociation by contact printing. *Nat. Biotechnol.* **2001**, *19*, 866-869.
- Bertschinger, D. R.; Beknazar, E.; Simonutti, M.; Safran, A. B.; Sahel, J. A.; Rosolen, S. G.; Picaud, S.; Salzmann, J. A review of in vivo animal studies in retinal prosthesis research. *Graefes Archive for Clinical and Experimental Ophthalmology* **2008**, *246*, 1505-1517.
- Besch, D.; Sachs, H.; Szurman, P.; Guelicher, D.; Wilke, R.; Reinert, S.; Zrenner, E.; Bartz-Schmidt, K. U.; Gekeler, F. Extraocular surgery for implantation of an active subretinal visual prosthesis with external connections: feasibility and outcome in seven patients. *Br. J. Ophthalmol.* **2008**, *92*, 1361-1368.
- Bettinger, C. J.; Langer, R.; Borenstein, J. T. Engineering Substrate Topography at the Micro- and Nanoscale to Control Cell Function. *Angewandte Chemie-International Edition* **2009**, *48*, 5406-5415.
- Bhatia, K.; Gibbin, K. P.; Nikolopoulos, T. P.; O'Donoghue, G. M. Surgical complications and their management in a series of 300 consecutive pediatric cochlear implantations. *Otol. Neurotol.* **2004**, *25*, 730-739.
- Bhattacharjee, N.; Li, N.; Keenan, T. M.; Folch, A. A neuron-benign microfluidic gradient generator for studying the response of mammalian neurons towards axon guidance factors. *Integrative Biology* **2010**, *2*, 669-679.

- Biela, S. A.; Su, Y.; Spatz, J. P.; Kemkemer, R. Different sensitivity of human endothelial cells, smooth muscle cells and fibroblasts to topography in the nano–micro range. *Acta Biomater.* **2009**, *5*, 2460-2466.
- Black, R. C.; Clark, G. M.; Patrick, J. F. Current Distribution Measurements within the Human Cochlea. *IEEE Trans. Biomed. Eng.* **1981**, *28*, 721-725.
- Black, R. C.; Clark, G. M.; Tong, Y. C.; Patrick, J. F. Current Distributions in Cochlear Stimulation. *Ann. N. Y. Acad. Sci.* **1983**, *405*, 137-145.
- Bobbio, A. The first endosseous alloplastic implant in the history of man. *Bull. Hist. Dent.* **1972**, *20*, 1-6.
- Borenstein, J. T.; Weinberg, E. J.; Orrick, B. K.; Sundback, C.; Kaazempur-Mofrad, M. R.; Vacanti, J. P. Microfabrication of three-dimensional engineered scaffolds. *Tissue Eng.* **2007**, *13*, 1837-1844.
- Bostrom, M.; Khalifa, S.; Bostrom, H.; Liu, W.; Friberg, U.; Rask-Andersen, H. Effects of Neurotrophic Factors on Growth and Glial Cell Alignment of Cultured Adult Spiral Ganglion Cells. *Audiol. Neurootol.* **2010**, *15*, 175-186.
- Branch, D. W.; Corey, J. M.; Weyhenmeyer, J. A.; Brewer, G. J.; Wheeler, B. C. Microstamp patterns of biomolecules for high-resolution neuronal networks. *Med. Biol. Eng. Comput.* **1998**, *36*, 135-141.
- Branch, D. W.; Wheeler, B. C.; Brewer, G. J.; Leckband, D. E. Long-term stability of grafted polyethylene glycol surfaces for use with microstamped substrates in neuronal cell culture. *Biomaterials* **2001**, *22*, 1035-1047.
- Brazzelli, M.; Murray, A.; Fraser, C. Efficacy and safety of sacral nerve stimulation for urinary urge incontinence: A systematic review. *J. Urol.* **2006**, *175*, 835-841.
- Bron, A.; Tripathi, R.; Tripathi, B. *Wolff's Anatomy of the Eye and Orbit*; London, UK, 2001; , pp 225-455.
- Brors, D.; Bodmer, D.; Pak, K.; Aletsee, C.; Schafers, M.; Dazert, S.; Ryan, A. F. EphA4 provides repulsive signals to developing cochlear ganglion neurites mediated through ephrin-B2 and-B3. *J. Comp. Neurol.* **2003**, *462*, 90-100.
- Brors, D.; Aletsee, C.; Schwager, K.; Mlynski, R.; Hansen, S.; Schäfers, M.; Ryan, A. F.; Dazert, S. Interaction of spiral ganglion neuron processes with alloplastic materials in vitro. *Hear. Res.* **2002**, *167*, 110-121.
- Brown, X. Q.; Ookawa, K.; Wong, J. Y. Evaluation of polydimethylsiloxane scaffolds with physiologically-relevant elastic moduli: interplay of substrate mechanics and surface chemistry effects on vascular smooth muscle cell response. *Biomaterials* **2005**, *26*, 3123-3129.

- Bryant, S. J.; Chowdhury, T. T.; Lee, D. A.; Bader, D. L.; Anseth, K. S. Crosslinking density influences chondrocyte metabolism in dynamically loaded photocrosslinked poly(ethylene glycol) hydrogels. *Ann. Biomed. Eng.* **2004**, *32*, 407-417.
- Bryant, S. J.; Cuy, J. L.; Hauch, K. D.; Ratner, B. D. Photo-patterning of porous hydrogels for tissue engineering. *Biomaterials* **2007**, *28*, 2978-2986.
- Bryant, S. J.; Nuttelman, C. R.; Anseth, K. S. Cytocompatibility of UV and visible light photoinitiating systems on cultured NIH/3T3 fibroblasts in vitro. *J. Biomat. Sci-Polym. E.* **2000**, *11*, 439-457.
- Bryant, S. J.; Hauch, K. D.; Ratner, B. D. Spatial Patterning of Thick Poly(2-hydroxyethyl methacrylate) Hydrogels. *Macromolecules* **2006**, *39*, 4395-4399.
- Bryers, J. D.; Giachelli, C. M.; Ratner, B. D. Engineering biomaterials to integrate and heal: The biocompatibility paradigm shifts. *Biotechnol. Bioeng.* **2012**, *109*, 1898-1911.
- Buddy, R.; Hoffman, A.; Schoen, F.; Lemons, J. *Biomaterials Science An Introduction to Materials in Medicine*; Academic Press: Waltham, MA, 2012; , pp 1573.
- Caspi, A.; Dorn, J. D.; McClure, K. H.; Humayun, M. S.; Greenberg, R. J.; McMahon, M. J. Feasibility Study of a Retinal Prosthesis. *Arch. Ophthalmol.* **2009**, *127*, 398-401.
- Chader, G. J.; Weiland, J.; Humayun, M. S. Artificial vision: needs, functioning, and testing of a retinal electronic prosthesis. *Neurotherapy: Progress in Restorative Neuroscience and Neurology* **2009**, *175*, 317-332.
- Charest, J.; Eliason, M.; Garcia, A.; King, W. Combined microscale mechanical topography and chemical patterns on polymer cell culture substrates. *Biomaterials* **2006**, *27*, 2487-2494.
- Charest, J. M.; Califano, J. P.; Carey, S. P.; Reinhart-King, C. A. Fabrication of Substrates with Defined Mechanical Properties and Topographical Features for the Study of Cell Migration. *Macromol. Biosci.* **2012**, *12*, 12-20.
- Chen, C. S. Mechanotransduction - a field pulling together? *J. Cell. Sci.* **2008**, *121*, 3285-3292.
- Chen, K.; Rowley, A. P.; Weiland, J. D. Elastic properties of porcine ocular posterior soft tissues. *J. Biomed. Mater. Res. Part A* **2010**, *93A*, 634-645.
- Chou, C.; Rivera, A. L.; Sakai, T.; Caplan, A. I.; Goldberg, V. M.; Welter, J. F.; Baskaran, H. Micrometer Scale Guidance of Mesenchymal Stem Cells to Form Structurally Oriented Cartilage Extracellular Matrix. *Tissue Eng. Part A* **2013**, *19*, 1081-1090.

- Chou, L.; Firth, J.; Uitto, V.; Brunette, D. Substratum surface topography alters cell shape and regulates fibronectin mRNA level, mRNA stability, secretion and assembly in human fibroblasts. *J. Cell. Sci.* **1995**, *108*, 1563-1573.
- Chou, L. S.; Firth, J. D.; Uitto, V. J.; Brunette, D. M. Substratum Surface-Topography Alters Cell-Shape and Regulates Fibronectin Messenger-Rna Level, Messenger-Rna Stability, Secretion and Assembly in Human Fibroblasts. *J. Cell. Sci.* **1995**, *108*, 1563-1573.
- Chou, S.; Cheng, C.; Chen, C.; LeDuc, P. R. Localized neurite outgrowth sensing via substrates with alternative rigidities. *Soft Matter* **2011**, *7*, 9871-9877.
- Chow, A. Y.; Chow, V. Y.; Packo, K. H.; Pollack, J. S.; Peyman, G. A.; Schuchard, R. The artificial silicon retina microchip for the treatment of vision loss from retinitis pigmentosa. *Arch. Ophthalmol.* **2004**, *122*, 460-469.
- Chowdhury, V.; Morley, J. W.; Coroneo, M. T. Evaluation of extralocular electrodes for a retinal prosthesis using evoked potentials in cat visual cortex. *J. Clin. Neurosci.* **2005**, *12*, 574-579.
- Clapper, J. D.; Pearce, M. E.; Guymon, C. A.; Salem, A. K. Biotinylated biodegradable nanotemplated hydrogel networks for cell interactive applications. *Biomacromol.* **2008**, *9*, 1188-1194.
- Clark, P.; Connolly, P.; Curtis, A. S. G.; Dow, J. A. T.; Wilkinson, C. D. W. Cell Guidance by Ultrafine Topography In Vitro. *J. Cell. Sci.* **1991**, *99*, 73-77.
- Clark, P.; Connolly, P.; Curtis, A. S. G.; Dow, J. A. T.; Wilkinson, C. D. W. Topographical Control of Cell Behavior .2. Multiple Grooved Substrata. *Development* **1990**, *108*, 635-644.
- Clark, P.; Connolly, P.; Curtis, A. S. G.; Dow, J. A. T.; Wilkinson, C. D. W. Topographical Control of Cell Behavior .1. Simple Step Cues. *Development* **1987**, *99*, 439-448.
- Clarke, J. C.; Tuft, B. W.; Clinger, J. D.; Levine, R.; Figueroa, L. S.; Allan Guymon, C.; Hansen, M. R. Micropatterned methacrylate polymers direct spiral ganglion neurite and Schwann cell growth. *Hear. Res.* **2011**, *278*, 96-105.
- Clements, I. P.; Kim, Y.; English, A. W.; Lu, X.; Chung, A.; Bellamkonda, R. V. Thin-film enhanced nerve guidance channels for peripheral nerve repair. *Biomaterials* **2009**, *30*, 3834-3846.
- Cohen, L.; Saunders, E.; Knight, M.; Cowan, R. Psychophysical measures in patients fitted with Contour (TM) and straight Nucleus electrode arrays. *Hear. Res.* **2006**, *212*, 160-175.

- Crubezy, E.; Murail, P.; Girard, L.; Bernadou, J. P. False teeth of the Roman world. *Nature* **1998**, *391*, 29-29.
- Csucs, G.; Kunzler, T.; Feldman, K.; Robin, F.; Spencer, N. D. Microcontact printing of macromolecules with submicrometer resolution by means of polyolefin stamps. *Langmuir* **2003**, *19*, 6104-6109.
- Csucs, G.; Michel, R.; Lussi, J. W.; Textor, M.; Danuser, G. Microcontact printing of novel co-polymers in combination with proteins for cell-biological applications. *Biomaterials* **2003**, *24*, 1713-1720.
- Cui, X. Y.; Wiler, J.; Dzaman, M.; Altschuler, R. A.; Martin, D. C. In vivo studies of polypyrrole/peptide coated neural probes. *Biomaterials* **2003**, *24*, 777-787.
- Cunningham, C. D.; Slattery, W. H.; Luxford, W. M. Postoperative infection in cochlear implant patients. *Otolaryngol.Head Neck Surg.* **2004**, *131*, 109-114.
- Curtis, A.; Wilkinson, C. Topographical control of cells. *Biomaterials* **1997**, *18*, 1573-1583.
- Curtis, A.; Wilkinson, C. Topographical control of cells. *Biomaterials* **1997**, *18*, 1573-1583.
- Cuvelier, D.; Rossier, O.; Bassereau, P.; Nassoy, P. Micropatterned "adherent/repellent" glass surfaces for studying the spreading kinetics of individual red blood cells onto protein-decorated substrates. *Euro. Biophys. J. Biophys. Lett.* **2003**, *32*, 342-354.
- Daemen, J.; Serruys, P. W. Drug-eluting stent update 2007 - Part II: Unsettled issues. *Circulation* **2007**, *116*, 961-968.
- Daemen, J.; Serruys, P. W. Drug-eluting stent update 2007 part I: a survey of current and future generation drug-eluting stents: meaningful advances or more of the same? *Circulation* **2007**, *116*, 316-328.
- Dalby, M. J.; Gadegaard, N.; Riehle, M. O.; Wilkinson, C. D. W.; Curtis, A. S. G. Investigating filopodia sensing using arrays of defined nano-pits down to 35 nm diameter in size. *Int. J. Biochem. Cell Biol.* **2004**, *36*, 2005-2015.
- Dalby, M. J.; Gadegaard, N.; Riehle, M. O.; Wilkinson, C. D. W.; Curtis, A. S. G. Investigating filopodia sensing using arrays of defined nano-pits down to 35 nm diameter in size. *Int. J. Biochem. Cell Biol.* **2004**, *36*, 2005-2015.
- Dalby, M. J.; Riehle, M. O.; Yarwood, S. J.; Wilkinson, C. D. W.; Curtis, A. S. G. Nucleus alignment and cell signaling in fibroblasts: response to a micro-grooved topography. *Exp. Cell Res.* **2003**, *284*, 274-282.

- Dalby, M. J.; Biggs, M. J. P.; Gadegaard, N.; Kalna, G.; Wilkinson, C. D. W.; Curtis, A. S. G. Nanotopographical stimulation of mechanotransduction and changes in interphase centromere positioning. *J. Cell. Biochem.* **2007**, *100*, 326-338.
- Dalby, M. J.; Biggs, M. J. P.; Gadegaard, N.; Kalna, G.; Wilkinson, C. D. W.; Curtis, A. S. G. Nanotopographical stimulation of mechanotransduction and changes in interphase centromere positioning. *J. Cell. Biochem.* **2007**, *100*, 326-338.
- Dalby, M. J.; Gadegaard, N.; Tare, R.; Andar, A.; Riehle, M. O.; Herzyk, P.; Wilkinson, C. D. W.; Oreffo, R. O. C. The control of human mesenchymal cell differentiation using nanoscale symmetry and disorder RID E-9243-2010 RID A-3427-2011. *Nat. Mater.* **2007**, *6*, 997-1003.
- Dalby, M. Topographically induced direct cell mechanotransduction. *Med. Eng. Phys.* **2005**, *27*, 730-742.
- Dalby, M.; Childs, S.; Riehle, M.; Johnstone, H.; Affrossman, S.; Curtis, A. Fibroblast reaction to island topography: changes in cytoskeleton and morphology with time. *Biomaterials* **2003**, *24*, 927-935.
- Dallos, P.; Popper, A.; Fay, R. *The Cochlea*; Springer Handbook of Auditory Research; Springer: New York, NY, **1996**, *8*, 551.
- Daly, W.; Yao, L.; Zeugolis, D.; Windebank, A.; Pandit, A. A biomaterials approach to peripheral nerve regeneration: bridging the peripheral nerve gap and enhancing functional recovery. *J. R. Soc. Interface* **2012**, *9*, 202-221.
- Daly, W. T.; Yao, L.; Abu-rub, M. T.; O'Connell, C.; Zeugolis, D. I.; Windebank, A. J.; Pandit, A. S. The effect of intraluminal contact mediated guidance signals on axonal mismatch during peripheral nerve repair. *Biomaterials* **2012**, *33*, 6660-6671.
- Danneman, P. J.; Mandrell, T. D. Evaluation of five agents/methods for anesthesia of neonatal rats. *Lab. Anim. Sci.* **1997**, *47*, 386-395.
- Davies, A. M. Neuronal survival: Early dependence on Schwann cells. *Curr. Biol.* **1998**, *8*, R15-R18.
- Dazert, S.; Kim, D.; Luo, L.; Aletsee, C.; Garfunkel, S.; Maciag, T.; Baird, A.; Ryan, A. F. Focal delivery of fibroblast growth factor-1 by transfected cells induces spiral ganglion neurite targeting in vitro. *J. Cell. Physiol.* **1998**, *177*, 123-129.
- Decker, C. Kinetic study and new applications of UV radiation curing. *Macromol. Rapid Commun.* **2002**, *23*, 1067-1093.
- Decker, C. The use of UV irradiation in polymerization. *Polym. Int.* **1998**, *45*, 133-141.

- DeForest, C. A.; Sims, E. A.; Anseth, K. S. Peptide-Functionalized Click Hydrogels with Independently Tunable Mechanics and Chemical Functionality for 3D Cell Culture. *Chem. Mater.* **2010**, *22*, 4783-4790.
- Delamarche, E.; Bernard, A.; Schmid, H.; Bietsch, A.; Michel, B.; Biebuyck, H. Microfluidic networks for chemical patterning of substrate: Design and application to bioassays. *J. Am. Chem. Soc.* **1998**, *120*, 500-508.
- Delamarche, E.; Bernard, A.; Schmid, H.; Michel, B.; Biebuyck, H. Patterned delivery of immunoglobulins to surfaces using microfluidic networks. *Science* **1997**, *276*, 779-781.
- Diehl, K. A.; Foley, J. D.; Nealey, P. F.; Murphy, C. J. Nanoscale topography modulates corneal epithelial cell migration. *J. Biomed. Mater. Res. Part A* **2005**, *75A*, 603-611.
- Discher, D. E.; Janmey, P.; Wang, Y. L. Tissue cells feel and respond to the stiffness of their substrate. *Science* **2005**, *310*, 1139-1143.
- Discher, D. E.; Janmey, P.; Wang, Y. Tissue Cells Feel and Respond to the Stiffness of Their Substrate. *Science* **2005**, *310*, 1139-1143.
- Dorman, M. F.; Loizou, P. C.; Fitzke, J.; Tu, Z. M. The recognition of sentences in noise by normal-hearing listeners using simulations of cochlear-implant signal processors with 6-20 channels. *J. Acoust. Soc. Am.* **1998**, *104*, 3583-3585.
- Dowell-Mesfin, N. M.; Abdul-Karim, M.; Turner, A. M. P.; Schanz, S.; Craighead, H. G.; Roysam, B.; Turner, J. N.; Shain, W. Topographically modified surfaces affect orientation and growth of hippocampal neurons. *J. Neural Eng.* **2004**, *1*, 78-90.
- Drury, J. L.; Mooney, D. J. Hydrogels for tissue engineering: scaffold design variables and applications. *Biomaterials* **2003**, *24*, 4337-4351.
- Dunn, G. A.; Brown, A. F. Alignment of Fibroblasts on Grooved Surfaces Described by a Simple Geometric Transformation. *J. Cell. Sci.* **1986**, *83*, 313-340.
- Edgahl, R. H.; Hume, D. M.; Schlang, H. A. Plastic venous prostheses. *Surg. Forum* **1955**, *5*, 235-41.
- Eisenbarth, E. Biomaterials for tissue engineering. *Adv.Eng. Mater.* **2007**, *9*, 1051-1060.
- Engler, A. J.; Griffin, M. A.; Sen, S.; Bonnetmann, C. G.; Sweeney, H. L.; Discher, D. E. Myotubes differentiate optimally on substrates with tissue-like stiffness: pathological implications for soft or stiff microenvironments. *J. Cell Biol.* **2004**, *166*, 877-887.
- Engler, A. J.; Sen, S.; Sweeney, H. L.; Discher, D. E. Matrix elasticity directs stem cell lineage specification. *Cell* **2006**, *126*, 677-689.

- Engler, A. J.; Carag-Krieger, C.; Johnson, C. P.; Raab, M.; Tang, H.; Speicher, D. W.; Sanger, J. W.; Sanger, J. M.; Discher, D. E. Embryonic cardiomyocytes beat best on a matrix with heart-like elasticity: scar-like rigidity inhibits beating. *J. Cell. Sci.* **2008**, *121*, 3794-3802.
- Engler, A. J.; Sen, S.; Sweeney, H. L.; Discher, D. E. Matrix elasticity directs stem cell lineage specification. *Cell* **2006**, *126*, 677-689.
- Engler, A. J.; Sen, S.; Sweeney, H. L.; Discher, D. E. Matrix Elasticity Directs Stem Cell Lineage Specification. *Cell* **2006**, *126*, 677-689.
- Espicom Business Intelligence Ltd *The World Medical Markets Fact Book*; **2008**.
- Evans, A. J.; Thompson, B. C.; Wallace, G. G.; Millard, R.; O'Leary, S. J.; Clark, G. M.; Shepherd, R. K.; Richardson, R. T. Promoting neurite outgrowth from spiral ganglion neuron explants using polypyrrole/BDNF-coated electrodes. *J. Biomed. Mater. Res. Part A* **2009**, *91A*, 241-250.
- Evans, A. R.; Euteneuer, S.; Chavez, E.; Mullen, L. M.; Hui, E. E.; Bhatia, S. N.; Ryan, A. F. Laminin and fibronectin modulate inner ear spiral ganglion neurite outgrowth in an in vitro alternate choice assay. *Dev. Neurobiol.* **2007**, *67*, 1721-1730.
- Eyckmans, J.; Boudou, T.; Yu, X.; Chen, C. S. A Hitchhiker's Guide to Mechanobiology. *Dev. Cell* **2011**, *21*, 35-47.
- Falconnet, D.; Csucs, G.; Grandin, H. M.; Textor, M. Surface engineering approaches to micropattern surfaces for cell-based assays. *Biomaterials* **2006**, *27*, 3044-3063.
- Falconnet, D.; Csucs, G.; Michelle Grandin, H.; Textor, M. Surface engineering approaches to micropattern surfaces for cell-based assays. *Biomaterials* **2006**, *27*, 3044-3063.
- Ferrari, A.; Cecchini, M.; Serresi, M.; Faraci, P.; Pisignano, D.; Beltram, F. Neuronal polarity selection by topography-induced focal adhesion control. *Biomaterials* **2010**, *31*, 4682-4694.
- Firszt, J. B.; Koch, D. B.; Downing, M.; Litvak, L. Current steering creates additional pitch percepts in adult cochlear implant recipients. *Otol. Neurotol.* **2007**, *28*, 629-636.
- Fisher, J. P.; Dean, D.; Engel, P. S.; Mikos, A. G. Photoinitiated polymerization of biomaterials. *Ann. Rev. Mater. Res.* **2001**, *31*, 171-181.
- Fisher, J. P.; Dean, D.; Engel, P. S.; Mikos, A. G. Photoinitiated polymerization of biomaterials. *Ann. Rev. Mater. Res.* **2001**, *31*, 171-181.

- Fitzgerald, M. B.; Shapiro, W. H.; McDonald, P. D.; Neuburger, H. S.; Ashburn-Reed, S.; Immerman, S.; Jethanamest, D.; Roland, J. T.; Svirsky, M. A. The effect of perimodiolar placement on speech perception and frequency discrimination by cochlear implant users. *Acta Otolaryngol.* **2007**, *127*, 378-383.
- Flanagan, L. A.; Ju, Y. E.; Marg, B.; Osterfield, M.; Janmey, P. A. Neurite branching on deformable substrates. *Neuroreport* **2002**, *13*, 2411-2415.
- Flanagan, L.; Ju, Y.; Marg, B.; Osterfield, M.; Janmey, P. Neurite branching on deformable substrates. *Neuroreport* **2002**, *13*, 2411-2415.
- Foley, J. D.; Grunwald, E. W.; Nealey, P. F.; Murphy, C. J. Cooperative modulation of neuritogenesis by PC12 cells by topography and nerve growth factor. *Biomaterials* **2005**, *26*, 3639-3644.
- Folkman, J.; Long, D. M. The use of Silicone Rubber as a Carrier for Prolonged Drug Therapy. *J. Surg. Res.* **1964**, *4*, 139-42.
- Fozdar, D. Y.; Lee, J. Y.; Schmidt, C. E.; Chen, S. Hippocampal neurons respond uniquely to topographies of various sizes and shapes. *Biofabrication* **2010**, *2*, 035005.
- Francisco, H.; Yellen, B. B.; Halverson, D. S.; Friedman, G.; Gallo, G. Regulation of axon guidance and extension by three-dimensional constraints. *Biomaterials* **2007**, *28*, 3398-3407.
- Frijns, J.; Briaire, J.; Grote, J. The importance of human cochlear anatomy for the results of modiolus-hugging multichannel cochlear implants. *Otol. Neurotol.* **2001**, *22*, 340-349.
- Frijns, J. H. M.; Kalkman, R. K.; Vanpoucke, F. J.; Bongers, J. S.; Briaire, J. J. Simultaneous and non-simultaneous dual electrode stimulation in cochlear implants: evidence for two neural response modalities. *Acta Otolaryngol.* **2009**, *129*, 433-439.
- Fu, R.; Wang, Y.; Liu, S.; Shih, T.; Lin, H.; Chen, Y.; Sung, J.; Lu, C.; Wei, J.; Wang, Z.; Huang, S.; Tsai, C.; Shyu, W.; Lin, S. Decellularization and Recellularization Technologies in Tissue Engineering. *Cell Trans.* **2014**, *23*, 621-630.
- Garini, Y.; Vermolen, B. J.; Young, I. T. From micro to nano: recent advances in high-resolution microscopy. *Curr. Opin. Biotechnol.* **2005**, *16*, 3-12.
- Gasiorowski, J. Z.; Liliensiek, S. J.; Russell, P.; Stephan, D. A.; Nealey, P. F.; Murphy, C. J. Alterations in gene expression of human vascular endothelial cells associated with nanotopographic cues. *Biomaterials* **2010**, *31*, 8882-8888.
- Gates, B.; Xu, Q.; Stewart, M.; Ryan, D.; Willson, C.; Whitesides, G. New approaches to nanofabrication: Molding, printing, and other techniques. *Chem. Rev.* **2005**, *105*, 1171-1196.

- Geisler, C. *From Sound to Synapse: Physiology of the Mammalian Ear*; Oxford University Press: New York, NY, **1998**.
- Gersuni, G. V.; Volokhov, A. A. On the electrical excitability of the auditory organ on the effect of alternating currents on the normal auditory apparatus. *J. Exp. Psychol.* **1936**, *19*, 370-382.
- Glockner, P.; Jung, T.; Struck, S.; Studer, K. *Radiation Curing for Coatings and Printing Inks: Technical Basics and Applications*; Vincentz Network GmbH & Co KG: Hannover, Germany, **2008**, 172.
- Glueckert, R.; Bitsche, M.; Miller, J. M.; Zhu, Y.; Prieskorn, D. M.; Altschuler, R. A.; Schrott-Fischer, A. Deafferentation-associated changes in afferent and efferent processes in the guinea pig cochlea and afferent regeneration with chronic intrascalar brain-derived neurotrophic factor and acidic fibroblast growth factor. *J. Comp. Neurol.* **2008**, *507*, 1602-1621.
- Göbbels, K.; Kuenzel, T.; van Ooyen, A.; Baumgartner, W.; Schnakenberg, U.; Bräunig, P. Neuronal cell growth on iridium oxide. *Biomaterials* **2010**, *31*, 1055-1067.
- Gomez, N.; Lu, Y.; Chen, S.; Schmidt, C. E. Immobilized nerve growth factor and microtopography have distinct effects on polarization versus axon elongation in hippocampal cells in culture. *Biomaterials* **2007**, *28*, 271-284.
- Greenberg, R. Analysis of electrical stimulation of the vertebrate retina - work towards a retinal prosthesis, The Johns Hopkins University, Baltimore, MD, **1998**.
- Griffith, L. G.; Naughton, G. Tissue engineering - Current challenges and expanding opportunities. *Science* **2002**, *295*, 1009-+.
- Gross, U.; Kinne, R.; Schmitz, H. J.; Strunz, V. The Response of Bone to Surface-Active Glasses Glass-Ceramics. *Crc Crit. Rev. Biocompat.* **1988**, *4*, 155-179.
- Guenther, E.; Troger, B.; Schlosshauer, B.; Zrenner, E. Long-term survival of retinal cell cultures on retinal implant materials. *Vision Res.* **1999**, *39*, 3988-3994.
- Gustavsson, P.; Johansson, F.; Kanje, M.; Wallman, L.; Linsmeier, C. E. Neurite guidance on protein micropatterns generated by a piezoelectric microdispenser. *Biomaterials* **2007**, *28*, 1141-1151.
- Hale, N. A.; Yang, Y.; Rajagopalan, P. Cell migration at the interface of a dual chemical-mechanical gradient. *ACS Appl. Mater. Interfaces* **2010**.
- Hansen, M. R.; Vijapurkar, U.; Koland, J. G.; Green, S. H. Reciprocal signaling between spiral ganglion neurons and Schwann cells involves neuregulin and neurotrophins. *Hear. Res.* **2001**, *161*, 87-98.

- Hansen, M. R.; Zha, X. M.; Bok, J.; Green, S. H. Multiple distinct signal pathways, including an autocrine neurotrophic mechanism, contribute to the survival-promoting effect of depolarization on spiral ganglion neurons in vitro. *J. Neurosci.* **2001**, *21*, 2256-2267.
- Hanson, J. N.; Motala, M. J.; Heien, M. L.; Gillette, M.; Sweedler, J.; Nuzzo, R. G. Textural guidance cues for controlling process outgrowth of mammalian neurons. *Lab Chip* **2009**, *9*, 122-131.
- Hao, Y.; Shih, H.; Muñoz, Z.; Kemp, A.; Lin, C. Visible light cured thiol-vinyl hydrogels with tunable degradation for 3D cell culture. *Acta Biomater.* **2014**, *10*, 104-114.
- Haq, F.; Anandan, V.; Keith, C.; Zhang, G. Neurite development in PC12 cells cultured on nanopillars and nanopores with sizes comparable with filopodia. *Int. J. Nanomed.* **2007**, *2*, 107-115.
- Hegarty, J.; Kay, A.; Green, S. Trophic support of cultured spiral ganglion neurons by depolarization exceeds and is additive with that by neurotrophins or cAMP and requires elevation of  $[Ca^{2+}]_i$  within a set range. *J. Neurosci.* **1997**, *17*, 1959-1970.
- Hench, L. L. Bioceramics - from Concept to Clinic. *J. Am. Ceram. Soc.* **1991**, *74*, 1487-1510.
- Hench, L. L.; Polak, J. M. Third-generation biomedical materials. *Science* **2002**, *295*, 1014-+.
- Hench, L. L.; Splinter, R. J.; Allen, W. C.; Greenlee, T. K. Bonding mechanisms at the interface of ceramic prosthetic materials. *J. Biomed. Mater. Res.* **1971**, *5*, 117-141.
- Hern, D. L.; Hubbell, J. A. Incorporation of adhesion peptides into nonadhesive hydrogels useful for tissue resurfacing. *J. Biomed. Mater. Res.* **1998**, *39*, 266-276.
- Hirono, T.; Torimitsu, K.; Kawana, A.; Fukuda, J. Recognition of artificial microstructures by sensory nerve-fibers in culture. *Brain Res.* **1988**, *446*, 189-194.
- Hoffman, A. S. The origins and evolution of "controlled" drug delivery systems. *J. Controlled Release* **2008**, *132*, 153-163.
- Hoffman-Kim, D.; Mitchel, J. A.; Bellamkonda, R. V. Topography, cell response, and nerve regeneration. *Annu. Rev. Biomed. Eng.* **2010**, *12*, 203-231.
- House, W. F.; Urban, J. Long-Term Results of Electrode Implantation and Electronic Stimulation of Cochlea in Man. *Ann. Otol. Rhinol. Laryngol.* **1973**, *82*, 504-517.
- Hsu, S. H.; Chen, C. Y.; Lu, P. S.; Lai, C. S.; Chen, C. J. Oriented Schwann cell growth on microgrooved surfaces. *Biotechnol. Bioeng.* **2005**, *92*, 579-588.

- Hsu, S.; Chen, C.; Lu, P. S.; Lai, C.; Chen, C. Oriented Schwann cell growth on microgrooved surfaces. *Biotechnol. Bioeng.* **2005**, *92*, 579-588.
- Hsu, S.; Lu, P. S.; Ni, H.; Su, C. Fabrication and evaluation of microgrooved polymers as peripheral nerve conduits. *Biomed. Microdevices* **2007**, *9*, 665-674.
- Hu, W. J.; Eaton, J. W.; Tang, L. P. Molecular basis of biomaterial-mediated foreign body reactions. *Blood* **2001**, *98*, 1231-1238.
- Huang Yan; Lue Xiaoying; Ma Jingwu; Huang Nan In vitro investigation of protein adsorption and platelet adhesion on inorganic biomaterial surfaces. *Appl. Surf. Sci.* **2008**, *255*, 257-259.
- Humayun, M. S.; Prince, M.; de Juan, E.; Barron, Y.; Moskowitz, M.; Klock, I. B.; Milam, A. H. Morphometric analysis of the extramacular retina from postmortem eyes with retinitis pigmentosa. *Invest. Ophthalmol. Vis. Sci.* **1999**, *40*, 143-148.
- Hume, P. S.; Anseth, K. S. Inducing local T cell apoptosis with anti-Fas-functionalized polymeric coatings fabricated via surface-initiated photopolymerizations. *Biomaterials* **2010**, *31*, 3166-3174.
- Humphries, J. D.; Byron, A.; Humphries, M. J. Integrin ligands at a glance. *J. Cell. Sci.* **2006**, *119*, 3901-3903.
- Hurtado, A.; Cregg, J. M.; Wang, H. B.; Wendell, D. F.; Oudega, M.; Gilbert, R. J.; McDonald, J. W. Robust CNS regeneration after complete spinal cord transection using aligned poly-L-lactic acid microfibers. *Biomaterials* **2011**, *32*, 6068-6079.
- Ijpm, F. F. A.; De Graaf, R. C. V.; Meek, M. F. The Early History of Tubulation in Nerve Repair. *J. Hand Surg. Euro. Vol.* **2008**, *33E*, 581-586.
- Jacchetti, E.; Di Rienzo, C.; Meucci, S.; Nocchi, F.; Beltram, F.; Cecchini, M. Wharton's Jelly human mesenchymal stem cell contact guidance by noisy nanotopographies. *Sci. Rep.* **2014**, *4*, 10.1038/srep03830.
- Jaegermann, P.; Lenzian, F.; Rist, G.; Mobius, K. Time-resolved ESR and endor during the photolysis of  $\omega,\omega$ -dimethoxy- $\omega$ -phenyl-acetophenone. *Chem. Phys. Lett.* **1987**, *140*, 615-619.
- Jeon, E.; Xu, N.; Xu, L.; Hansen, M. R. Influence of central glia on spiral ganglion neuron neurite growth. *Neuroscience* **2011**, *177*, 321-334.
- Jeon, S.; Menard, E.; Park, J.; Maria, J.; Meitl, M.; Zaumseil, J.; Rogers, J. Three-dimensional nanofabrication with rubber stamps and conformable photomasks. *Adv. Mater.* **2004**, *16*, 1369-1373.
- Johansson, F.; Carlberg, P.; Danielsen, N.; Montelius, L.; Kanje, M. Axonal outgrowth on nano-imprinted patterns. *Biomaterials* **2006**, *27*, 1251-1258.

- Jones, R. C.; Stevens, S. S.; Lurie, M. H. Three mechanisms of hearing by electrical stimulation. *J. Acoust. Soc. Am.* **1940**, *12*, 281-290.
- Kalil, K.; Dent, E. Touch and go: guidance cues signal to the growth cone cytoskeleton. *Curr. Opin. Neurobiol.* **2005**, *15*, 521-526.
- Kam, L.; Boxer, S. G. Cell adhesion to protein-micropatterned-supported lipid bilayer membranes. *J. Biomed. Mater. Res.* **2001**, *55*, 487-495.
- Kam, L.; Shain, W.; Turner, J.; Bizios, R. Axonal outgrowth of hippocampal neurons on micro-scale networks of polylysine-conjugated laminin. *Biomaterials* **2001**, *22*, 1049-1054.
- Kao, W. Y. Evaluation of protein-modulated macrophage behavior on biomaterials: designing biomimetic materials for cellular engineering. *Biomaterials* **1999**, *20*, 2213-2221.
- Kapoor, Y.; Thomas, J. C.; Tan, G.; John, V. T.; Chauhan, A. Surfactant-laden soft contact lenses for extended delivery of ophthalmic drugs. *Biomaterials* **2009**, *30*, 867-878.
- Karuri, N. W.; Liliensiek, S.; Teixeira, A. I.; Abrams, G.; Campbell, S.; Nealey, P. F.; Murphy, C. J. Biological length scale topography enhances cell-substratum adhesion of human corneal epithelial cells. *J. Cell. Sci.* **2004**, *117*, 3153-3164.
- Karuri, N. W.; Porri, T. J.; Albrecht, R. M.; Murphy, C. J.; Nealey, P. F. Nano- and Microscale Holes Modulate Cell-Substrate Adhesion, Cytoskeletal Organization, and Integrin Localization in Sv40 Human Corneal Epithelial Cells. *IEEE Trans. Nanobiosci.* **2006**, *5*, 273-280.
- Kaur, M.; Srivastava, A. K. Photopolymerization: A review. *J. Macromol. Sci-Polym. Rev.* **2002**, *C42*, 481-512.
- Kazemi, M.; Basham, E.; Sivaprakasam, M.; Wang, G.; Rodger, D.; Weiland, J.; Tai, Y. C.; Liu, W.; Humayun, M. A test microchip for evaluation of hermetic packaging technology for biomedical prosthetic implants. *IEEE Eng. Med. Biol. Soc.* **2004**, *6*, 4093-5.
- Kemppainen, J. M.; Hollister, S. J. Tailoring the mechanical properties of 3D-designed poly(glycerol sebacate) scaffolds for cartilage applications. *J. Biomed. Mater. Res. Part A* **2010**, *94A*, 9-18.
- Kenny, S. M.; Buggy, M. Bone cements and fillers: A review. *J. Mater. Sci. Mat. Med.* **2003**, *14*, 923-938.
- Khire, V. S.; Harant, A. W.; Watkins, A. W.; Anseth, K. S.; Bowman, C. N. Ultrathin patterned polymer films on surfaces using thiol-ene polymerizations. *Macromolecules* **2006**, *39*, 5081-5086.

- Khire, V. S.; Lee, T. Y.; Bowman, C. N. Surface modification using thiol-acrylate conjugate addition reactions. *Macromolecules* **2007**, *40*, 5669-5677.
- Kim, I. L.; Khetan, S.; Baker, B. M.; Chen, C. S.; Burdick, J. A. Fibrous hyaluronic acid hydrogels that direct MSC chondrogenesis through mechanical and adhesive cues. *Biomaterials* **2013**, *34*, 5571-5580.
- Kim, S. H.; Ha, H. J.; Ko, Y. K.; Yoon, S. J.; Rhee, J. M.; Kim, M. S.; Lee, H. B.; Khang, G. Correlation of proliferation, morphology and biological responses of fibroblasts on LDPE with different surface wettability. *J. Biomater. Sci.-Polym. Ed.* **2007**, *18*, 609-622.
- Klein, C. L.; Scholl, M.; Maelicke, A. Neuronal networks in vitro: formation and organization on biofunctionalized surfaces. *J. Mater. Sci. Mater. Med.* **1999**, *10*, 721-727.
- Kloxin, A. M.; Benton, J. A.; Anseth, K. S. In situ elasticity modulation with dynamic substrates to direct cell phenotype. *Biomaterials* **2010**, *31*, 1-8.
- Kloxin, A. M.; Kasko, A. M.; Salinas, C. N.; Anseth, K. S. Photodegradable hydrogels for dynamic tuning of physical and chemical properties. *Science* **2009**, *324*, 59-63.
- Knop, K.; Hoogenboom, R.; Fischer, D.; Schubert, U. S. Poly(ethylene glycol) in Drug Delivery: Pros and Cons as Well as Potential Alternatives. *Angew. Chem. Int. Ed.* **2010**, *49*, 6288-6308.
- Koh, H. S.; Yong, T.; Teo, W. E.; Chan, C. K.; Puhaindran, M. E.; Tan, T. C.; Lim, A.; Lim, B. H.; Ramakrishna, S. In vivo study of novel nanofibrous intra-luminal guidance channels to promote nerve regeneration. *J. Neural Eng.* **2010**, *7*, 046003.
- Kolff, W. J. The artificial kidney and its effect on the development of other artificial organs. *Nat. Med.* **2002**, *8*, 1063-1065.
- Kolff, W. J. Early years of artificial organs at the Cleveland Clinic - Part II: Open heart surgery and artificial hearts. *Asaio J.* **1998**, *44*, 123-128.
- Kong, H. J.; Polte, T. R.; Alsberg, E.; Mooney, D. J. FRET measurements of cell-traction forces and nano-scale clustering of adhesion ligands varied by substrate stiffness. *Proc. Natl. Acad. Sci. U. S. A.* **2005**, *102*, 4300-4305.
- Konofaos, P.; Halen, J. P. Nerve repair by means of tubulization: Past, present, future. *J. Reconstr. Microsurg.* **2013**, *29*, 149-163.
- Kubo, K.; Att, W.; Yamada, M.; Ohmi, K.; Tsukimura, N.; Suzuki, T.; Maeda, H.; Ogawa, T. Microtopography of titanium suppresses osteoblastic differentiation but enhances chondroblastic differentiation of rat femoral periosteum-derived cells. *J. Biomed. Mater. Res. Part A* **2008**, *87A*, 380-391.

- Kundu, A.; Micholt, L.; Friedrich, S.; Rand, D. R.; Bartic, C.; Braeken, D.; Levchenko, A. Superimposed topographic and chemical cues synergistically guide neurite outgrowth. *Lab Chip* **2013**, *13*, 3070-3081.
- Lampe, K. J.; Antaris, A. L.; Heilshorn, S. C. Design of three-dimensional engineered protein hydrogels for tailored control of neurite growth. *Acta Biomater.* **2013**, *9*, 5590-5599.
- Langer, R.; Vacanti, J. P. Tissue Engineering. *Science* **1993**, *260*, 920-926.
- Lauer, L.; Klein, C.; Offenhausser, A. Spot compliant neuronal networks by structure optimized micro-contact printing. *Biomaterials* **2001**, *22*, 1925-1932.
- Lawrence, B. D.; Cronin-Golomb, M.; Georgakoudi, I.; Kaplan, D. L.; Omenetto, F. G. Bioactive silk protein biomaterial systems for optical devices. *Biomacromolecules* **2008**, *9*, 1214-1220.
- Lawson, H. C.; Sampath, P.; Bohan, E.; Park, M. C.; Hussain, N.; Olivi, A.; Weingart, J.; Kleinberg, L.; Brem, H. Interstitial chemotherapy for malignant gliomas: the Johns Hopkins experience. *J. Neurooncol.* **2007**, *83*, 61-70.
- Leach, J. B.; Achyuta, A. K.; Murthy, S. K. Bridging the Divide between Neuroprosthetic Design, Tissue Engineering and Neurobiology. *Front. Neuroeng.* **2010**, *2*, 18.
- Leach, J. B.; Brown, X. Q.; Jacot, J. G.; DiMilla, P. A.; Wong, J. Y. Neurite outgrowth and branching of PC12 cells on very soft substrates sharply decreases below a threshold of substrate rigidity. *J. Neural Eng.* **2007**, *4*, 26-34.
- Leake, P. A.; Hradek, G. T. Cochlear Pathology of Long-Term Neomycin Induced Deafness in Cats. *Hear. Res.* **1988**, *33*, 11-34.
- Lee, D.; Choi, B.; Park, J.; Zhu, S.; Kim, B.; Huh, J.; Lee, S.; Jung, J.; Kim, S. Nerve regeneration with the use of a poly(L-lactide-co-glycolic acid)-coated collagen tube filled with collagen gel. *J. Craniomaxillofac. Surg.* **2006**, *34*, 50-56.
- Lee, J. H.; Lee, J. W.; Khang, G.; Lee, H. B. Interaction of cells on chargeable functional group gradient surfaces. *Biomaterials* **1997**, *18*, 351-358.
- Lee, K. Y.; Mooney, D. J. Hydrogels for tissue engineering. *Chem. Rev.* **2001**, *101*, 1869-1879.
- Lee, T. Y.; Guymon, C. A.; Jonsson, E. S.; Hait, S.; Hoyle, C. E. Synthesis, initiation, and polymerization of photoinitiating monomers. *Macromolecules* **2005**, *38*, 7529-7531.
- Lefebvre, P. P.; Leprince, P.; Weber, T.; Rigo, J. M.; Delree, P.; Moonen, G. Neuronotrophic Effect of Developing Otic Vesicle on Cochleovestibular Neurons - Evidence for Nerve Growth-Factor Involvement. *Brain Res.* **1990**, *507*, 254-260.

- Lefebvre, P. P.; Vandewater, T. R.; Weber, T.; Rogister, B.; Moonen, G. Growth-Factor interactions in cultures of dissociated adult acoustic ganglia - Neuronotrophic effects. *Brain Res.* **1991**, *567*, 306-312.
- Leng, T.; Wu, P.; Mehenti, N. Z.; Bent, S. F.; Marmor, M. F.; Blumenkranz, M. S.; Fishman, H. A. Directed retinal nerve cell growth for use in a retinal prosthesis interface. *Invest. Ophthalmol. Vis. Sci.* **2004**, *45*, 4132-4137.
- Lewis, K. J.; Anseth, K. S. Hydrogel scaffolds to study cell biology in four dimensions. *MRS Bull* **2013**, *38*, 260-268.
- Li, G. N.; Liu, J.; Hoffman-Kim, D. Multi-molecular gradients of permissive and inhibitory cues direct neurite outgrowth. *Ann. Biomed. Eng.* **2008**, *36*, 889-904.
- Li, J.; McNally, H.; Shi, R. Enhanced neurite alignment on micro-patterned poly-L-lactic acid films. *J. Biomed. Mater. Res. Part A* **2008**, *87A*, 392-404.
- Li, N.; Folch, A. Integration of topographical and biochemical cues by axons during growth on microfabricated 3-D substrates. *Exp. Cell Res.* **2005**, *311*, 307-316.
- Li, S.; Li, H.; Wang, Z. Orientation of spiral ganglion neurite extension in electrical fields of charge-balanced biphasic pulses and direct current in vitro. *Hear. Res.* **2010**, *267*, 111-118.
- Li, W.; Tuli, R.; Huang, X.; Laquerriere, P.; Tuan, R. Multilineage differentiation of human mesenchymal stem cells in a three-dimensional nanofibrous scaffold. *Biomaterials* **2005**, *26*, 5158-5166.
- Liliensiek, S. J.; Wood, J. A.; Yong, J.; Auerbach, R.; Nealey, P. F.; Murphy, C. J. Modulation of human vascular endothelial cell behaviors by nanotopographic cues. *Biomaterials* **2010**, *31*, 5418-5426.
- Lim, J. Y.; Donahue, H. J. Cell sensing and response to micro- and nanostructured surfaces produced by chemical and topographic patterning. *Tissue Eng.* **2007**, *13*, 1879-1891.
- Lin, C.; Anseth, K. S. PEG Hydrogels for the controlled release of biomolecules in regenerative medicine. *Pharm. Res.* **2009**, *26*, 631-643.
- Lo, C. M.; Wang, H. B.; Dembo, M.; Wang, Y. L. Cell movement is guided by the rigidity of the substrate. *Biophys. J.* **2000**, *79*, 144-152.
- Loeb, G. The functional replacement of the ear. *Sci. Am.* **1985**, *252*, 104-&.
- Loizou, P. C. Introduction to cochlear implants. *IEEE Eng. Med. Biol. Mag.* **1999**, *18*, 32-42.

- Lovell, L.; Berchtold, K.; Elliott, J.; Lu, H.; Bowman, C. Understanding the kinetics and network formation of dimethacrylate dental resins. *Polym. Adv. Technol.* **2001**, *12*, 335-345.
- Lu, H.; Stansbury, J. W.; Bowman, C. N. Towards the elucidation of shrinkage stress development and relaxation in dental composites. *Dental Mater.* **2004**, *20*, 979-986.
- Lu, M.; Hsiang, S.; Lai, T.; Yao, C.; Lin, L.; Chen, Y. Influence of cross-linking degree of a biodegradable genipin-cross-linked gelatin guide on peripheral nerve regeneration. *J. Biomat. Sci-Polym. E.* **2007**, *18*, 843-863.
- Lundborg, G. A 25-year perspective of peripheral nerve surgery: Evolving neuroscientific concepts and clinical significance. *J. Hand Surg. Am. Vol.* **2000**, *25A*, 391-414.
- Luo, N.; Metters, A.; Hutchison, J.; Bowman, C.; Anseth, K. A methacrylated photoiniferter as a chemical basis for microlithography: Micropatterning based on photografting polymerization. *Macromolecules* **2003**, *36*, 6739-6745.
- Lutolf, M. P.; Hubbell, J. A. Synthetic biomaterials as instructive extracellular microenvironments for morphogenesis in tissue engineering. *Nat. Biotechnol.* **2005**, *23*, 47-55.
- Mahoney, M. J.; Anseth, K. S. Three-dimensional growth and function of neural tissue in degradable polyethylene glycol hydrogels. *Biomaterials* **2006**, *27*, 2265-2274.
- Mahoney, M.; Chen, R.; Tan, J.; Saltzman, W. The influence of microchannels on neurite growth and architecture. *Biomaterials* **2005**, *26*, 771-778.
- Malgrange, B.; Lefebvre, P.; VandeWater, T. R. V.; Staecker, H.; Moonen, G. Effects of neurotrophins on early auditory neurones in cell culture. *Neuroreport* **1996**, *7*, 913-917.
- Marzella, P. L.; Gillespie, L. N.; Clark, G. M.; Bartlett, P. F.; Kilpatrick, T. J. The neurotrophins act synergistically with LIF and members of the TGF-beta superfamily to promote the survival of spiral ganglia neurons in vitro. *Hear. Res.* **1999**, *138*, 73-80.
- Mason, B. N.; Starchenko, A.; Williams, R. M.; Bonassar, L. J.; Reinhart-King, C. A. Tuning three-dimensional collagen matrix stiffness independently of collagen concentration modulates endothelial cell behavior. *Acta Biomater.* **2013**, *9*, 4635-4644.
- Masters, K. S.; Shah, D. N.; Leinwand, L. A.; Anseth, K. S. Crosslinked hyaluronan scaffolds as a biologically active carrier for valvular interstitial cells. *Biomaterials* **2005**, *26*, 2517-2525.

- Mata, A.; Kim, E. J.; Boehm, C. A.; Fleischman, A. J.; Muschler, G. F.; Roy, S. A three-dimensional scaffold with precise micro-architecture and surface micro-textures. *Biomaterials* **2009**, *30*, 4610-4617.
- Matsumoto, K.; Ohnishi, K.; Kiyotani, T.; Sekine, T.; Ueda, H.; Nakamura, T.; Endo, K.; Shimizu, Y. Peripheral nerve regeneration across an 80-mm gap bridged by a polyglycolic acid (PGA)-collagen tube filled with laminin-coated collagen fibers: a histological and electrophysiological evaluation of regenerated nerves. *Brain Res.* **2000**, *868*, 315-328.
- Mattotti, M.; Alvarez, Z.; Ortega, J. A.; Planell, J. A.; Engel, E.; Alcántara, S. Inducing functional radial glia-like progenitors from cortical astrocyte cultures using micropatterned PMMA. *Biomaterials* **2012**, *33*, 1759-1770.
- Mayer, M.; Yang, J.; Gitlin, I.; Gracias, D. H.; Whitesides, G. M. Micropatterned agarose gels for stamping arrays of proteins and gradients of proteins. *Proteomics* **2004**, *4*, 2366-2376.
- McCarthy, K.; Devellis, J. Preparation of separate astroglial and oligodendroglial cell-cultures from rat cerebral tissue. *J. Cell Biol.* **1980**, *85*, 890-902.
- McDermott, H.; McKay, C.; Vandali, A. A new portable sound processor for the University-Of-Melbourne Nucleus limited multielectrode cochlear implant. *J. Acoust. Soc. Am.* **1992**, *91*, 3367-3371.
- McDermott, H. J. Music perception with cochlear implants: a review. *Trends in Amp.* **2004**, *8*, 49-82.
- McMahon, T.; Zadnik, K. Twenty-five years of contact lenses - The impact on the cornea and ophthalmic practice. *Cornea* **2000**, *19*, 730-740.
- Mehenti, N. Z.; Peterman, M. C.; Leng, T.; Marmor, M. F.; Blumenkranz, M. S.; Bent, S. F. A retinal interface based on neurite micropatterning for single cell stimulation. *Invest. Ophthalmol. Vis. Sci.* **2003**, *44*, U704-U704.
- Metcalfe, A. D.; Ferguson, M. W. J. Tissue engineering of replacement skin: the crossroads of biomaterials, wound healing, embryonic development, stem cells and regeneration. *J. R. Soc. Interface* **2007**, *4*, 413-437.
- Mey, J.; Brook, G.; Hodde, D.; Kriebel, A. Electrospun Fibers as Substrates for Peripheral Nerve Regeneration. *Biomed. Appl. Poly. Nanofib.* **2012**, *246*, 131-170.
- Michelson, R. Electrical stimulation of human cochlea - Preliminary report. *Arch. Otolaryngol.* **1971**, *93*, 317-&.
- Micholt, L.; Gartner, A.; Prodanov, D.; Braeken, D.; Dotti, C. G.; Bartic, C. Substrate determines neuronal polarization and growth In Vitro. *PLoS One* **2013**, *8*, e66170.

- Miller, C.; Jeftinija, S.; Mallapragada, S. Synergistic effects of physical and chemical guidance cues on neurite alignment and outgrowth on biodegradable polymer substrates. *Tissue Eng.* **2002**, *8*, 367-378.
- Miller, C.; Jeftinija, S.; Mallapragada, S. Micropatterned Schwann cell-seeded biodegradable polymer substrates significantly enhance neurite alignment and outgrowth. *Tissue Eng.* **2001**, *7*, 705-715.
- Miller, J.; Chi, D.; O'Keefe, L.; Kruszka, P.; Raphael, Y.; Altschuler, R. Neurotrophins can enhance spiral ganglion cell survival after inner hair cell loss. *Int. J. Dev. Neurosci.* **1997**, *15*, 631-643.
- Miller, J. M.; Le Prell, C. G.; Prieskorn, D. M.; Wys, N. L.; Altschuler, R. A. Delayed neurotrophin treatment following deafness rescues spiral ganglion cells from death and promotes regrowth of auditory nerve peripheral processes: Effects of brain-derived neurotrophic factor and fibroblast growth factor. *J. Neurosci. Res.* **2007**, *85*, 1959-1969.
- Miyoshi, H.; Adachi, T.; Ju, J.; Lee, S. M.; Cho, D. J.; Ko, J. S.; Uchida, G.; Yamagata, Y. Characteristics of motility-based filtering of adherent cells on microgrooved surfaces. *Biomaterials* **2012**, *33*, 395-401.
- Moglia, R. S.; Robinson, J. L.; Muschenborn, A. D.; Touchet, T. J.; Maitland, D. J.; Cosgriff-Hernandez, E. Injectable polyMIPE scaffolds for soft tissue regeneration. *Polymer* **2014**, *55*, 426-434.
- Montezuma, S. R.; Loewenstein, J.; Scholz, C.; Rizzo, J. F. Biocompatibility of materials implanted into the subretinal space of Yucatan pigs. *Invest. Ophthalmol. Vis. Sci.* **2006**, *47*, 3514-3522.
- Morris, J. K.; Lin, W.; Hauser, C.; Marchuk, Y.; Getman, D.; Lee, K. Rescue of the cardiac defect in ErbB2 mutant mice reveals essential roles of ErbB2 in peripheral nervous system development. *Neuron* **1999**, *23*, 273-283.
- Moses, J. W.; Leon, M. B.; Popma, J. J.; Fitzgerald, P. J.; Holmes, D. R.; O'Shaughnessy, C.; Caputo, R. P.; Kereiakes, D. J.; Williams, D. O.; Teirstein, P. S.; Jaeger, J. L.; SIRIUS Investigators sirolimus-eluting stents versus standard stents in patients with stenosis in a native coronary artery. *N. Engl. J. Med.* **2003**, *349*, 1315-1323.
- Nadol, J.; Young, Y.; Glynn, R. Survival of spiral ganglion-cells in profound sensorineural hearing-loss - Implications for cochlear implantation. *Ann. Otol. Rhinol. Laryngol.* **1989**, *98*, 411-416.
- Nagata, I.; Nakatsuji, N. Rodent CNS neuroblasts exhibit both perpendicular and parallel contact guidance on the aligned parallel neurite bundle. *Development* **1991**, *112*, 581-590.

- Nakazawa, G.; Vorpahl, M.; Finn, A. V.; Narula, J.; Virmani, R. One step forward and two steps back with drug-eluting-stents from preventing restenosis to causing late thrombosis and nouveau atherosclerosis. *JACC-Cardiovas. Imag.* **2009**, *2*, 625-628.
- Neckers, D. Architecture with photopolymerization. *Polym. Eng. Sci.* **1992**, *32*, 1481-1489.
- Neubrand, V. E.; Thomas, C.; Schmidt, S.; Debant, A.; Schiavo, G. Kidins220/ARMS regulates Rac1-dependent neurite outgrowth by direct interaction with the RhoGEF Trio. *J. Cell Sci.* **2010**, *123*, 2111-2123.
- Nichol, J. W.; Koshy, S. T.; Bae, H.; Hwang, C. M.; Yamanlar, S.; Khademhosseini, A. Cell-laden microengineered gelatin methacrylate hydrogels. *Biomaterials* **2010**, *31*, 5536-5544.
- Norde, W.; Horbett, T. A.; Brash, J. L. In *Proteins at Interfaces III: Introductory Overview*; American Chemical Society: **2012**, *1120*, 1-34.
- Nurcombe, V. Laminin in neural development. *Pharmacol. Ther.* **1992**, *56*, 247-264.
- Odian, G. In *Determination of Absolute Rate Constants; Principles of Polymerization*; John Wiley & Sons Inc: Hoboken, New Jersey, **2004**, *4*, 264-271.
- O'Donnell, M.; Chance, R. K.; Bashaw, G. J. Axon growth and guidance: Receptor regulation and signal transduction. *Annu. Rev. Neurosci.* **2009**, *32*, 383-412.
- O'Leary, S. J.; Richardson, R. R.; McDermott, H. J. Principles of design and biological approaches for improving the selectivity of cochlear implant electrodes. *J. Neural Eng.* **2009**, *6*, 055002.
- Oliva, A. A.; James, C. D.; Kingman, C. E.; Craighead, H. G.; Banker, G. A. Patterning axonal guidance molecules using a novel strategy for microcontact printing. *Neurochem. Res.* **2003**, *28*, 1639-1648.
- Oliveira, S. M.; Song, W.; Alves, N. M.; Mano, J. F. Chemical modification of bioinspired superhydrophobic polystyrene surfaces to control cell attachment/proliferation RID A-4418-2009. *Soft Matter* **2011**, *7*, 8932-8941.
- Ong, A. T.; Serruys, P. W. Technology insight: an overview of research in drug-eluting stents. *Nat. Clin. Prac. Cardiovas. Med.* **2005**, *2*, 647-658.
- Paasche, G.; Tasche, C.; Stoeber, T.; Lesinski-Schiedat, A.; Lenarz, T. The long-term effects of modified electrode surfaces and intracochlear corticosteroids on postoperative impedances in cochlear implant patients. *Otol. Neurotol.* **2009**, *30*, 592-598.
- Pabari, A.; Yang, S. Y.; Seifalian, A. M.; Mosahebi, A. Modern surgical management of peripheral nerve gap. *J. Plas. Reconstruc. Aesth. Surg.* **2010**, *63*, 1941-1948.

- Palanker, D.; Vankov, A.; Huie, P.; Baccus, S. Design of a high-resolution optoelectronic retinal prosthesis. *J. Neural Eng.* **2005**, *2*, S105-20.
- Palchesko, R. N.; Zhang, L.; Sun, Y.; Feinberg, A. W. Development of polydimethylsiloxane substrates with tunable elastic modulus to study cell mechanobiology in muscle and nerve. *PLoS One* **2012**, *7*, e51499.
- Palmaz, J. C.; Sibbitt, R. R.; Reuter, S. R.; Garcia, F.; Tio, F. O. Expandable intrahepatic Portacaval-Shunt Stents - Early experience in the dog. *Am. J. Roentgenol.* **1985**, *145*, 821-825.
- Pameijer, C. H.; Zmener, O. Resin materials for root canal obturation. *Dent. Clin. North Am.* **2010**, *54*, 325-344.
- Park, J. S.; Chu, J. S.; Tsou, A. D.; Diop, R.; Tang, Z.; Wang, A.; Li, S. The effect of matrix stiffness on the differentiation of mesenchymal stem cells in response to TGF- $\beta$ . *Biomaterials* **2011**, *32*, 3921-3930.
- Patrick, J. F.; Busby, P. A.; Gibson, P. J. The development of the Nucleus Freedom Cochlear implant system. *Trends in Amp.* **2006**, *10*, 175-200.
- Peckham, P. H.; Keith, M. W.; Kilgore, K. L.; Grill, J. H.; Wuolle, K. S.; Thrope, G. B.; Gorman, P.; Hobby, J.; Mulcahey, M. J.; Carroll, S.; Hentz, V. R.; Wiegner, A.; Implantable neuroprosthesis Res Grp efficacy of an implanted neuroprosthesis for restoring hand grasp in tetraplegia: A multicenter study. *Arch. Phys. Med. Rehabil.* **2001**, *82*, 1380-1388.
- Peckham, P. H.; Knutson, J. S. Functional electrical stimulation for neuromuscular applications. *Annu. Rev. Biomed. Eng.* **2005**, *7*, 327-360.
- Peppas, N. A.; Hilt, J. Z.; Khademhosseini, A.; Langer, R. Hydrogels in biology and medicine: From molecular principles to bionanotechnology. *Adv. Mater.* **2006**, *18*, 1345-1360.
- Peterman, M.; Mehenti, N.; Bilbao, K.; Lee, C.; Leng, T.; Noolandi, J.; Bent, S.; Blumenkranz, M.; Fishman, H. The artificial synapse chip: A flexible retinal interface based on directed retinal cell growth and neurotransmitter stimulation. *Artif. Organs* **2003**, *27*, 975-985.
- Petrie, T. A.; Raynor, J. E.; Reyes, C. D.; Burns, K. L.; Collard, D. M.; Garcia, A. J. The effect of integrin-specific bioactive coatings on tissue healing and implant osseointegration. *Biomaterials* **2008**, *29*, 2849-2857.
- Pettingill, L. N.; Richardson, R. T.; Wise, A. K.; O'Leary, S. J.; Shepherd, R. K. Neurotrophic factors and neural prostheses: Potential clinical applications based upon findings in the auditory system. *IEEE Trans. Biomed. Eng.* **2007**, *54*, 1138-1148.

- Peyman, G.; Chow, A. Y.; Liang, C. P.; Chow, V. Y.; Perlman, J. I.; Peachey, N. S. Subretinal semiconductor microphotodiode array. *Ophthalmic Surg. Lasers* **1998**, *29*, 234-241.
- Pfingst, B. E.; Bowling, S. A.; Colesa, D. J.; Garadat, S. N.; Raphael, Y.; Shibata, S. B.; Strahl, S. B.; Su, G. L.; Zhou, N. Cochlear infrastructure for electrical hearing. *Hear. Res.* **2011**, *281*, 65-73.
- Phifer, C. B.; Terry, L. M. Use of hypothermia for general-anesthesia in preweanling rodents. *Physiol. Behav.* **1986**, *38*, 887-890.
- Popper, A.; Fay, R. *The Mammalian Auditory Pathway: Neurophysiology*; Springer-Verlag: New York, NY, **1991**.
- Promenade 'Round the Cochlea. Cross section of single turn of the cochlea, <http://www.neuroreille.com/promenade/english/cochlea/fcochlea.htm> (accessed July 3, **2014**).
- Quick, D. J.; Anseth, K. S. Gene delivery in tissue engineering: A photopolymer platform to coencapsulate cells and plasmid DNA. *Pharmaceut. Res.* **2003**, *20*, 1730-1737.
- Rajnicek, A. M.; Britland, S.; McCaig, C. D. Contact guidance of CNS neurites on grooved quartz: influence of groove dimensions, neuronal age and cell type. *J. Cell. Sci.* **1997**, *110*, 2905-2913.
- Ratner, B.; Hoffman, A.; Schoen, F.; Lemons, J. In *An Introduction to Materials in Medicine*; Academic Press: **2004**; pp 10-11.
- Ratner, B. D.; Bryant, S. J. Biomaterials: Where we have been and where we are going. *Annu. Rev. Biomed. Eng.* **2004**, *6*, 41-75.
- Rebscher, S. J.; Hetherington, A.; Bonham, B.; Wardrop, P.; Whinney, D.; Leake, P. A. Considerations for design of future cochlear implant electrode arrays: Electrode array stiffness, size, and depth of insertion. *J. Rehabil. Res. Dev.* **2008**, *45*, 731-747.
- Rho, J. Y.; Ashman, R. B.; Turner, C. H. Young's modulus of trabecular and cortical bone material: Ultrasonic and microtensile measurements. *J. Biomech.* **1993**, *26*, 111-119.
- Richardson, J. A.; Rementer, C. W.; Bruder, J. M.; Hoffman-Kim, D. Guidance of dorsal root ganglion neurites and Schwann cells by isolated Schwann cell topography on poly(dimethyl siloxane) conduits and films. *J. Neural Eng.* **2011**, *8*, 046015.
- Richardson, R. T.; Noushi, F.; O'Leary, S. Inner ear therapy for neural preservation. *Audiol. Neurootol.* **2006**, *11*, 343-356.

- Richardson, R. T.; Wise, A. K.; Thompson, B. C.; Flynn, B. O.; Atkinson, P. J.; Fretwell, N. J.; Fallon, J. B.; Wallace, G. G.; Shepherd, R. K.; Clark, G. M.; O'Leary, S. J. Polypyrrole-coated electrodes for the delivery of charge and neurotrophins to cochlear neurons. *Biomaterials* **2009**, *30*, 2614-2624.
- Richter, B.; Aschendorff, A.; Lohnstein, P.; Husstedt, H.; Nagursky, H.; Laszig, R. The Nucleus Contour electrode array: A radiological and histological study. *Laryngoscope* **2001**, *111*, 508-514.
- Ridley, N. Intraocular acrylic lenses. *Trans. Ophthalmol. Soc. U. K.* **1951**, 617-621.
- Ripoll, C.; Rebillard, G. A simple technique to efficiently dissociate primary auditory neurons from 5 day-old rat cochleas. *J. Neurosci. Methods* **1997**, *73*, 123-128.
- Rizzo, J. F.; Wyatt, J.; Humayun, M.; de Juan, E.; Liu, W. T.; Chow, A.; Eckmiller, R.; Zrenner, E.; Yagi, T.; Abrams, G. Retinal prosthesis - An encouraging first decade with major challenges ahead. *Ophthalmol.* **2001**, *108*, 13-14.
- Roehm, P.; Hansen, M. Strategies to preserve or regenerate spiral ganglion neurons. *Curr. Opin. Otolaryngol. Head Neck Surg.* **2005**, *13(5)*, 294-300.
- Roehm, P. C.; Xu, N.; Woodson, E. A.; Green, S. H.; Hansen, M. R. Membrane depolarization inhibits spiral ganglion neurite growth via activation of multiple types of voltage sensitive calcium channels and calpain. *Mol. Cell. Neurosci.* **2008**, *37*, 376-387.
- Roessler, G.; Laube, T.; Brockmann, C.; Kirschkamp, T.; Mazinani, B.; Goertz, M.; Koch, C.; Krisch, I.; Sellhaus, B.; Trieu, H. K.; Weis, J.; Bornfeld, N.; Roethgen, H.; Messner, A.; Mokwa, W.; Walter, P. Implantation and explantation of a wireless epiretinal retina implant device: Observations during the EPIRET3 prospective clinical trial. *Invest. Ophthalmol. Vis. Sci.* **2009**, *50*, 3003-3008.
- Rubinstein, J. T. How cochlear implants encode speech. *Curr. Opin. Otolaryngol. Head Neck Surg.* **2004**, *12*, 444-8.
- Rydholm, A. E.; Held, N. L.; Benoit, D. S. W.; Bowman, C. N.; Anseth, K. S. Modifying network chemistry in thiol-acrylate photopolymers through postpolymerization functionalization to control cell-material interactions. *J. Biomed. Mater. Res. Part A* **2008**, *86A*, 23-30.
- Sakaguchi, H.; Fujikado, T.; Fang, X. Y.; Kanda, H.; Osanai, M.; Nakauchi, K.; Ikuno, Y.; Kamei, M.; Yagi, T.; Nishimura, S.; Ohji, M.; Yagi, T.; Tano, Y. Transretinal electrical stimulation with a suprachoroidal multichannel electrode in rabbit eyes. *Jpn. J. Ophthalmol.* **2004**, *48*, 256-261.
- Sarig-Nadir, O.; Livnat, N.; Zajdman, R.; Shoham, S.; Seliktar, D. Laser photoablation of guidance microchannels into hydrogels directs cell growth in three dimensions. *Biophys. J.* **2009**, *96*, 4743-4752.

- Schmalenberg, K. E.; Uhrich, K. E. Micropatterned polymer substrates control alignment of proliferating Schwann cells to direct neuronal regeneration. *Biomaterials* **2005**, *26*, 1423-1430.
- Schmid, H.; Michel, B. Siloxane polymers for high-resolution, high-accuracy soft lithography. *Macromolecules* **2000**, *33*, 3042-3049.
- Schmidt, R. C.; Healy, K. E. Controlling biological interfaces on the nanometer length scale. *J. Biomed. Mater. Res. Part A* **2009**, *90A*, 1252-1261.
- Shandurina, A. N.; Panin, A. V.; Sologubova, E. K.; Kolotov, A. V.; Goncharenko, O. I.; Nikol'skii, A. V.; Logunov VYu Results of the use of therapeutic periorbital electrostimulation in neurological patients with partial atrophy of the optic nerves. *Neurosci. Behav. Physiol.* **1996**, *26*, 137-42.
- Shannon, R. V.; Fu, Q. J.; Galvin, J. The number of spectral channels required for speech recognition depends on the difficulty of the listening situation. *Acta Otolaryngol. Suppl.* **2004**, (552), 50-54.
- Shepherd, R. K.; Roberts, L. A.; Paolini, A. G. Long-term sensorineural hearing loss induces functional changes in the rat auditory nerve. *Eur. J. Neurosci.* **2004**, *20*, 3131-3140.
- Shibata, S. B.; Budenz, C. L.; Bowling, S. A.; Pflugst, B. E.; Raphael, Y. Nerve maintenance and regeneration in the damaged cochlea. *Hear. Res.* **2011**, *281*, 56-64.
- Shin, H. S.; Kim, H. J.; Min, S. K.; Kim, S. H.; Lee, B. M.; Jeon, N. L. Compartmental culture of embryonic stem cell-derived neurons in microfluidic devices for use in axonal biology. *Biotechnol. Lett.* **2010**, *32*, 1063-1070.
- Shintani, K.; Shechtman, D. L.; Gurwood, A. S. Review and update: Current treatment trends for patients with retinitis pigmentosa. *Optom. J. Am. Optom. Assoc.* **2009**, *80*, 384-401.
- Simmons, F. B. Electrical Stimulation of Auditory Nerve in Man. *Arch. Otolaryngol.* **1966**, *84*, 2-&.
- Simmons, F. B.; Epley, J. M.; Lummis, R. C.; Guttman, N.; Frishkop. L.; Harmon, L. D.; Zwicker, E. Auditory Nerve - Electrical Stimulation in Man. *Science* **1965**, *148*, 104.
- Singh, A. V.; Patil, R.; Thombre, D. K.; Gade, W. N. Micro-nanopatterning as tool to study the role of physicochemical properties on cell-surface interactions. *J. Biomed. Mater. Res. Part A* **2013**, *101*, 3019-3032.
- Singhvi, R.; Kumar, A.; Lopez, G. P.; Stephanopoulos, G. N.; Wang, D. I.; Whitesides, G. M.; Ingber, D. E. Engineering cell-shape and function. *Science* **1994**, *264*, 696-698.

- Singhvi, R.; Stephanopoulos, G.; Wang, D. I. Effects of substratum morphology on cell physiology - Review. *Biotechnol. Bioeng.* **1994**, *43*, 764-771.
- Sly, D. J.; Heffer, L. F.; White, M. W.; Shepherd, R. K.; Birch, M. G.; Minter, R. L.; Nelson, N. E.; Wise, A. K.; O'Leary, S. J. Deafness alters auditory nerve fibre responses to cochlear implant stimulation. *Eur. J. Neurosci.* **2007**, *26*, 510-522.
- Smith, D. M.; Li, C. Y.; Bunning, T. J. Light-directed mesoscale phase separation via holographic polymerization. *J. Poly. Sci. Part B Poly. Phys.* **2014**, *52*, 232-250.
- Snik, A. F.; Mylanus, E. A.; Cremers, C. W. The bone-anchored hearing aid - A solution for previously unresolved otologic problems. *Otolaryngol. Clin. North Am.* **2001**, *34*, 365.
- Snyder, R. L.; Middlebrooks, J. C.; Bonham, B. H. Cochlear implant electrode configuration effects on activation threshold and tonotopic selectivity. *Hear. Res.* **2008**, *235*, 23-38.
- Snyder, R. L.; Middlebrooks, J. C.; Bonham, B. H. Cochlear implant electrode configuration effects on activation threshold and tonotopic selectivity. *Hear. Res.* **2008**, *235*, 23-38.
- Solouk, A.; Cousins, B. G.; Mirzadeh, H.; Solati-Hashtjin, M.; Najarian, S.; Seifalian, A. M. Surface modification of POSS-nanocomposite biomaterials using reactive oxygen plasma treatment for cardiovascular surgical implant applications. *Biotechnol. Appl. Biochem.* **2011**, *58*, 147-161.
- Song, M.; Uhrich, K. E. Optimal micropattern dimensions enhance neurite outgrowth rates, lengths, and orientations. *Ann. Biomed. Eng.* **2007**, *35*, 1812-1820.
- Sousa, J. E.; Serruys, P. W.; Costa, M. A. New frontiers in cardiology - Drug-eluting stents: Part I. *Circulation* **2003**, *107*, 2274-2279.
- Sousa, J. E.; Serruys, P. W.; Costa, M. A. New frontiers in cardiology - Drug-eluting stents: Part II. *Circulation* **2003**, *107*, 2383-2389.
- Spivey, E. C.; Khaing, Z. Z.; Shear, J. B.; Schmidt, C. E. The fundamental role of subcellular topography in peripheral nerve repair therapies. *Biomaterials* **2012**, *33*, 4264-4276.
- Spoendlin, H. Retrograde Degeneration of Cochlear Nerve. *Acta Otolaryngol.* **1975**, *79*, 266-275.
- St John, P.; Davis, R.; Cady, N.; Czajka, J.; Batt, C.; Craighead, H. Diffraction-based cell detection using a microcontact printed antibody grating. *Anal. Chem.* **1998**, *70*, 1108-1111.

- Staecker, H.; Kopke, R.; Malgrange, B.; Lefebvre, P.; VandeWater, T. NT-3 and/or BDNF therapy prevents loss of auditory neurons following loss of hair cells. *Neuroreport* **1996**, *7*, 889-894.
- Stansbury, J. W. Curing dental resins and composites by photopolymerization. *J. Esthet. Dent.* **2000**, *12*, 300-8.
- Stansbury, J. W.; Bowman, C. N.; Newman, S. M. Shining a light on dental composite restoratives. *Phys Today* **2008**, *61*, 82-83.
- Sterman, S.; Marsden, J. G. Silane coupling agents. *Ind. Eng. Chem.* **1966**, *58*, 33.
- Stett, A.; Mai, A.; Herrmann, T. Retinal charge sensitivity and spatial discrimination obtainable by subretinal implants: Key lessons learned from isolated chicken retina. *J. Neural Eng.* **2007**, *4*, S7-S16.
- Stevens, S. S. On hearing by electrical stimulation. *J. Acoust. Soc. Am.* **1937**, *8*, 191-195.
- Stevens, S. S.; Jones, R. C. The mechanism of hearing by electrical stimulation. *J. Acoust. Soc. Am.* **1939**, *10*, 261-269.
- Straley, K. S.; Foo, C. W.; Heilshorn, S. C. Biomaterial design strategies for the treatment of spinal cord injuries. *J. Neurotrauma* **2010**, *27*, 1-19.
- Sun, T.; Kovac, J.; Voldman, J. Image-based single-cell sorting via dual-photopolymerized microwell arrays. *Anal. Chem.* **2014**, *86*, 977-981.
- Sundararaghavan, H. G.; Monteiro, G. A.; Firestein, B. L.; Shreiber, D. I. Neurite growth in 3D collagen gels with gradients of mechanical properties. *Biotechnol. Bioeng.* **2009**, *102*, 632-643.
- Tamada, Y.; Ikada, Y. Cell adhesion to plasma-treated polymer surfaces. *Polymer* **1993**, *34*, 2208-2212.
- Tang, L. P.; Eaton, J. W. Fibrin(ogen) mediates acute inflammatory responses to biomaterials. *J. Exp. Med.* **1993**, *178*, 2147-2156.
- Tawfick, S.; De Volder, M.; Copic, D.; Park, S. J.; Oliver, C. R.; Polsen, E. S.; Roberts, M. J.; Hart, A. J. Engineering of micro- and nanostructured surfaces with anisotropic geometries and properties. *Adv. Mater.* **2012**, *24*, 1628-1674.
- Tehranirokh, M.; Kouzani, A. Z.; Francis, P. S.; Kanwar, J. R. Microfluidic devices for cell cultivation and proliferation. *Biomicrofluidics* **2013**, *7*, 051502.
- Teixeira, A. I.; Abrams, G. A.; Bertics, P. J.; Murphy, C. J.; Nealey, P. F. Epithelial contact guidance on well-defined micro- and nanostructured substrates. *J. Cell. Sci.* **2003**, *116*, 1881-1892.

- Teixeira, A. I.; McKie, G. A.; Foley, J. D.; Berticsc, P. J.; Nealey, P. F.; Murphy, C. J. The effect of environmental factors on the response of human corneal epithelial cells to nanoscale substrate topography. *Biomaterials* **2006**, *27*, 3945-3954.
- Teixeira, A.; McKie, G.; Foley, J.; Berticsc, P.; Nealey, P.; Murphy, C. The effect of environmental factors on the response of human corneal epithelial cells to nanoscale substrate topography. *Biomaterials* **2006**, *27*, 3945-3954.
- Tjellstrom, A.; Hakansson, B.; Granstrom, G. Bone-anchored hearing aids - Current status in adults and children. *Otolaryngol. Clin. North Am.* **2001**, *34*, 337.
- Toba, T.; Nakamura, T.; Shimizu, Y.; Matsumoto, K.; Ohnishi, K.; Fukuda, S.; Yoshitani, M.; Ueda, H.; Hori, Y.; Endo, K. Regeneration of canine peroneal nerve with the use of a polyglycolic acid-collagen tube filled with laminin-soaked collagen sponge: A comparative study of collagen sponge and collagen fibers as filling materials for nerve conduits. *J. Biomed. Mater. Res.* **2001**, *58*, 622-630.
- Totonelli, G.; Maghsoudlou, P.; Fishman, J. M.; Orlando, G.; Ansari, T.; Sibbons, P.; Birchall, M. A.; Pierro, A.; Eaton, S.; De Coppi, P. Esophageal tissue engineering: A new approach for esophageal replacement. *World J. Gastroenterol.* **2012**, *18*, 6900-6907.
- Tuft, B. W.; Li, S.; Xu, L.; Clarke, J. C.; White, S. P.; Guymon, B. A.; Perez, K. X.; Hansen, M. R.; Guymon, C. A. Photopolymerized microfeatures for directed spiral ganglion neurite and Schwann cell growth. *Biomaterials* **2013**, *34*, 42-54.
- Tuft, B. W.; Xu, L.; White, S. P.; Seline, A. E.; Erwood, A. M.; Hansen, M. R.; Guymon, C. A. Neural pathfinding on uni- and multidirectional photopolymerized micropatterns. *ACS Appl. Mater. Interfaces* **2014**, [dx.doi.org/10.1021/am501622a](https://doi.org/10.1021/am501622a)
- Tykocinski, M.; Cohen, L. T.; Cowan, R. S. Measurement and analysis of access resistance and polarization impedance in cochlear implant recipients. *Otol. Neurotol.* **2005**, *26*, 948-956.
- Tykocinski, M.; Cohen, L. T.; Pyman, B. C.; Roland, T.; Treaba, C.; Palamara, J.; Dahm, M. C.; Shepherd, R. K.; Xu, J.; Cowan, R. S.; Cohen, N. L.; Clark, G. M. Comparison of electrode position in the human cochlea using various perimodiolar electrode arrays. *Am. J. Otol.* **2000**, *21*, 205-211.
- Tykocinski, M.; Cohen, L.; Pyman, B.; Roland, T.; Treaba, C.; Palamara, J.; Dahm, M.; Shepherd, R.; Xu, J.; Cowan, R.; Cohen, N.; Clark, G. Comparison of electrode position in the human cochlea using various perimodiolar electrode arrays. *Am. J. Otol.* **2000**, *21*, 205-211.
- Uludag, H.; De Vos, P.; Tresco, P. A. Technology of mammalian cell encapsulation. *Adv. Drug Deliv. Rev.* **2000**, *42*, 29-64.

- Vallet-Regi, M.; Balas, F.; Arcos, D. Mesoporous materials for drug delivery. *Angew. Chem. Int. Ed.* **2007**, *46*, 7548-7558.
- van der Beek, F. B.; Boermans, P. P.; Verbist, B. M.; Briaire, J. J.; Frijns, J. H. Clinical evaluation of the clarion CII HiFocus 1 with and without positioner. *Ear Hear.* **2005**, *26*, 577-592.
- Virmani, R.; Farb, A. Pathology of in-stent restenosis. *Curr. Opin. Lipidol.* **1999**, *10*, 499-506.
- Walba, D. M.; Liberko, C. A.; Korblova, E.; Farrow, M.; Furtak, T. E.; Chow, B. C.; Schwartz, D. K.; Freeman, A. S.; Douglas, K.; Williams, S. D.; Klitnick, A. F.; Clark, N. A. Self-assembled monolayers for liquid crystal alignment: simple preparation on glass using alkyltrialkoxysilanes. *Liq. Cryst.* **2004**, *31*, 481-489.
- Walsh, J.; Manwaring, M.; Tresco, P. Directional neurite outgrowth is enhanced by engineered meningeal cell-coated substrates. *Tissue Eng.* **2005**, *11*, 1085-1094.
- Wang, X.; Hu, W.; Cao, Y.; Yao, J.; Wu, J.; Gu, X. Dog sciatic nerve regeneration across a 30-mm defect bridged by a chitosan/PGA artificial nerve graft. *Brain* **2005**, *128*, 1897-1910.
- Wang, Y.; Chen, C. S. Cell adhesion and mechanical stimulation in the regulation of mesenchymal stem cell differentiation. *J. Cell. Mol. Med.* **2013**, *17*, 823-832.
- Wangensteen, K. J.; Kalliainen, L. K. Collagen tube conduits in peripheral nerve repair: A retrospective analysis. *Hand (N. Y)* **2009**.
- Weetall, H. H. Preparation of immobilized proteins covalently coupled through silane coupling agents to inorganic supports. *Appl. Biochem. Biotechnol.* **1993**, *41*, 157-188.
- White, R. L. Review of current status of cochlear prostheses. *IEEE Trans. Biomed. Eng.* **1982**, *29*, 233-238.
- Whitton, D. S.; Tieu, D.; Grover, M.; Reilly, B.; Coulson, M. T. Spontaneous association of glial cells with regrowing neurites in mixed cultures of dissociated spiral ganglia. *Neuroscience* **2009**, *161*, 227-235.
- Wikipedia. Cochlear Implant. [http://en.wikipedia.org/wiki/Cochlear\\_implant](http://en.wikipedia.org/wiki/Cochlear_implant) (accessed July 3, **2014**).
- Wikipedia. Scanning Electron Microscope. [http://en.wikipedia.org/w/index.php?title=Scanning\\_electron\\_microscope&oldid=608525556](http://en.wikipedia.org/w/index.php?title=Scanning_electron_microscope&oldid=608525556) (accessed June 8, **2014**).
- Williams, D. Definitions in biomaterials. *Proc. Cons. Conf. Euro. Soc. Biomater.* **1987**, *4*.

- Willson, C.; Trinquet, B. The evolution of materials for the photolithographic process. *J. Photopolym. Sci. Tech.* **2003**, *16*, 621-627.
- Wilson, B. S.; Dorman, M. F. Cochlear implants: A remarkable past and a brilliant future. *Hear. Res.* **2008**, *242*, 3-21.
- Wilson, C. J.; Clegg, R. E.; Leavesley, D. I.; Percy, M. J. Mediation of biomaterial-cell interactions by adsorbed proteins: A review. *Tissue Eng.* **2005**, *11*, 1-18.
- Winter, J. O.; Cogan, S. F.; Rizzo J. F. Retinal prostheses: current challenges and future outlook. *J. Biomat. Sci-Polym. E.* **2007**, *18*, 1031-1055.
- Wise, A. K.; Richardson, R.; Hardman, J.; Clark, G.; O'Leary, S. Resprouting and survival of guinea pig cochlear neurons in response to the administration of the neurotrophins brain-derived neurotrophic factor and neurotrophin-3. *J. Comp. Neurol.* **2005**, *487*, 147-165.
- Wise, A.; Hume, C.; Flynn, B.; Jeelall, Y.; Suhr, C.; Sgro, B.; O'Leary, S.; Shepherd, R.; Richardson, R. Effects of localized neurotrophin gene expression on spiral ganglion neuron resprouting in the deafened cochlea. *Mol. Ther.* **2010**.
- Wittig, J. H.; Ryan, A. F.; Asbeck, P. M. A reusable microfluidic plate with alternate-choice architecture for assessing growth preference in tissue culture. *J. Neurosci. Methods* **2005**, *144*, 79-89.
- Worthington, K. S.; Wiley, L. A.; Bartlett, A. M.; Stone, E. M.; Mullins, R. F.; Salem, A. K.; Guymon, C. A.; Tucker, B. A. Mechanical properties of murine and porcine ocular tissues in compression. *Exp. Eye Res.* **2014**, *121*, 194-199.
- Wright, A.; Davis, A.; Bredberg, G.; Ulehlova, L.; Spencer, H.; Bock, G.; Felix, H.; Iurato, S.; Johnsson, L. G.; Pauler, M. Hair cell distributions in the normal human cochlea. *Acta Otolaryngol.* **1987**, 1-48.
- Wylie, R. G.; Ahsan, S.; Aizawa, Y.; Maxwell, K. L.; Morshead, C. M.; Shoichet, M. S. Spatially controlled simultaneous patterning of multiple growth factors in three-dimensional hydrogels. *Nat. Mater.* **2011**, *10*, 799-806.
- Wylie, R. G.; Shoichet, M. S. Three-dimensional spatial patterning of proteins in hydrogels. *Biomacromolecules* **2011**, *12*, 3789-3796.
- Xiao, Y.; Friis, E. A.; Gehrke, S. H.; Detamore, M. S. Mechanical testing of hydrogels in cartilage tissue engineering: Beyond the compressive modulus. *Tissue Eng. Part B Rev.* **2013**, *19*, 403-412.
- Yagci, Y.; Jockusch, S.; Turro, N. J. Photoinitiated polymerization: Advances, challenges, and opportunities. *Macromolecules* **2010**, *43*, 6245-6260.

- Yao, L.; Pandit, A.; Yao, S.; McCaig, C. D. Electric field-guided neuron migration: A novel approach in neurogenesis. *Tissue Eng. Part B Rev.* **2011**, *17*, 143-153.
- Yao, L.; Wang, S.; Cui, W.; Sherlock, R.; O'Connell, C.; Damodaran, G.; Gorman, A.; Windebank, A.; Pandit, A. Effect of functionalized micropatterned PLGA on guided neurite growth. *Acta Biomater.* **2009**, *5*, 580-588.
- Yim, E. K.; Pang, S. W.; Leong, K. W. Synthetic nanostructures inducing differentiation of human mesenchymal stem cells into neuronal lineage. *Exp. Cell Res.* **2007**, *313*, 1820-1829.
- Ylikoski, J.; Pirvola, U.; Moshnyakov, M.; Palgi, J.; Arumäe, U.; Saarna, M. Expression patterns of neurotrophin and their receptor mRNAs in the rat inner ear. *Hear. Res.* **1993**, *65*, 69-78.
- Yoshii, S.; Oka, M. Collagen filaments as a scaffold for nerve regeneration. *J. Biomed. Mater. Res.* **2001**, *56*, 400-405.
- Yoshii, S.; Oka, M.; Shima, M.; Taniguchi, A.; Akagi, M. Bridging a 30-mm nerve defect using collagen filaments. *J. Biomed. Mater. Res. Part A* **2003**, *67A*, 467-474.
- Young, J.; Fox, S.; Anseth, K. A novel device for producing three-dimensional objects. *J. Manufac. Sci. Eng. Trans. ASME* **1999**, *121*, 474-477.
- Yu, L. M.; Miller, F. D.; Shoichet, M. S. The use of immobilized neurotrophins to support neuron survival and guide nerve fiber growth in compartmentalized chambers. *Biomaterials* **2010**, *31*, 6987-6999.
- Yu, T. T.; Shoichet, M. S. Guided cell adhesion and outgrowth in peptide-modified channels for neural tissue engineering. *Biomaterials* **2005**, *26*, 1507-1514.
- Zeng, F.; Rebscher, S.; Harrison, W.; Sun, X.; Feng, H. Cochlear implants: system design, integration, and evaluation. *IEEE Rev. Biomed. Eng.* **2008**, *1*, 115-42.
- Zheng, J. L.; Gao, W. Q. Differential damage to auditory neurons and hair cells by ototoxins and neuroprotection by specific neurotrophins in rat cochlear organotypic cultures. *Eur. J. Neurosci.* **1996**, *8*, 1897-1905.
- Zhu, J. Bioactive modification of poly(ethylene glycol) hydrogels for tissue engineering. *Biomaterials* **2010**, *31*, 4639-4656.
- Zwiers, R.; Dortant, G. Aspherical lenses produced by a fast high-precision replication process using UV-curable coatings. *Appl. Opt.* **1985**, *24*, 4483-4488.
- Zwolan, T.; Kileny, P.; Smith, S.; Mills, D.; Koch, D.; Osberger, M. Adult cochlear implant patient performance with evolving electrode technology. *Otol. Neurotol.* **2001**, *22*, 844-849.

Zysset, P. K.; Edward G. X.; Hoffer, E. C.; Moore, K. E.; Goldstein, S. A. Elastic modulus and hardness of cortical and trabecular bone lamellae measured by nanoindentation in the human femur. *J. Biomech.* **1999**, *32*, 1005-1012.